Mechanisms of Delivery and Mode of Action of Type VI Secretion System Effectors

Inauguraldissertation
zur
Erlangung der Würde eines Doktors der Philosophie
vorgelegt der
Philosophisch-Naturwissenschaftlichen Fakultät
der Universität Basel

von
Peter David Ringel
aus den Vereinigten Staaten von Amerika und Deutschland

Basel, 2018

Genehmigt von der Philosophisch-Naturwissenschaftlichen Fakultät

auf Antrag von

Prof. Dr. Marek Basler
Fakultätsverantwortlicher und Dissertationsleiter

Prof. Dr. Urs Jenal
Korreferent

Basel, den 12.12.2017

Prof. Dr. Martin Spiess
Dekan

It's not what you look at that matters, it's what you see.

Henry David Thoreau

Summary

In order to manipulate their environment, bacteria evolved a diverse set of secretion systems. Three of these were found to be able to inject their substrates directly into target cells, the type VI secretion system (T6SS) being the most recently discovered of these. The T6SS shares structural and functional homology with other contractile nanomachines such as the contractile phages. It is capable of delivering its substrates into both pro- and eukaryotes in a contact dependent manner and has become a major player in the field of microbial interactions. Recently, medium and high resolution structural data of T6SS subcomplexes and *in situ* structures provided detailed mechanistic insights into its functioning, further supported by live cell fluorescence microscopy of the assembly dynamics. Nonetheless, the role of some of the conserved core components is not yet fully understood even less so for the associated components. Moreover, despite its implication in numerous processes, the effector repertoire remains poorly characterized.

In this thesis, both the effector repertoire and the functional contribution of selected T6SS components were characterized in *Acinetobacter baylyi* ADP1. We developed a new scarless chromosomal mutagenesis method for *A. baylyi* ADP1 and fluorescently labeled structural components of the T6SS using this method. Furthermore, we constructed in-frame deletions of selected T6SS components and evaluated their role by observing the T6SS dynamics, secretion capacity, target cell lysis and the ability to inhibit a competitor. The results of the fluorescence microscopy in combination with the sensitive lysis assay show that certain components, previously thought to be required for T6SS assembly, are in fact dispensable. Furthermore, we observed that most mutations which diminished the T6SS activity reduced the number of active T6SS structures but did not affect the sheath dynamics. This indicates, that these components are involved in a step preceding the contractile tail formation. Despite ongoing concerted efforts, we were so far unable to fluorescently label secreted components.

We identified and characterized five cargo effectors and their corresponding immunity proteins. One of the effectors was disrupted by an insertion element and could be restored. All five effectors exhibited antibacterial activity and did not cross-react with non-cognate immunity proteins. The morphological changes of prey cells targeted by the effectors were observed by fluorescence microscopy of competition mixtures and allowed us to confirm the predicted peptidoglycan amidase activity of Tae1 and the phospholipase activity of

Tle1. Although the bioinformatic predictions together with the observed morphological changes and the lysis phenotype of prey cells targeted by the remaining effectors hinted at the subcellular location of their respective targets, the targets themselves remain to be identified. Furthermore, we constructed an effector deficient strain which retained wild-type T6SS activity and elicited the retaliatory attack of *Pseudomonas aeruginosa*, but failed to inhibit or lyse prey cells. Transcriptome data further indicated, that the damage inflicted by the effector deficient strain does not induce a stress response in the prey.

Recently the T6SS was shown to be involved in the horizontal gene transfer of naturally competent *Vibrio cholerae*. Since *A. baylyi* ADP1 is known to be naturally competent, we tested whether its T6SS also contributes to horizontal gene transfer. Not only could we demonstrate that the T6SS facilitates the acquisition of DNA from prey cells, but also that lytic effectors are superior to non-lytic effectors suggesting that a lytic effector set may increase the ability to acquire DNA from a diverse range of bacteria. These findings provide further evidence that the T6SS mediated horizontal gene transfer may be a general characteristic of naturally competent bacteria bearing a T6SS.

To better understand the role of the T6SS in shaping polymicrobial communities, we employed individual based modelling of interbacterial competition mixtures, the results of which we confirmed by performing the corresponding bacterial competition. We found that the contact dependent antagonistic interactions led to a segregation of the competitors minimizing their contact surface. Once segregated, the prey cells were able to survive or even outgrow the attack of a predator so long as the growth within the domain equaled or outweighed the killing on the surface of the domain. We further demonstrated that this critical domain size, beyond which the prey would survive, depends on the growth rate ratio of the competitors and the attack rate. Recently, others showed that this segregation of the competitors promotes the evolution of public goods.

Contents

Chapter I

Introduction

I.1 Introduction

The compartmentalization achieved by biological membranes, protein structures and other biomolecules forming cell envelopes, allows for reactions to take place in a confined space and thus under controllable conditions. All prokaryotes possess a cytoplasmic membrane whilst diderm bacteria (Gupta, 1998) additionally possess an outer membrane enclosing the periplasmic space. In order for membrane impermeable substances to enter or leave these compartments, a large number of translocation systems and channels have evolved. To date, nine secretion systems have been discovered (Desvaux et al., 2009; Lasica et al., 2017). In addition to translocating substrates across the own cell envelope, these may also be injected into target cells to manipulate them to the benefit of the injecting cell. So far, only three secretion systems are known to be able to inject their substrates into a target cell, which are the non-flagellar type III secretion system (T3SS) (Deng et al., 2017), the type IV secretion system (T4SS) (Christie et al., 2014) and the type VI secretion system (T6SS) (Alteri and Mobley, 2016).

I.1.1 The non-flagellar type III secretion system

Since its discovery in *Yersinia* in 1990 by the group of Guy Cornelis (Michiels et al., 1990), the T3SS has attracted significant attention due to its pivotal role in the virulence of devastating diseases such as plague (Plano and Schesser, 2013) and typhoid fever (Kaur and Jain, 2012). Nevertheless, the T3SS may also contribute to symbiotic interactions as shown for *Rhizobium* legume interactions (Fauvart and Michiels, 2008; Viprey et al., 1998). The T3SS likely evolved from the bacterial flagellum and shares both sequence and structural as well as functional homology with the flagellar system (Abby and Rocha, 2012). It consists of three parts, a cytoplasmic complex, a large envelope spanning basal body and the extracellular needle or pilus, protruding from the basal body and carrying a tip complex at the end (Portaliou et al., 2016). Although the T3SSs of different bacteria have been visualized by electron microscopy, the cytoplasmic complex was usually lacking (Deng et al., 2017; Kubori et al., 1998). Recently, the *in situ* molecular architecture of the SPI-1 T3SS of *Salmonella enterica* was dissected using cryo-electron tomography by comparing the structures obtained with tagged components and from deletion mutants with those of the wild type. This yielded very detailed structural data of the cytoplasmic complex and of the remaining secretion system (Hu et al., 2017). In another study, the T3SS of *Chlamydia* could be observed *in situ* both in contact with the membrane of the eukaryotic host and in absence of the contact, providing an unprecedented view of the structural

rearrangements induced upon binding (Nans et al., 2015). After the needle contacts the target cell membrane, a translocation pore is established and the injection of effectors is triggered (Armentrout and Rietsch, 2016; Blocker et al., 1999; Cherradi et al., 2013; Guignot and Tran Van Nhieu, 2016; Murillo et al., 2016; Nans et al., 2015; Russo et al., 2016; Veenendaal et al., 2007). The cytoplasmic complex is thought to constitute the sorting platform which recruits the substrates for secretion (Hu et al., 2015; Lara-Tejero et al., 2011; Makino et al., 2016). The substrates are then secreted in a partially unfolded state through the basal body and the narrow needle into the target cell (Dohlich et al., 2014; Fujii et al., 2012; Loquet et al., 2012; Radics et al., 2013). A fascinating insight into the effector translocation was gained through the observation of T3SS structures with trapped effectors by cryo-electron microscopy (Dohlich et al., 2014; Radics et al., 2013). While the unfolding of the substrate is mostly energized by ATP hydrolysis, the actual secretion seems to be powered by the proton motif force (Akeda and Galán, 2005; Erhardt et al., 2014; Lee and Rietsch, 2015; Wilharm et al., 2004). The secretion of the substrates and effectors is strictly hierarchical, both in time and sequence, especially because some of the effectors have antagonistic activities (Büttner, 2012; Mills et al., 2008). The effector repertoire is very diverse and each effector set is tailored to fulfill a specific function. Many effectors manipulate central cellular processes such as cytoskeletal dynamics, host immune responses and signal transduction pathways (Büttner, 2012, 2016; van der Heijden and Finlay, 2012; Raymond et al., 2013). It should be noted that some data suggest the existence of a two-step mechanism in which neither the translocon nor the effectors are directly incorporated into the target cell by the T3SS (Akopyan et al., 2011; Edgren et al., 2012).

I.1.2 The type IV secretion system

The T4SSs are a diverse family of secretion systems which can inject substrates into both eu- and prokaryotes. Moreover, their substrates are not restricted to proteins and may originate from either the cytoplasm or the periplasm (Gonzalez-Rivera et al., 2016; Locht et al., 2011; Pantoja et al., 2002). Apart from functioning as injection system, there are also T4SSs, which secrete DNA into the extracellular space as in *Neisseria gonorrhoeae* (Hamilton et al., 2005) or even take up DNA like in *Helicobacter pylori* (Hofreuter et al., 2001). Similarly, effector proteins, such as pertussis toxin, may be secreted into the extracellular medium instead of being injected (Locht et al., 2011).

In Gram-negative bacteria the T4SS consists of an envelope spanning complex and an extracellular pilus. Electron microscopy revealed, that the envelope spanning complex

consists of a large outer membrane complex which is connected to the inner membrane complex by a thin stalk, but it remains unclear from where in this structure the pilus emanates (Ghosal et al., 2017; Low et al., 2014; Redzej et al., 2017). Whether the pilus serves as a conduit or only as an attachment device is still under debate, although it has been demonstrated, that conjugation can take place without requiring direct cell contact (Babić et al., 2008; Shu et al., 2008; Trokter et al., 2014). The translocation and unfolding of substrates is powered by cytoplasmic ATPases (Christie et al., 2014).

A well known class of T4SSs are the conjugation systems, which primarily inject single stranded DNA coupled to carrier proteins (Ilangovan et al., 2015; Lederberg and Tatum, 1953). The transfer of mobile genetic elements (MGEs) and integrative and conjugative elements (ICEs) has significantly contributed to the spread of antibiotic resistances and pathogenicity islands (Juhas, 2015). Additionally, the T4SS can inject DNA into eukaryotes where it may be integrated into the chromosome. The integration is facilitated by the accompanying proteins. A prototypical example of this is *Agrobacterium tumefaciens* which induces tumorigenesis in plants by injecting and integrating oncogenic T-DNA (Pitzschke and Hirt, 2010).

The diversity of the T4SSs is also reflected in its effector repertoire and may range from a single proteinaceous effector, exemplified by *H. pylori* which only injects the oncoprotein CagA (Backert et al., 2015), to over 300 different effectors injected by *Legionella pneumophila* in order to create a customized intracellular niche (So et al., 2015). However, T4SSs can also inject other substrates such as components of the peptidoglycan (Suarez et al., 2015; Viala et al., 2004). Recently the first T4SS which is able to kill bacteria by translocating toxic effectors was identified in *Xanthomonas* (Souza et al., 2015).

Overall this functional plasticity likely makes the T4SS one of the most versatile macromolecular translocation systems.

I.1.3 The type VI secretion system

The T6SS is the most recently discovered injection system (Pukatzki et al., 2006). Prior to the discovery of the T6SS, phenotypes of mutants, now known to abolish T6SS activity, had been reported (Bladergroen et al., 2003; Enos-Berlage et al., 2005; Folkesson et al., 2002; Nano et al., 2004; Parsons and Heffron, 2005; Potvin et al., 2003; Roest et al., 1997; Srinivasa Rao et al., 2004; Wang et al., 1998; Williams et al., 1996). These results and others derived from *in vivo* transcriptional profiling (Das et al., 2000; Golovliov et al.,

1997) initiated an *in silico* analysis of what became known as IcmF associated homologous proteins (IAHP) (Das and Chaudhuri, 2003). With the discovery of the T6SS in a screen for *Vibrio cholerae* virulence factors of non-O1/O139 strains conferring resistance to unicellular eukaryote predation (Pukatzki et al., 2006) it was shown, that IAHP clusters encode T6SSs. Gene clusters encoding T6SSs are found in >25 % of sequenced Gram-negative bacteria with a high prevalence among proteobacteria (Bingle et al., 2008; Shrivastava and Mande, 2008). Additionally, secretion systems related to the proteobacterial T6SS were discovered in *Francisella* (de Bruin et al., 2007), *Bacteroidetes* (Russell et al., 2014) and *Amoebophilus asiaticus* (Böck et al., 2017). Together these form four distinct phylogenetic groups, of which the proteobacterial group can further be subdivided into six subgroups (Barret et al., 2011, 2013; Boyer et al., 2009). Multiple T6SSs may be encoded on a genome, up to six were found in *Burkholderia pseudomallei* (Shalom et al., 2007), each of which can have a distinct role such as targeting bacteria or eukaryotes (Schwarz et al., 2010).

IAHP were initially implicated to be involved in host association and interaction (Bladergroen et al., 2003; Das and Chaudhuri, 2003; Folkesson et al., 2002; Moore et al., 2002; Srinivasa Rao et al., 2004). Early work on the T6SS supported this assumption (Brzuszkiewicz et al., 2006; Dudley et al., 2006; Mougous et al., 2006; Pukatzki et al., 2006, 2007; Schell et al., 2007; Seshadri et al., 2006; Shalom et al., 2007; Zheng and Leung, 2007). Shortly thereafter it had been recognized that T6SSs are not necessarily restricted to pathogenic or symbiotic species, although it was unknown, which role the T6SS may have in such cases (Bingle et al., 2008; Boyer et al., 2009; Persson et al., 2009). The discovery of the antibacterial activity of a T6SS in *Pseudomonas aeruginosa* opened a whole new perspective (Hood et al., 2010). Since then, the T6SS has been implicated to participate in a wide variety of processes, the most prominent of which remain to be pathogenicity (Hachani et al., 2016) and interbacterial competition (Alcoforado Diniz et al., 2015).

I.1.4 Structure and function of the type VI secretion system

The canonical proteobacterial T6SSs consist of 13 conserved components (type six secretion [Tss] components) and a variable number of accessory proteins (*tss*-associated gene [Tag] components) (Boyer et al., 2009; Lin et al., 2013; Shalom et al., 2007; Weber et al., 2016; Zheng and Leung, 2007; Zheng et al., 2011). It was found to share structural and functional homologies with contractile structures such as contractile bacteriophages (Leiman et al., 2009; Lossi et al., 2011, 2013; Pell et al., 2009; Pukatzki et al., 2007) or

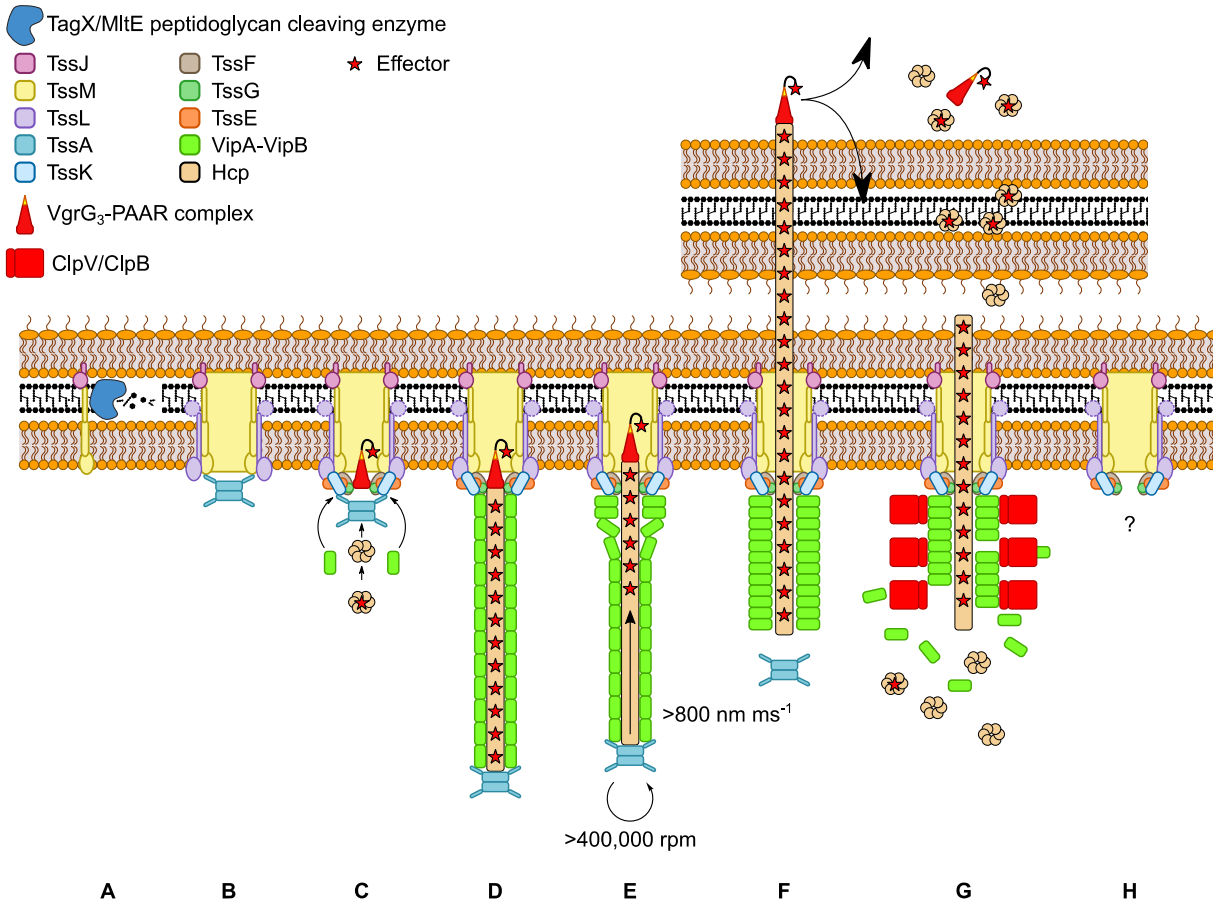

Figure I.1.1: Model of the T6SS structure and dynamics
(A) First TssJ associates with TssM which recruits an enzyme to locally degrade the peptidoglycan. (B) The TssJM complex forms and associates with TssA and TssL. The baseplate comlex forms on the basis of the envelope spanning complex, possibly assisted by TssA, consisting of TssE, TssF, TssG, TssK and a VgrG trimer with a PAAR tip protein, both associated with their respective effectors. (C-D) This likely induces the co-polymerization of the inner Hcp tube and the contractile sheath, consisting of VipA-VipB heterodimers, in the extended state. The Hcp hexamers may also carry effectors. The subunits are added at the end distal to the baseplate during the co-polymerization which is facilitated by TssA. (E) The sheath contracts propelling the inner tube and the spike complex with their associated effectors into the extracellular space or into the target cell. The contraction is envisioned to progress as a wave along the sheath starting from the baseplate. (F) The effectors are delivered to the cytoplasm and the periplasm of the target cell. (G) The contracted sheath is recycled in an ATP dependent manner by ClpV. Likely the Hcp subunits which were not ejected can be reused. (H) The fate of the membrane complex is not yet clear. Some evidence suggests that it may be reused. For a detailed explanation please see the main text.

R-type pyocins (Ge et al., 2015) as recently confirmed by solving the structure of the T6SS in contracted (Clemens et al., 2015; Kudryashev et al., 2015) and also in extended conformation (Chang et al., 2017; Wang et al., 2017) by cryo electron microscopy (cryo-EM) and cryo electron tomography (cryo-ET) respectively. The T6SS is thought to consist of three distinct subassemblies, the envelope spanning complex, the baseplate complex and the contractile tail (see Fig. I.1.1).

I.1.4.1 The envelope spanning complex

Results obtained by fluorescence microscopy suggest, that the assembly of a T6SS starts with the envelope spanning complex (Brunet et al., 2015; Durand et al., 2015; Gerc et al.,

2015; Zoued et al., 2016). First, the outer membrane protein TssJ (Aschtgen et al., 2008) associates with the inner membrane protein TssM, together spanning the envelope (Felisberto-Rodrigues et al., 2011; Zheng and Leung, 2007). Even though some TssM homologs bear a Walker A or B motif, the hydrolysis of ATP is only required in some species like *A. tumefaciens* (Ma et al., 2009b, 2012) and is dispensable in others like *Edwardsiella tarda* (Zheng and Leung, 2007).

The usual peptidoglycan pores are too small to accommodate the entire envelope spanning complex, but recently an outer membrane bound lytic transglycosylase (Santin and Cascales, 2017) and a membrane bound L-alanyl-D-glutamic acid carboxypeptidase (Weber et al., 2016) were described to form the required pores by locally degrading the peptidoglycan. However, these enzymes are not universally conserved and are not necessarily encoded in the T6SS clusters (Santin and Cascales, 2017).

The TssJM envelope spanning complex was shown to recruit TssA (Zoued et al., 2016). Thereafter or concomitantly TssL associates with the TssJMA complex (Aschtgen et al., 2010a, 2010b, 2012; Durand et al., 2012, 2015; Ma et al., 2009b; Zheng and Leung, 2007; Zoued et al., 2016). The structure of the assembled TssJML envelope spanning complex has been solved with a resolution of 11.6 Å using negative stain EM, revealing a C_5 symmetric structure containing ten copies of each of the proteins (Durand et al., 2015). This complex may be anchored to the peptidoglycan either by a peptidoglycan binding domain carried by TssL, then referred to as evolved TssL (Ma et al., 2009b), or by an accessory component, which may also be membrane bound like TagL (Aschtgen et al., 2010b) or constitute a periplasmic protein like TagN (Aschtgen et al., 2010a). Even though it has been hypothesized, that the peptidoglycan binding domains anchor the T6SS to the cell wall in order to withstand the forces generated by the injection event, it should be noted, that there are species lacking a component with an obvious peptidoglycan binding domain like *V. cholerae* and *E. tarda* (Aschtgen et al., 2010a). Recently it has been demonstrated, that peptidoglycan is dispensable for T6SS activity in *V. cholerae* (Vettiger et al., 2017).

I.1.4.2 The baseplate complex

On the basis of the envelope spanning complex the baseplate complex forms, consisting of TssE (Basler et al., 2012; Kudryashev et al., 2015; Lossi et al., 2011; Zoued et al., 2016), TssF, TssG (Logger et al., 2016), TssK (Brunet et al., 2015; English et al., 2014; Zoued et al., 2013), VgrG (Brunet et al., 2015), and in some organisms also a TssA variant

(Planamente et al., 2016). VgrG was first to be recognized as a potential component of the baseplate due to its homology with the $(gp27)_3$-$(gp5)_3$ tail spike/hub complex of the T4 phage. VgrGs form trimeric complexes, whose tips are further sharpened by a PAAR protein (Brunet et al., 2015; Hachani et al., 2011; Leiman et al., 2009; Pukatzki et al., 2007; Rigard et al., 2016; Shneider et al., 2013; Spínola-Amilibia et al., 2016; Sycheva et al.; Uchida et al., 2014). Furthermore, the VgrG trimers serve as polymerization base for the Hcp tube (Brunet et al., 2014; Lin et al., 2013). Shortly thereafter, TssE was proposed to constitute a component of the T6SS baseplate structure, because it shares significant homology with gp25, which forms a part of the T4 phage baseplate wedge, and because it could be co-purified with the contractile T6SS tail (Basler et al., 2012; Brackmann et al., 2017a; Leiman et al., 2009; Lossi et al., 2011). Moreover, TssE was shown to interact with the cytoplasmic domain of TssL (Zoued et al., 2016). The baseplate protein forming most interactions is TssK, which was shown to form trimers and to interact with the cytoplasmic domains of TssL and TssM as well as TssA (English et al., 2014; Logger et al., 2016; Nguyen et al., 2017; Zoued et al., 2013). Additionally, it could be demonstrated, that TssK interacts with a subcomplex formed by TssF and TssG while these do not interact with TssK individually (Brunet et al., 2015; English et al., 2014). Moreover, TssK interacts with VipB and Hcp, which are part of the contractile tail structure (Zoued et al., 2013). As already mentioned, TssF and TssG are required to form a subcomplex in order to interact with TssK, which is also required for their interaction with VgrG (Brunet et al., 2015; English et al., 2014). Nevertheless, both TssF and TssG can form certain interactions independent of one another. Apart from TssG, TssF was demonstrated to interact with TssE and Hcp (Brunet et al., 2015). TssG on the other hand interacts with the cytoplasmic domain of TssM as well as TssE, VipB and Hcp (Brunet et al., 2015; Logger et al., 2016). On the basis of the T4 baseplate structure, TssF was recently found to share homology with gp6 and TssG with gp7 (Brunet et al., 2015; Taylor et al., 2016). Furthermore, in accordance with this structural model, it was possible to purify a TssE-$TssF_2$-TssG-$TssK_3$ complex, which was proposed to constitute a baseplate wedge (English et al., 2014; Taylor et al., 2016). Thereafter, the structure of the baseplate complex was solved at a resolution of 8.0 Å by cryo-EM, allowing for a more detailed model (Nazarov et al., 2018). According to the stoichiometry derived from the volume-to-mass ratio, the baseplate complex consists of six copies of TssE, TssF homo-dimers and TssG, which is likely connected to the membrane complex by six TssK homo-trimers, overall forming a C_6 symmetric structure around the trimeric VgrG-PAAR complex (Nazarov et al., 2018). This is in agreement with the

previous model derived from the T4 baseplate structure (Nazarov et al., 2018; Taylor et al., 2016). This structure also provides a cavity to accommodate multiple effectors decorating the spike complex of up to approx. 450 kDa (Nazarov et al., 2018). Moreover, the N-terminal parts of the TssK trimer have been reported to form a structure similar to that of the receptor-binding protein (RBP) of siphophages, which binds to the remaining baseplate complex, while the C-terminus binds to the envelope spanning complex, strongly suggesting, that TssK evolved to connect the phage like baseplate complex to the envelope spanning complex (Nazarov et al., 2018; Nguyen et al., 2017). However, it is unclear how the C_6 symmetric baseplate structure can bind to the C_5 symmetric envelope spanning complex (Durand et al., 2015; Nazarov et al., 2018).

A special role was attributed to TssA, which is thought to be involved in priming and possibly recruiting the components not only of the baseplate structure, but also the contractile tail, which will be addressed later on, and was shown to interact with the TssJM complex, TssE, TssK as well as VgrG, Hcp and VipB (English et al., 2014; Zoued et al., 2016, 2017). TssA was described to form a homo-dodecamer with D_6 symmetry, and although TssJLM-TssA complexes could be observed by negative-stain EM, it remains unclear, how the symmetry mismatch towards the C_5 symmetric TssJLM complex is accounted for (Durand et al., 2015; Zoued et al., 2016, 2017).

It should be noted however, that another protein, also termed TssA, sharing the N-terminal ImpA_N domain (PF06812), but differing in its C-terminal part, was proposed to constitute a component of the baseplate complex (Planamente et al., 2016). From here on, this protein will be referred to as TssA1, in the absence of which there was no detectable Hcp1, VgrG1a and Tse3 secretion (Planamente et al., 2016). Nevertheless, fluorescence microscopy revealed the formation of fluorescently labeled TssB1 foci, even in the absence of TssA1, suggesting that, although to a reduced extent, T6SS structures are still able to form (Planamente et al., 2016). TssA1 was shown to interact with the baseplate components TssF, TssK and VgrG as well as the contractile tail components VipA and Hcp (Planamente et al., 2016). Immunogold-labeling localized TssA1 at one of the contracted VipA-VipB sheath ends (Planamente et al., 2016). Furthermore, TssA1 was shown to interact with ClpV, possibly indicating, that TssA1 may be recycled by ClpV in a fashion similar to the contracted sheath (Planamente et al., 2016).

Finally, there is yet another TssA variant, termed TagA, also bearing the N-terminal ImpA_N domain, while the C-terminus contains a putative transmembrane domain and a VasL domain, the role of which remains to be elucidated (Zoued et al., 2017).

Some of the above described protein interactions are not easily reconcilable with the putative localization and function derived from phage baseplate homologs (recently reviewed in (Brackmann et al., 2017b)). These interactions may be reminiscent of intermediate steps or transient complexes, forming throughout the assembly of the respective complexes. Yet, it should be kept in mind, that this conundrum may arise simply because the interactions were often determined by co-immunoprecipitation and bacterial two hybrid assays, which by themselves gave differing results for different fusion constructs.

I.1.4.3 The contractile tail

Once the baseplate structure has formed on the base of the envelope spanning complex, the contractile sheath assembles on it. The formation of the contractile tail complex is thought to progress as a co-polymerization of the inner Hcp tube with the contractile sheath in its extended conformation (Basler, 2015; Brunet et al., 2014). Hcp shares homology with gpV of the λ phage, which is not a contractile phage, and gp19 of the T4 phage, which forms the spike tube (Leiman et al., 2009; Mougous et al., 2006; Pell et al., 2009). Depending on the concentration, Hcp forms stable homo-hexameric rings in solution (Jobichen et al., 2010; Lim et al., 2015; Mougous et al., 2006; Ruiz et al., 2015; Silverman et al., 2013). The crystal packing gave differing results as to how the Hcp homo-hexameric subunits stack to form a tube (Douzi et al., 2014; Filippova et al.; Jobichen et al., 2010; Lim et al., 2015; Mougous et al., 2006; Osipiuk et al., 2011; Ruiz et al., 2015). By specifically introducing cysteines and crosslinking these by oxidation, polymeric Hcp tubes could be obtained, in which the homo-hexameric rings were stacked in a head to tail fashion (Ballister et al., 2008; Brunet et al., 2014; Douzi et al., 2014). Using engineered Hcp variants bearing cysteines, which allowed the discrimination between the different stacking modes, it could be demonstrated, that the head to tail stacking is likely the productive form, while other forms arise in absence of any of the baseplate proteins (Brunet et al., 2014, 2015). Based on the predictions, these structures would assemble by linear head to tail stacking of the Hcp homo-hexamers, leading to tubes lacking helicity (Brunet et al., 2014). As elaborated below, the surrounding contractile sheath, with which Hcp interacts, exhibits helicity, which would lead to a mismatch between the Hcp tube and the contractile sheath. Recent cryo-ET and cryo-EM

data of extended T6SS structures revealed, that *in vivo* Hcp tubes have the same helical parameters as the surrounding contractile sheath (Chang et al., 2017; Wang et al., 2017). The absence of higher polymers of Hcp homo-hexamers in solution and the low affinity of the Hcp homo-hexamers towards themselves suggest, that the Hcp tube is stabilized by the surrounding contractile sheath (Douzi et al., 2014).

This contractile sheath is composed of hexamers of VipA-VipB heterodimers, forming a six stranded helical tube, the core of which shares structural homology with other contractile systems such as the T4 phage (Basler et al., 2012; Bönemann et al., 2009; Chang et al., 2017; Clemens et al., 2015; Kudryashev et al., 2015; Leiman et al., 2009; Lossi et al., 2013; Wang et al., 2017). Due to its homology with gp25, which forms part of the T4 baseplate wedge, and recent structural data, TssE was proposed to form the base for the polymerization of the contractile sheath (Kudryashev et al., 2015). Although often described to be essential, more sensitive assays revealed, that secretion competent T6SS structures can form even in the absence of TssE, albeit with a much lower frequency (Basler et al., 2012; Brunet et al., 2015; Vettiger and Basler, 2016; Weber et al., 2016; Zheng et al., 2011). The breakthrough observation of the assembly, contraction and disassembly of VipA-sfGFP fluorescently labeled contractile sheath *in vivo* provided first evidence for the inverted contractile phage mechanism; this was previously proposed based on structural homologies of T6SS components (Basler et al., 2012). Furthermore, the authors were able to observe two different conformations of the contractile tail by cryo-ET, one of which was narrower, longer and supposedly filled by the Hcp tube, the other was broader, shorter and apparently hollow (Basler et al., 2012). The long, narrow and filled form was proposed to represent the extended state, whereas the short, broad and empty form was proposed to represent the contracted state of the contractile tail (Basler et al., 2012). By now, both the contracted and extended contractile tail structures could be solved, providing clear evidence for the inverted contractile phage model (Chang et al., 2017; Clemens et al., 2015; Kube et al., 2014; Kudryashev et al., 2015; Wang et al., 2017).

Using an elegant fluorescence recovery after photobleaching (FRAP) experiment it was recently demonstrated, that contractile sheath subunits are exclusively incorporated at the end distal to the baseplate (Vettiger et al., 2017). Furthermore, the authors provide convincing evidence that, at least in *V. cholerae*, there is no regulation of the contractile T6SS tail length, which can elongate up to several micrometers in spheroplasts, limited only by the cell size (Vettiger et al., 2017). Fluorescence microscopy revealed, that after

the recruitment of the baseplate complex, the TssA homo-dodecamer remains attached to the growing end of the contractile tail structure (Zoued et al., 2016). The authors postulate, that apart from its involvement in the formation of the baseplate, TssA primes and coordinates the polymerization of the contractile tail of the T6SS (Zoued et al., 2016). The central part of the TssA homo-dodecamer consists of head-to-head stacked homo-hexamers, formed by the C-terminal parts of the TssA subunits. These hexamers consist of six triangular wedges which were hypothesized to allow Hcp passage upon rearrangement, further supported by the interaction of this domain with Hcp and VgrG (Zoued et al., 2016). Furthermore, in addition to the interaction of TssA with VipB, molecular docking of TssA to an extended and contracted sheath model suggested a higher binding affinity to the extended state, which the authors propose may indicate, that TssA stabilizes the extended conformation of the sheath retaining it in a metastable configuration (Zoued et al., 2016). The exact mechanism of the tail-subunit incorporation remains to be elucidated (Zoued et al., 2016, 2017).

I.1.4.4 The sheath contraction

What exactly triggers the contraction of the sheath is still unclear, however, in analogy to T4 phage tails, the contraction is envisioned to progress from the baseplate as a wave along the sheath (Basler, 2015; Leiman and Shneider, 2012; Moody, 1967, 1973; Wang et al., 2017). This putative mechanism is further supported by a recent rational mutagenesis of the sheath components yielding noncontractile sheath (Brackmann et al., 2017a; Wang et al., 2017). Among other findings, these studies identified inter-strand and inter-ring linkers, which propagate the contraction in a ring to ring fashion, supporting the wave like contraction mechanism (Brackmann et al., 2017a; Wang et al., 2017). To date, the contraction event could not be time resolved, but was shown to progress with at least 800 nm ms^{-1} and lead to a reduction in length of approx. 50 % (Basler et al., 2012; Vettiger et al., 2017). Furthermore, the contraction of a sheath ring results in a rotation of 5.8 ° of both the downstream sheath subunits as well as the coupled PAAR-VgrG-Hcp complex, surmounting in a counter clockwise rotational speed of at least 477,000 revolutions per minute (rpm), releasing the impressive total energy of approx. 44,000 kcal mol^{-1} (Wang et al., 2017). Among other things, the long sheath length has been hypothesized to be required in order to translocate large hydrophilic substrates by increasing the energy release, which is thought to be proportional to the sheath length (Vettiger et al., 2017). Even though the total energy release is likely proportional to the sheath length, I would assume, that the

force generated at any point in time should only be dependent on the contraction wave, because only the contracting sheath rings contribute to the force generation. Thus, I hypothesize, that the force generation is independent of the sheath length, if the sheath is significantly longer than the contraction wave and assuming that the friction generated by the longer sheath is negligible. Obviously, these assumptions will be violated at both extremes of sheath length.

Hcp has been described to interact with VipA (Brunet et al., 2014), but the structural data of the extended T6SS tail suggests, that the interaction is actually fostered by an attachment α-helix of VipB similar to what has been observed for pyocins (Chang et al., 2017; Ge et al., 2015; Wang et al., 2017). During the contraction of a sheath ring, the interaction with Hcp is released, which indicates that, based on the contraction wave model, the Hcp tube is held by the remaining yet uncontracted sheath, thus conveying the translation of the PAAR-VgrG-Hcp complex, which may be assisted by the TssA cap complex (Wang et al., 2017; Zoued et al., 2016).

I.1.4.5 Recycling of the contracted sheath by ClpV

Unlike Hcp, the contractile sheath subunits have the propensity to form higher order molecular aggregates when present at high concentration and in the absence of ClpV (Bönemann et al., 2009; Lossi et al., 2013). These aggregates resemble the structures formed by contracted T4 sheath or polysheath (Leiman et al., 2009). Interestingly, these aggregates could be disassembled by the AAA+ ATPase ClpV in an ATP dependent manner (Bönemann et al., 2009). Indeed, *in vivo* the contracted sheath is selectively disassembled by ClpV, which specifically interacts with VipB (Basler and Mekalanos, 2012; Basler et al., 2012; Douzi et al., 2016; Kapitein et al., 2013; Kube et al., 2014; Pietrosiuk et al., 2011), in some cases assisted by TagJ, which in turn binds to VipA (Förster et al., 2014; Lossi et al., 2012). Interestingly, ClpV is neither essential for T6SS mediated killing nor for the formation of contractile T6SS structures, although both takes place to a greatly reduced extent in the absence of ClpV (Basler et al., 2012; Zheng et al., 2011). In *Francisella novicida*, which does not encode a homolog of ClpV, the related chaperone ClpB fulfils this function (Brodmann et al., 2017). The structures of both the extended and contracted T6SS sheath substantiate the prior hypothesis, that the specific disassembly of the contracted sheath is due to the steric inaccessibility of domain 3 bearing the ClpV binding site in the extended state, which is exposed upon contraction (Basler and Mekalanos, 2012; Chang et al., 2017; Kapitein et al., 2013; Kube et al., 2014; Kudryashev

et al., 2015; Wang et al., 2017). The disassembly of the contracted sheath was suggested to restore the high energy state of the VipA-VipB subunits, although the mechanistic details remain to be elucidated (Basler and Mekalanos, 2012; Basler et al., 2012; Douzi et al., 2016; Kapitein et al., 2013; Kube et al., 2014; Pietrosiuk et al., 2011).

I.1.4.6 Rearming the T6SS

Due to the low stability of the Hcp tube in absence of the stabilizing sheath interactions, the ejected tube and the remaining tube exposed by the sheath recycling, will likely dissociate, and retained subunits may be reused (Douzi et al., 2014). The fate of the baseplate and membrane complex may vary depending on the species. In *Escherichia coli* it has been shown, that both the membrane complexes and the baseplates likely preassemble, and that they may be reused for multiple secretion events (Brunet et al., 2015; Durand et al., 2015). In *Serratia marcescens* TssL has been shown to form mobile foci, possibly suggesting the preassembly of partial envelope spanning complexes not yet associated with TssJ (Gerc et al., 2015). It remains unknown, how the localization or relocalization of the T6SS is achieved, considering, that the formation of the envelope spanning complex requires the local degradation of peptidoglycan, and that the complex may be anchored to the peptidoglycan, the formation of static reusable envelope spanning complexes is appealing (Aschtgen et al., 2010a; Brunet et al., 2015; Durand et al., 2015; Santin and Cascales, 2017; Weber et al., 2016), but likely not sufficient to explain the Tit-for-tat T6SS dynamics of *P. aeruginosa*, which requires the precise and timely localization of the T6SS (Basler and Mekalanos, 2012; Basler et al., 2013).

I.1.4.7 Posttranslational regulation of the T6SS

Overall differing T6SS dynamics have been observed. In *V. cholerae* the T6SS was described to continuously fire indiscriminately at the surrounding (Basler et al., 2012). In stark contrast, the H1-T6SS in *P. aeruginosa* was shown to specifically launch retaliatory attacks (Basler et al., 2013). In order to achieve this, the assembly of the T6SS is localized to the site of an outer membrane damage (Basler and Mekalanos, 2012; Basler et al., 2013; Ho et al., 2013; Wilton et al., 2016). The localization and the posttranslational activation of the H1-T6SS was shown to depend on the TagQRST-PpkA-Fha1 signaling cascade (Basler et al., 2013; Casabona et al., 2013; Hsu et al., 2009; Mougous et al., 2007). TagQRST likely transduces the signal to the membrane bound serine-threonine kinase PpkA, which in turn phosphorylates Fha1 (Casabona et al., 2013; Hsu et al., 2009; Mougous et al., 2007). The phosphorylated Fha1 localizes and activates the H1-T6SS by a still

unknown mechanism (Mougous et al., 2007). Fha1 was shown to form a complex with ClpV also in the absence of PpkA, the role of which is unclear (Hsu et al., 2009). The phosphorylated Fha1 is then dephosphorylated by PppA, inactivating the T6SS (Mougous et al., 2007). Similar to the H1-T6SS in *P. aeruginosa*, the T6SS activation by Fha phosphorylation has also been observed in *S. marcescens*, in which the input signal seems to differ as it lacks the TagQRST components (Fritsch et al., 2013). In contrast, TssL is phosphorylated by PpkA in *A. tumefaciens*, which then activates the ATPase activity of TssM. Thereafter, Fha binds to the phosphorylated TssL, activating the T6SS (Lin et al., 2014). In addition to the threonine phosphorylation pathway, the H1-T6SS in *P. aeruginosa* is independently posttranslationally regulated by TagF (Silverman et al., 2011). TagF is a repressor of the H1-T6SS, which inhibits the T6SS activity by an unknown mechanism (Silverman et al., 2011). The derepression of the T6SS in absence of TagF requires the presence of Fha1, but neither the threonine phosphorylation pathway nor the phosphorylation of Fha1 (Silverman et al., 2011). Thus it has been hypothesized, that different signals may either activate the H1-T6SS by the threonine phosphorylation pathway or the derepression via TagF (Silverman et al., 2011). Interestingly, TagF is also present in some species which lack both the threonine phosphorylation pathway and an identifiable homolog of Fha, like *Acinetobacter baylyi* (Weber et al., 2013), or only the threonine phosphorylation pathway (Silverman et al., 2011). Furthermore, TagF occurs as a TagF-PppA fusion in some strains (Silverman et al., 2011). Taken together there seems to exist a wide variety of posttranslational regulatory pathways likely adapted to the specific function of the respective T6SS.

With regard to the subcellular localization of the T6SS it is intriguing, that a number of T6SS have been observed to exhibit preferential polar localization, all of which were described to be targeting eukaryotes (Brodmann et al., 2017; Schwarz et al., 2010, 2014; Wan et al., 2017).

I.1.5 Type VI secretion system effectors

As a consequence of the above described injection mechanism, the delivery of T6SS cargo or components is strictly contact dependent (Hood et al., 2010; Pukatzki et al., 2006). Recently, an elegant bacterial competition assay was used to elucidate the subcellular localization of T6SS components injected into diderm bacteria, revealing, that they may be injected into the cytoplasm of the target cells (Vettiger and Basler, 2016). The authors also demonstrated, that the injected T6SS components could be reused by isogenic sister cells

lacking secreted components (Vettiger and Basler, 2016). In order to simplify the following discussion, any secreted/injected cargo or component of the T6SS eliciting an effect in the target will be referred to as an effector.

So far, the secreted components Hcp, VgrG and PAAR were solely treated as structural components of the T6SS. Due to the previous definition, these components may constitute effectors even in the absence of an identifiable catalytically active domain. For example, Hcp of *Aeromonas hydrophila* SSU inhibits the phagocytosis and induces the production of IL-10 and TGF-β by macrophages even without the need to be injected into the target cell (Suarez et al., 2010a). Additionally, it induces apoptosis when expressed in HeLa cells (Suarez et al., 2008). However, many T6SS effectors described to date constitute either extensions of the secreted structural components, then termed evolved effectors, or proteins, which bind noncovalently to the structural components, then termed cargo effectors (reviewed in (Alcoforado Diniz et al., 2015)). By now, both evolved and cargo effectors have been identified for each secreted T6SS component, making the T6SS an incredibly versatile delivery system.

I.1.5.1 The T6SS as a versatile effector delivery system

The first identified evolved effector was VgrG-1 of *V. cholerae* V52, which carries an actin crosslinking domain as a C-terminal extension (Pukatzki et al., 2007). Already in this paper, the authors identified a large number of VgrG homologs carrying C-terminal extensions with a predicted catalytic activity using a bioinformatic approach (Pukatzki et al., 2007). As mentioned before, VgrGs trimerize, forming a part of the spike complex (Hachani et al., 2011; Leiman et al., 2009; Pukatzki et al., 2007; Spínola-Amilibia et al., 2016; Sycheva et al.; Uchida et al., 2014). Apart from homo-trimers, these may also form hetero-trimers and thereby possibly inject multiple different effectors at the same time (Brooks et al., 2013; Hachani et al., 2011; Pukatzki et al., 2006, 2007). In some cases at least one of the VgrGs must not carry a C-terminal extension, which may indicate, that there is a spacial constraint (Pukatzki et al., 2006, 2007). Alternatively, it may be a consequence of only a certain combination of VgrGs being able to form a trimer (Pukatzki et al., 2007; Zheng et al., 2011). Interestingly, the C-terminal domain is not necessarily essential for the translocation and may be exchanged, further suggesting, that a new T6SS effector may be created by fusing a toxic domain to the C-terminus of a VgrG (Ho et al., 2017; Ma et al., 2009a). Apart from the evolved effector VgrGs, there are others that carry only a small C-terminal domain, which fosters noncovalent protein-protein interactions with a specific cargo

effector, usually found genetically linked to its VgrG (Bondage et al., 2016; Flaugnatti et al., 2016; Hachani et al., 2014). Similar to the evolved effector VgrGs, swapping the C-terminal protein-protein interaction domains retargets the corresponding cargo effectors to the respective VgrGs (Bondage et al., 2016). Moreover, a specific effector adaptor may be required to facilitate the binding of an effector to its corresponding VgrG, which itself is not secreted (Bondage et al., 2016; Liang et al., 2015; Miyata et al., 2013; Unterweger et al., 2015). Furthermore, VgrGs carrying a catalytically active C-terminal extension may additionally bind other effectors noncovalently (Dong et al., 2013; Unterweger et al., 2015). The number of co-encoded VgrGs varies widely among the bacteria and may range from 1 to 32, yielding an incredible combinatorial diversity (Ho et al., 2014). Unexpectedly, certain VgrGs, not carrying a C-terminal toxin domain, were found to be secreted independent of a T6SS, some of which are still able to induce target killing to a low level, suggesting the co-translocation of their cargo effector (Barker et al., 2009; Hachani et al., 2011; Weber et al., 2013, 2016). Moreover, some VgrGs and T6SS effectors may also be translocated from the cytosol to the periplasm in a T6SS independent manner, which was hypothesized to allow effectors with a periplasmic target to be translocated to the periplasm when injected into the cytoplasm by the T6SS (Ho et al., 2017).

As previously mentioned, the VgrG trimers are further sharpened by a PAAR protein (Rigard et al., 2016; Shneider et al., 2013). These PAAR proteins may carry N- or C-terminal extensions or both, which may constitute toxin domains or domains facilitating protein-protein interactions (Bondage et al., 2016; Diniz and Coulthurst, 2015; Fritsch et al., 2013; Hachani et al., 2014; Ma et al., 2014; Rigard et al., 2016; Shneider et al., 2013; Whitney et al., 2014; Zhang et al., 2012). Similar to the specific VgrG-effector interaction, also the PAAR-VgrG interaction may be specific (Cianfanelli et al., 2016; Hachani et al., 2014; Whitney et al., 2014), but there are also cases in which distinct PAAR bearing proteins bind to the same VgrG protein with different affinities (Cianfanelli et al., 2016). Again in analogy to the effectors, some PAAR proteins require a specific adapter protein in order to bind to the VgrG complex, albeit the adapter is not secreted (Bondage et al., 2016; Cianfanelli et al., 2016; Diniz and Coulthurst, 2015; Whitney et al., 2015).

The VgrG-PAAR spike complex, although possibly decorated with multiple toxins, only transports a rather small number of effectors upon its ejection. On the other hand, a large number of Hcp subunits is secreted/injected. Indeed, a variety of small effectors have been identified, which bind noncovalently to the lumen of the Hcp hexamers (Silverman et al.,

2013; Zheng and Leung, 2007). Finally, Hcp proteins carrying a C-terminal toxin domain were also recently identified (Blondel et al., 2009; Ma et al., 2017). With an inner diameter of approx. 40 Å, the lumen of the Hcp tube is rather small (Mougous et al., 2006) indicating, that the Hcp tube is likely not entirely composed of Hcp proteins carrying an effector domain. Indeed, two Hcp proteins, which do not carry a C-terminal extension, were found to be essential for the secretion of the evolved Hcp effector suggesting, that these form a hetero-hexamer (Ma et al., 2017).

I.1.5.2 The diverse T6SS effector repertoire

Although many phenotypes were attributed to the T6SS, only few of these were investigated to the level of individual secreted/injected effectors or its components, and even less have been characterized biochemically (Hachani et al., 2016). One way to group the effectors is by their targeted kingdom. As a consequence of their subcellular target, some effectors only target prokaryotes or eukaryotes, whereas others target components conserved in both pro- and eukaryotes constituting cross-kingdom effectors. As elaborated in the following sections, many effectors characterized to date target conserved subcellular components. Apart from toxic effectors, three T6SS substrates, involved in zinc (Wang et al., 2015), manganese (Si et al., 2017) and iron (Lin et al., 2017) acquisition, have recently been identified, further expanding the repertoire of the T6SS.

The immense diversity of T6SS effectors is, at least in part, fostered by their modularity, which enables the reuse or adaptation of existing toxin domains. The effectors often belong to the group of polymorphic toxins, which consist of an N-terminal trafficking domain and an exchangeable C-terminal toxin domain (Jamet and Nassif, 2015; Zhang et al., 2012). I would however suggest to extend the definition of polymorphic toxins to any type of modular toxin, which consists of a trafficking domain, be it N- or C-terminal, and interchangeable toxin domains. A prominent group of polymorphic T6SS toxins is formed by the rearrangement hotspot (RHS) and YD repeat containing proteins, which carry highly variable C-terminal toxin domains (Koskiniemi et al., 2013; Zhang et al., 2012). The RHS domain was shown to form a large cage or shell like structure, consisting of β-sheets, which accommodates the toxic C-terminal domain (Busby et al., 2013). As detailed before, effectors may constitute extensions of secreted structural components, which are exchangeable within certain limits, thus also forming polymorphic toxins (Zhang et al., 2012). Another group of polymorphic toxins is formed by the “marker for type six effectors” (MIX) motif, bearing effectors often found genetically linked to secreted T6SS

components (Salomon, 2016; Salomon et al., 2014). Furthermore, at least the cargo effectors, translocated by the VgrG/PAAR spike complex, often bind to protein-protein interaction domains carried by the structural components which, when exchanged, can retarget the corresponding effector (Bondage et al., 2016). This indicates, that the cargo effectors may also form a group of "indirect" polymorphic toxins. Apart from entirely different toxins, the coevolution of effectors and immunity proteins was shown to yield non-cross reactive, and thereby incompatible, effector-immunity subfamilies (Cardarelli et al., 2015; Unterweger et al., 2014).

Interestingly, the intra-species competition or self from non-self discrimination may be determined by differing sets of T6SS effectors as exemplified by *V. cholerae* (Borgeaud et al., 2015; Thomas et al., 2017; Unterweger et al., 2014), *Bacteroides fragilis* (Chatzidaki-Livanis et al., 2016; Hecht et al., 2016; Russell et al., 2014; Wexler et al., 2016) and *Proteus mirabilis* (Alteri et al., 2013; Wenren et al., 2013). Different *V. cholerae* strains were found to harbor diverse effector sets, which leads to the competition of strains with incompatible sets and coexistence of strains with the same set (Unterweger et al., 2014). Strikingly, the toxigenic *V. cholerae* strains all carry compatible effector sets (Unterweger et al., 2014). Similarly, different *B. fragilis* strains compete by means of their effector set (Chatzidaki-Livanis et al., 2016; Hecht et al., 2016; Wexler et al., 2016). There are both symbiotic and enterotoxigenic *B. fragilis* strains, the latter cause acute diarrhea and are associated with inflammatory bowel disease as well as colon cancer (reviewed in (Brennan and Garrett, 2016)). A recent study found that certain nontoxigenic strains are able to utilize their T6SS to outcompete toxigenic strains in a C57BL/6J mouse model (Hecht et al., 2016). This exciting result serves as a proof of principle to use symbiotic strains, capable of outcompeting the toxigenic strains, as a therapeutic strategy (Hecht et al., 2016). *P. mirabilis* is known to exhibit territorial behavior, and different incompatible strains do not mix when swarming, forming a macroscopically visible boundary known as Dienes line at their interface (Dienes, 1946). This was later shown to be a T6SS dependent phenotype and to rely on incompatible effector sets (Alteri et al., 2013; Wenren et al., 2013).

I.1.5.3 Anti-eukaryotic effectors

The first T6SS effector to have been characterized was VgrG-1 from *V. cholerae*, which carries a C-terminal actin crosslinking domain (Pukatzki et al., 2006, 2007), the injection of which is dependent on the phagocytosis of the bacterium (Ma et al., 2009a). The crosslinking of actin then prevents any further phagocytosis, protecting the remaining

bacteria (Ma et al., 2009a). In an infant mouse model, the fluid accumulation in the intestine was solely dependent on the actin crosslinking domain of VgrG-1 (Ma and Mekalanos, 2010). Another VgrG, injected by *A. hydrophila*, was shown to carry a C-terminal vegetative insecticidal protein (VIP-2) domain, catalyzing the ADP ribosylation of actin, which disrupts the actin cytoskeleton and induces apoptosis in HeLa cells (Suarez et al., 2010b). The cargo effector TecA, secreted by *Burkholderia cenocepacia*, inactivates the RhoA and Rac1 GTPases by deamidating a conserved asparagine in the switch-I region, thereby disrupting the actin cytoskeleton and inducing the caspase-1 inflammasome (Aubert et al., 2016). In an intranasal mouse model, the TecA deficient *B. cenocepacia* was no longer able to cause a lung inflammation (Aubert et al., 2016). However, the activation of the innate immune system by TecA protected mice against *B. cenocepacia* infection in a peritoneal infection model, whereas the mice succumbed the infection with the TecA deficient strain (Aubert et al., 2016). *E. tarda* on the other hand prevents the NLRP3 inflammasome activation by injecting the cargo effector EvpP, which interferes with ASC oligomerization by suppressing the cytoplasmic Ca^{2+} increase, precluding the activation of the Ca^{2+}-dependent c-Jun N-terminal kinase (Chen et al., 2017).

Contrary to preventing phagocytosis, VgrG2b of *P. aeruginosa* PAO1 can induce its microtubule dependent uptake by nonphagocytic HeLa or Calu-3 cells (Sana et al., 2012, 2015). The microtubule dependent uptake is facilitated by the interaction of the C-terminal domain of VgrG2b with the γ-tubulin ring complex, the mechanism of which remains to be elucidated (Sana et al., 2015).

Once phagocytosed, bacteria are usually confronted with reactive oxygen species (ROS), which the recently discovered Mn-catalase KatN, secreted/injected by the T6SS of the enterohemorrhagic *E. coli* EDL933, detoxifies (Wan et al., 2017). The survival of the KatN deficient strain was significantly reduced in RAW264.7 macrophages, primary peritoneal macrophages, but not in the BALB/c mouse model (Wan et al., 2017). *Yersinia pseudotuberculosis* secretes YezP, a zinc binding protein, via its T6SS-4, which plays a crucial role in Zn^{2+} acquisition (Wang et al., 2015). The Zn^{2+} acquisition is in turn involved in the protection of the bacterium against oxidative stress, especially the formation of hydroxyl radicals (Wang et al., 2015). Consistent with this role, a YezP deficient strain is attenuated in its virulence towards C57BL/6 mice (Wang et al., 2015). Similarly, *Burkholderia thailandensis* secretes TseM, a Mn^{2+} binding protein, via its T6SS-4, which contributes to the Mn^{2+} scavenging and is also implicated in the resistance towards

oxidative stress (Si et al., 2017). It should be noted, that these metal scavenging pathways may also contribute to interbacterial competition.

Burkholderia spp. secrete VgrG-5 via the T6SS-5, the C-terminal domain of which induces the membrane fusion of adjacent mammalian host cells, leading to the well known multinucleated giant cells (MNGC) phenotype (Schwarz et al., 2014). The lack of the C-terminal domain renders *B. thailandensis* avirulent in the aerosol infection C57BL/6 mouse model (Schwarz et al., 2014).

As mentioned before, also structural components, which do not carry an apparent catalytic domain, may elicit an effect in the target. Among these Hcp of *A. hydrophila* SSU has been shown to induce apoptosis in HeLa cells (Suarez et al., 2008) and inhibit the phagocytosis by macrophages (Suarez et al., 2010a), the mechanism of which remains unknown. Purified Hcp1 of *E. coli* K1 added to the growth medium of human brain microvascular endothelial cells induced the formation of actin stress fibers and apoptosis by caspase 8 (Zhou et al., 2012).

I.1.5.4 Anti-prokaryotic effectors

Unlike anti-eukaryotic effectors, which cause no harm to the secreting bacterium, the anti-prokaryotic and cross-kingdom effectors are always found co-encoded with their cognate immunity protein (Alcoforado Diniz et al., 2015).

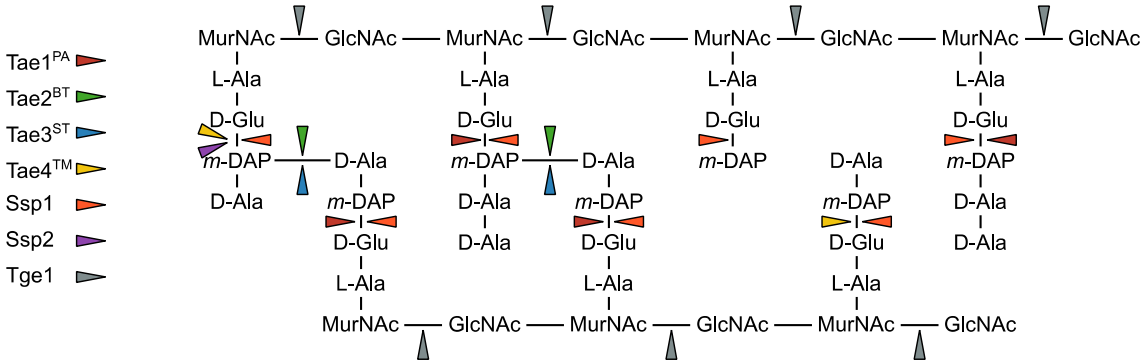

Figure I.1.2: Peptidoglycan targeting effectors
The cleavage sites of biochemically characterize peptidoglycan targeting T6SS effectors are indicated by colored arrows. Please refer to the main text for additional details.

A large family of anti-prokaryotic T6SS effectors is formed by the peptidoglycan amidases (Tae; see Fig. I.1.2), which is comprised of four distinct groups (Russell et al., 2012). Tae1, secreted by *P. aeruginosa*, belongs to group 1 and cleaves the γ-D-glutamyl-L-*meso*-diaminopimelic acid isopeptide bond in the donor peptide of the tetra-tetra peptide crosslinks and the non-crosslinked pentapeptide as well as both donor

and acceptor peptides of penta-tetra peptide crosslinks (Chou et al., 2012; Hood et al., 2010; Russell et al., 2011). Unlike Tae1, Tae2, which belongs to class 2, and is secreted by the T6SS-1 of *B. thailandensis*, cleaves the D,D-amide bond of the *meso*-diaminopimelic acid D-alanine crosslink (Russell et al., 2012). A representative peptidoglycan amidase of class 3, $Tae3^{ST}$ of *Salmonella* Typhi, was demonstrated to have the same target as Tae2 (Russell et al., 2012). $Tae4^{TM}$ of *Salmonella* Typhimurium, a representative of class 4, was shown to hydrolyze the γ-D-glutamyl-L-*meso*-diaminopimelic acid isopeptide bond in the acceptor peptide and non-crosslinked tetrapeptides, unlike Tae1 (Russell et al., 2012). The biochemical characterization of two class 4 peptidoglycan amidase effectors from *S. marcescens* indicated that there is also functional diversity within the classes (English et al., 2012; Srikannathasan et al., 2013). While Ssp1 and Ssp2 both cleave the γ-D-glutamyl-L-*meso*-diaminopimelic acid isopeptide bond, Ssp2 only cleaves the acceptor peptide of the cross-linked tetrapeptides, whereas Ssp1 cleaves monomeric tripeptides, tetrapeptides, pentapeptides as well as both crosslinked forms of tetra-penta and tetra-tetra peptides of both acceptor and donor peptides (Srikannathasan et al., 2013). *V. cholerae* secretes the putative amidase TseH, which has been demonstrated to cleave peptidoglycan, but the precise target remains to be elucidated (Altindis et al., 2015).

In addition to the amidases also a family of glycoside hydrolases (Tge; see Fig. I.1.2) targets the peptidoglycan, which is comprised of three groups (Whitney et al., 2013). The muramidase Tge1 of *P. aeruginosa* belongs to group 1 and hydrolyzes the β(1,4) bond between *N*-acetylmuramic acid and *N*-acetyl-D-glucosamine (Russell et al., 2011). Another effector, Tge2, of *Pseudomonas protegens* belonging to group 2, was shown to cleave peptidoglycan, but due to its similarity to *N*-acetylglucosaminidases its cleavage target remains to be elucidated (Whitney et al., 2013). Similarly, *V. cholerae* secretes VgrG-3, which carries a C-terminal glycoside hydrolase domain unrelated to the Tge family (Brooks et al., 2013; Dong et al., 2013; Yang et al., 2014). Interestingly, even though some of the peptidoglycan targeting enzymes are capable of cleaving the peptidoglycan of Gram-positive bacteria, the survival of the Gram-positive bacteria was not affected in competition experiments (Chou et al., 2012; MacIntyre et al., 2010; Schwarz et al., 2010).

Another class of anti-prokaryotic effectors are the DNAses. The RhsA and RhsB effectors secreted by *Dickeya dadantii* were the first T6SS DNAse effectors to be described (Koskiniemi et al., 2013). Both share a very similar N-terminal domain but carry differing C-terminal toxin domains (Koskiniemi et al., 2013). RhsA carries an NS_2 endonuclease

domain, whereas RhsB carries a HNH-endonuclease domain (Koskiniemi et al., 2013). *S. marcescens* also employs an RHS domain containing effector, Rhs2, which bears a C-terminal HNH-endonuclease domain (Diniz and Coulthurst, 2015). *E. coli* secretes Hcp-ET1, which bears a C-terminal HNH-nuclease domain or an Hcp carrying a Pyocin S3-Colicin-DNAse fusion domain (Ma et al., 2017). Alternatively, an Hcp, bearing only the Pyocin S3 domain, may be encoded together with a cargo Colicin-DNAase, both of which are secreted (Ma et al., 2017). Effectors belonging to a distinct superfamily of DNAses were identified in *A. tumefaciens*, which secretes Tde1 and Tde2, both of which carry a C-terminal toxin_43 DNAse domain (Ma et al., 2014; Zhang et al., 2012). DNAses could potentially also target eukaryotes, but those described to date were only implied in interbacterial competition.

The T6SS effector Tse6, secreted by *P. aeruginosa*, is a glycohydrolase and targets the conserved coenzymes nicotinamide adenine dinucleotide (NAD^+) and the related phosphorylated form $NADP^+$, cleaving off the nicotinamide moiety (Whitney et al., 2014, 2015). The depletion of $NAD(P)^+$ leads to stasis of the targeted bacteria (Whitney et al., 2014, 2015). Tse6 bears a PAAR domain surrounded by three putative transmembrane helices. Interestingly, Tse6 increasingly partitions to the membrane in absence of its specific VgrG and further requires binding to the elongation factor Tu in order to access the target cytoplasm, the mechanism of which is not yet understood (Whitney et al., 2015).

Another effector, Tse2, secreted by *P. aeruginosa* was suggested to require NAD^+ to elicit its toxic effect, although the mechanism remains unknown (Robb et al., 2016). When ectopically expressed, Tse2 induces stasis in both bacteria and eukaryotes, but it is seemingly only targeted to bacteria (Hood et al., 2010). In agreement with its putative NAD^+ dependence, the target of Tse2 resides in the bacterial cytoplasm (Li et al., 2012).

Although these are only anti-prokaryotic effectors, the interbacterial competition may affect the pathogenicity towards a eukaryotic host by outcompeting other bacteria, as demonstrated for *V. cholerae*, *Salmonella* Typhimurium and *A. tumefaciens* (Fu et al., 2013; Ma et al., 2014; Sana et al., 2016). In contrast, certain symbiotic *B. fragilis* strains are capable of displacing related enterotoxigenic strains in a murine host by use of their T6SS (Hecht et al., 2016).

I.1.5.5 Cross-kingdom effectors

A large family of cross-kingdom effectors is formed by the phospholipases, which may not only exert toxicity towards their target by disintegrating the membrane, but may also interfere with membrane associated signaling pathways like the phosphatidylinositol 3-kinase (PI3K)/Akt signaling pathway (Jiang et al., 2014; Russell et al., 2013). The phospholipases are grouped into five classes of which the classes 1-4 bear a GXSXG catalytic motif, whereas members of class 5 carry a HXKXXXXD catalytic motif (Russell et al., 2013). Tle1 of *B. thailandensis* catalyzes the hydrolysis of the *sn*-2 ester bond of phospholipids, whereas Tle2 of *V. cholerae* targets the *sn*-1 ester bond, both of which carry the GXSXG catalytic motif and were shown to exert antibacterial activity (Dong et al., 2013; Russell et al., 2013). Tle2 of *V. cholerae* also contributes to the resistance towards amoebae predation (Dong et al., 2013). Another member of the class 1 phospholipases, Tle1 from *E. coli*, hydrolyzes both the *sn*-1 and *sn*-2 ester bonds and exerts antibacterial activity but did not affect *Caenorhabditis elegans* (Flaugnatti et al., 2016). Tle1 from *P. aeruginosa* also hydrolyzes the *sn*-2 ester bond, whereas the activity on the *sn*-1 bond was not assessed (Hu et al., 2014). On the other hand, Tle5 of *P. aeruginosa* carries the HXKXXXXD catalytic motif and was demonstrated to constitute a PLD enzyme, hydrolyzing the phosphate ester bond of the polar head group preferentially targeting phosphatidylethanolamine (Russell et al., 2013). Surprisingly, also Tle5 exerted antibacterial activity, although PLD activity is usually associated with anti-eukaryotic effectors (Russell et al., 2013). Shortly thereafter, another T6SS associated class 5 phospholipase, PldB, was identified in *P. aeruginosa*, which was also shown to exert antibacterial activity (Jiang et al., 2014). Interestingly, the phospholipases exhibited a higher antibacterial activity when targeted to the periplasm, which is in agreement with the periplasmic localization of the corresponding immunity proteins, the reason for which remains to be elucidated (Jiang et al., 2014; Russell et al., 2013). It was further demonstrated that, apart from their antibacterial activity, Tle5 and PldB can also directly interact with the Akt1 and Akt2 kinases and thereby promote phagocytosis in a PLD dependent way (Jiang et al., 2014; Sana et al., 2012). Unexpectedly, neither of the PLD phospholipases exerted toxicity towards HeLa cells (Jiang et al., 2014). Recently also an Hcp bearing a C-terminal phospholipase domain, belonging to class 1, has been identified (Ma et al., 2017). This phospholipase is secreted by *E. coli* and was demonstrated to contribute to interbacterial competition (Ma et al., 2017).

Another unrelated membrane targeting effector is VasX, which is secreted by *V. cholerae* and is required for its virulence towards *Dictyostelium discoideum* but also intoxicates bacteria (Dong et al., 2013; Miyata et al., 2011, 2013). VasX shares weak structural homology with pore-forming colicins, interacts with phosphatidic acid and phosphatidylinositol phosphates and was demonstrated to dissipate the inner membrane potential (Miyata et al., 2011, 2013; Zheng et al., 2011). Interestingly, VasX is only toxic when located in the periplasm, which is a feature shared with pore-forming colicins, thus VasX was proposed to be a colicin like effector (Espesset et al., 1994; Miyata et al., 2013).

I.1.5.6 Immunity proteins

As mentioned before, the anti-prokaryotic and cross-kingdom effectors are always found co-encoded with a corresponding immunity protein (Alcoforado Diniz et al., 2015). Interestingly, there may be more than one immunity protein encoded genetically linked to the corresponding effector, all of which may contribute to immunity (Flaugnatti et al., 2016; Jiang et al., 2014; Ma et al., 2017; Russell et al., 2012, 2013; Salomon et al., 2015; Weber et al., 2016; Zhang et al., 2012). These paralogs have been hypothesized to evolve faster due to the relaxed selective pressure and may confer immunity towards diverging effectors arising in the population (Kirchberger et al., 2017; Zhang et al., 2012). Similarly, entire effector-immunity pairs may be duplicated, possibly allowing for the divergence of each module (Russell et al., 2013). Additionally, orphan immunity proteins were also found, possibly conferring immunity against effectors utilized by competitors (English et al., 2012; Kirchberger et al., 2017; Russell et al., 2012) as recently demonstrated for *B. fragilis* (Wexler et al., 2016). Interestingly, the immunity protein $Tai3^{TY}$ not only confers immunity towards its cognate effector $Tae3^{TY}$ but was also able to protect against $Tae2^{BT}$, which belongs to a different class of the Tae effectors and originates from a different bacterium (Russell et al., 2012). Moreover, the immunity protein encoding genes may be regulated independently of the effector, such that the bacteria are always immune to their own attacks (Miyata et al., 2013). In *P. mirabilis* the co-evolution and divergence of an effector-immunity pair contributes to the self from non-self discrimination (Cardarelli et al., 2015). Both the toxin IdsD and the antitoxin IdsE contain variable regions, and only the antitoxin carrying the variable region, that matches that of the toxin, can bind and thereby detoxify it (Cardarelli et al., 2015). Moreover, a strain may encode multiple IdsE variants, which cannot inactivate the toxin, suggesting that these orphan antitoxins confer resistance to IdsD proteins from other strains, thereby permitting colony mixing or invasion to take place

(Cardarelli et al., 2015). A similar observation was made for different subfamilies of effector-immunity pairs in *V. cholerae* (Unterweger et al., 2014).

I.1.6 *Acinetobacter baylyi* ADP1

The model organism used throughout most of this study is *A. baylyi* ADP1, a microencapsulated derivative of the soil isolate *A. baylyi* BD4 (Juni and Janik, 1969). This Gram-negative aerobic non-flagellated chemoheterotroph bacterium is closely related to the emerging opportunistic pathogens of the genus *Acinetobacter* (Barbe et al., 2004; Lee et al., 2017). Its natural competence renders it easily genetically amenable (Juni and Janik, 1969; Metzgar et al., 2004). Furthermore, *A. baylyi* ADP1 encodes a single constitutively active antibacterial T6SS (Berardinis et al., 2008; Shneider et al., 2013; Weber et al., 2013, 2016).

While the work presented here was in progress, the essentiality of the T6SS components encoded in the core T6SS cluster was assessed by another group (Weber et al., 2016). The essentiality was asserted by subjecting insertion mutants to an Hcp secretion assay (Berardinis et al., 2008; Weber et al., 2016). As detailed in research article I, more sensitive assays and the use of marker less deletion mutants did not entirely confirm these results. Apart from the outer membrane protein TssJ, *A. baylyi* ADP1 encodes the complete set of conserved T6SS components all of which were found to be essential for Hcp secretion (Shneider et al., 2013; Weber et al., 2013, 2016). Interestingly, the putative peptidoglycan anchoring component TagN was shown to be dispensable for T6SS activity and the Hcp secretion even increased in its absence (Aschtgen et al., 2010a; Weber et al., 2016). Although demonstrated to be capable of outcompeting bacteria in a T6SS dependent manner, the effector repertoire of *A. baylyi* ADP1 remained uncharacterized (Shneider et al., 2013; Weber et al., 2013).

As mentioned before, the T6SS of *A. baylyi* ADP1 is constitutively active under laboratory conditions (Shneider et al., 2013; Weber et al., 2013, 2016). This is despite the presence of TagF, which acts as a posttranslational repressor of the T6SS in *P. aeruginosa*, and the absence of an identifiable ortholog of Fha, which is essential for the derepression of the T6SS in *P. aeruginosa* (Silverman et al., 2011; Weber et al., 2016). Nevertheless, the TagF deficient strain was shown to secrete more Hcp (Weber et al., 2016). Interestingly, in multidrug resistant *Acinetobacter baumannii* the T6SS is often repressed under laboratory conditions (Repizo et al., 2015; Weber et al., 2013, 2015). Intriguingly, three of the clinical

A. baumannii isolates produced Hcp but did not secrete it, suggesting, that the T6SS is posttranslationally repressed in these strains (Repizo et al., 2015). Remarkably, other strains were shown to harbor a self-transmissible resistance plasmid encoding TetR-like transcriptional repressors of the T6SS (Weber et al., 2015). The loss of the plasmid derepresses the T6SS but coincides with the loss of the antibiotic resistance (Weber et al., 2015). Furthermore, the ectopic expression of any of the two repressors could repress the T6SS in other *Acinetobacter* species including *A. baylyi* ADP1 (Weber et al., 2015). Based on these observations it has been hypothesized that, when co-infecting a host, the frequent loss of the plasmid promotes T6SS mediated interbacterial competition. Upon treatment with antibiotics both the competitors and the bacteria having lost the plasmid will be inhibited, but due to the inhibition of the competitors there is no need of utilizing the T6SS. This intricate strategy provides a benefit as long as the competing bacteria are susceptible to the antibiotics (Weber et al., 2015, 2017).

As previously mentioned *A. baylyi* ADP1 is naturally competent (Juni and Janik, 1969). In *V. cholerae* the T6SS is part of the competence regulon, which is induced upon growth on chitinous surfaces (Borgeaud et al., 2015). When competed against a sensitive strain on such a surface, *V. cholerae* can lyse the competitors and thereafter take up the liberated DNA for subsequent homologous recombination (Borgeaud et al., 2015). A part of the enormous T6SS effector diversity of *V. cholerae* has been attributed to such horizontal gene transfer events (Borgeaud et al., 2015; Thomas et al., 2017; Unterweger et al., 2014). Unlike *V. cholerae*, *A. baylyi* ADP1 is competent throughout most of its growth (Palmen et al., 1992, 1993). Thus, we reasoned, that naturally competent *Acinetobacter* may also employ their T6SS to acquire new genes from competitors.

I.2 Aims of this thesis

The T6SS has become a major player in the field of microbial interactions. Although recent structural and functional studies rapidly advanced the understanding of the T6SS, the mechanistic role of some of the core components remain vaguely defined and the contributions of the associated components are even less well understood. Moreover, despite its implication in a wide variety of processes the effector repertoire of the T6SS is poorly characterized.

This thesis focuses on the characterization of both associated and selected core components of the T6SS in *A. baylyi* ADP1 with respect to their functional contributions, using a set of complementary methods. *A. baylyi* ADP1 was chosen as model organism because it encodes a single constitutively active antibacterial T6SS which had not been functionally characterized and it is closely related to the emerging opportunistic pathogens of the genus *Acinetobacter*. Since the T6SS effector repertoire of *A. baylyi* ADP1 is unknown these will be identified using a bioinformatic approach and characterized with regard to their antibacterial activity. The natural competence of *A. baylyi* ADP1 suggests that its T6SS may be involved in the horizontal gene transfer as demonstrated for *V. cholerae*. Therefore, the role of the T6SS and its effectors in the acquisition of genetic material from prey strains will be investigated.

Apart from trying to decipher the mechanistic details of the T6SS also its impact on mixed bacterial populations is of interest. Using a modelling approach the influence of the T6SS on interbacterial competitions is to be investigated. The predictions of this model are further to be experimentally validated.

Chapter II

Results

II.1 Research Article I

The Role of Type VI Secretion System Effectors in Target Cell Lysis and Subsequent Horizontal Gene Transfer

Peter David Ringel,[1] Di Hu,[1,2] and Marek Basler[1,3,*]

[1] Focal Area Infection Biology, Biozentrum, University of Basel, Klingelbergstrasse 50/70, CH - 4056 Basel, Switzerland

[2] Present address: GE Healthcare Shanghai, No. 1 Huatuo Road, Pudong New District, Shanghai, China

[3] Lead Contact

* Correspondence: marek.basler@unibas.ch

Cell Reports, Volume 21, Issue 13, December 26th, 2017, Pages 3927-3940

Statement of contribution

I constructed the effector mutants, the immunity deficient mutants, the ACIAD2693 deficient mutant and the optimized counter-selectable cassette. I performed the experiments described in this manuscript and wrote the initial draft.

Cell Reports

Article

The Role of Type VI Secretion System Effectors in Target Cell Lysis and Subsequent Horizontal Gene Transfer

Graphical Abstract

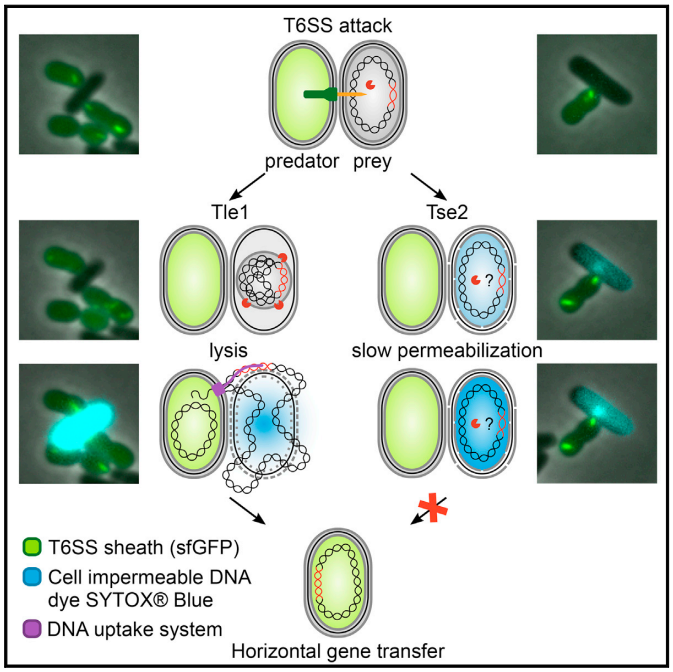

Highlights

- *Acinetobacter baylyi* assembles a dynamic antibacterial type VI secretion system
- Killing and lysis of prey bacteria differs for each of the five effectors
- Gene transfer from prey to predator depends on delivery of lytic effectors

Authors

Peter David Ringel, Di Hu, Marek Basler

Correspondence

marek.basler@unibas.ch

In Brief

Ringel et al. show that naturally competent *Acinetobacter baylyi* ADP1 uses its type VI secretion system to kill bacterial competition by delivery of five different effectors. Lysis of prey cells induced by delivery of lytic effectors is required for efficient transfer of DNA from prey to predator.

Ringel et al., 2017, Cell Reports *21*, 3927–3940
December 26, 2017 © 2017 The Authors.
https://doi.org/10.1016/j.celrep.2017.12.020

Cell Reports
Article

OPEN ACCESS
CellPress

The Role of Type VI Secretion System Effectors in Target Cell Lysis and Subsequent Horizontal Gene Transfer

Peter David Ringel,[1] Di Hu,[1,2] and Marek Basler[1,3,*]
[1]Focal Area Infection Biology, Biozentrum, University of Basel, Klingelbergstrasse 50/70, CH-4056 Basel, Switzerland
[2]Present address: GE Healthcare Shanghai, No. 1 Huatuo Road, Pudong New District, Shanghai, China
[3]Lead Contact
*Correspondence: marek.basler@unibas.ch
https://doi.org/10.1016/j.celrep.2017.12.020

SUMMARY

Bacteria use type VI secretion systems (T6SSs) to manipulate host cells during pathogenesis or to kill competing bacteria, which, in some cases, increases horizontal gene transfer. These functions largely depend on T6SS regulation, dynamics, and the set of effectors that the system delivers into the target cells. Here, we show that *Acinetobacter baylyi* ADP1 assembles a highly dynamic T6SS capable of killing and lysing bacterial cells. T6SS function depends on conserved T6SS components as well as *Acinetobacter*-specific genes of unknown function. Five different effectors, encoded next to VgrG or PAAR proteins and their cognate immunity proteins, cause distinct changes in the prey cells, resulting in various degrees of their lysis. Prey lysis correlates with the rate of DNA transfer from prey to predator, suggesting that lytic effectors are required for efficient T6SS-dependent horizontal gene transfer in naturally competent bacteria.

INTRODUCTION

Bacteria secrete various substrates by specialized secretion systems to manipulate their environment (Costa et al., 2015). The type VI secretion system (T6SS) (Pukatzki et al., 2006) gene clusters are found in more than 25% of all sequenced Gram-negative bacteria, but mostly in the proteobacteria (Bingle et al., 2008). Systems similar to the proteobacterial T6SS have been discovered in *Francisella* (de Bruin et al., 2007; Clemens et al., 2015), *Bacteroidetes* (Russell et al., 2014a), and more recently in *Amoebophilus asiaticus* (Böck et al., 2017), overall constituting four phylogenetically distinct subgroups.

The T6SS is composed of three distinct substructures: the membrane complex, the baseplate, and the sheath-tube complex (Basler et al., 2012; Chang et al., 2017). The envelope-spanning membrane complex is usually composed of TssJ, TssL, and TssM and anchors the T6SS to the cell envelope (Durand et al., 2015). The baseplate is composed of TssE, TssF, TssG, TssK (Brunet et al., 2015), and, in some organisms, a TssA variant (Planamente et al., 2016). The baseplate serves as a platform for the polymerization of the contractile sheath-tube complex and connects it to the membrane complex. The contractile sheath, consisting of VipA (TssB) and VipB (TssC), forms around the inner tube, which is composed of Hcp (Clemens et al., 2015; Kudryashev et al., 2015; Wang et al., 2017), by adding the sheath subunits at the end that is distal from the baseplate (Vettiger et al., 2017). The initiation of the assembly and the polymerization may require TssA (Zoued et al., 2016). Furthermore, a spike complex is situated at the tip of the Hcp tube, which is composed of a VgrG trimer (Pukatzki et al., 2007) and a PAAR protein (Shneider et al., 2013). The contraction of the sheath is thought to propel the Hcp tube with its associated spike complex into the extracellular medium or the target cell (Basler et al., 2012; Vettiger and Basler, 2016; Wang et al., 2017). The contracted sheath is recycled in an ATP-dependent manner by ClpV or ClpB (Basler and Mekalanos, 2012; Bönemann et al., 2009; Brodmann et al., 2017).

T6SS effectors may constitute extensions of any of the secreted components Hcp, VgrG, or PAAR (Pukatzki et al., 2007; Shneider et al., 2013; Ma et al., 2017), or bind non-covalently to these, then termed "cargo" effectors (Bondage et al., 2016; Hachani et al., 2014; Shneider et al., 2013; Silverman et al., 2013). Some cargo effectors require an adaptor/chaperone protein for secretion, which are not secreted themselves (Liang et al., 2015; Unterweger et al., 2015). To prevent self-intoxication, anti-bacterial effectors are accompanied by cognate immunity proteins, often encoded in close proximity to the corresponding effector (Alcoforado Diniz et al., 2015; Dong et al., 2013; Russell et al., 2014b).

Interestingly, the T6SS of *Vibrio cholerae* is part of the competence regulon, and therefore, killing of target cells may contribute to horizontal gene transfer (Borgeaud et al., 2015). *Acinetobacter baylyi* ADP1 is naturally competent throughout most of its growth (Leong et al., 2017) and encodes a single constitutively active antibacterial T6SS (Basler et al., 2013; Weber et al., 2013). Recently, the combination of natural competence and T6SS-mediated bacterial killing in *A. baylyi* was shown to contribute to the transfer of a plasmid from target cells to the predator, suggesting that this may play a role in the spread of antibiotic resistance in the related *A. baumannii* strains (Cooper et al., 2017).

Here, we characterized the dynamics of the T6SS of *A. baylyi* ADP1 using live-cell fluorescence microscopy and identified and characterized five T6SS effectors and their cognate immunity proteins. We could demonstrate that none of the effectors are

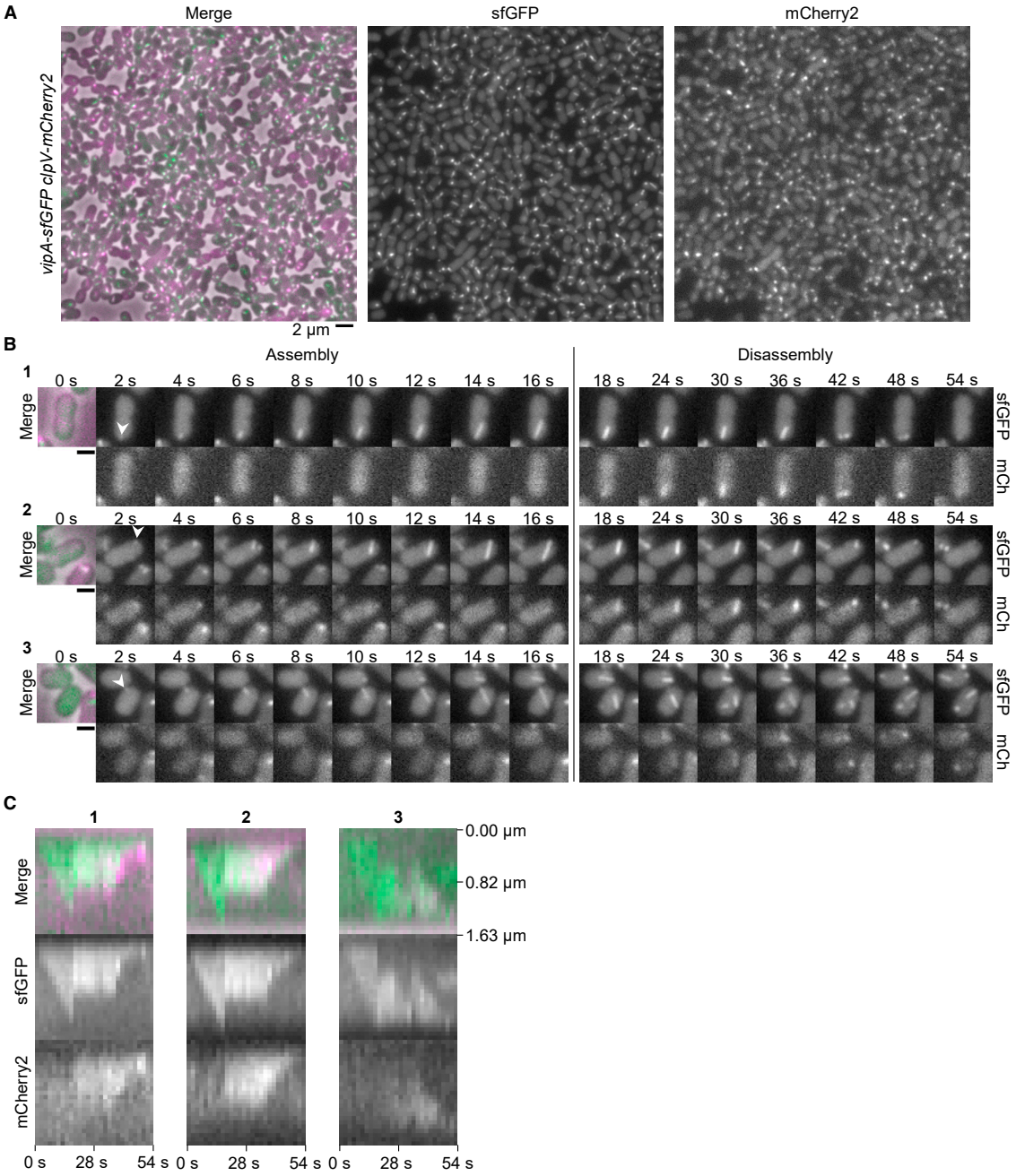

Figure 1. The T6SS Sheath Forms Dynamic Structures in *A. baylyi* ADP1

(A) Large field of view of the parental *A. baylyi* ADP1 *vipA-sfGFP clpV-mCherry2*. The images show: the merge of phase contrast, GFP (in green), and mCherry (in magenta) channels on the left, the GFP channel in the middle, and the mCherry channel on the right.

(B) Three examples of time-lapse imaging of T6SS assembly, contraction, and subsequent disassembly by ClpV. The first frame on the left shows a merge of phase contrast, GFP (in green), and mCherry (in magenta) channels. The frames in the upper rows show fluorescence in the GFP channel (sheath), and the bottom

(legend continued on next page)

required for T6SS assembly and that each kills the target cells by a distinct mechanism. Moreover, we demonstrate that the efficiency of horizontal gene transfer, promoted by the T6SS-mediated lysis of sensitive bacteria, depends on the mechanism of target cell killing.

RESULTS

T6SS Activity in *A. baylyi* ADP1 Correlates with the Formation of Dynamic Sheaths Disassembled by ClpV

To describe the dynamics of the T6SS assembly in ADP1, we first constructed a *vipA-sfGFP* and *clpV-mCherry2* strain, which then served as a parental strain for in-frame deletion mutants unless indicated otherwise (Figure S1A). Live-cell fluorescence microscopy showed that T6SS sheath structures assembled in approximately 15.0 ± 4.2 s (average ± SD, n = 60) and contracted shortly thereafter. Usually, only a single assembling sheath could be observed per cell at any given time. Occasionally, T6SS sheaths polymerized across the whole cell and bent, presumably due to colliding with the cell envelope. On contraction, ClpV-mCherry2 co-localized with the contracted sheath and disassembled it within approximately 40.1 ± 13.4 s (n = 60; Figures 1B and 1C; Movie S2). Importantly, the T6SS activity of the *vipA-sfGFP/clpV-mCherry2* strain was indistinguishable from that of the wild-type strain in its ability to lyse or inhibit growth of *Escherichia coli* as well as secrete Hcp (Figures 2B and 2C), indicating that the fluorescent protein tags have no influence on the T6SS function.

No Hcp could be detected in the supernatant of the Δ*tssM* strain (Figure 2C) and neither the Δ*hcp* nor the Δ*tssM* strains inhibited the growth of *E. coli* or induced its lysis (Figure 2B). Moreover, no dynamic sheath structures were detected in the Δ*tssM* or Δ*hcp* strains (Figure 2A), however, some static VipA-sfGFP foci were observed in the Δ*tssM* strain. This was in contrast to the Δ*tssE* strain, in which we found dynamic VipA-sfGFP foci associated with the cell periphery (Movie S1). Nonetheless, those are unlikely to be functional assemblies, because we were unable to detect Hcp in the supernatant of the Δ*tssE* strain, and the recovery and lysis of *E. coli* were indistinguishable from that of the Δ*tssM* strain (Figures 2B and 2C). We cannot exclude a potential polar effect of the *tssE* deletion on the downstream-encoded TssF and TssG, which were shown to be essential components of T6SS (Brunet et al., 2015; Weber et al., 2016). Although TssE homology to gp25 of the T4 phage suggests its critical role in the assembly and function of T6SS (Kudryashev et al., 2015; Taylor et al., 2016), it was shown for *V. cholerae* that a Δ*tssE* strain retains detectable T6SS activity (Vettiger and Basler, 2016).

TagN, TagF, ACIAD2693, and ACIAD2698 Are Largely Dispensable for T6SS Activity

TagN was proposed to be required for anchoring the T6SS to the peptidoglycan (Aschtgen et al., 2010). In ADP1, the TagN homolog (ACIAD2682) is the only protein encoded in the core cluster bearing a predicted peptidoglycan binding domain and a cleavable N-terminal signal sequence. Surprisingly, the Δ*tagN* strain secreted Hcp and displayed only an intermediate phenotype both in the quantitative competition assay and the lysis assay (Figures 2B and 2C). Furthermore, it had fewer active T6SS structures (Figure 2A; Movie S1). Peptidoglycan was shown to be dispensable for the T6SS activity in *V. cholerae* (Vettiger et al., 2017). However, *V. cholerae* seems to lack T6SS-associated peptidoglycan anchoring proteins (Aschtgen et al., 2010).

Very little is known about the *Acinetobacter*-specific T6SS components ACIAD2693 and ACIAD2698. ACIAD2698 contains a single predicted N-terminal transmembrane helix with the C terminus being disordered and residing in the periplasm. A similar analysis suggested that ACIAD2693 carries a cleavable N-terminal signal sequence and an intrinsically unstructured C-terminal region.

The Δ*ACIAD2698* strain was phenotypically indistinguishable from the parental strain (Figures 2A–2C; Movie S1). On the other hand, the Δ*ACIAD2693* strain secreted Hcp, but displayed an intermediate phenotype in the quantitative *E. coli* competition assay (Figures 2B and 2C). Even though the *E. coli* inhibition was significantly decreased in the absence of ACIAD2693, the lysis of *E. coli* was indistinguishable from that induced by the parental strain (Figure 2B). The decreased inhibition of *E. coli* is in agreement with the reduction in the number of sheath assemblies per cell (Figure 2A). However, the dynamics of the individual T6SS structures were unaltered (Movie S1). Even though *ACIAD2693* overlaps with the essential *vipA*, a polar effect is unlikely the reason for the decreased T6SS activity since the VipA-sfGFP fluorescence was comparable to that of the parental strain (Figure 2A).

TagF was reported to act as a posttranslational repressor of the H1-T6SS in *Pseudomonas aeruginosa* PAO1 (Silverman et al., 2011). However, we observed no change in *E. coli* inhibition or frequency of T6SS sheath assembly in the Δ*tagF* strain. Furthermore, both the lysis of *E. coli* and the Hcp secretion were unaffected (Figures 2A–2C; Movie S1). This suggests that TagF has a different function in *A. baylyi* ADP1 or that it does not act as a repressor under the tested conditions.

TagX and ACIAD2685 Are Required for the Initiation of the T6SS Sheath Assembly

The recently characterized L,D-endopeptidase TagX is thought to be involved in forming a hole in the peptidoglycan, allowing the assembly of the T6SS (Weber et al., 2016). Accordingly, we were unable to detect Hcp in the supernatant of the Δ*tagX* strain, and the *E. coli* inhibition was similar to that caused by the Δ*tssM* strain (Figures 2B and 2C). Interestingly, the more sensitive CPRG conversion assay indicated that the Δ*tagX* strain is still capable of lysing *E. coli*, although to a much lesser extent than the parental strain (Figure 2B), suggesting that the T6SS is still partially active in the absence of TagX. This was

rows show fluorescence in the mCherry channel (ClpV). The arrows indicate the sites where new T6SS sheath structures are forming. The scale bars represent 1 μm.

(C) Kymographs depicting the three examples of assembly, contraction, and subsequent disassembly of the T6SS sheath structures shown in (B). The line for generating the kymogram was drawn along the long axis of the highlighted structure.

See also Movies S1 and S2.

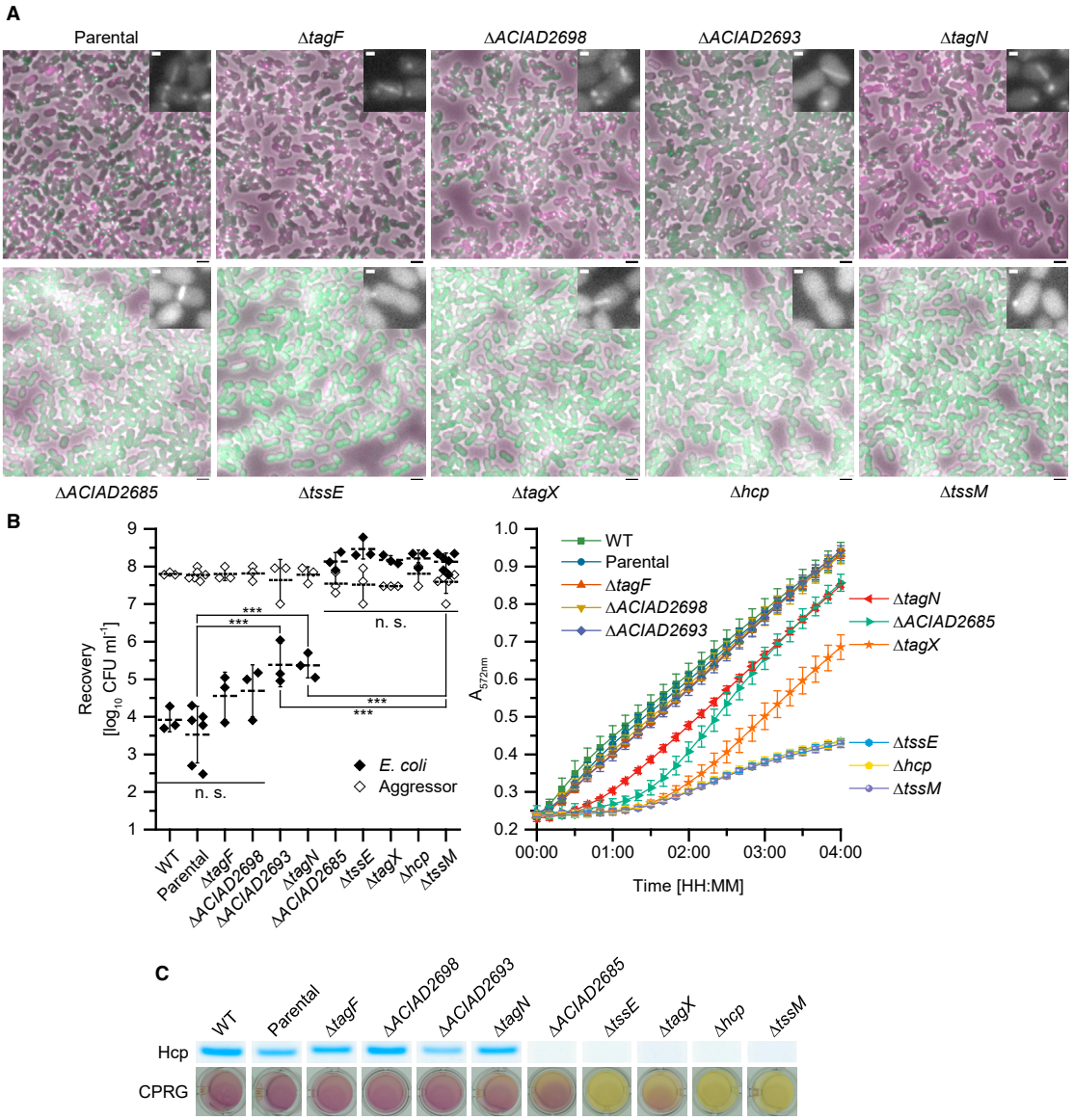

Figure 2. Characterization of Selected T6SS Components of *A. baylyi* ADP1

(A) Large fields of view of the indicated mutants of *A. baylyi* ADP1 showing the merge of phase contrast, GFP (for VipA-sfGFP in green), and mCherry (for ClpV-mCherry2 in magenta) channels. A close up of the GFP channel of a selected region of interest is shown as an inset. The scale bars of the large fields of view represent 2 μm and those of the insets represent 0.5 μm.

(B) The quantitative competition assay measuring recovery of the indicated strains after 4 hr of coincubation of *E. coli* with the indicated aggressor strains is shown on the left. The error bars indicate the SD, the long dashed lines indicate the mean value of the *E. coli* recovery, and the short dashed lines indicate the mean value of the aggressor recovery. n. s. = not significant; ***$p < 0.001$. Lysis assays measuring CPRG conversion upon release of LacZ from *E. coli* cells incubated with the indicated *A. baylyi* strains for the indicated time are shown on the right. The lysis assays were performed in biological triplicate and technical hexaplicate for all competitions except for the parental and the Δ*tssM* strains for which biological and technical hexaplicates were performed.

(C) Hcp detected in the culture supernatant of the indicated strains after trichloroacetic acid (TCA) precipitation, separation by PAGE and subsequent staining with Coomassie. Representative pictures of the endpoints of the lysis assays from (B) are shown for comparison.

See also Figures S1 and S4 as well as Movie S1.

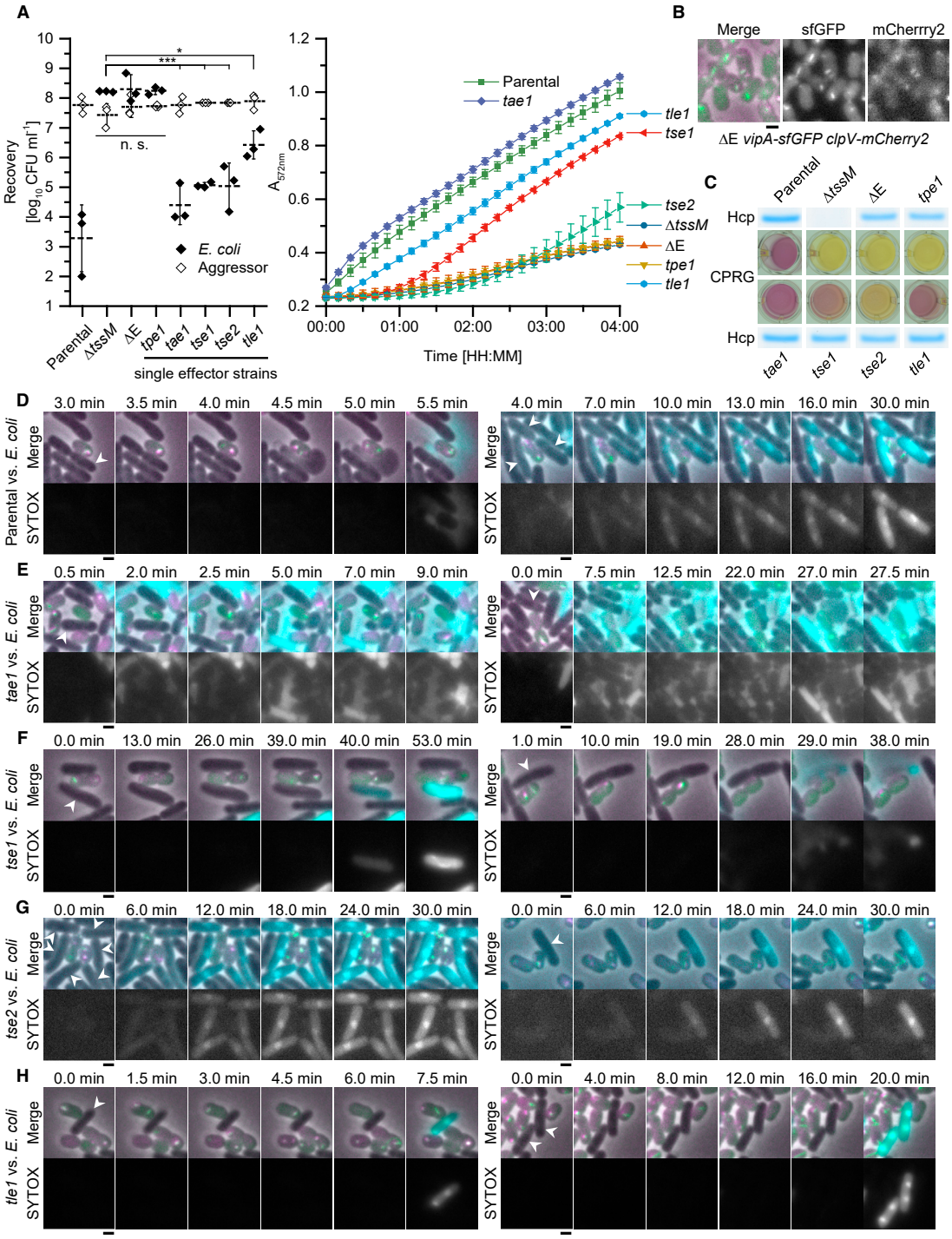

(legend on next page)

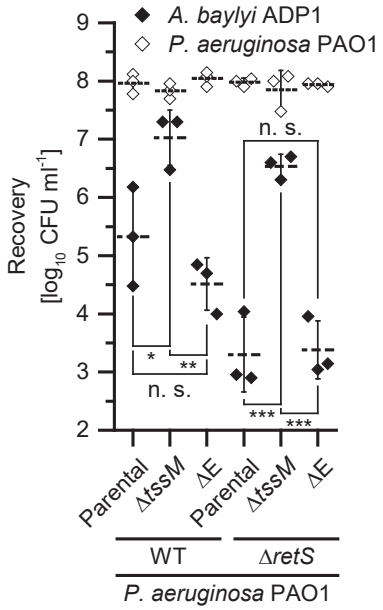

Figure 4. The T6SS Effectors of *A. baylyi* ADP1 Are Dispensable for Eliciting Retaliation from *P. aeruginosa* PAO1

Quantitative competition assays measuring recovery of the indicated *A. baylyi* and *P. aeruginosa* strains upon 4 hr of coincubation. The dashed lines indicate the means and the error bars indicate the SD. n. s. = not significant; *p < 0.05; **p < 0.01; ***p < 0.001.

See also Figure S4.

confirmed by fluorescence microscopy, which revealed a strongly reduced frequency of T6SS sheath assembly initiation (Figure 2A; Movie S1), indicating that TagX is dispensable for the T6SS mode of action after the assembly is initiated by a TagX-independent mechanism.

Bioinformatic analysis of ACIAD2685 suggested the presence of two N-terminal transmembrane helices and that the N- and C-termini are localized in the cytoplasm. The T6SS activity of the Δ*ACIAD2685* strain was severely attenuated. There was no detectable Hcp secretion and no inhibition of *E. coli* (Figures 2B and 2C). However, the more sensitive CPRG conversion assay indicated that *E. coli* lysis was still occurring, albeit to a severely reduced extent (Figure 2B). These results are in agreement with the strongly reduced frequency of T6SS assembly observed by fluorescence microscopy, similar to what had been observed for the Δ*tagX* strain (Figure 2A; Movie S1). TssM is encoded right downstream of ACIAD2685, therefore, we cannot exclude a potential polar effect of the in-frame deletion.

Five Identified T6SS Effectors Are Dispensable for T6SS Dynamics and Hcp Secretion

The fact that T6SS effectors are often found encoded in an operon with a secreted structural component and the cognate immunity protein allowed us to identify five putative effectors and their cognate immunity proteins in *A. baylyi* ADP1 (Figure S1B). An effector-deficient strain (ΔE), lacking all five identified effectors, was still able to secrete Hcp, and its T6SS activity and dynamics, observed by fluorescence microscopy, were unaffected (Figures 3B and 3C; Movie S1). However, we were unable to detect a growth inhibition of *E. coli* or its lysis when competed against the ΔE strain (Figure 3A). Moreover, no *E. coli* permeabilization was detected by fluorescence microscopy using SYTOX Blue as a cell permeability reporter (Movie S3). This suggests that there is no remaining antibacterial effector secreted by the ΔE strain, and that none of the effectors are structural or functional components of the secretion system itself.

To test if the T6SS in the ΔE strain is capable of inflicting damage, we co-incubated the strain with both *P. aeruginosa* PAO1 and its Δ*retS* variant. Interestingly, both the wild-type and the Δ*retS* strain inhibited the *A. baylyi* ΔE strain to the same level as its parental strain. However, the inhibition of *A. baylyi* was significantly reduced when the Δ*tssM* strain was co-incubated with the *P. aeruginosa* wild-type or Δ*retS* strains (Figure 4). This is consistent with previous observations (Basler et al., 2013; Wilton et al., 2016) and suggests that the ΔE strain is likely damaging at least the outer membrane of target cells and thus induces retaliation by *P. aeruginosa*.

Figure 3. *A. baylyi* ADP1 deploys antibacterial T6SS effectors eliciting distinct lysis phenotypes

(A) Quantitative competition assay measuring recovery of the indicated strains after 4 h of coincubation of *E. coli* with the indicated aggressor strains is shown on the left. The error bars indicate the standard deviation, the long dashed lines indicate the means of the *E. coli* recovery and the short dashed lines indicate the means of the aggressor recovery. Lysis assays measuring CPRG conversion upon release of LacZ from *E. coli* cells incubated with the indicated *A. baylyi* strains for the indicated time is shown on the right. The lysis assays were performed in biological triplicate and in at least technical tetraplicate. n. s. = not significant; * = p < 0.05; *** = p < 0.01.

(B) Representative image of effector deficient strain (ΔE *vipA-sfGFP clpV-mCherry2*) shows the merge of phase contrast, GFP (in green) and mCherry (in magenta) channels on the left; the GFP channel in the middle; and mCherry channel on the right. The scale bar is equivalent to 1 μm.

(C) Hcp detected in the culture supernatant of the indicated strains after TCA precipitation, separation by PAGE, and subsequent staining with Coomassie. For comparison, representative images of the endpoints of the lysis assay from (A) are shown.

(D–H) Time-lapse microscopy of the competitions of the parental strain (D) and the *tae1* (E), *tse1* (F), *tse2* (G), and *tle1* (H) single effector *A. baylyi* ADP1 strains with *E. coli*. The representative frames were chosen to illustrate the distinct lysis phenotypes elicited by the indicated effectors. The top rows show a merge of phase contrast, GFP (for VipA-sfGFP in green), mCherry (for ClpV-mCherry2 in magenta), and SYTOX (in cyan) channels. The bottom rows show the increase in the fluorescence of the cell-impermeable DNA stain SYTOX Blue on the loss of cell membrane integrity. The scale bars represent 1 μm. The arrows indicate the cells that lose membrane integrity throughout the time lapse. Except for (F), the competitions were imaged every 30 s for 30 min. For (F), the competitions were imaged every 1 min for 1 hr.

See also Figures S1, S2, and S4 as well as Movies S1 and S3.

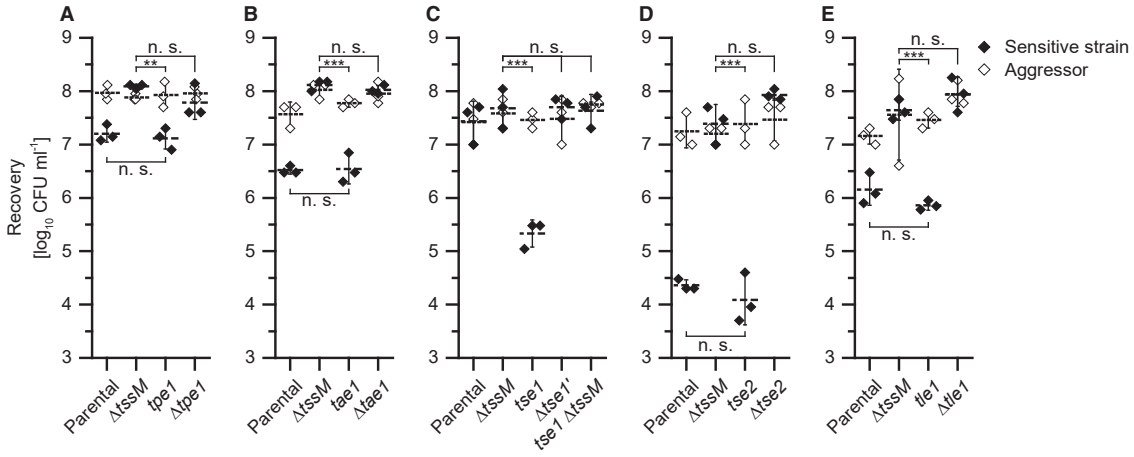

Figure 5. There Is No Crosstalk between the Five T6SS Effectors and Their Cognate Immunity Proteins

(A–E) Quantitative competition assays measuring recovery of the sensitive strains and the specified mutants after 4 hr of coincubation. The error bars indicate the SD, the long dashed lines indicate the mean recovery of the sensitive strains and the short dashed lines indicate the mean recovery of the aggressors. n. s. = not significant; *p < 0.05; **p < 0.01; ***p < 0.001.

(A) Δ*tpe1-tpi1*::*rpsL'-kan*^{R} used as the sensitive strain.

(B) Δ*tae1-tai1*::*rpsL'-kan*^{R} used as the sensitive strain.

(C) Δ*tap1-tsi1b*::*rpsL'-kan*^{R} used as the sensitive strain.

(D) Δ*tse2* Δ*tsi2a-tsi2b*::*rpsL'-kan*^{R} used as the sensitive strain.

(E) Δ*tli1-tle1*::*rpsL'-kan*^{R} used as the sensitive strain.

To investigate the role of the individual effectors, strains lacking all but one of the effectors (single effector strains) were constructed. All five single effector strains secreted Hcp and displayed sheath dynamics similar to the parental strain (Figures 3C–3H; Movie S3). The strains were tested for their ability to lyse or inhibit growth of *E. coli* (Figure 3A). To dissect the mode of action of the individual effectors, we also incubated the strains with *E. coli* and imaged the competition for 30 min to 1 h at 30°C on a Luria-Bertani (LB) agarose pad containing SYTOX Blue as an indicator for cell permeability (Figures 3D–3H; Movie S3). Since putative immunity proteins were identified in the vicinity of the effectors, we constructed strains lacking the immunity-effector pairs and tested their growth inhibition due to interactions with the corresponding single effector, the parental, the single effector deletion, and the Δ*tssM* strains (Figures 5A–5E).

The Putative Metallopeptidase Tpe1 Is a T6SS Effector and Tpi1 Is Its Cognate Immunity Protein

The smallest of the putative effectors, Tpe1 (ACIAD0053), is encoded in an operon with two PAAR proteins (Figure S1B). It is predicted to contain a zinc metallopeptidase active site, PS00142 (Figure S1C). The single effector strain was unable to significantly reduce the recovery of *E. coli* or induce its lysis (Figures 3A and 3C). Additionally, the imaging of the competition with *E. coli* showed no increase in signal from the DNA-binding dye SYTOX Blue, suggesting that no *E. coli* cell permeabilization was occurring (Movie S3).

The protein encoded downstream of Tpe1, which we termed Tpi1 (ACIAD0054), contains a predicted N-terminal transmembrane helix, and we hypothesized it to constitute the cognate immunity protein to Tpe1 (Figure S1B). The competition of the sensitive strain (lacking both Tpe1 and Tpi1) against the parental and the single effector strains led to a significantly reduced recovery of the sensitive strain, whereas there was no such reduction when competed against the Δ*tssM* and the Δ*tpe1* strains (Figure 5A). This indicates that Tpe1 is a T6SS effector and Tpi1 is its corresponding immunity protein. The fact that no *E. coli* inhibition or lysis was detected suggests that either *E. coli* is resistant to the action of Tpe1 or that *E. coli* can outgrow its effects without lysis.

Tae1 Is a Peptidoglycan-Targeting T6SS Effector and Tai1 Is Its Cognate Immunity Protein

The remaining putative T6SS effectors are encoded downstream of VgrGs. Bioinformatic analysis of the sequence of Tae1 (ACIAD0168) suggested that it is a peptidoglycan-hydrolyzing amidase, which has no clear homology to any of the four currently known families (Russell et al., 2012). Tae1 contains two predicted peptidoglycan-binding domains (LysM, PF01476.19, and IPR002477), a D-alanyl-D-alanine carboxypeptidase zinc-binding domain (IPR009045) and a peptidoglycan-hydrolyzing domain (hydrolase_2, PF07486.11; Figure S1C), suggesting that Tae1 cleaves the peptide crosslinks of peptidoglycan. The single effector strain significantly reduced the recovery of *E. coli* and induced its lysis to a level comparable to that of the parental strain (Figures 3A and 3C). Imaging the competition with *E. coli* revealed that lysing *E. coli* often round up and burst (Figure 3E; Movie S3), which is consistent with

the prediction that Tae1 encodes a peptidoglycan-targeting effector.

The gene downstream of *tae1* encodes a protein we termed Tai1 (ACIAD0169), which carries a predicted cleavable N-terminal signal sequence, suggesting that Tai1 is the cognate immunity protein of Tae1. When the Δ*tae1*/Δ*tai1* strain was competed with the parental strain or the Tae1 single effector strain, the recovery of the Δ*tae1*/Δ*tai1* strain was significantly reduced. This was fully dependent on T6SS activity and presence of *tae1*, since the recovery was restored when competed against the Δ*tae1* and the Δ*tssM* strains (Figure 5B). This indicates that Tae1 is a peptidoglycan-targeting T6SS effector and that Tai1 is the cognate immunity protein.

The Restored Tse1 Is a T6SS Effector and Tsi1a or Tsi1b Are Its Cognate Immunity Proteins

Downstream of VgrG2 (ACIAD1788), a protein we termed Tap1 (ACIAD1789) is encoded that shows weak homology to the DUF4123 domain found in T6SS effector chaperones (TECs), also referred to as adaptor proteins (Liang et al., 2015; Unterweger et al., 2015). The downstream gene terminates at a copy of the insertion element IS1236, suggesting that the original gene was disrupted by IS1236 (Figure S1B). Indeed, a BLAST search of the N-terminal fragment Tse1' (ACIAD1790) in the UniParc (The UniProt Consortium, 2017) database yielded longer proteins in various *Acinetobacter* strains, which were in the genomic neighborhood of VgrG and Tap1 homologs and whose N-terminal regions were similar to Tse1'.

We removed the insertion sequence (IS) element and restored the full-length Tse1 based on the multiple sequence alignment with the homologous effectors (ACIAD1790–1794 fusion; Figures S1B and S2). The full-length Tse1 is predicted to carry four C-terminal transmembrane helices and had a low-quality match for the short-chain dehydrogenase/reductase active site (PS00061; Figure S1C). The single effector strain significantly reduced the recovery of *E. coli* and led to intermediate lysis of *E. coli* in the CPRG conversion assay (Figures 3A and 3C). The competition microscopy showed that, in some cases, lysis proceeded similar to what had been observed for Tae1, where *E. coli* rounded up and then burst, whereas in other cases, *E. coli* shrinks slightly and lyses (Figure 3F; Movie S3). Both processes take longer compared with the lysis induced by the other effectors.

Two putative immunity proteins sharing 82% sequence identity are encoded downstream of Tse1, which we termed Tsi1a (ACIAD1795) and Tsi1b (ACIAD1796; Figure S1B). A Tse1 ortholog was only found in *Burkholderia cenocepacia* (excluding *Acinetobacter*), and immunity protein duplications were restricted to *Acinetobacter*, ranging from one to three copies (Figure S3A). Both Tsi1a and Tsi1b are predicted to contain four transmembrane helices. The sensitive strain (lacking both Tsi1a and Tsi1b) was inhibited by the single effector strain carrying the restored Tse1 (Figure 5C). However, no inhibition was observed when competed against the Δ*tssM* strain or the Δ*tse1'* strain as well as the parental strain containing the IS element. When *tssM* was deleted in the single Tse1 effector strain, no reduction in recovery of the sensitive strain could be detected (Figure 5C). This confirms that Tse1 is secreted in a T6SS-dependent manner and that Tsi1a, Tsi1b, or both are the cognate immunity proteins.

Tse2 Is a T6SS Effector and Tsi2a or Tsi2b Are Its Cognate Immunity Proteins

Tse2 (ACIAD3114) is a homolog of the recently described $Tse3_{AB}$ (ACX60_11695) in *A. baumannii* ATCC 17978, which was found to be an antibacterial effector, but its mechanism of action remained unknown (Weber et al., 2016). The single effector strain significantly reduced the recovery of *E. coli*, however, lysis, indicated by the CPRG conversion assay, was delayed compared with the other single effector strains (Figure 3A). Interestingly, *E. coli* only slowly gained SYTOX Blue signal during its interaction with the Tse2 single effector strain, and the signal remained low. This is in contrast to what we observed when *E. coli* was lysed by other effectors (Figure 3G; Movie S3). The slow increase in SYTOX Blue signal suggests that Tse2 leads to a low-level permeabilization of *E. coli*, which is consistent with the delayed conversion of CPRG by LacZ and suggests that the cell envelope remains largely impermeable to CPRG and LacZ.

The two putative immunity proteins Tsi2a (ACIAD3112) and Tsi2b (ACIAD3113), encoded in the opposite direction downstream of the effector (Figure S1B), are predicted to contain a cleavable N-terminal signal sequence, indicating that they are periplasmically localized and suggesting that the subcellular target of Tse2 is accessible from the periplasm. The recovery of the Δ*tsi2a*/Δ*tsi2b*/Δ*tse2*-sensitive strain was significantly reduced after incubation with the parental or the single effector strain, but unchanged when incubated with the Δ*tssM* or Δ*tse2* strains (Figure 5D). These data indicate that Tse2 is a T6SS effector and that Tsi2a, Tsi2b, or both confer immunity toward Tse2.

A manual inspection of gene ortholog neighborhoods of *tse2* revealed the presence of Tse2 homologs mostly in γ-proteobacteria, but also in α- and β-proteobacteria. Multiple copies of the immunity proteins, up to five consecutive ones in *Klebsiella pneumonia* W14 and *Photorhabdus luminescens* subsp. *luminescens* DSM 3368, were a common feature in γ-proteobacteria, but only two duplications were observed for β-proteobacteria, and none were observed for α-proteobacteria (Figure S3B). Immunity protein duplications seem to be common, and all may contribute to immunity (Jiang et al., 2014; Russell et al., 2013; Zhang et al., 2012). These evolved paralogs were speculated to provide immunity against diverged corresponding effectors arising in the population (Kirchberger et al., 2017; Zhang et al., 2012).

The Phospholipase Tle1 Is a T6SS Effector and Tli1 Is Its Cognate Immunity Protein

Tle1 (ACIAD3425) was predicted to be a phospholipase belonging to family 4 of T6SS-associated phospholipases (Russell et al., 2013). It matches an alpha/beta-hydrolase fold (Gene3D 3.40.50.1820) and the abhydrolase_5 domain (PF12695.5; Figure S1C). The Tle1 single effector strain significantly reduced the recovery of *E. coli* and led to intermediate lysis of *E. coli* in the CPRG conversion assay (Figures 3A and 3C). Surprisingly, when the Tle1 single effector strain was co-incubated with *E. coli*, the *E. coli* cells first shrank without an increase of SYTOX Blue signal and then reinflated, coinciding with their permeabilization (Figure 3H; Movie S3).

The putative immunity protein is co-encoded in the same operon upstream of *tle1*, which we termed Tli1 (ACIAD3426). Tli1 carries a predicted cleavable N-terminal signal sequence as is common for the cognate phospholipase immunity proteins (Russell et al., 2013). The recovery of the sensitive strain was significantly reduced when competed against the parental or single effector strain. The recovery was restored when competed against the Δ*tssM* or the Δ*tle1* strains (Figure 5E). These results confirm that Tle1 is a T6SS effector and that Tli1 is its cognate immunity protein.

The T6SS-Mediated Lysis of Prey Contributes to Horizontal Gene Transfer

T6SS-mediated killing of prey cells by the naturally competent *A. baylyi* ADP1 can liberate the DNA of the prey and thereby promote horizontal gene transfer (Cooper et al., 2017). We speculated that effectors causing the release of cellular content, like Tae1 and Tle1, should cause a higher transformation rate than those not directly leading to lysis, like Tse2. To test this hypothesis, we competed a spectinomycin-resistant, T6SS-active *A. baylyi* ADP1 derivative (T6SS$^+$) against the Tle1- and the Tse2-sensitive strains (Figures 6A and 6B). The sensitive strains carry the kanamycin resistance cassette, disrupting the immunity protein-encoding genes. Successful transfer of DNA can thus be monitored by selecting for spectinomycin and kanamycin double-resistant strains.

To account for DNA transfer independent of T6SS-mediated killing, a T6SS-deficient, spectinomycin-resistant strain (T6SS$^-$) was used as a control strain. To exclude possible differences in uptake and integration of the counter-selectable cassettes from the Tle1- and Tse2-sensitive strains, we transformed the T6SS$^+$ strain with equal amounts of the genomic DNA of both sensitive strains and enumerated the resulting double-resistant mutants. The number of transformants obtained with the genomic DNA was not significantly different, indicating that both cassettes incorporate with similar efficiency (Figure 6A).

When we incubated the T6SS$^+$ strain with the Tle1- and Tse2-sensitive strains, we observed reduced recoveries of the sensitive strains comparable with those obtained during our previous assays (compare Figures 5D and 5E with Figure 6B). In addition, similar to the observations made for the competition with *E. coli*, the lipase effector Tle1 induced lysis of the non-immune *A. baylyi* strain (*vipA-sfGFP clpV-mCherry2 Δtli1-tle1*) as documented by the leakage of DNA out of cells, the decrease in contrast of the bacterial cytosol, and the rapid accumulation of SYTOX Blue signal (Figures 6C). On the other hand, the Tse2-effector-mediated killing resulted in a high level of inhibition of the non-immune *A. baylyi* strain (*vipA-sfGFP clpV-mCherry2 Δtse2 Δtsi2a-tsi2b*; Figure 6B), however, no clear cell lysis was observed, and the cells accumulated SYTOX Blue rather slowly (Figure 6D). Importantly, the competition of the T6SS$^+$ strain with the Tle1-sensitive strain produced significantly more double-resistant mutants than the competition of the T6SS$^+$ strain with the Tse2-sensitive strain or the T6SS-independent transfer (Figure 6A). Overall, these data suggest that the mechanisms of killing and lysis of target cells have major implications for DNA release and thus efficiency of horizontal gene transfer.

DISCUSSION

Imaging of *A. baylyi* ADP1 T6SS sheath dynamics and the use of a sensitive target cell lysis assay allowed us to identify *Acinetobacter*-specific T6SS components, which are required for efficient initiation of sheath assembly (Table 1). We predicted and characterized five distinct effectors and their immunity proteins and show that the mechanism of target cell killing influences the efficiency of gene acquisition from prey cells.

We show that a markerless in-frame deletion of *ACIAD2693* only has a partial effect on the T6SS function, and in many assays, the deletion strain displayed a phenotype similar to that of the wild-type *A. baylyi* (Figures 2A–2C; Movie S1). A likely explanation for the discrepancy with the previous results is a potential polar effect on the downstream *vipA* (*tssB*) gene resulting from generating insertion mutants using a Tdk-Kan^R cassette (Weber et al., 2016).

ACIAD2685 and TagX were proposed to be essential for T6SS-mediated Hcp secretion (Weber et al., 2016). Interestingly, we show that the strains lacking ACIAD2685 or TagX occasionally assemble sheath structures that display dynamics similar to that of the parental strain (Figure 2A; Movie S1). Importantly, the prey cell lysis assay shows that those assemblies are functional, which suggests that ACIAD2685 and TagX influence the frequency of T6SS sheath assembly rather than the function of the individual T6SS structures (Figure 2B). This is consistent with the fact that TagX is an L,D-endopeptidase cleaving the peptide crosslinks of the peptidoglycan, which was proposed to form holes in the peptidoglycan to allow assembly of the T6SS (Weber et al., 2016). Similarly, the lytic transglycosylase MltE was recently shown to be recruited by the TssM of the Sci-1 in *E. coli* EAEC 17-2 to fulfil the same purpose (Santin and Cascales, 2017). Therefore, the low number of T6SS assemblies detected in the Δ*tagX* strain may be due to the formation of holes in the peptidoglycan during its remodeling or aging. Although the phenotype of the Δ*ACIAD2685* strain is similar to that of the Δ*tagX* strain, the lack of conserved domains prevents predicting its function.

We identified five T6SS effectors and their corresponding immunity proteins in *A. baylyi* ADP1, a putative metallopeptidase (Tpe1), a peptidoglycan-hydrolyzing amidase (Tae1), a phospholipase (Tle1), and two effectors (Tse1, and Tse2) representing new classes of effectors for which no enzymatic activity could be predicted or deduced from the lysis phenotype. Interestingly, the *A. baylyi* strain lacking all five effectors (ΔE) was unable to inhibit *E. coli* or induce cell membrane leakage (Figures 3A and 3C; Movie S3). This is despite the fact that the ΔE strain assembles dynamic T6SSs secreting wild-type levels of Hcp (Figures 3B and 3C; Movie S1). The ΔE strain also provokes retaliation by *P. aeruginosa* (Figure 4) since it is killed as well as the wild-type *A. baylyi* strain. This suggests that the retaliation from *P. aeruginosa* is independent of effector delivery and is rather a response to membrane perturbations as indicated previously (Basler et al., 2013; Ho et al., 2013; Wilton et al., 2016). Interestingly, this also means that mere puncturing of the target cell membrane is insufficient for killing or lysis of target cells and that the delivery of effector proteins is required. This is consistent with observations that even multiple puncturing of

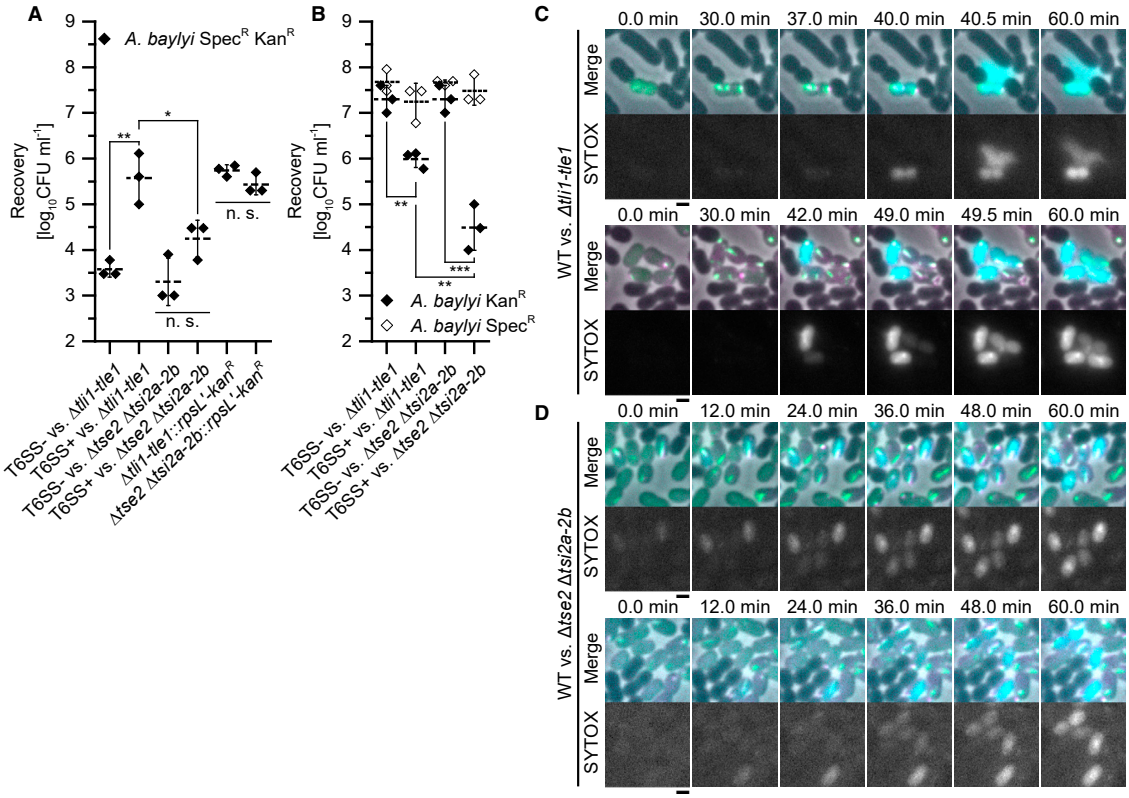

Figure 6. The Level of Horizontal Gene Transfer Depends on the Mechanism of Prey Cell Killing

(A) The level of DNA transfer between the indicated strains was tested by enumerating the clones having acquired a resistance cassette after 4 hr of coincubation. The control transformations of the T6SS$^+$ strain with genomic DNA are labeled as Δ*tli1-tle1*::*rpsL'-kan*^{R} and Δ*tse2* Δ*tsi2a-2b*::*rpsL'-kan*^{R}.

(B) Quantitative competition assay measuring the recovery of the indicated strains coincubated as in (A). The dashed lines indicate the means and the error bars indicate the SD. n. s. = not significant; *p < 0.05; **p < 0.01; *** p < 0.001.

(C and D) Time-lapse microscopy illustrating the distinct lysis phenotypes of the Δ*tli1-tle1* (C) and the Δ*tse2* Δ*tsi2a-2b* (D) sensitive strains (*vipA-sfGFP clpV-mcherry2* background) incubated with unlabeled wild-type *A. baylyi* ADP1. The top rows show a merge of phase contrast, GFP (green), mCherry (magenta), and SYTOX (cyan) channels. The bottom rows show the increase in the fluorescence of the cell-impermeable DNA stain SYTOX Blue upon the loss of cell membrane integrity. The mixtures were imaged every 30 s for 1 hr. The scale bars represent 1 μm.

diderm bacteria with an atomic force microscopy (AFM) tip does not affect their viability, which was explained by the "self-healing" capabilities of the cell envelope after AFM tip removal (Suo et al., 2009). On the other hand, R-type pyocins, which are structurally and mechanistically related to the T6SS, insert a tube into the target cell envelope, which results in ion leakage and cell killing (Ge et al., 2015; Michel-Briand and Baysse, 2002). This therefore suggests that the T6SS tube is likely unstable, and after delivery to the target cell, the Hcp tube dissociates, allowing the membranes to reseal.

All of the identified T6SS effectors (except Tpe1) were capable of significantly inhibiting or lysing *E. coli* (Figures 3A and 3C). Similarly, other bacteria carrying antibacterial effectors were often shown to deploy more than one antibacterial effector (Alcoforado Diniz et al., 2015). For example, *V. cholerae* has been demonstrated to utilize effector sets for intraspecific competition, where strains with incompatible combinations of effectors and immunity proteins will intoxicate one another (Unterweger et al., 2014). Interestingly, the T6SS of *V. cholerae* is involved in horizontal gene transfer (Borgeaud et al., 2015), and *V. cholerae* was also shown to be capable of acquiring new effector-immunity pairs or of exchanging old ones while retaining the corresponding immunity protein (Kirchberger et al., 2017; Unterweger et al., 2014). Similarly, the T6SS of the naturally competent *A. baylyi* ADP1 was recently shown to promote transfer of a plasmid from prey to predator (Cooper et al., 2017). The related *A. baumannii* strains, while not generally naturally competent under laboratory conditions, carry similar genes required to uptake DNA and kill target cells. It is therefore tempting to speculate that the T6SS-mediated killing of target cells by *A. baumannii* could be contributing to the highly efficient spread of drug resistance genes (Cooper et al., 2017), especially

Table 1. Summary of Knockout Phenotypes

Deletion	Competitor Inhibition	Hcp	Dynamics	Lysis	Previously Observed Phenotypes
tssE	0	0	+/0	0	approximately 1,000-fold less active in *V. cholerae* with no detectable competitor CFU reduction, but residual prey lysis (Vettiger and Basler, 2016)
tagF	+++	+++	+++	+++	increased Hcp secretion in *P. aeruginosa* (Silverman et al., 2011) and *B. cenocepacia* (Aubert et al., 2015)
tagN	++	+++	++	++	this study and Weber et al., 2016
tagX	0	0	+	+	this study and Weber et al., 2016
ACIAD2685	0	0	+	++	this study and Weber et al., 2016
ACIAD2693	++	++	++	+++	this study and Weber et al., 2016
ACIAD2698	+++	+++	+++	+++	this study and Weber et al., 2016

The phenotypes are given as qualitative values: +++, similar to wild-type; ++, attenuated; +, detectable; 0, not detectable.

if competence and T6SS would be co-regulated as in *V. cholerae* (Borgeaud et al., 2015). However, it is also important to mention that many organisms, including *Acinetobacter* and *Vibrio*, may secrete DNases in a T6SS-dependent and -independent manner, which could decrease the rate of horizontal gene transfer.

Overall, potentially all bacteria that encode an anti-bacterial T6SS and DNA uptake machinery could use their T6SS to acquire new genes. In addition to *Vibrio* and *Acinetobacter*, this could be relevant for *Campylobacter*, *Pseudomonas*, *Agrobacterium*, and *Ralstonia*. Members of these genera were predicted to harbor a T6SS (Li et al., 2015) and to be naturally competent (reviewed in Johnston et al., 2014). The targeted lysis and acquisition of genes from bacteria occupying a certain environmental niche may provide an advantage to the T6SS-positive bacteria since the target bacteria likely carry genes that evolved to enhance survival in the niche (Veening and Blokesch, 2017). Importantly, the rate of horizontal gene transfer mediated by T6SSs will vary for each prey-predator pair, because the frequency of DNA acquisition depends on the mode of target cell killing (Figure 6). This suggests that for efficient DNA acquisition from various prey cells, a diverse set of lytic effectors delivered by the predator may be beneficial, as certain prey cells may be immune to some of those effectors.

EXPERIMENTAL PROCEDURES

Bioinformatic analyses were carried out as described in the Supplemental Experimental Procedures.

Culturing of the Bacterial Strains

The strains were grown shaking at 200 rpm and 30°C or 37°C in LB broth or on LB agar (LA) plates (1.3% [w/v] agar). The media were supplemented with the appropriate antibiotics. For *E. coli* MG1655 Gm^R, 15 μg/mL gentamicin was added, for *A. baylyi* ADP1 *rpsL*-K88R derivatives, 50 μg/mL streptomycin was added, and for *A. baylyi* ADP1 strains carrying the positive/negative selection cassette, 50 μg/mL kanamycin was added. The strains carrying a spectinomycin resistance cassette were grown in the presence of 300 μg/mL spectinomycin. *P. aeruginosa* PAO1 was first grown on an LA plate overnight, and then an LB overnight culture supplemented with 20 μg/mL irgasan was started from the plate. The strains used in this study are listed in Table S1.

Construction of the Positive/Negative Selection Cassette

A positive/negative selection cassette was constructed based on the recessive streptomycin resistance conferred by the genomic *rpsL*-K88R mutation (Lederberg, 1951). The positive/negative selection cassette used in this study consists of a synthetic gene encoding the native RpsL of *A. baylyi* ADP1 (IDT) under the control of the native P_{rpsL} and the *aph(3′)-Ia* conferring kanamycin resistance under the control of the P_{bla} from the pRSFDuet-1 (Novagen). The cassette was assembled using overlap extension PCR. The synthetic gene encoding the native RpsL of *A. baylyi* ADP1 was designed such that most codons were exchanged by non-identical synonymous codons to avoid recombination with the genomic *rpsL*-K88R allele. This cassette was inserted into *vipA* and sequenced. Whenever the cassette was needed, it was amplified from the genomic DNA of this initial strain. The full sequence of the cassette is in Data S1.

Generation of Chromosomal *A. baylyi* ADP1 Mutants

A. baylyi ADP1 mutants were generated based on the methods described earlier (Metzgar et al., 2004) with the modifications outlined below. The homologous flanking regions were typically chosen to be between 500 and 800 bp in length. Primers were derived from the *A. baylyi* ADP1 genomic DNA sequence (NC_005966.1 obtained from NCBI). To transform DNA to *A. baylyi*, an overnight culture was washed with LB and diluted 1:50 or 1:20 into fresh LB. The culture was then regrown for 5 hr or 2 hr and 45 min, respectively, shaking at 30°C and 200 rpm. Thereafter, a few microliters of the agarose gel-purified DNA fragment bearing the desired mutation were added to the culture, which was kept shaking at 30°C and 200 rpm for ≥1 hr. Subsequently, cells from a 1-mL culture were plated on an LA plate supplemented with the appropriate antibiotic. When selecting for the loss of the counter-selectable cassette, 100 μg/ml streptomycin was used. The efficiency of the negative selection was routinely over 90%. After re-streaking for single colonies, the success of the mutagenesis was assessed by colony PCR and subsequent sequencing. For mutants in which the target gene was disrupted by the insertion of the counter-selectable cassette, additional mutations in the disrupted gene were tolerated. PCRs for sequencing, cloning, and construction of deletion cassettes were either performed with the Q5 High-Fidelity DNA Polymerase (NEB) or with Herculase II (Agilent). Colony PCRs were performed with Taq DNA Polymerase (Sigma-Aldrich) or Q5 High-Fidelity DNA Polymerase. The mutations generated in this study are listed in Table S2.

Quantitative Competition Assays

The quantitative competition assays were performed in biological triplicates starting from three separate overnight cultures of the predator and prey strains. The *vipA-sfGFP*- and *clpV-mCherry2*-labeled parental strain served as the positive control, and the derived Δ*tssM* strain served as the negative control. After overnight cultivation, the cultures were washed once with LB to remove the antibiotic. Thereafter, the *A. baylyi* ADP1 strains were diluted 1:20, the *E. coli* MG1655 $Gent^R$ was diluted 1:100, *P. aeruginosa* PAO1 was

diluted 1:40, and *P. aeruginosa* PAO1 Δ*retS* was diluted 1:20 in 3 mL fresh LB. These cultures were incubated shaking at 200 rpm and 30°C for approximately 2 hr 40 min to reach an optical density at 600 nm (OD_{600nm}) of 0.6–1.4 and then pelleted at 20,000 × g for 2 min. The pellets were resuspended in fresh LB to reach an OD_{600nm} of approximately 10. The predator and prey strains were mixed at a ratio of 1:1, and 5 μL of the mixtures were spotted on a pre-dried LA plate. The spots were allowed to dry, and then the competition was carried out at 30°C for 4 hr. Thereafter, the spots were excised from the plate, and the bacteria were resuspended in 0.5 mL LB. These suspensions were 7× serially diluted 1:10 with LB, and 5 μL of each sample was spotted on both a prey- and a predator-selective plate. For streptomycin-resistant *A. baylyi* ADP1 derivatives, 100 μg/mL streptomycin was used. For the other strains, the usual antibiotic concentrations were used. These plates were incubated at room temperature (RT) or 30°C until colonies were visible. For the comparisons, one-way ANOVA ($\alpha = 0.05$) with a subsequent Tukey post hoc test was performed using OriginPro 2016G.

Horizontal Gene Transfer Assay

The horizontal gene transfer assay was carried out as described for the quantitative competition assay, except that the serial dilutions of the recovered bacteria were spotted on three LA plates supplemented with 300 μg/mL spectinomycin, 50 μg/mL kanamycin, and both 300 μg/mL spectinomycin and 50 μg/mL kanamycin. For the control transformations, 203 ng of the prey strain genomic DNA was added to the concentrated predator instead of the concentrated prey strains. Thereafter, the assay was carried out as described for testing horizontal gene transfer between two strains.

Hcp Secretion Assay

For the Hcp secretion assay the *A. baylyi* ADP1 derivatives were regrown as described for the quantitative competition assay. Thereafter, 1 mL of the cultures were centrifuged for 1 min at 10,000 × g and 4°C. A total of 100 μL ice-cold 100% trichloroacetic acid (w/v; Sigma-Aldrich) was added to 900 μL of the supernatants, incubated on ice for 10 min with intermittent vortexing and then centrifuged for 5 min at 14,000 × g and 4°C. The pellets were washed with ice-cold acetone, dried at RT, and then resuspended in 20 μL 1× NuPAGE LDS sample buffer (Thermo Fisher Scientific); 2.22 μL 1 M dithiothreitol was added and then incubated at 70°C for 10 min. Three-quarters of these samples were loaded onto NuPAGE 4%–12% Bis-Tris 1.0-mm, 12-well protein gels (Thermo Fisher Scientific), which were run in MES buffer (Thermo Fisher Scientific) for 35 min at 200 V. The gels were stained with InstantBlue Coomassie protein stain (Expedeon) overnight and then destained with distilled water. The assay was performed in biological duplicate. The whole gels are shown in Figure S4.

Lysis Assay

The lysis assay is based on the chromogenic hydrolysis of the cell-impermeable β-galactosidase substrate chlorophenol red-β-D-galactopyranoside (CPRG; Sigma-Aldrich) (Vettiger and Basler, 2016) upon lysis of *E. coli* MG1655 $Gent^R$. The assay was carried out similarly to the quantitative competition assay described above, except that *E. coli* was regrown in the presence of 100 μM isopropyl-β-D-thiogalactoside (IPTG) to pre-induce the β-galactosidase. After pelleting, the *E. coli* pellet was resuspended in LB supplemented with 100 μM IPTG. Only 3 μL of the competition mixtures were spotted on 150 μL LA supplemented with 100 μM IPTG and 20 μg/mL CPRG in a flat-bottom 96-well plate in hexaplicate, leaving out the outer most wells. The spots were allowed to dry. Thereafter, the plate was incubated at 30°C without a lid in an Epoch 2 plate reader (BioTek) for 4 hr while measuring the absorption at 572 nm every 10 min. When the measurement was finished, a picture of a representative plate was taken. The SDs of the biological triplicates were calculated from the averages of the technical hexaplicates except where noted otherwise.

Fluorescence Microscopy

For imaging the T6SS dynamics of the *A. baylyi* ADP1 mutants and the competition microscopy, the strains were regrown, concentrated, and mixed, when appropriate, as described for the quantitative competition assay. The concentrated culture or mixture was spotted on a thin pad of 1% (w/v) agarose in LB, covered with a glass coverslip, and imaged. For the competition microscopy, the pad was supplemented with 0.5 μM SYTOX Blue Nucleic Acid Stain (Thermo Fisher Scientific). The microscopic imaging was performed at least in biological duplicate.

The following setup was used for microscopy: a Nikon Ti-E inverted motorized microscope with Perfect Focus System and Plan Apo 100× Oil Ph3 DM (NA, 1.4) objective lens, SPECTRA X light engine (Lumencor) and ET-ECFP (Chroma #49001), ET-GFP (Chroma #49002), and ET-mCherry (Chroma #49008) filter set. A pco.edge 4.2 (PCO, Germany) scientific complementary metal-oxide-semiconductor (sCMOS) camera (pixel size, 65 nm) and VisiView software (Visitron Systems, Germany) were used to record the images. The power output of the SPECTRA X light engine was set to 20% for all excitation wavelengths. The sfGFP and SYTOX Blue images were acquired with 100-ms exposure, whereas the mCherry2 images were acquired with 200-ms exposure. A climate chamber mounted around the stage and a heating collar around the objective were used to perform the imaging at 30°C and 95% relative humidity (R. H.). The obtained images were post-processed with Fiji (Schindelin et al., 2012) and custom software based on StackReg (Thévenaz et al., 1998). The contrast settings were adjusted such that the whole display range was used for the bright field channel (0–65535). For the other channels, the minimal value was set as the lower bound, and the upper bound was set to allow 5% of the pixels to saturate. The same contrast settings were used for each frame of a time lapse.

Statistical Analysis

The number of biological replicates is indicated for each experiment. When measuring the colony forming units (CFUs) per milliliter, first the decadic logarithm was taken, and then the averages and SDs were calculated from the transformed values. For the comparisons, one-way ANOVA ($\alpha = 0.05$) with a Tukey post hoc test was performed using OriginPro 2016G. For the CPRG assays, the averages and the SDs of the biological replicates were calculated from the averages of the technical replicates.

SUPPLEMENTAL INFORMATION

Supplemental Information includes Supplemental Experimental Procedures, four figures, two tables, three movies, and one data file and can be found with this article online at https://doi.org/10.1016/j.celrep.2017.12.020.

ACKNOWLEDGMENTS

This work was supported by Swiss National Science Foundation Starting Grant BSSGI0_155778 and the University of Basel. P.D.R. was supported by the Biozentrum Basel International Ph.D. Program, Fellowships for Excellence.

AUTHOR CONTRIBUTIONS

Conceptualization, M.B. and P.D.R.; Methodology, M.B., D.H., and P.D.R.; Investigation, D.H. and P.D.R.; Writing – Original Draft, M.B. and P.D.R.; Writing – Review & Editing, M.B. and P.D.R.; Funding Acquisition, M.B.; Resources, M.B.; Supervision, M.B.

DECLARATION OF INTERESTS

The authors declare no competing interests.

Received: August 25, 2017
Revised: November 22, 2017
Accepted: December 5, 2017
Published: December 26, 2017

REFERENCES

Alcoforado Diniz, J., Liu, Y.-C., and Coulthurst, S.J. (2015). Molecular weaponry: diverse effectors delivered by the Type VI secretion system. Cell. Microbiol. *17*, 1742–1751.

Aschtgen, M.-S., Thomas, M.S., and Cascales, E. (2010). Anchoring the type VI secretion system to the peptidoglycan: TssL, TagL, TagP… what else? Virulence *1*, 535–540.

Aubert, D.F., Hu, S., and Valvano, M.A. (2015). Quantification of type VI secretion system activity in macrophages infected with *Burkholderia cenocepacia*. Microbiology *161*, 2161–2173.

Basler, M., and Mekalanos, J.J. (2012). Type 6 secretion dynamics within and between bacterial cells. Science *337*, 815.

Basler, M., Pilhofer, M., Henderson, G.P., Jensen, G.J., and Mekalanos, J.J. (2012). Type VI secretion requires a dynamic contractile phage tail-like structure. Nature *483*, 182–186.

Basler, M., Ho, B.T., and Mekalanos, J.J. (2013). Tit-for-tat: type VI secretion system counterattack during bacterial cell-cell interactions. Cell *152*, 884–894.

Bingle, L.E., Bailey, C.M., and Pallen, M.J. (2008). Type VI secretion: a beginner's guide. Curr. Opin. Microbiol. *11*, 3–8.

Böck, D., Medeiros, J.M., Tsao, H.-F., Penz, T., Weiss, G.L., Aistleitner, K., Horn, M., and Pilhofer, M. (2017). In situ architecture, function, and evolution of a contractile injection system. Science *357*, 713–717.

Bondage, D.D., Lin, J.-S., Ma, L.-S., Kuo, C.-H., and Lai, E.-M. (2016). VgrG C terminus confers the type VI effector transport specificity and is required for binding with PAAR and adaptor-effector complex. Proc. Natl. Acad. Sci. USA *113*, E3931–E3940.

Bönemann, G., Pietrosiuk, A., Diemand, A., Zentgraf, H., and Mogk, A. (2009). Remodelling of VipA/VipB tubules by ClpV-mediated threading is crucial for type VI protein secretion. EMBO J. *28*, 315–325.

Borgeaud, S., Metzger, L.C., Scrignari, T., and Blokesch, M. (2015). The type VI secretion system of *Vibrio cholerae* fosters horizontal gene transfer. Science *347*, 63–67.

Brodmann, M., Dreier, R.F., Broz, P., and Basler, M. (2017). *Francisella* requires dynamic type VI secretion system and ClpB to deliver effectors for phagosomal escape. Nat. Commun. *8*, 15853.

Brunet, Y.R., Zoued, A., Boyer, F., Douzi, B., and Cascales, E. (2015). The type VI secretion TssEFGK-VgrG phage-like baseplate is recruited to the TssJLM membrane complex via multiple contacts and serves as assembly platform for tail tube/sheath polymerization. PLoS Genet. *11*, e1005545.

Chang, Y.-W., Rettberg, L.A., Ortega, D.R., and Jensen, G.J. (2017). In vivo structures of an intact type VI secretion system revealed by electron cryotomography. EMBO Rep. *18*, 1090–1099.

Clemens, D.L., Ge, P., Lee, B.-Y., Horwitz, M.A., and Zhou, Z.H. (2015). Atomic structure of T6SS reveals interlaced array essential to function. Cell *160*, 940–951.

Cooper, R.M., Tsimring, L., and Hasty, J. (2017). Inter-species population dynamics enhance microbial horizontal gene transfer and spread of antibiotic resistance. eLife *6*, e25950.

Costa, T.R.D., Felisberto-Rodrigues, C., Meir, A., Prevost, M.S., Redzej, A., Trokter, M., and Waksman, G. (2015). Secretion systems in Gram-negative bacteria: structural and mechanistic insights. Nat. Rev. Microbiol. *13*, 343–359.

de Bruin, O.M., Ludu, J.S., and Nano, F.E. (2007). The *Francisella* pathogenicity island protein IglA localizes to the bacterial cytoplasm and is needed for intracellular growth. BMC Microbiol. *7*, 1.

Dong, T.G., Ho, B.T., Yoder-Himes, D.R., and Mekalanos, J.J. (2013). Identification of T6SS-dependent effector and immunity proteins by Tn-seq in *Vibrio cholerae*. Proc. Natl. Acad. Sci. USA *110*, 2623–2628.

Durand, E., Nguyen, V.S., Zoued, A., Logger, L., Péhau-Arnaudet, G., Aschtgen, M.-S., Spinelli, S., Desmyter, A., Bardiaux, B., Dujeancourt, A., et al. (2015). Biogenesis and structure of a type VI secretion membrane core complex. Nature *523*, 555–560.

Ge, P., Scholl, D., Leiman, P.G., Yu, X., Miller, J.F., and Zhou, Z.H. (2015). Atomic structures of a bactericidal contractile nanotube in its pre- and post-contraction states. Nat. Struct. Mol. Biol. *22*, 377–382.

Hachani, A., Allsopp, L.P., Oduko, Y., and Filloux, A. (2014). The VgrG proteins are "à la carte" delivery systems for bacterial type VI effectors. J. Biol. Chem. *289*, 17872–17884.

Ho, B.T., Basler, M., and Mekalanos, J.J. (2013). Type 6 secretion system-mediated immunity to type 4 secretion system-mediated gene transfer. Science *342*, 250–253.

Jiang, F., Waterfield, N.R., Yang, J., Yang, G., and Jin, Q. (2014). A *Pseudomonas aeruginosa* type VI secretion phospholipase D effector targets both prokaryotic and eukaryotic cells. Cell Host Microbe *15*, 600–610.

Johnston, C., Martin, B., Fichant, G., Polard, P., and Claverys, J.-P. (2014). Bacterial transformation: distribution, shared mechanisms and divergent control. Nat. Rev. Microbiol. *12*, 181–196.

Kirchberger, P.C., Unterweger, D., Provenzano, D., Pukatzki, S., and Boucher, Y. (2017). Sequential displacement of Type VI Secretion System effector genes leads to evolution of diverse immunity gene arrays in *Vibrio cholerae*. Sci. Rep. *7*, 45133.

Kudryashev, M., Wang, R.Y.-R., Brackmann, M., Scherer, S., Maier, T., Baker, D., DiMaio, F., Stahlberg, H., Egelman, E.H., and Basler, M. (2015). Structure of the type VI secretion system contractile sheath. Cell *160*, 952–962.

Lederberg, J. (1951). Streptomycin resistance; a genetically recessive mutation. J. Bacteriol. *61*, 549–550.

Leong, C.G., Boyd, C.M., Roush, K.S., Tenente, R., Lang, K.M., and Lostroh, C.P. (2017). Succinate, iron chelation, and monovalent cations affect the transformation efficiency of *Acinetobacter baylyi* ATCC 33305 during growth in complex media. Can. J. Microbiol. *63*, 851–856.

Li, J., Yao, Y., Xu, H.H., Hao, L., Deng, Z., Rajakumar, K., and Ou, H.-Y. (2015). SecReT6: a web-based resource for type VI secretion systems found in bacteria. Environ. Microbiol. *17*, 2196–2202.

Liang, X., Moore, R., Wilton, M., Wong, M.J.Q., Lam, L., and Dong, T.G. (2015). Identification of divergent type VI secretion effectors using a conserved chaperone domain. Proc. Natl. Acad. Sci. USA *112*, 9106–9111.

Ma, J., Pan, Z., Huang, J., Sun, M., Lu, C., and Yao, H. (2017). The Hcp proteins fused with diverse extended-toxin domains represent a novel pattern of antibacterial effectors in type VI secretion systems. Virulence *8*, 1189–1202.

Metzgar, D., Bacher, J.M., Pezo, V., Reader, J., Döring, V., Schimmel, P., Marlière, P., and de Crécy-Lagard, V. (2004). *Acinetobacter* sp. ADP1: an ideal model organism for genetic analysis and genome engineering. Nucleic Acids Res. *32*, 5780–5790.

Michel-Briand, Y., and Baysse, C. (2002). The pyocins of *Pseudomonas aeruginosa*. Biochimie *84*, 499–510.

Planamente, S., Salih, O., Manoli, E., Albesa-Jové, D., Freemont, P.S., and Filloux, A. (2016). TssA forms a gp6-like ring attached to the type VI secretion sheath. EMBO J. *35*, 1613–1627.

Pukatzki, S., Ma, A.T., Sturtevant, D., Krastins, B., Sarracino, D., Nelson, W.C., Heidelberg, J.F., and Mekalanos, J.J. (2006). Identification of a conserved bacterial protein secretion system in *Vibrio cholerae* using the *Dictyostelium* host model system. Proc. Natl. Acad. Sci. USA *103*, 1528–1533.

Pukatzki, S., Ma, A.T., Revel, A.T., Sturtevant, D., and Mekalanos, J.J. (2007). Type VI secretion system translocates a phage tail spike-like protein into target cells where it cross-links actin. Proc. Natl. Acad. Sci. USA *104*, 15508–15513.

Russell, A.B., Singh, P., Brittnacher, M., Bui, N.K., Hood, R.D., Carl, M.A., Agnello, D.M., Schwarz, S., Goodlett, D.R., Vollmer, W., and Mougous, J.D. (2012). A widespread bacterial type VI secretion effector superfamily identified using a heuristic approach. Cell Host Microbe *11*, 538–549.

Russell, A.B., LeRoux, M., Hathazi, K., Agnello, D.M., Ishikawa, T., Wiggins, P.A., Wai, S.N., and Mougous, J.D. (2013). Diverse type VI secretion phospholipases are functionally plastic antibacterial effectors. Nature *496*, 508–512.

Russell, A.B., Wexler, A.G., Harding, B.N., Whitney, J.C., Bohn, A.J., Goo, Y.A., Tran, B.Q., Barry, N.A., Zheng, H., Peterson, S.B., et al. (2014a). A type VI secretion-related pathway in *Bacteroidetes* mediates interbacterial antagonism. Cell Host Microbe *16*, 227–236.

Russell, A.B., Peterson, S.B., and Mougous, J.D. (2014b). Type VI secretion system effectors: poisons with a purpose. Nat. Rev. Microbiol. *12*, 137–148.

Santin, Y.G., and Cascales, E. (2017). Domestication of a housekeeping transglycosylase for assembly of a Type VI secretion system. EMBO Rep. *18*, 138–149.

Schindelin, J., Arganda-Carreras, I., Frise, E., Kaynig, V., Longair, M., Pietzsch, T., Preibisch, S., Rueden, C., Saalfeld, S., Schmid, B., et al. (2012). Fiji: an open-source platform for biological-image analysis. Nat. Methods *9*, 676–682.

Shneider, M.M., Buth, S.A., Ho, B.T., Basler, M., Mekalanos, J.J., and Leiman, P.G. (2013). PAAR-repeat proteins sharpen and diversify the type VI secretion system spike. Nature *500*, 350–353.

Silverman, J.M., Austin, L.S., Hsu, F., Hicks, K.G., Hood, R.D., and Mougous, J.D. (2011). Separate inputs modulate phosphorylation-dependent and -independent type VI secretion activation. Mol. Microbiol. *82*, 1277–1290.

Silverman, J.M., Agnello, D.M., Zheng, H., Andrews, B.T., Li, M., Catalano, C.E., Gonen, T., and Mougous, J.D. (2013). Haemolysin coregulated protein is an exported receptor and chaperone of type VI secretion substrates. Mol. Cell *51*, 584–593.

Suo, Z., Avci, R., Deliorman, M., Yang, X., and Pascual, D.W. (2009). Bacteria survive multiple puncturings of their cell walls. Langmuir *25*, 4588–4594.

Taylor, N.M.I., Prokhorov, N.S., Guerrero-Ferreira, R.C., Shneider, M.M., Browning, C., Goldie, K.N., Stahlberg, H., and Leiman, P.G. (2016). Structure of the T4 baseplate and its function in triggering sheath contraction. Nature *533*, 346–352.

The UniProt Consortium (2017). UniProt: the universal protein knowledgebase. Nucleic Acids Res. *45* (*D1*), D158–D169.

Thévenaz, P., Ruttimann, U.E., and Unser, M. (1998). A pyramid approach to subpixel registration based on intensity. IEEE Trans. Image Process. *7*, 27–41.

Unterweger, D., Miyata, S.T., Bachmann, V., Brooks, T.M., Mullins, T., Kostiuk, B., Provenzano, D., and Pukatzki, S. (2014). The *Vibrio cholerae* type VI secretion system employs diverse effector modules for intraspecific competition. Nat. Commun. *5*, 3549.

Unterweger, D., Kostiuk, B., Ötjengerdes, R., Wilton, A., Diaz-Satizabal, L., and Pukatzki, S. (2015). Chimeric adaptor proteins translocate diverse type VI secretion system effectors in *Vibrio cholerae*. EMBO J. *34*, 2198–2210.

Veening, J.-W., and Blokesch, M. (2017). Interbacterial predation as a strategy for DNA acquisition in naturally competent bacteria. Nat. Rev. Microbiol. *15*, 621–629.

Vettiger, A., and Basler, M. (2016). Type VI secretion system substrates are transferred and reused among sister cells. Cell *167*, 99–110.e12.

Vettiger, A., Winter, J., Lin, L., and Basler, M. (2017). The type VI secretion system sheath assembles at the end distal from the membrane anchor. Nat. Commun. *8*, 16088.

Wang, J., Brackmann, M., Castaño-Díez, D., Kudryashev, M., Goldie, K.N., Maier, T., Stahlberg, H., and Basler, M. (2017). Cryo-EM structure of the extended type VI secretion system sheath-tube complex. Nat. Microbiol. *2*, 1507–1512.

Weber, B.S., Miyata, S.T., Iwashkiw, J.A., Mortensen, B.L., Skaar, E.P., Pukatzki, S., and Feldman, M.F. (2013). Genomic and functional analysis of the type VI secretion system in *Acinetobacter*. PLoS ONE *8*, e55142.

Weber, B.S., Hennon, S.W., Wright, M.S., Scott, N.E., de Berardinis, V., Foster, L.J., Ayala, J.A., Adams, M.D., and Feldman, M.F. (2016). Genetic dissection of the type VI secretion system in *Acinetobacter* and identification of a novel peptidoglycan hydrolase, TagX, required for its biogenesis. MBio *7*, e01253–e16.

Wilton, M., Wong, M.J.Q., Tang, L., Liang, X., Moore, R., Parkins, M.D., Lewenza, S., and Dong, T.G. (2016). Chelation of membrane-bound cations by extracellular DNA activates the type VI secretion system in *Pseudomonas aeruginosa*. Infect. Immun. *84*, 2355–2361.

Zhang, D., de Souza, R.F., Anantharaman, V., Iyer, L.M., and Aravind, L. (2012). Polymorphic toxin systems: Comprehensive characterization of trafficking modes, processing, mechanisms of action, immunity and ecology using comparative genomics. Biol. Direct *7*, 18.

Zoued, A., Durand, E., Brunet, Y.R., Spinelli, S., Douzi, B., Guzzo, M., Flaugnatti, N., Legrand, P., Journet, L., Fronzes, R., et al. (2016). Priming and polymerization of a bacterial contractile tail structure. Nature *531*, 59–63.

Cell Reports, Volume *21*

Supplemental Information

The Role of Type VI Secretion System Effectors in Target Cell Lysis and Subsequent Horizontal Gene Transfer

Peter David Ringel, Di Hu, and Marek Basler

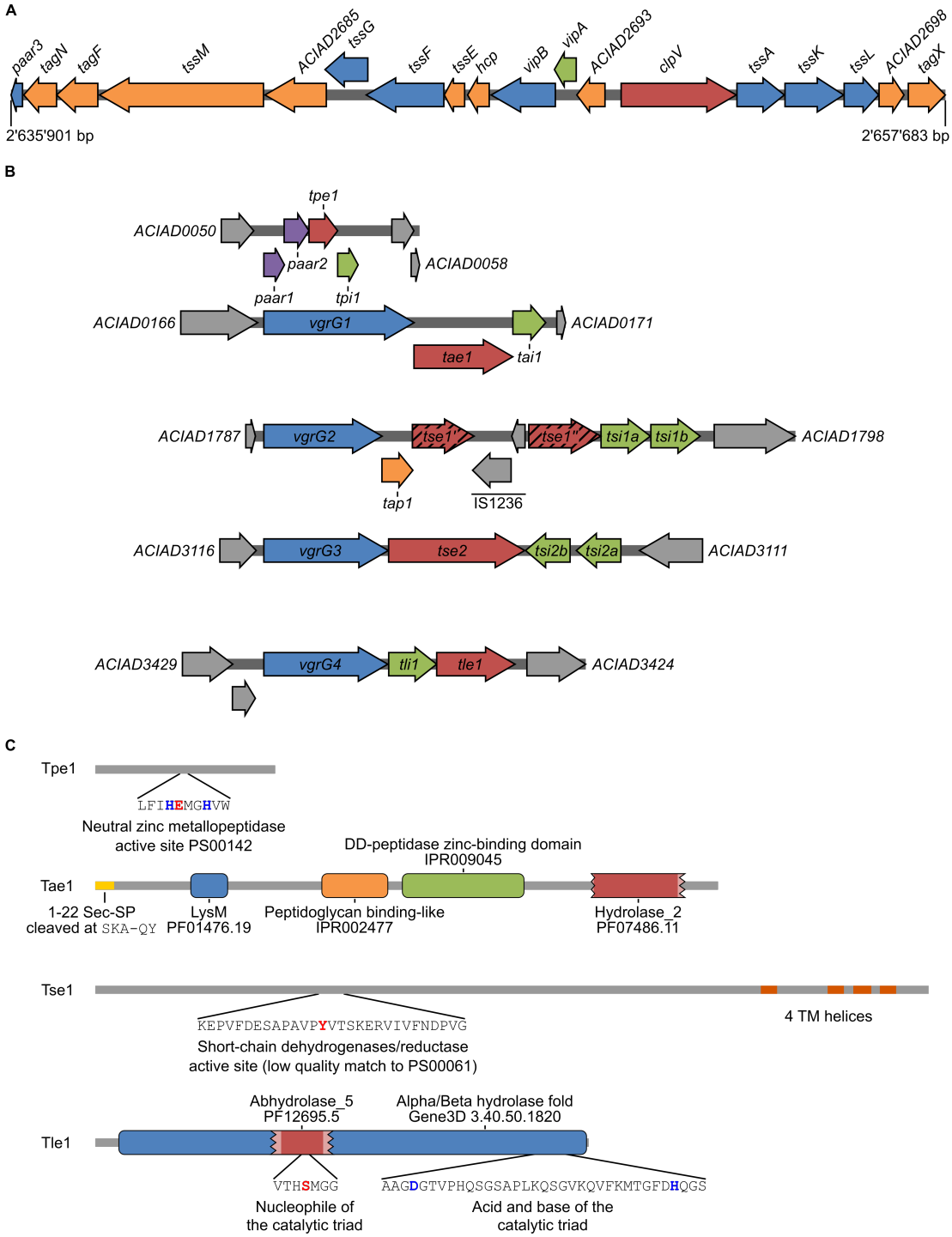

Figure S1. T6SS core and effector loci of *A. baylyi* ADP1 and the predicted conserved domains of the effectors, Related to Figure 2, Figure 3, Figure 5 and Table 1

(A) Core T6SS locus of *A. baylyi* ADP1. The T6SS components under investigation in this study are depicted in orange, *vipA*, tagged with sfGFP, and *clpV*, tagged with mCherry2, are depicted in green and red respectively. The remaining components are depicted in blue. **(B)** The effector loci of *A. baylyi* ADP1 are drawn to scale. Structural tip components are depicted in purple and blue, the effectors are depicted in red, the immunity protein encoding genes are depicted in green, the T6SS effector chaperone encoding gene is depicted in orange and T6SS unrelated genes are depicted in gray. **(C)** The predicted conserved domains, catalytic residues and patterns of the T6SS effectors are indicated. Tse2 is omitted because there were no matches to any conserved elements. The predictions were carried out as described in the supplemental experimental procedures.

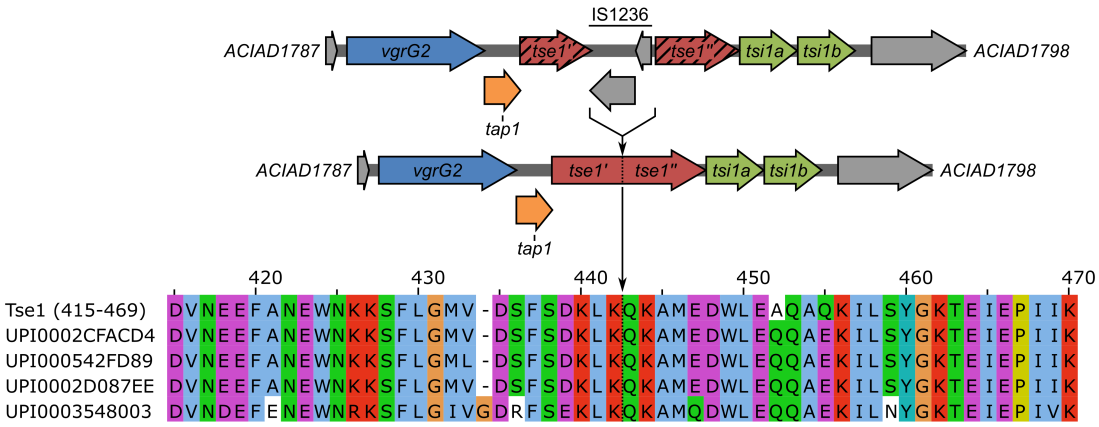

Figure S2. Restoration of Tse1, Related to Figure 3 and Figure 4

A copy of the insertion element IS1236 was removed to restore Tse1 based on the alignment with the indicated proteins. The arrow indicates the site where Tse1' and Tse1'' were fused genetically.

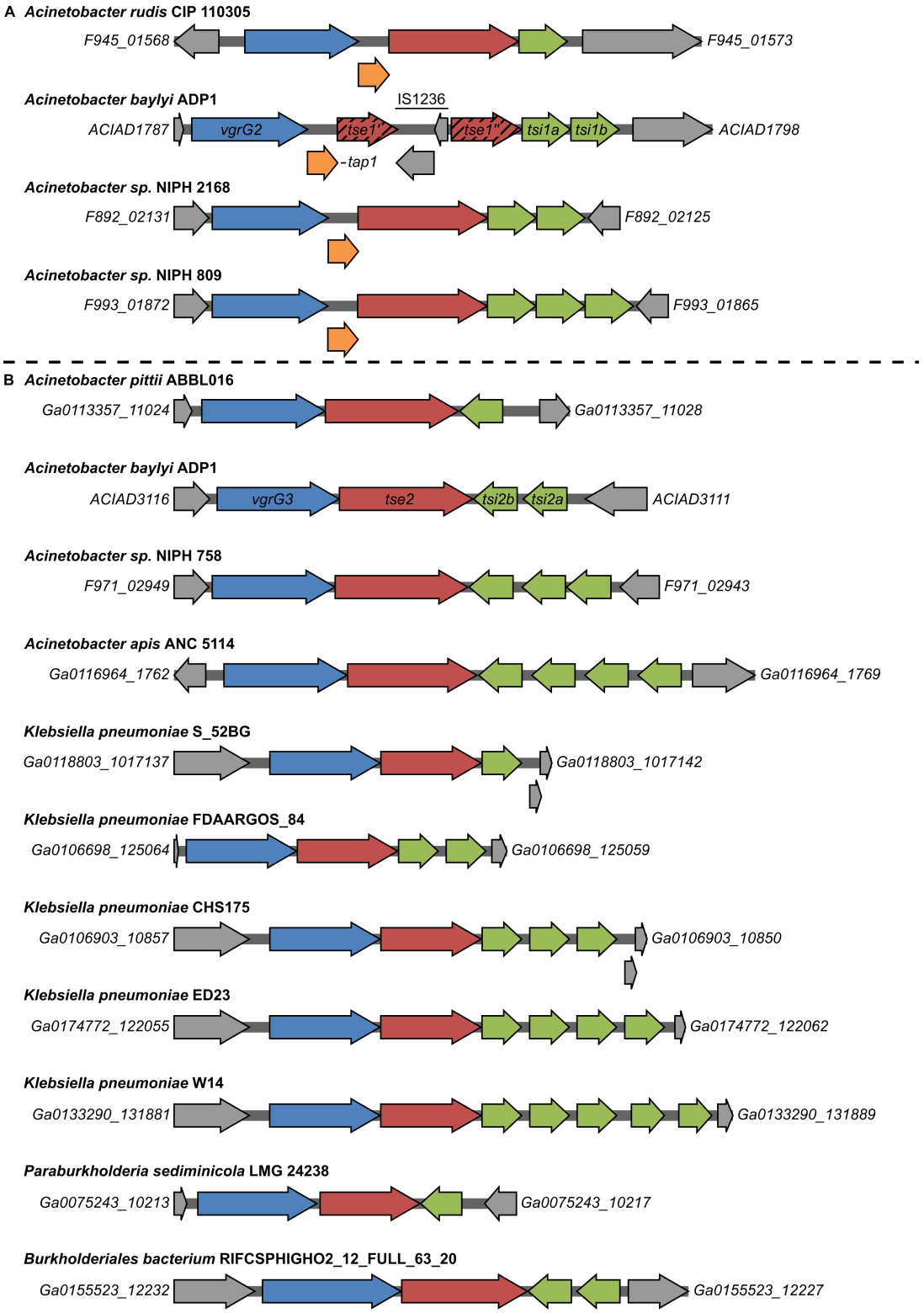

Figure S3. Duplications of immunity protein encoding genes are a common feature, Related to Figure 5
(A) Depicted are selected loci encoding an ortholog (min. 30 % identity at the DNA level) of Tse1. **(B)** Selected loci encoding a Tse2 ortholog (min. 30 % identity at the DNA level). Genes encoding a structural spike component are depicted in blue, those encoding a putative T6SS effector chaperone are depicted in orange, the effectors and their orthologs are depicted in red, the genes encoding a putative immunity protein are depicted in green and unrelated genes are depicted in gray.

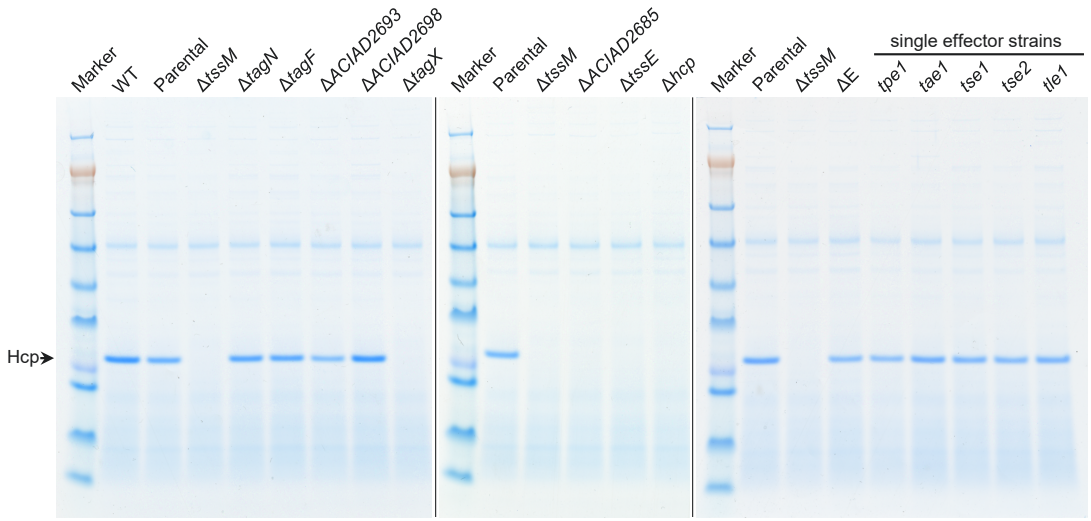

Figure S4. Hcp secretion of the *Acinetobacter baylyi* ADP1 T6SS mutants, Related to Figure 2 and Figure 3
Hcp secretion of the indicated T6SS mutants of *A. baylyi* ADP1 visualized by coomassie staining of TCA precipitated culture supernatants separated on NuPAGE® 4-12% Bis-Tris 1.0 mm protein gels (representative images). The SeeBlue® Plus2 pre-stained protein ladder (10 µl) was used as marker.

Supplemental Movie Legends

Movie S1. T6SS dynamics of the core locus mutants, Related to Figure 1, Figure 2 and Figure 3
The indicated mutants were imaged at 30 °C and 95 % R. H. on an LB 1 % (w/v) agarose pad for 5 min every 5 sec. Two examples are given for each mutant. Time is given as minutes : seconds. As mentioned in the methods, the contrast settings were adjusted separately for each timelapse, but within each timelapse the same settings were used.

Movie S2. The T6SS of the parental strain is highly dynamic, Related to Figure 1
The parental strain, in which VipA and ClpV were tagged with sfGFP and mCherry2 respectively, was imaged at 30 °C and 95 % R. H. on an LB 1 % (w/v) agarose pad for 2 min every 2 sec. Twenty examples of extension contraction and disassembly cycles are shown. Time is given as minutes : seconds. As pointed out in the methods, the contrast settings were adjusted separately for each timelapse, but within each timelapse the same settings were used.

Movie S3. The effectors are not required for T6SS activity and each effector elicits a distinct lysis phenotype of *E. coli*, Related to Figure 3
The indicated mutants were competed with *E. coli* at a ratio of 1:1 on an LB 1 % (w/v) agarose pad, while imaging at 30 °C and 95 % R. H. for 30 min every 30 s or, in case of the ΔE strain, the *tpe1* single effector strain, the *tse1* single effector strain and the Δ*tssM* strain, for 1 h every 1 min. The pad was supplemented with the cell impermeable DNA stain SYTOX® Blue (0.5 µM) as indicator for loss of membrane integrity. Four examples are shown for each competition. Time is given as hours : minutes : seconds. As pointed out in the methods, the contrast settings were adjusted separately for each timelapse, but within each timelapse the same settings were used.

Table S1: Bacterial strains used in this study, Related to Experimental Procedures

Bacterial strains	Genotype	Reference
***Acinetobacter baylyi* ADP1 (ATCC 33305) derivatives**		
T6SS+	Δ*paar1-paar2*::P_{bla}-*aadA*	(Shneider et al., 2013)
T6SS-	Δ2'644'572-2'653'574::P_{bla}-*aadA*	(Basler et al., 2013)
WT	*rpsL*-K88R	(Basler et al., 2013)
Parental	WT *vipA-sfGFP clpV-mCherry2*	This study
	Parental Δ*tagN*	This study
	Parental Δ*tagF*	This study
	Parental Δ*tssM*	This study
	Parental Δ*ACIAD2685*	This study
	Parental Δ*tssE*	This study
	Parental Δ*hcp*	This study
	Parental Δ*ACIAD2693*	This study
	Parental Δ*ACIAD2698*	This study
	Parental Δ*tagX*	This study
	Parental Δ*tae1* Δ*tse1'* Δ*tse2* Δ*tle1*	This study
	Parental Δ*tpe1* Δ*tse1'* Δ*tse2* Δ*tle1*	This study
	Parental Δ*tpe1* Δ*tae1* Δ*tse2* Δ*tle1* Δ(*ACIAD1791-ACIAD1792*)	This study
	Parental Δ*tssM* Δ*tpe1* Δ*tae1* Δ*tse2* Δ*tle1* Δ(*ACIAD1791-ACIAD1792*)	This study
	Parental Δ*tpe1* Δ*tae1* Δ*tse1'* Δ*tle1*	This study
	Parental Δ*tpe1* Δ*tae1* Δ*tse1'* Δ*tse2*	This study
	Parental Δ*tpe1* Δ*tae1* Δ*tse1'* Δ*tse2* Δ*tle1*	This study
	Parental Δ*tpe1-tpi1*::P_{rpsL}-*rpsL'*-P_{bla}-*aph(3')-Ia*	This study
	Parental Δ*tae1-tai1*::P_{rpsL}-*rpsL'*-P_{bla}-*aph(3')-Ia*	This study
	Parental Δ*tap1-tsi1b*::P_{rpsL}-*rpsL'*-P_{bla}-*aph(3')-Ia*	This study
	Parental Δ*tse2* Δ*tsi2a-tsi2b*::P_{rpsL}-*rpsL'*-P_{bla}-*aph(3')-Ia*	This study
	Parental Δ*tli1-tle1*::P_{rpsL}-*rpsL'*-P_{bla}-*aph(3')-Ia*	This study
	Parental Δ*tpe1*	This study
	Parental Δ*tae1*	This study
	Parental Δ*tse1'*	This study
	Parental Δ*tse2*	This study
	Parental Δ*tle1*	This study
***Escherichia coli* MG1655 Gm^R**		
	Gm^R	(Basler et al., 2013)
***Pseudomonas aeruginosa* PAO1**		
WT		(Basler et al., 2013)
	WT Δ*retS*	(Basler et al., 2013)

Table S2: Clean- and insertion deletion mutants, Related to Experimental Procedures
The vertical bar indicates the fusion site after the in-frame deletion of the target gene. The genes disrupted by insertion of a selectable cassette are given as (base before insertion)|(base after insertion) where the numbering is in accordance with the *A. baylyi* ADP1 genome (accession number NC_005966.1).

Mutation	Peptide scar
vipA-sfGFP	2'648'597 …KLSAEVDHE|AAAGG|**sfGFP**|KLSAEVDHE
clpV-mCherry2	2'652'785 …TIKETEA|AAAGGG|**mCherry2**|TIKETEA
Δ*tagN*	MKTRHATQLKLC|RKNRRIEFEVL
Δ*tagF*	MQQINTTPLYYG|LKLFRQTFLDE
Δ*tssM*	MYTILGYLWQYI|AVTTPPPVGER
Δ*ACIAD2685*	MLFADRSRSMIKKIISVLVLV|ISEIEQEEEAA
Δ*tssE*	MNLDHLYPFGFR|TTQQYVISAQT
Δ*hcp*	MKDIYVQFRGKY|SLSNNTASYAA
Δ*ACIAD2693*	MRKSIVFSAILV|KSSTNPFESLK
Δ*ACIAD2698*	MAQEKPTSLRIL|IVNTPKPTEAQ
Δ*tagX*	MFKALLPQSKQK|AEGQLTANAAS
Δ*tpe1*	MGLNIIENNLDK|IYEEKISEVIK
Δ*tae1*	MNKKSLVTIQLL|KIVLPKNFKGI
Δ*tse1'*	MTDNNVAEKYRYDRCETCERLGSF|KDVNEEFANEWNKKSFLGMVDSFSDKLKLIL DSIVDNKSL
Δ*tse2*	MNKYNVLEYSIIFYDQRNKELANVRYSLVFFPVSGGKETFTHVTNEKGRTKPIRL| ILAPFEQDELNPTMHQA
Δ*tle1*	MANKTIAQTGSATS|TQVKRSVLYSIVKIIKENNIQPKFR
Δ*tpe1-tpi1*::P$_{rpsL}$-*rpsL'*-P$_{bla}$- *aph(3')-Ia*	56'107|56'780
Δ*tae1-tai1*::P$_{rpsL}$-*rpsL'*-P$_{bla}$- *aph(3')-Ia*	170'297|172'958
Δ*tap1-tsi1b*::P$_{rpsL}$-*rpsL'*-P$_{bla}$- *aph(3')-Ia*	1'797'681|1'804'585
Δ*tsi2a-tsi2b*::P$_{rpsL}$-*rpsL'*-P$_{bla}$- *aph(3')-Ia*	3'038'344(+TAA)|3'040'350
Δ*tli1-tle1*::P$_{rpsL}$-*rpsL'*-P$_{bla}$- *aph(3')-Ia*	3'339'677|3'342'316

Supplemental Experimental Procedures

Bioinformatics

Bioinformatic analyses of the proteins of interest were performed using CD-Search (Marchler-Bauer and Bryant, 2004; Marchler-Bauer et al., 2011, 2015, 2017), CCTOP (Dobson et al., 2015), HHpred (Alva et al., 2016; Söding et al., 2005), HMMER (Finn et al., 2015), InterProScan (Finn et al., 2017; Jones et al., 2014), Phobius (Käll et al., 2004, 2007), Phyre2 (Kelley et al., 2015), PRED-TAT (Bagos et al., 2010), ScanProsite (de Castro et al., 2006; Sigrist et al., 2013), SignalP 4.1 (Petersen et al., 2011) and SWISS-MODEL (Arnold et al., 2006; Biasini et al., 2014; Guex et al., 2009; Kiefer et al., 2009). Synteny analyses were carried out using IMG/M (Markowitz et al., 2012). Sequence alignments were performed with T-Coffee (Notredame et al., 2000). The taxonomic distributions of proteins of interest were obtained by running at most three rounds of jackhammer (Finn et al., 2015) using UniProtKB as source database (The UniProt Consortium, 2017) and inspecting the taxonomic distribution of the matches. Alignments were visualized using Jalview (Waterhouse et al., 2009).

Supplemental References

Alva, V., Nam, S.-Z., Söding, J., and Lupas, A.N. (2016). The MPI bioinformatics Toolkit as an integrative platform for advanced protein sequence and structure analysis. Nucleic Acids Res. *44*, W410-415.

Arnold, K., Bordoli, L., Kopp, J., and Schwede, T. (2006). The SWISS-MODEL workspace: a web-based environment for protein structure homology modelling. Bioinforma. Oxf. Engl. *22*, 195–201.

Bagos, P.G., Nikolaou, E.P., Liakopoulos, T.D., and Tsirigos, K.D. (2010). Combined prediction of Tat and Sec signal peptides with hidden Markov models. Bioinforma. Oxf. Engl. *26*, 2811–2817.

Biasini, M., Bienert, S., Waterhouse, A., Arnold, K., Studer, G., Schmidt, T., Kiefer, F., Cassarino, T.G., Bertoni, M., Bordoli, L., et al. (2014). SWISS-MODEL: modelling protein tertiary and quaternary structure using evolutionary information. Nucleic Acids Res. *42*, W252-8.

de Castro, E., Sigrist, C.J.A., Gattiker, A., Bulliard, V., Langendijk-Genevaux, P.S., Gasteiger, E., Bairoch, A., and Hulo, N. (2006). ScanProsite: detection of PROSITE signature matches and ProRule-associated functional and structural residues in proteins. Nucleic Acids Res. *34*, W362-365.

Dobson, L., Reményi, I., and Tusnády, G.E. (2015). CCTOP: a Consensus Constrained TOPology prediction web server. Nucleic Acids Res. *43*, W408–W412.

Finn, R.D., Clements, J., Arndt, W., Miller, B.L., Wheeler, T.J., Schreiber, F., Bateman, A., and Eddy, S.R. (2015). HMMER web server: 2015 update. Nucleic Acids Res. *43*, W30–W38.

Finn, R.D., Attwood, T.K., Babbitt, P.C., Bateman, A., Bork, P., Bridge, A.J., Chang, H.-Y., Dosztányi, Z., El-Gebali, S., Fraser, M., et al. (2017). InterPro in 2017—beyond protein family and domain annotations. Nucleic Acids Res. *45*, D190–D199.

Guex, N., Peitsch, M.C., and Schwede, T. (2009). Automated comparative protein structure modeling with SWISS-MODEL and Swiss-PdbViewer: a historical perspective. Electrophoresis *30 Suppl 1*, S162-73.

Jones, P., Binns, D., Chang, H.-Y., Fraser, M., Li, W., McAnulla, C., McWilliam, H., Maslen, J., Mitchell, A., Nuka, G., et al. (2014). InterProScan 5: genome-scale protein function classification. Bioinformatics *30*, 1236–1240.

Käll, L., Krogh, A., and Sonnhammer, E.L.L. (2004). A combined transmembrane topology and signal peptide prediction method. J. Mol. Biol. *338*, 1027–1036.

Käll, L., Krogh, A., and Sonnhammer, E.L.L. (2007). Advantages of combined transmembrane topology and signal peptide prediction--the Phobius web server. Nucleic Acids Res. *35*, W429-432.

Kelley, L.A., Mezulis, S., Yates, C.M., Wass, M.N., and Sternberg, M.J.E. (2015). The Phyre2 web portal for protein modeling, prediction and analysis. Nat. Protoc. *10*, 845–858.

Kiefer, F., Arnold, K., Künzli, M., Bordoli, L., and Schwede, T. (2009). The SWISS-MODEL Repository and associated resources. Nucleic Acids Res. *37*, D387-92.

Marchler-Bauer, A., and Bryant, S.H. (2004). CD-Search: protein domain annotations on the fly. Nucleic Acids Res. *32*, W327-31.

Marchler-Bauer, A., Lu, S., Anderson, J.B., Chitsaz, F., Derbyshire, M.K., DeWeese-Scott, C., Fong, J.H., Geer, L.Y., Geer, R.C., Gonzales, N.R., et al. (2011). CDD: a Conserved Domain Database for the functional annotation of proteins. Nucleic Acids Res. *39*, D225-9.

Marchler-Bauer, A., Derbyshire, M.K., Gonzales, N.R., Lu, S., Chitsaz, F., Geer, L.Y., Geer, R.C., He, J., Gwadz, M., Hurwitz, D.I., et al. (2015). CDD: NCBI's conserved domain database. Nucleic Acids Res. *43*, D222-6.

Marchler-Bauer, A., Bo, Y., Han, L., He, J., Lanczycki, C.J., Lu, S., Chitsaz, F., Derbyshire, M.K., Geer, R.C., Gonzales, N.R., et al. (2017). CDD/SPARCLE: functional classification of proteins via subfamily domain architectures. Nucleic Acids Res. *45*, D200–D203.

Markowitz, V.M., Chen, I.-M.A., Palaniappan, K., Chu, K., Szeto, E., Grechkin, Y., Ratner, A., Jacob, B., Huang, J., Williams, P., et al. (2012). IMG: the integrated microbial genomes database and comparative analysis system. Nucleic Acids Res. *40*, D115–D122.

Notredame, C., Higgins, D.G., and Heringa, J. (2000). T-Coffee: A novel method for fast and accurate multiple sequence alignment. J. Mol. Biol. *302*, 205–217.

Petersen, T.N., Brunak, S., Heijne, G., and Nielsen, H. (2011). SignalP 4.0: discriminating signal peptides from transmembrane regions. Nat. Methods *8*, 785–786.

Sigrist, C.J.A., de Castro, E., Cerutti, L., Cuche, B.A., Hulo, N., Bridge, A., Bougueleret, L., and Xenarios, I. (2013). New and continuing developments at PROSITE. Nucleic Acids Res. *41*, D344-347.

Söding, J., Biegert, A., and Lupas, A.N. (2005). The HHpred interactive server for protein homology detection and structure prediction. Nucleic Acids Res. *33*, W244-8.

Waterhouse, A.M., Procter, J.B., Martin, D.M.A., Clamp, M., and Barton, G.J. (2009). Jalview Version 2--a multiple sequence alignment editor and analysis workbench. Bioinformatics *25*, 1189–1191.

The figures in this research article will be referenced by prepending the chapter and section number to the figure number, e. g. Fig. II.1.1 for figure 1.

Supplemental Information:

The supplemental data file S1 may be found in the appendix page 142. The supplemental movies may be found at https://doi.org/10.1016/j.celrep.2017.12.020.

II.2 Additional results related to research article I

II.2.1 Transcriptional profiling of prey cells by RNA sequencing

To gain further insight into the potential subcellular targets of the individual T6SS effectors the transcriptome of both the predator and the prey were analyzed by RNA sequencing. A similar approach previously demonstrated the generation of ROS by lethal attacks including those of the T6SS (Dong et al., 2015).

In this study the single effector *A. baylyi* ADP1 derivatives, described in research article I, were competed against *E. coli* MG1655 Gent^R which served as prey. Unlike the previous approach in which the entire RNA was extracted from the competition mixture (Dong et al., 2015), here, only the RNA of bacteria which could be recovered from the competition was extracted. Initially, the competitions were carried out as described for the previous study (Dong et al., 2015). However, the recovery of the prey strain was reduced to such an extent, that the ratio between the RNA of the prey and that of the aggressor would be too low for sequencing. Furthermore, it was noticed that the recovery of bacteria from the nitrocellulose filters was severely reduced when the prey was lysed during the competition. To reduce the lysis, the competitions were carried out at 30 °C for 30 min and only a 1:1 ratio instead of a 10:1 ratio of aggressor to prey. Nevertheless, the recovery of the prey was still too low for the Tae1 single effector strain, but the time of the competition could not be shortened below 30 min in order to obtain a discernable transcriptional response. Therefore, the Tae1 single effector strain was excluded from the analysis. Furthermore, since the Tpe1 single effector strain did not reduce the recovery of the prey it was also omitted.

Finally, the procedure was carried out as follows: The prey and predator strains were regrown and concentrated to an OD_{600nm} of approx. 10 as described for the bacterial competition assay in research article I. The concentrated cultures were mixed in a 1:1 ratio and spotted on 0.22 µm nitrocellulose filters on predried LA plates. The competitions were incubated at 30 °C for 30 min. Thereafter, the bacteria were resuspended in 1.5 ml ice cold LB of which 100 µl were used to measure the OD_{600nm} and 1 ml was pelleted. The pellet was washed once with LB and then the RNA was extracted using the Direct-zol™ RNA isolation kit (Zymo Research). The prey to predator ratio was determined from the residual bacterial suspension by serial dilution and CFU plating as described in research article I.

The RNA concentration and quality were assessed by agarose gel electrophoresis and spectrophotometric measurement of the quality parameters. Thereafter, the samples were

submitted to the quantitative genomics facility for ribosomal RNA depletion (Illumina Ribo-Zero rRNA Removal Kit) and sequencing library preparation (Illumina TruSeq Stranded mRNA Library Kit). The libraries were sequenced on an Illumina NextSeq 500 with a read length of 150 to increase the number of unambiguously mapping reads for both the aggressor and the prey.

The results are still preliminary and only one biological replicate has been sequenced so far. The RIN^e quality scores obtained by the sequencing facility indicated a poor integrity of the RNA obtained from the single effector strain competitions, but a high RNA quality for the control competitions with a T6SS deficient strain and the effector deficient strain. Nevertheless, the sequencing results were of good quality, as assessed with FastQC (Andrews, 2010), but it should be kept in mind that the results may be biased by the degraded RNA fragments (Wang et al., 2016). The data were analyzed using SPARTA (Johnson et al., 2016) and edgeR (Robinson et al., 2010). To perform the pathway enrichment analysis without replicates the dispersion was set to 0.04 as suggested by the author (Robinson et al., 2010).

Interestingly, no differentially expressed genes were found when comparing the transcriptomes of the prey competed against the T6SS deficient and the effector deficient predators. Unexpectedly, this indicates that puncturing by the T6SS does not even increase the stress sensed by the prey. The previously reported strong induction of the oxidative stress regulon was not evident from the data obtained with the single effector strains (Dong et al., 2015). This might be explained by the different competition conditions and by the different RNA isolation strategies. A multidimensional scaling plot revealed that the transcriptomes of the prey are more similar when targeted by Tse2 or Tle1, whereas they differ when targeted by Tse1. Further studies are needed to confirm these results and to elucidate which roles these pathways play (compare Table II.2.1 with Table II.2.2 and Table II.2.3). Additionally, the sequencing also yielded the transcriptomes of the aggressors which remain to be analyzed.

Table II.2.1: KEGG pathway enrichment analysis for the Tse1 single effector strain competition
The P-values were omitted due to the lack of replicates. N denotes the number of genes in the pathway, Up the number of upregulated and down the number of downregulated genes.

Pathways upregulated	**KEGG**	**N**	**Up**	**Down**
Ribosome	eco03010	69	23	7
Bacterial chemotaxis	eco02030	18	9	5
Two-component system	eco02020	127	33	26
Polyketide sugar unit biosynthesis	eco00523	6	4	1
Lipopolysaccharide biosynthesis	eco00540	31	11	3
Pathways downregulated	**KEGG**	**N**	**Up**	**Down**
Metabolic pathways	eco01100	637	73	187
ABC transporters	eco02010	149	14	58
Oxidative phosphorylation	eco00190	42	7	24
Biosynthesis of secondary metabolites	eco01110	290	30	95
Aminoacyl-tRNA biosynthesis	eco00970	98	6	40

Table II.2.2: KEGG pathway enrichment analysis for the Tse2 single effector strain competition
The P-values were omitted due to the lack of replicates. N denotes the number of genes in the pathway, Up the number of upregulated and down the number of downregulated genes.

Pathways upregulated	**KEGG**	**N**	**Up**	**Down**
Aminoacyl-tRNA biosynthesis	eco00970	98	41	1
Bacterial chemotaxis	eco02030	18	10	5
Nitrogen metabolism	eco00910	18	8	1
Two-component system	eco02020	127	25	15
Taurine and hypotaurine metabolism	eco00430	5	3	0
Pathways downregulated	**KEGG**	**N**	**Up**	**Down**
Microbial metabolism in diverse environments	eco01120	203	25	61
Galactose metabolism	eco00052	28	0	16
Biosynthesis of antibiotics	eco01130	200	12	56
ABC transporters	eco02010	149	10	45
Carbon metabolism	eco01200	104	9	34

Table II.2.3: KEGG pathway enrichment analysis for the Tle1 single effector strain competition
The P-values were omitted due to the lack of replicates. N denotes the number of genes in the pathway, Up the number of upregulated and down the number of downregulated genes.

Pathways upregulated	**KEGG**	**N**	**Up**	**Down**
Histidine metabolism	eco00340	8	6	0
Two-component system	eco02020	127	23	11
Biosynthesis of amino acids	eco01230	115	21	5
Arginine biosynthesis	eco00220	16	7	1
Biosynthesis of secondary metabolites	eco01110	290	35	26
Pathways downregulated	**KEGG**	**N**	**Up**	**Down**
Galactose metabolism	eco00052	28	0	12
Flagellar assembly	eco02040	29	0	12
Biosynthesis of siderophore group nonribosomal peptides	eco01053	7	0	6
Phosphotransferase system (PTS)	eco02060	30	0	11
Phenylalanine metabolism	eco00360	13	1	6

II.2.2 Labeling of secreted T6SS components

Although both the sheath dynamics as well as various baseplate and envelope spanning complex components were visualized by fluorescence microscopy, a direct imaging of the secretion of the inner tube, the spike complex or any other secreted substrate could not yet be achieved (Basler and Mekalanos, 2012; Basler et al., 2012; Brunet et al., 2015; Durand et al., 2015; Gerc et al., 2015; Zoued et al., 2016). Recently, the reuse or recycling of effectors and secreted structural components by sister cells was demonstrated for various T6SS active species (Vettiger and Basler, 2016). These results indicate, that at least some of the injections reach the cytoplasm. However, imaging the mode of secretion and injection may reveal additional subtleties.

Fluorescently labeling the secreted T6SS components is a demanding task. The low number of spike components secreted in a contraction event would render them challenging to detect by fluorescence microscopy. Because of the large assemblies formed by Hcp it poses the most promising target for labeling. Nevertheless, the spacial restrictions imposed by the dimensions of the lumen of the Hcp tube need to be considered. The inner diameter of the Hcp tube is approx. 40 Å (Mougous et al., 2006) and there may be constrictions in the cavity of the Hcp tube (Brackmann et al.; Wang et al., 2017).

II.2.2.1 Using fluorescent- and conditional fluorescent proteins to label Hcp

As mentioned in the introduction, Hcp proteins bearing C-terminal extensions were recently identified in *E. coli*. These rely on Hcp proteins which lack C-terminal extensions for their secretion, likely by forming hetero-hexamers or even sparsely labeled tubes to accommodate the spacial constraints (Blondel et al., 2009; Ma et al., 2017). Similarly, the expression of labeled Hcp derivatives on top of the unlabeled Hcp background was proposed to exert a similar function. Indeed, there is a report in which a β-lactamase labeled Hcp expressed in the wild-type background could be secreted by the T6SS (Zhou et al., 2012).

Prior experiments using complete and sub saturated labeling of Hcp with msfGFP did not result in visible labeling of the Hcp tube when it is formed at all (unpublished data from Prof. Basler). Dr. Schneider then used the smaller fluorescence-activating and absorption-shifting tag (Y-FAST), which is 125 amino acids in length, in combination with HMBR (Plamont et al., 2016; 2016), in the synthesis of which I assisted, which also did not yield visibly labeled structures. Another experiment performed by Dr. Schneider using CreiLOV

(Mukherjee et al., 2015), which forms a smaller fluorophore of only 119 amino acids, also failed to produce visible structures.

II.2.2.2 Using bioorthogonal labeling strategies to visualize Hcp

To reduce the size of the fluorophore even further while maintaining high quantum yield, bioorthogonal labeling was considered. The major challenges with this approach are the cell permeability of the dye, the biocompatibility of the reaction and the chemoselectivity as well as the reaction rate. In this case the biocompatibility is especially crucial, because the T6SS structures need to remain dynamic and thus the cell must remain viable at least for a short period of time.

In recent years the demand for such methods has increased steadily and a vast number of systems have been developed which may be grouped into ligand binding and self-labeling enzymatic domains (Schneider and Basler, 2016), self-labeling or affinity oligopeptide tags (Lotze et al., 2016), enzymatically labeled oligopeptide tags and the introduction of bioorthogonal reactive groups by incorporation of unnatural amino acids (Chen and Wu, 2016; L. Oliveira et al., 2017; Nikić and Lemke, 2015). These tags may either form covalent bonds with the labeling reagents or they may be bound with high affinity (Chen and Wu, 2016). The labeling by unnatural amino acids can further be subdivided in site specific and global incorporation. The site specific incorporation is usually achieved by genetic code expansion such as stop codon suppression and less commonly by quadruplet codon suppression or sense codon reassignment (Dumas et al., 2015). The global labeling on the other hand may be achieved by the incorporation of an amino acid analogon by the native translation machinery such as L-azidohomoalanine (Dumas et al., 2015; Kiick et al., 2002).

The polypeptide tags were excluded due to their size, since Y-FAST and CreiLOV did not yield visibly labeled structures. The use of unnatural amino acids greatly extends the available labeling chemistry, moreover, the site specific incorporation allows for precise engineering of the protein. The small size of self-labeling oligopeptide tags and the ease of their incorporation also seemed a viable option. As elaborated below we thus chose to proceed with these options.

II.2.2.2.1 Site specific unnatural amino acid labeling of Hcp

Currently, the highest reaction rate and chemoselectivity are yielded by the recently introduced strain-promoted inverse electron demand Diels-Alder cycloaddition

(SPIEDAC) (the interested reader is referred to the following reviews (Cserép et al., 2015; Lang and Chin, 2014; Mayer and Lang, 2017)). Initially, 1,2,4,5-Tetrazines were observed to react with unsaturated compounds in an inverse electron demand Diels-Alder cycloaddition (IEDDA) forming dihydropyridazines which can further isomerize or oxidize to the aromatic pyridazine (Carboni and Lindsey, 1959). In fact, the reaction comprises a Diels-Alder cycloaddition followed by a retro Diels-Alder elimination of molecular nitrogen making the reaction irreversible under physiological conditions. The enhanced reactivity of ring-strained dienophiles was noticed during a kinetic study (Thalhammer et al., 1990) and was later applied in a bioorthogonal labeling reaction (Blackman et al., 2008). The following generation of asymmetric 3-(*p*-Benzylamino)-1,2,4,5-tetrazine derivatives, which remain stable in aqueous solution (Devaraj et al., 2009), have the additional benefit of being able to act as an intramolecular FRET or PET acceptor for the coupled fluorophore, thus acting as a fluorogenic probe when reacting with strained alkenes (Devaraj et al., 2010). The 1,2,4,5-Tetrazines may however also react with strained alkynes such as exo-Bicyclo[6.1.0]non-4-yn-9-ylmethanol (BCN) directly yielding the corresponding pyridazine (see Figure II.2.1) which also significantly changes the spectral properties of the tetrazine moiety (Chen et al., 2012; Lang et al., 2012). Furthermore, using BCN avoids the possible isomerization of strained alkenes to their much less reactive *cis*-form (Lang et al., 2012; Taylor et al., 2011).

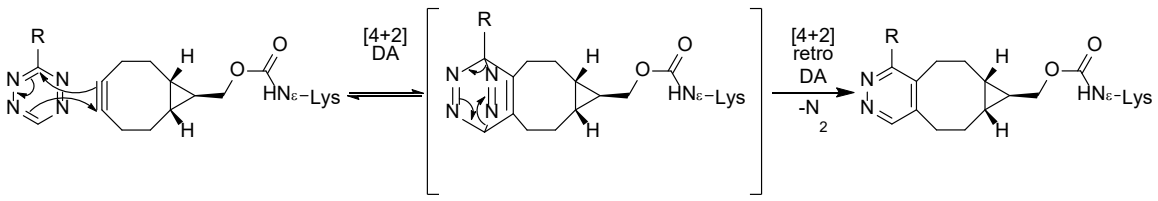

Figure II.2.1: SPIEDAC coupling of a 1,2,4,5-tetrazine derivative with Nε-BCN-L-lysine

Due to the commercial availability of the reactants and the advantages mentioned above the labeling strategy employing Nε-BCN-L-lysine as dienophile in combination with the 3-(*p*-Benzylamino)-1,2,4,5-tetrazine diene was chosen (Lang et al., 2012). The Nε-BCN-L-lysine is site specifically incorporated into the target protein by amber stop codon suppression. This is achieved by the orthogonal pair of the evolved pyrrolysyl-tRNA synthetase (BCNRS) and the $tRNA_{CUA}$ from *Methanosarcina barkeri* (Lang et al., 2012).

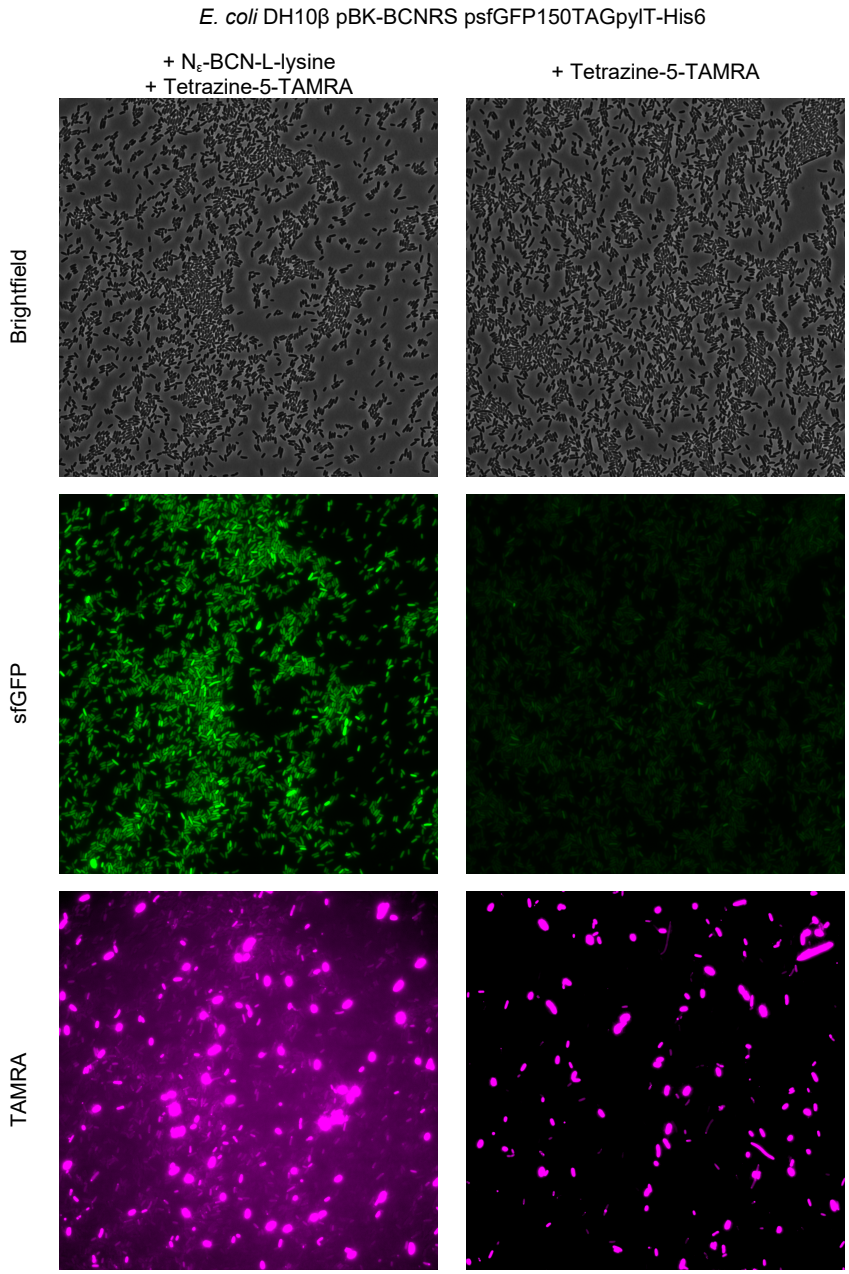

Figure II.2.2: Incorporation of N_{ε}-BCN-L-lysine and subsequent staining with Tetrazine-5-TAMRA
Here, Tetrazine-5-TAMRA stands for 3-(*p*-Benzylamino)-1,2,4,5-tetrazine-5-carboxytetramethylrhodamine (from Jena Bioscience GmbH). Briefly, the strain carrying the labeling plasmids was regrown in the presence of 70 µg/ml ampicillin and 12.5 µg/ml tetracycline in 5 ml LB shaking at 37 °C and 200 rpm to an OD_{600nm} of approx. 0.4. Then, the culture was split into two cultures, à 2 ml and 2 mM Nε-BCN-L-lysine from an 80 mM stock dissolved in 0.1 M $NaOH_{(aq)}$ (Nikić et al., 2014) were added to one of the cultures whereas the equivalent amount of 0.1 M $NaOH_{(aq)}$ were added to the control culture (Nε-BCN-L-lysine was acquired from SiChem). Additionally, 0.2 % arabinose were added to each culture, which were then incubated shaking at 37 °C and 200 rpm for another 1 h 30 min. The cultures were pelleted by centrifuging 2 min at 8000 x g. The pellets were washed three times with 1 ml 10 % DMSO in LB to remove the Nε-BCN-L-lysine. Thereafter, the pellets were resuspended in 100 µl PBS and 40 µM Tetrazine-5-TAMRA were added (from a 2 mM stock solution in DMSO). The reactions were incubated 10 min at 37 °C. Subsequently the cells were pelleted by centrifugation and the pellets were washed four times for 5 min with 10 % DMSO in LB to remove the remaining Tetrazine-5-TAMRA. The pellets were resuspended in 50 µl PBS and subjected to microscopy on 1 % agarose PBS pads. The same contrast settings were applied to the images of the sample and the control without the Nε-BCN-L-lysine for comparison.

The cell permeable TAMRA was selected as tetrazine coupled fluorophore (Murrey et al., 2015), because acetate esters of fluorescein, although cell permeable, are non-fluorescent until the esters are hydrolyzed by ubiquitous esterases, the product of which is membrane impermeable and thus accumulates over time (Rotman and Papermaster, 1966). It should be noted that although this reaction was described to be specific (Lang et al., 2012), a significant amount of off target labeling may occur when the TAMRA-tetrazine-conjugate is used at concentrations above 2 µM (Murrey et al., 2015).

Initial trials using this labeling strategy in *E. coli* DH10β confirmed the successful incorporation of the N_ε-BCN-L-lysine into a C-terminally His_6-tagged sfGFP variant bearing a TAG stop codon at position 150 resulting in green fluorescence (see Figure II.2.2). However, it turned out, that some cells retained unspecifically bound dye independent of the supplementation with N_ε-BCN-L-lysine, increasing the overall fluorescence to an extent, that the specific labeling was only visible as background. To remove the excess dye, a harsher washing protocol was adapted using 5 % DMSO with 0.2 % Pluronic F-127 (from Sigma-Aldrich) in PBS for ten washes (Plass et al., 2012). Nonetheless, even this excessive washing protocol was not sufficient to remove the unspecifically bound dye (data not shown). Similar complications were recently reported elsewhere (Kipper et al., 2017). Longer washing protocols are not feasible for labeling secreted T6SS components, because of the cytotoxicity of the wash buffer and the potential continuous secretion of labeled components. Nevertheless, it was tried to transfer the labeling plasmids into *V. cholerae* 2740-80 in close collaboration with Dr. Schneider. I constructed the plasmid derivatives and Dr. Schneider transformed them to *V. cholerae* 2740-80. The original psfGFP150TAGpylT-His6 only yielded a low transformation rate and I suspected, that the tetracycline resistance, conferred by the plasmid, was not sufficient, thus I constructed derivatives conferring kanamycin, gentamycin and spectinomycin resistance. The plasmid bearing the kanamycin resistance cassette proved most useful. Strains harboring both required labeling plasmids had a severe growth defect and could not be revived from cryogenic cultures. The supplementation with Nε-BCN-L-lysine, to avoid the accumulation of uncharged $tRNA_{CUA}$ or the repression by adding 1 % glucose, did not alleviate the growth defect. Similar results were achieved when I transferred the $tRNA_{CUA}$ to pBAD24 and the BCNRS to pBAD33.

II.2.2.2.2 Using the tetracysteine tag to label Hcp

The small self-labeling oligopeptide tags were considered as an alternative labeling strategy of which the tetracysteine tag was chosen, because it was previously used in bacteria to monitor the secretion of T3SS substrates (Enninga et al., 2005; VanEngelenburg and Palmer, 2008). Again, the procedures were carried out in close collaboration with Dr. Schneider for whom I constructed or designed the tagged constructs, unless noted otherwise, who then transformed them to *V. cholerae* and performed the staining and the microscopy.

The specifically designed cooperative tetracysteine hairpin binder is known to react with the membrane permeable 4',5'-bis(1,3,2-Dithiarsolan-2-yl)fluorescein (FlAsH-EDT_2) in a fluorogenic reaction (Griffin et al., 1998). The binding modality of an optimized dodecapeptide (FLNCCPGCCMEP) (Martin et al., 2005) with 4,6-Diarsaneylresorufin (ReAsH), another fluorogenic hairpin binder, has been solved by NMR (Madani et al., 2009). The fluorogenicity is attributed to the rotamer-restricted fluorescence of the aryl-fluorophore with regard to the As-aryl substituents (Walker et al., 2016). The reaction is reversible and displaces the 1,2-Ethanedithiol (EDT) antidote. Furthermore, the off-target binding is tunable by administering EDT or 2,3-Dimercaptopropane-1-ol (British anti-Lewisite [BAL]) during the washing procedure (Adams et al., 2002; Albert Griffin et al., 2000; Griffin et al., 1998).

Based on the *in situ* structure of the Hcp tube in *V. cholerae* (Wang et al., 2017), both N- and C-terminal tetracysteine tags were designed. The structure indicated that only the N-terminus would point into the lumen of the Hcp-tube, but prior experiments with C-terminal His_6-tagged Hcp suggested that the tag did not interfere with the tube assembly. Both the affinity optimized dodecapeptide FLNCCPGCCMEP (Martin et al., 2005) and the smallest binding hexapeptide CCPGCC (Griffin et al., 1998) were chosen for the experiments. Previous results from Prof. Basler indicated, that a direct fusion of the dodecapeptide to the N- or C-terminus of Hcp would not complement (unpublished), therefore a GGGGS linker was used for N-terminal fusions and an AAAGG linker was used for C-terminal fusions. Only the C-terminal hexapeptide tag construct was able to restore T6SS activity in an Hcp deficient strain. Upon adding the FlAsH-EDT_2-reagent, the Hcp aggregated and the T6SS activity seized (data not shown).

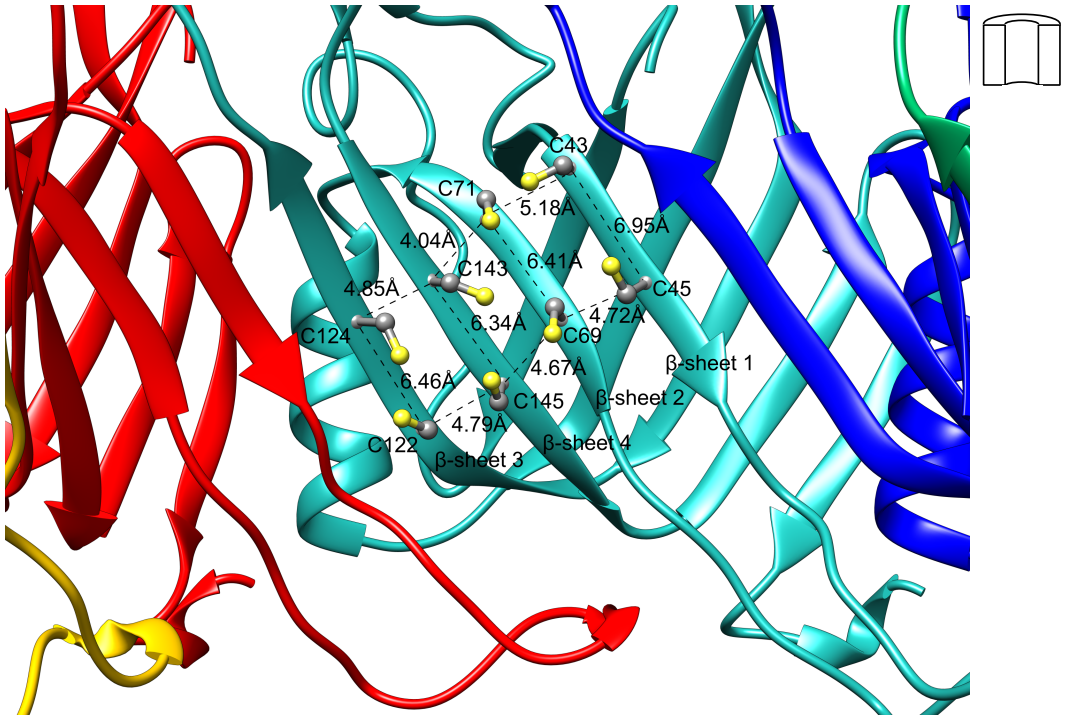

Figure II.2.3: β-sheet tetracysteine constructs forming FlAsH binding sites in the lumen of the Hcp tube

Depicted is the lumen of a Hcp hexamer modeled by Dr. Wang. The residues, which were exchanged to cysteines, are indicated on the turquoise subunit. The conformations of the cysteines were modeled using UCSF Chimera (Pettersen et al., 2004) together with the dynameomics rotamer library (Scouras and Daggett, 2011) and are for illustrative purposes only. The distances between the residues are measured from their Cα-atoms. Mutants with the following combinations of β-sheet cysteine exchanges were constructed and tested: β-sheet 1 with β-sheet 2, β-sheet 2 with β-sheet 4 and β-sheet 3 with β-sheet 4.

Since most of the Hcp-protein is made up of antiparallel-β-sheets, another labeling strategy based on the incorporation of cysteines into β-sheet-structures with the appropriate spacing and facing the same side to yield a FlAsH binding site was chosen (Krishnan and Gierasch, 2008). Four antiparallel-β-sheets face the lumen of the Hcp-tube. Thus, all three possible combinations were constructed (see Figure II.2.3). I designed the mutations and Dr. Schneider constructed and tested the mutants. None of the β-sheet-tetracysteine Hcp derivatives restored the T6SS dynamics in an Hcp deficient strain.

There are two potentially accessible loops in Hcp facing the lumen of the tube. Thus, I helped Dr. Schneider to design constructs bearing the tetracysteine tag in these loops. Dr. Schneider constructed the mutants and tested them. Unfortunately, the loops did not allow the cysteines to face in the same direction, reducing the chance to bind FlAsH (see Figure II.2.4), nonetheless the flexibility of the loops may allow for sufficient rearrangement. Furthermore, the loops may participate in the stacking of the Hcp hexamers which may be distorted when the loops adopt the engineered hairpin conformation.

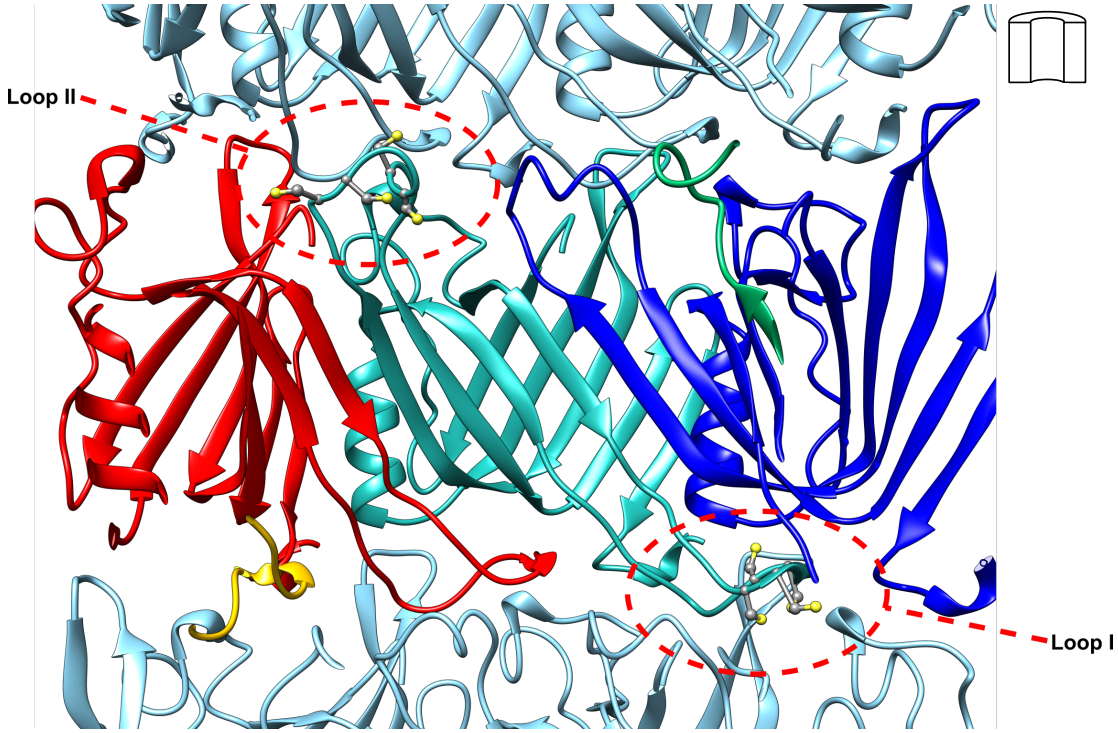

Figure II.2.4: Incorporation of the tetracysteine tag into luminal loops of Hcp
Depicted is the lumen of a Hcp stack modeled by Dr. Wang. The loops, which were modified to bear the tetracysteine tag, are indicated for the turquoise subunit. The conformations of the cysteines were modeled using UCSF Chimera (Pettersen et al., 2004) together with the dynameomics rotamer library (Scouras and Daggett, 2011) and are for illustrative purposes only. The loop mutants were constructed separately. The following residues were exchanged in loop I: P54→C, Q55→C, S56→P, Q58→C, P59→C. For loop II the following residues were exchanged: Q131→C, D132→C, A134→G, K135→C, S136→C.

Both loop mutants did not restore T6SS activity in a Hcp deficient strain. Dr. Schneider then constructed and tested a C-terminal tetracysteine tagged Hcp in *P. aeruginosa* PAO1 and two loop mutants bearing a tetracysteine tag, however none of them complemented.

II.2.2.2.3 Using fluorescent noncanonical amino acid tagging to label Hcp

The previous labeling strategies all aimed to site specifically label Hcp. However, alternatively the entire proteome may be labeled. Then, employing the previously described reuse of injected T6SS components (Vettiger and Basler, 2016), the labeled components may be injected into unlabeled cells which can use the injected components to assemble T6SSs of their own. Since the unlabeled cells are devoid of any background signal the newly assembled structures should be visible.

Such global labeling may be achieved by using the bioorthogonal noncanonical amino acid tagging (BONCAT) (Dieterich et al., 2006) or fluorescent noncanonical amino acid tagging (FUNCAT) (Dieterich et al., 2010) strategies. The advantage of FUNCAT is the use of naturally incorporated noncanonical amino acids, alleviating the need for genetic code expansion or stop codon suppression (Hatzenpichler et al., 2014; Kiick et al., 2002). The

original FUNCAT strategy used the copper catalyzed click reaction (Rostovtsev et al., 2002; Tornøe et al., 2002) to label either incorporated L-azidohomoalanine (AHA) or L-homopropargylglycine (HPG) (Dieterich et al., 2010). The cytotoxicity of the Cu(I) catalyst would be preventive for our use, yet employing strained cycloalkynes circumvents the need of a catalyst for the 1,3-dipolar Huisgen cycloaddition termed strain-promoted azide-alkyne cycloaddition (SPAAC) (Agard et al., 2004; Blomquist and Liu, 1953). A number of such strained alkynes were developed (Dommerholt et al., 2016) of which mostly the dibenzoannulated cyclooctynes are commercially available. As usual, reactivity has to be balanced against stability and selectivity, therefore mostly the medium reactive but stable dibenzoazacyclooctyne (DIBAC) (Debets et al., 2010) and the less reactive dibenzocyclooctanol (DIBO) (Ning et al., 2008) fluorophore conjugates are commercially available. Additionally, the even less reactive BCN (Dommerholt et al., 2010) derivatives are available which may also be used in the SPIEDAC reaction (Chen et al., 2012). Various bioorthogonal *in vivo* labeling strategies were recently evaluated in a systematic study in eukaryotes, highlighting that, apart from reactivity and selectivity, also the cell permeability of the conjugates plays a crucial role (Murrey et al., 2015). Hence using the less reactive, but also less hydrophobic, BCN-fluorophore conjugates may be beneficial compared to the more reactive and hydrophobic DIBO or DIBAC conjugates. Apart from the reactive groups, the choice of the conjugated fluorophore also significantly affects the cell permeability. Many of the commercially available dyes do not disclose the actual chemical compound and were only tested with eukaryotes. This encumbers the choice of the conjugate. Both TAMRA and Cy3 were considered as cell permeable dyes based on recent reports (Kipper et al., 2017; Murrey et al., 2015) and their commercial availability as conjugates. Although commonly used to increase hydrophilicity, and consequently water solubility, without introducing charges, a PEG linker between the reactive group and the fluorophore may also decrease cell permeability (Kipper et al., 2017), therefore both TAMRA-PEG_4-DBCO (Hatzenpichler et al., 2014) and TAMRA-DIBO were chosen as conjugates. Additionally, Cy3-DBCO was selected (see Figure II.2.5). These fluorophore conjugates are too hydrophobic to wash them out of the membrane; therefore, it is unlikely that labeled Hcp structures can be observed in the stained donor strain.

The naturally incorporated AHA is a surrogate for L-methionine and is activated at a rate of approx. 390^{-1} compared to that of L-methionine (Kiick et al., 2002). Therefore, the substitution of L-methionine by AHA will not be complete when performed in a

L-methionine prototrophic strain. In all three of the T6SS model organisms *A. baylyi* ADP1, *P. aeruginosa* PAO1 and *V. cholerae* 2740-80, commonly used in the group, none of the naturally occurring L-methionines is pointing into the lumen of the Hcp hexamer. Consequently, the azide moiety will likely be inaccessible for the labeling reagent. Therefore, an Hcp2$_{Vc}$-K69M mutant was constructed for *V. cholerae* 2740-80 and an Hcp$_{ADP1}$-L61M mutant was constructed for *A. baylyi* ADP1. These residues are located in one of the inner central β-sheets and point into the lumen of the Hcp hexamer.

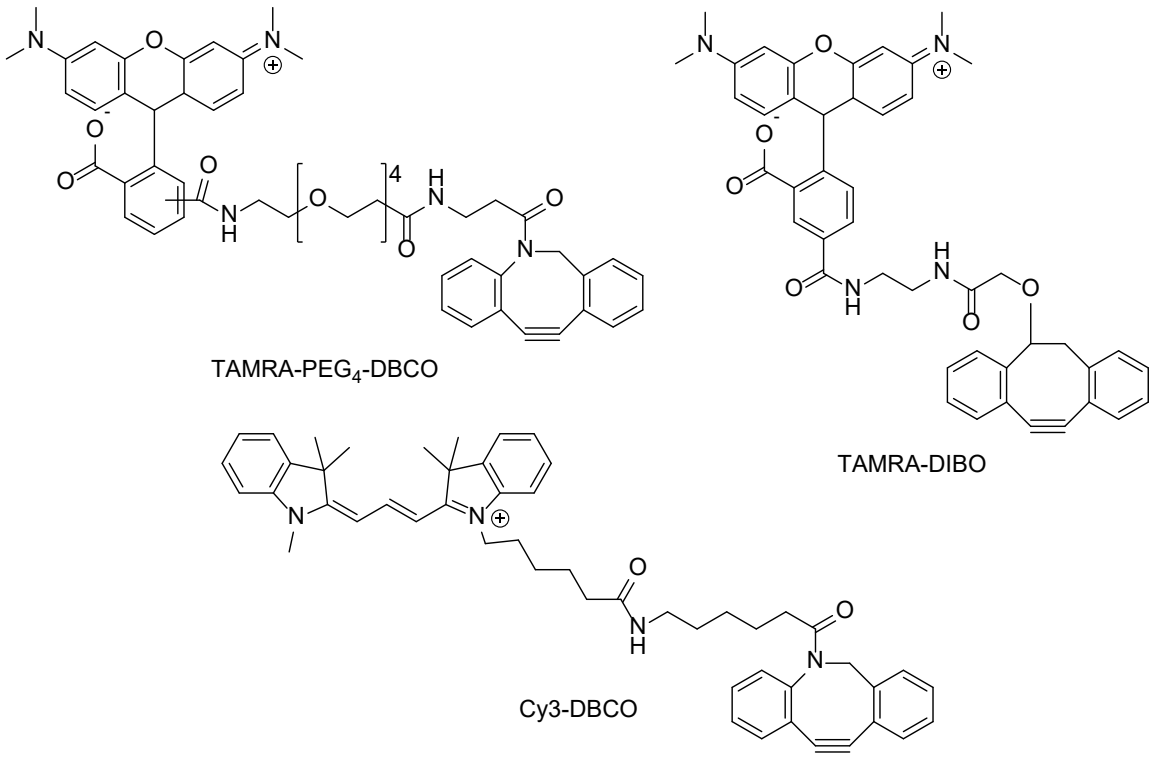

Figure II.2.5: Strained cycloalkyne-fluorophore conjugates used for SPAAC labeling

Neidhardt's rich defined methionine free medium with either glucose or glycerol as carbon source was chosen for the labeling (Neidhardt et al., 1974). Preliminary experiments with *A. baylyi* ADP1 did not yield a stable growth. The Hcp deficient *V. cholerae* 2740-80 carrying pBAD24-Hcp2-K69M grew with glycerol as a carbon source. However, there was no significant T6SS activity after the completion of the labeling procedure.

II.2.2.2.4 Summary and outlook for the Hcp labeling

Extensive attempts were made to label Hcp *in vivo* in collaboration with Dr. Schneider and Dr. Wang. The tags either did not yield enough signal to distinguish them from the background or disrupted the assembly of the Hcp tube. The bioorthogonal labeling, using unnatural amino acids, is promising due to the small size and the high photostability of

organic fluorophores. However, this may require the adaptation of the $tRNA_{CUA}$/pyrrolysyl-tRNA synthetase pair to the selected model organism or the choice of a different model organism. Furthermore, the subsequent staining procedure has to be revised in order to reduce the amount of unspecifically bound dye. Alternatively, fluorogenic substrates with a higher turn-on-ratio could be employed, alleviating the need to remove excess dye (Carlson et al., 2013; Devaraj et al., 2010; Ji et al., 2017; Knorr et al., 2016; L. Oliveira et al., 2017; Meimetis et al., 2014; Shang et al., 2017; Vázquez et al., 2017; Wieczorek et al., 2014, 2017; Wu et al., 2014a, 2014b). To date, the dye-conjugate with the highest turn-on-ratio of 11,000 x, in the class of SPIEDAC reactions, is HELIOS 388Me (Meimetis et al., 2014).

Recently, electroporation was established to deliver *ex vivo* labeled biomolecules into microorganisms (Aigrain et al., 2015; Crawford et al., 2013; Paolo et al., 2016; Sustarsic et al., 2014). This would allow to produce Hcp in a different organism which can tolerate the labeling plasmids, label the purified Hcp and electroporate it into the target organism. This would also alleviate the need to remove unspecifically bound dye and permit a broader range of fluorophores and labeling chemistry to be used.

The FUNCAT strategy also seems promising. Different methionine free growth media may yield better growth and optimizing the staining procedure may help to reduce the negative effects on the T6SS activity. Nevertheless, it may be challenging to obtain long T6SS structures because of the low quantity of injected components (Vettiger and Basler, 2016). Due to the high photostability and quantum yields of the organic fluorophores it may be possible to inject the labeled Hcp into cells which themselves express low quantities of Hcp, thereby generating sparsely labeled Hcp tubes which may still be visible.

II.3 Utility Software Developed for Image Registration

A common preprocessing step in the image analysis of time lapse microscopy data is the alignment or registration of the image stack. The frequent use of such microscopy techniques throughout this thesis resulted in a significant amount of computation time required to perform the image registration. An additional limitation was that the registration program used could not be executed in parallel and that each dimension had to be aligned separately. This incited the improvement of the registration program.

II.3.1 Introduction

The image registration software which had been used was the ImageJ (Schneider et al., 2012) plugin StackReg, which in turn is based on TurboReg (Thévenaz et al., 1998). The plugin is widely used and is considered stable and fast although somewhat inconvenient for multidimensional stacks, because each dimension needs to be aligned separately. Aligning the dimensions separately not only increases the computational load, but may also lead to disparities between the alignments of different dimensions. Because StackReg saves each frame as a temporary image file with a hardcoded name and then passes it as a parameter to TurboReg, the StackReg instances must not be run in parallel, otherwise the instances will overwrite the temporary images of the other instance leading to unpredictable behavior. Some of these shortcomings were addressed in derived projects like PoorMan3Dreg (Liebling, 2010), HyperStackReg (Sharma, 2015), MultiStackRegistration (Busse and Miura, 2016) and TimeLapseReg (Sahdev et al., 2017). However, these projects still rely on the proven TurboReg base (Thévenaz et al., 1998).

The multiresolution subpixel precision registration algorithm, described by Thévenaz et al., 1998, employs affine transformations and an isotropic intensity scaling factor to minimize the mean square intensity difference (ε^2) between the reference dataset and the alignment target. The datasets may be two- or three-dimensional, but the algorithm can be generalized to support datasets of any dimension. During the alignment the data are represented as interpolating symmetric cubic uniform B-splines to allow for resampling (Unser et al., 1993a), spatial differentiation and interpolation (efficient implementations described and reviewed in (Unser et al., 1993b, 1993c)). Furthermore, Thévenaz et al., 1998 describe a modified Marquardt-Levenberg optimization algorithm (ML*) which reduces the computational burden by calculating the gradient of ε^2 about a fixed point in the parameter space ($\Delta p = 0$). Additionally, the use of image pyramids regularizes the optimization problem and reduces the number of iterations required at high resolution, decreasing the

computational cost and increasing the stability of the alignment. Using only a subset of the affine transformations, especially restricting them to the homomorphic case or the rigid body transformations, significantly reduces the degrees of freedom.

II.3.2 Implementation of a parallel stack registration program

Since the registration algorithm was already highly optimized, only its implementation was considered for optimization. The implementation should allow to run multiple instances in parallel and the transformations derived from one dimension should be propagated to the other dimensions to reduce the computational cost and avoid alignment disparities between the dimensions. Because volumetric data were seldomly acquired in the group of Prof. Basler, the three-dimensional case was not considered, also avoiding the potential Gimbal lock resulting from the use of Euler angles to describe the rotations. Furthermore, the transformations were restricted to the homomorphic case because of the inherent properties of widefield microscopy. In TurboReg the algorithm had been implemented serially, apart from the conversion to the B-spline coefficients and the construction of the image pyramid. Because many of the steps are independent or separable it was proposed, that a parallel implementation should provide a performance benefit.

For the following discussion it should be noted, that the licenses of TurboReg and StackReg prohibit creating and distributing derivative works. Therefore, permission was obtained from the authors to create and use derivative works within the scope of this thesis.

In recent years the parallelization has extended beyond the central processing unit (CPU) to the General Purpose Computation on Graphics Processing Units (GPGPU) increasing the number of parallel tasks dramatically. However, there are a number of important constraints when using GPUs among which are memory access coalescing, the single instruction multiple thread (SIMT) synchronous stepping of a processing element (PE) and the avoidance of execution- or data access divergence resulting from the previous two constraints. Taking these constraints into account usually requires specifically designing the implementation for this purpose and thus a direct execution of the serial implementation would often result in a reduced performance. Parallelization was considered using a bottom up approach starting from the pixel level independence. To implement the parallelized versions OpenCL™ C was chosen, because it is an open standard not bound to a single hardware manufacturer and supports heterogenous computing (Stone et al., 2010).

As a first step the images have to be converted into the B-spline coefficients (direct B-spline transform). Using the *z*-transform, Unser et al., 1991 described how to efficiently perform this task by successively applying linear causal and anticausal infinite impulse response filters (IIR) (Unser et al., 1991). Indeed, an implementation of these recursive linear filters has been written for the GPU in CUDA® (Ruijters and Thévenaz, 2012). Their implementation however only leverages the row and column independence to introduce parallelism which can be sufficient to hide latencies for large images, but an even higher parallelism may be achieved by combining the filters and applying these on blocks as recently proposed (Maximo, 2016; Nehab et al., 2011). This not only increases the amount of parallelism but also enables a more efficient use of the faster shared local memory. It should be noted however, that Unser et al., 1991 also presented and alternative sum decomposition of the *z*-transformed filter allowing the recursive linear causal and anticausal filters to be applied independently and then to employ a successive finite impulse response filter (FIR) to combine the results (Unser et al., 1991). This allows to increase the parallelism, but incurs more memory access and requires three times as much memory to hold the intermediate results. Because the pyramids are only constructed once for each image and the most costly part of the calculation is the iterative ML* optimization, the implementation proposed here was based on the column and row parallel implementation (Ruijters and Thévenaz, 2012).

In the next step the image-, coefficient- and derivative-pyramids are constructed, which involves the successive application of a set of filters (see Figure II.3.1) (Unser et al., 1991, 1993a). These filters can be grouped into IIR filters, with column and row independence, and separable FIR filters, with pixel level independence, yielding the highest possible degree of parallelism. As mentioned before, the algorithm may be generalized to any number of dimensions. From the transfer functions of the applied filters it becomes evident, that each dataset dimension is independent (Unser et al., 1993b), hence the row and column independence of the IIR filters and the implicit separability of the FIR filters (see Figure II.3.1). Furthermore, the IIR filters can perform their operations in-place, whereas the FIR filters constitute out-of-place modifiers, requiring an additional buffer to hold the result.

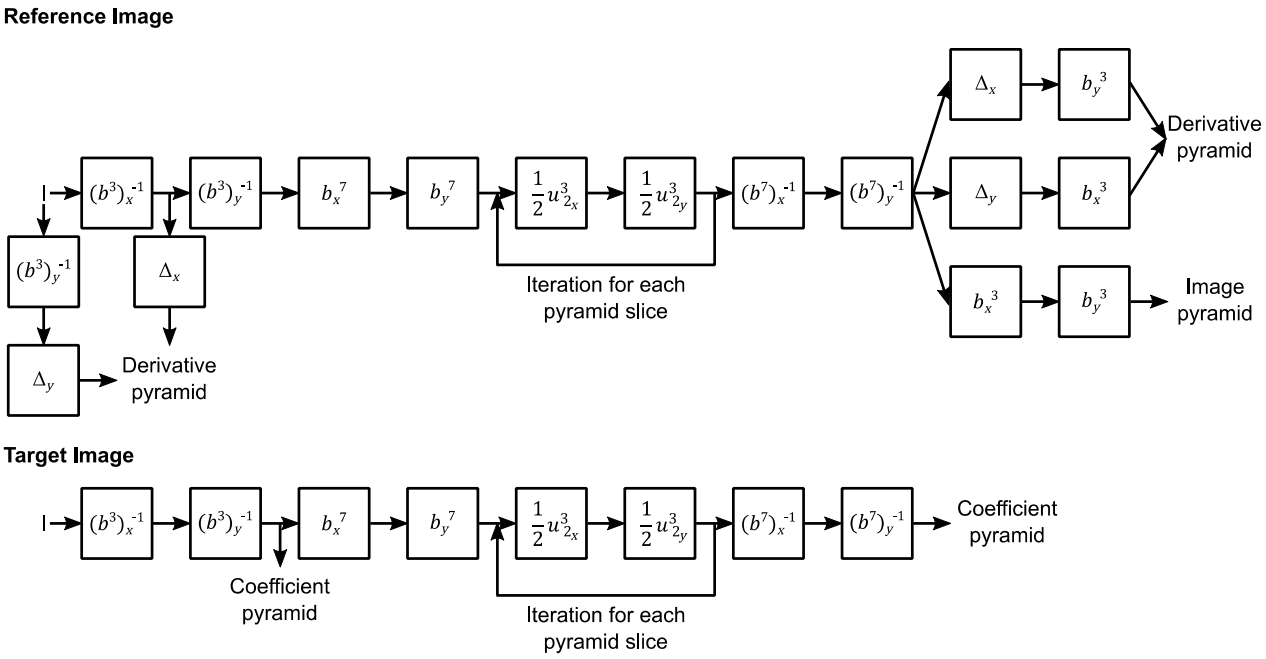

Impulse response	Transfer function	Type	Poles
$b^3(k)$	$\frac{1}{6}(z+4+z^{-1})$	FIR	-
$b^7(k)$	$\frac{1}{5040}(2416+1191[z+z^{-1}]+120[z^2+z^{-2}]+z^3+z^{-3})$	FIR	-
$u_2^3(k)$	$\frac{1}{8}(z^2+4z+6+4z^{-1}+z^{-2})$	FIR	-
$\Delta(k)$	$\frac{1}{2}(z-z^{-1})$	FIR	-
$(b^3)^{-1}(k)$	$\frac{6}{z+4+z^{-1}}$	IIR	$z_1=\sqrt{3}-2$
$(b^7)^{-1}(k)$	$\frac{5040}{2416+1191[z+z^{-1}]+120[z^2+z^{-2}]+z^3+z^{-3}}$	IIR	$z_1=-0.53528$ $z_2=-0.12256$ $z_3=-0.00914$

Figure II.3.1: Filter cascade for image-, coefficient- and derivative-pyramid construction
The filter subscript used in the block diagram indicates the image dimension to which the filter is applied. The I stands for the input image. In the table $\forall k \in \mathbb{Z}$ and only the poles satisfying $|z_i| < 1, i = 1, \dots, \lfloor n/2 \rfloor$, with n being the degree of the B-spline, are given.

The amount of memory available on a graphics card is more limited than that accessible to the CPU, but because transferring data over the bus is expensive, the entire procedure should be carried out using only GPU resident memory. Therefore, efficiently reusing the GPU resident buffers is crucial.

Next, the registration is performed based on the constructed pyramids. The procedure consists of applying the ML* algorithm to minimize ε^2 by adjusting the transformation parameters for each resolution level. The parameters are scaled up between the resolution levels. The implementation in TurboReg uses an affine transformation matrix derived from landmarks to describe the transformation (Thévenaz et al., 1998). This circumvents the need to invert the affine matrix, the equivalent of which may be obtained by deriving the affine matrix from the inverted set of landmarks. However, the use of landmarks is unnecessary and by explicitly employing the transformation parameters both the affine transformation matrix and the corresponding inverse transformation matrix may be constructed at any time. Moreover, using the transformation parameters for combining transformations avoids the need for orthonormalization of the matrices resulting from matrix multiplication which will become important later. The calculation of the difference between the reference and the target is pixel level independent. To avoid actually transforming the target an inversely transformed orthonormal base, which was implemented by using an inversely transformed normalized subpixel access vector, was employed in TurboReg (Thévenaz et al., 1998). The same concept was used in the implementation presented here. Furthermore, even though the difference can be calculated independently for each pixel, calculating the sum yielding ε^2 would require global synchronization, which is not available in OpenCL™. Additionally, this would serialize the calculation. The same is true for the parallel calculation of the gradient and the hessian matrix required by the ML* algorithm. This parallel reduction problem is common and an elegant solution using a cascaded parallel tree sum reduction in combination with a sequential reduction was proposed by Dr. Harris in 2007 taking Brent's theorem into account. The proposed algorithm was adapted such that the block sizes are not required to be powers of two.

The alignment of an image to its reference can be performed independent of the remaining images and can thus be parallelized. However, especially during time-lapse microscopy of fast growing bacteria or when aligning Z-sections, frames taken at a late timepoint or at a great Z-distance may not share significant similarity with the reference anymore. The global transformation of a distant frame to its reference may be decomposed into the transformations of each preceding frame. The alignment of each frame to its preceding frame is also independent resulting in a local transformation. Therefore, the local transformations can be calculated in parallel first, then the local transformations have to be

combined to yield the global transformations and finally the global transformations may be applied independently. Such an algorithm had already been implemented in StackReg (Thévenaz et al., 1998), but the local transformations were represented in form of affine matrices, which were multiplied to yield the global transformations. From a mathematical point of view this allows any type of affine transformations to be combined using the same method, however this procedure is not necessarily numerically stable, possibly requiring a computationally intensive orthonormalization of the resulting matrix. As mentioned before, I chose to explicitly employ the transformation parameters, allowing a trivial combination of the transformations from which an orthonormal transformation may then be derived. Yet, this requires specifically implementing the combination of the transformations for each type of transformation.

Although the independent alignment of the images is a deterministic process, the number of iterations required to perform an alignment cannot be determined in advance. Consequently, equally splitting the dataset may result in an unequal distribution of computational load and thus idling computational units. To avoid this problem a work stealing scheduler was used instead (Blumofe and Leiserson, 1999).

As mentioned before, the use of image pyramids has the benefit of reducing the number of iterations at high resolution. Similarly, the computation speed can be significantly increased by using single precision floating point numbers instead of double precision floating point numbers. Not only is the computation itself faster, but also the memory access, due to the smaller size. Most cameras used for scientific imaging have a bit depth of no more than 24 bit, therefore such an image may be represented as single precision floating point numbers without a severe loss of information. Thus, I propose to use a hybrid precision model where the pyramids are constructed using single precision floating point numbers. The alignment is carried out at single precision and the resulting parameters are used as optimal initial parameters for a final round of optimization at double precision. Furthermore, taking the maximum attainable precision of single precision floating point numbers into account, the initialization of the causal coefficient used during the direct B-spline transform may be simplified as previously suggested (Ruijters and Thévenaz, 2012).

To increase the parallelism even more, the implementation was also adapted for the CPU such that both the CPU and the GPU could run in parallel.

II.3.3 Performance comparison

To simplify its use, the new registration program was implemented as an ImageJ plugin (Schneider et al., 2012). A test dataset comprised of 60 timepoints and 4 channels each 2048 by 2048 pixels with a bit depth of 16 bit was obtained using time-lapse microscopy and was used to compare the performance of the implementations. Two different computer systems were used for the comparison, one with an Intel® Xeon® CPU E3-1270 v5 processor and an NVIDIA Quadro K2200 graphics card, referred to as C1, the other with an Intel® Core™ i7-6700K processor and an NVIDIA GeForce® GTX 1080 founders edition graphics card, referred to as C2.

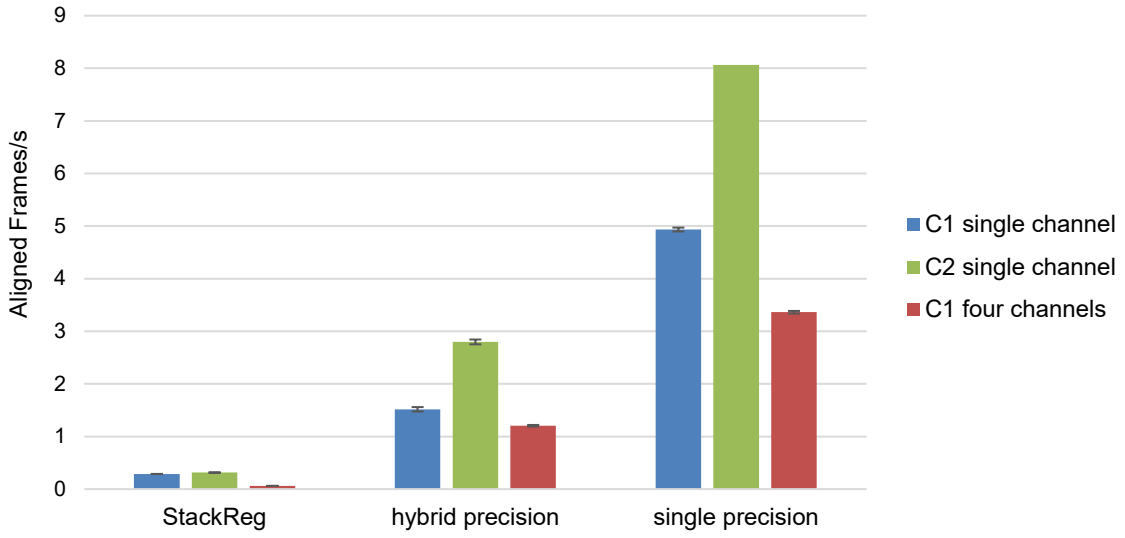

Figure II.3.2: Performance comparison of the different parallel registration implementations
The error bars indicate the standard deviation of 10 runs.

The average performance gain of the hybrid precision implementation on the single channel image stack was 8.9 fold on C2 and 5.2 fold on C1. Additionally, an implementation using only single precision floating point values yielded an overall 25.6 fold performance gain on C2 which may be beneficial if high accuracy is less of a concern. For the four channel image an additional performance gain of 19.5 fold was achieved by the propagation of the transformations to the remaining channels. Furthermore, the implementation presented here enables the user to export the transformations. As an example, these may be used to inversely transform regions of interest defined in the aligned stack to obtain non-interpolated pixel values from the untransformed images.

Taken together a new parallel registration implementation was presented which utilizes both the GPU and the CPU yielding significant performance improvements.

II.4 Research Article II

Established Microbial Colonies Can Survive Type VI Secretion Assault

David Bruce Borenstein[1], Peter Ringel[2], Marek Basler[2], Ned S. Wingreen[1,3*]

[1] Princeton University, Lewis-Sigler Institute for Integrative Genomics, Princeton, New Jersey, United States of America

[2] Universität Basel, Biozentrum, Basel, Switzerland

[3] Princeton University, Department of Molecular Biology, Princeton, New Jersey, United States of America

* correspondence to: wingreen@princeton.edu

PLoS Computational Biology, Volume 11, Issue 10, October 20th, 2015, e1004520

Statement of contribution

I performed the competition experiments, contributed to the biological data analysis and to the revision of the manuscript.

PLOS | COMPUTATIONAL BIOLOGY

RESEARCH ARTICLE

Established Microbial Colonies Can Survive Type VI Secretion Assault

David Bruce Borenstein[1], Peter Ringel[2], Marek Basler[2], Ned S. Wingreen[1,3]*

1 Princeton University, Lewis-Sigler Institute for Integrative Genomics, Princeton, New Jersey, United States of America, **2** Universität Basel, Biozentrum, Basel, Switzerland, **3** Princeton University, Department of Molecular Biology, Princeton, New Jersey, United States of America

* wingreen@princeton.edu

OPEN ACCESS

Citation: Borenstein DB, Ringel P, Basler M, Wingreen NS (2015) Established Microbial Colonies Can Survive Type VI Secretion Assault. PLoS Comput Biol 11(10): e1004520. doi:10.1371/journal.pcbi.1004520

Editor: Roland R Regoes, ETH Zurich, SWITZERLAND

Received: March 2, 2015

Accepted: August 24, 2015

Published: October 20, 2015

Data Availability Statement: All relevant data are within the paper and its Supporting Information files.

Funding: This work was supported in part by National Science Foundation Grants PHY-1305525, MCB-1119232, and MCB-1344191, the Eric and Wendy Schmidt Transformative Technology Fund, SNSF Starting Grant BSSGI0_155778, and the University of Basel. PR was supported by the Biozentrum Basel International PhD Program "Fellowships for Excellence." The funders had no role in study design, data collection and analysis, decision to publish, or preparation of the manuscript.

Abstract

Type VI secretion (T6S) is a cell-to-cell injection system that can be used as a microbial weapon. T6S kills vulnerable cells, and is present in close to 25% of sequenced Gram-negative bacteria. To examine the ecological role of T6S among bacteria, we competed self-immune T6S+ cells and T6S-sensitive cells in simulated range expansions. As killing takes place only at the interface between sensitive and T6S+ strains, while growth takes place everywhere, sufficiently large domains of sensitive cells can achieve net growth in the face of attack. Indeed T6S-sensitive cells can often outgrow their T6S+ competitors. We validated these findings through *in vivo* competition experiments between T6S+ *Vibrio cholerae* and T6S-sensitive *Escherichia coli*. We found that *E. coli* can survive and even dominate so long as they have an adequate opportunity to form microcolonies at the outset of the competition. Finally, in simulated competitions between two equivalent and mutually sensitive T6S+ strains, the more numerous strain has an advantage that increases with the T6S attack rate. We conclude that sufficiently large domains of T6S-sensitive individuals can survive attack and potentially outcompete self-immune T6S+ bacteria.

Author Summary

Type VI secretion (T6S) is a cell-to-cell injection system that can be used as a microbial weapon. T6S kills vulnerable cells, and is present in a significant fraction of bacteria. Given the tactical advantage conferred by T6S, the system's lack of universality suggests limits to its effectiveness relative to its costs. In our study, we use theory and experiments to identify the limits of T6S as a cell-to-cell weapon. We find that cell birth inside an existing colony can offset cell death due to T6S killing at the colony's edge, helping sufficiently large ("established") groups of sensitive cells to survive. T6S has been extensively studied because of its implications in both disease and inter-microbial competition. The present study is the first to identify the practical limits of T6S as a killing mechanism.

PLOS | COMPUTATIONAL BIOLOGY

Competing Interests: The authors have declared that no competing interests exist.

Introduction

Microbes employ a staggering range of extracellular tools to engineer their immediate environment [1–6]. Very often, that environment is defined by the multitude of other cells in close proximity. These neighbors pose both a threat and an opportunity, and represent an important target for manipulation [7–10].

The Type VI secretion system (T6SS) is a mechanism for direct cell-to-cell manipulation through the translocation of effector proteins. The T6SS consists of a helical sheath, surrounding an inner tube with associated effectors, and a baseplate attached to the bacterial cell wall (Fig 1a) [11, 12]. The T6SS is functionally close to the contractile phage tail, with which it shares evolutionary origins [13–17]. When triggered, the sheath contracts rapidly, pushing the effector through a specialized pore and into a neighboring cell [18–22].

Specialized T6SSs can directly damage both prokaryotic and eukaryotic target cells through the translocation of toxic proteins directly into the target cell. T6SSs are observed to cause death via numerous mechanisms in both bacteria and eukaryotes (Fig 1b; S1 Video) [13, 18, 23–28]. In fact, many species have developed multiple, specialized T6SSs [26]; for example, *Burkholderia thailandensis* has five separate T6SSs, which allow it to attack both prokaryotic and eukaryotic cells [29]. T6SSs are present in approximately 25% of the Gram-negative genomes studied by Boyer and colleagues [30]. Antibacterial T6SSs appear to be found with cognate immunity proteins in every case [26]. Given this tactical advantage, one might expect T6S to be even more widespread. The lack of universality of the T6SS suggests that there are limits to its utility relative to its costs.

To address the question of T6S's utility, we focused on the case of cell-to-cell killing between bacteria. We explored this scenario through the use of individual-based models (IBMs; also called "agent-based models"). IBMs simulate the behavior of many, possibly different individuals each of which obeys rules that dictate the individual's behavior as a function of its immediate environment. IBMs are a common tool in ecology, and have been widely used in the study of spatially explicit biological processes. Examples at the multicellular scale include the evolution of cancer, the spread of disease, and the dispersal of plants [31–38]; IBMs are also used to

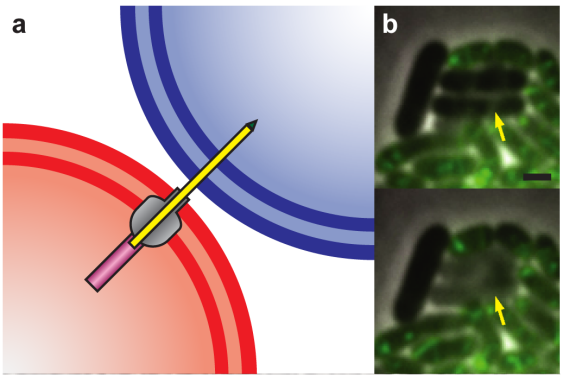

Fig 1. Function and mechanism of the T6S system. (a) The T6S system consists of a contractile outer sheath (purple), an inner tube (yellow), a membrane complex and baseplate (grey) and spike proteins (green). The contractile sheath pushes the inner tube through the baseplate and membrane complex, causing the tube to penetrate the target cell. (b) Competition between *V. cholerae* str. 2740–80 (sheath labeled with GFP) and *E. coli* MG1655 (unlabeled). Arrow shows *E. coli* cells that undergo lysis. Panels are taken two minutes apart; scale bar 1 μm.

doi:10.1371/journal.pcbi.1004520.g001

study dynamics at the subcellular scale [39]. More generally, IBMs have been used to address a wide range of questions concerning cooperation and conflict, of which T6S strategy can be viewed as an example [40–45].

In this study, we develop a series of IBMs. The first competes self-immune T6S+ and sensitive individuals in a range expansion, analogous to a surface colony (2D) or a biofilm (3D). We find that cell growth from the inside of a sufficiently large (or "established") domain can offset cell death at the interface between a T6S-sensitive strain and a self-immune T6S attacker. Consequently, given a sufficiently large domain, T6S-sensitive strains can survive T6S attack. The sensitive strain does not require a growth advantage to survive; in fact, the sensitive strain can resist elimination even with a slower growth rate. Given even a small growth advantage, the T6S-sensitive strain can outcompete a self-immune T6S+ competitor. In a variant on the original model, we also find that moderate nutrient limitation has a negligible effect on competition outcomes.

We validated these findings through *in vivo* competition experiments between T6S+ *Vibrio cholerae* and T6S-sensitive *Escherichia coli*. In these 2D plate assays, *E. coli* can form microcolonies that survive, provided the initial local density of *V. cholerae* is not too high. Along similar lines, simulated competitions between mutually sensitive T6S+ strains (strains that are self-immune but sensitive to one another) reveal that the initially more numerous strain benefits most from higher attack rates. We conclude with a discussion of the ecological impact of T6SSs.

Materials and Methods

Competition experiments

Escherichia coli MG1655 $Gent^R$ (LacZ+) was competed against *Vibrio cholerae* str. 2740–80 (LacZ-), similarly to what was described previously [19]. *E. coli* and *V. cholerae* were each grown from frozen stocks in Luria-Bertani broth (LB), supplemented with the appropriate antibiotic, shaking overnight at 37°C and 200 rpm. The cells were washed twice with LB before being diluted to an OD_{600nm} of 0.5. To confirm that the initial number of viable cells were comparable among the competition assays, the colony forming units (CFUs) were determined by serially diluting the washed and diluted *V. cholerae* and *E. coli* cultures 10-fold in 96-well plates in triplicate. Thereafter, 5 μL of each dilution were spotted on an LB agar plate (LA).

For the competition assays, the cultures were mixed in a 1:1 ratio, which was then serially diluted 3-fold in a 96-well plate. For selected dilutions 5 μL were spotted on a LA/IPTG 100 μM/X-Gal 40 μg/mL plate in duplicate. The competition plates were incubated at 37°C overnight. To determine the *E. coli* to *V. cholerae* ratios resulting from the competition assays, the CFUs of both strains were determined for each spot. This was achieved by excising the spots from the competition assay plates and resuspendig the bacteria in 1 mL LB by vigorously vortexing for at least 15 sec. These suspensions were serially diluted 10-fold in 96-well plates and 5 μL of each dilution were spotted on LA plates supplemented with the appropriate antibiotic. The CFU plates where either incubated at 37°C overnight or at lower temperatures until colonies were visible. Images of the plates were taken on a white light transilluminator. Timelapse movies of the competition assay were obtained by preparing the competition assay plates and the pre-competition CFU plates as described before, except that the competition mixtures were only spotted once. The competition assay plate was incubated at 37°C on a white light transilluminator while taking an image every 10 min over 24 h using a Nikon D5200. The contrast, brightness and white balance of the images were adjusted using Adobe Photoshop CS5. The same settings were applied to all timelapse images. Thereafter the images were further processed and converted to a video using Fiji [46].

PLOS | COMPUTATIONAL BIOLOGY

The growth rate determination was carried out under the same conditions as the killing assay. The same cultures (OD_{600nm} = 0.5) were individually spotted on LA plates and incubated at 37°C. Every hour the CFU was determined from a spot of each strain, as described for the endpoint killing assay. The growth rate was then derived from the parameters of the fit of an exponential curve. For the *E. coli* MG1655 $Gent^R$ overnight cultures and selective CFU plates the growth medium was supplemented with 15 μg /mL Gentamicin, whereas for *V. cholerae* str. 2740–80 50 μg /mL Streptomycin was added.

Imaging of a competition between *E. coli* and *V. cholerae* VipA-msfGFP strains was performed under conditions similar to those used previously for imaging of T6SS activity in *V. cholerae* [17]. Strains were grown to $OD_{600nm} \approx 1$ and mixed at a 1:1 ratio on an LB 1% agarose pad. Imaging started after 10–20 min and was performed at 37°C for the indicated number of frames and at the indicated frame rate.

Simulations

Computer models were implemented using Nanoverse 0.x, a prototype of our freely available individual-based modeling platform [47]. In Nanoverse, individual agents (e.g. cells) occupy spaces on a regular lattice. In every step of a simulation, one or more individuals perform a series of behaviors; if multiple individuals act simultaneously, the events are resolved in random order.

Two types of individual cells are included in the simulations (Fig 2a and 2b): self-immune T6S+ ("T6S+") cells, shown in red, and sensitive T6S- ("sensitive") cells, shown in blue. (Self-sensitive T6S+ strains "self-destruct" rapidly in simulations, and indeed have not been observed in nature.) Every cell has an associated probability of cell division per step of the simulation. The T6S+ division rate α_t is taken as the (inverse) time unit of the system and is set equal to 1. The sensitive division rate α_s is generally set higher than α_t, as only T6S+ cells pay the cost of maintaing the T6S. Upon cell division, a copy of the dividing cell is placed in a vacant space adjacent to the dividing cell (Fig 2a). If no vacancies exist adjacent to the dividing cell, nearby cells are pushed out of the way to make room (S1 Text).

Each T6S+ cell has a fixed rate γ of initiating an attack (Fig 2b). The attack is then resolved according to an individual-based rule: attack exactly one randomly chosen nearest neighbor if

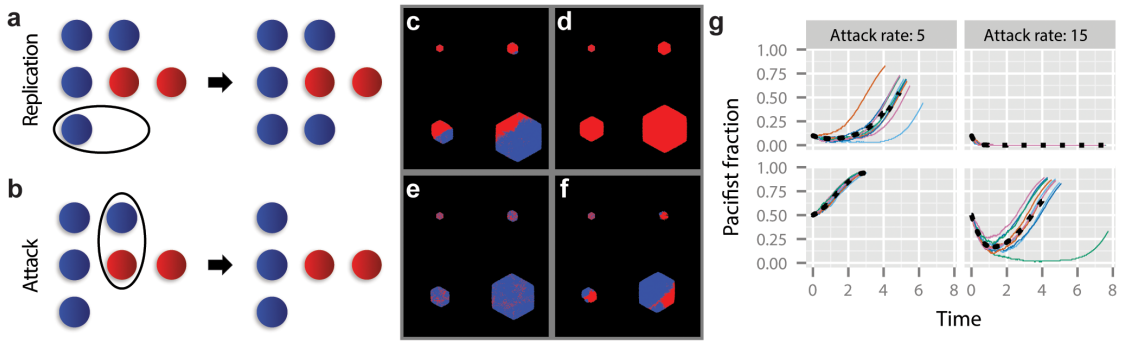

Fig 2. A simple spatial model of T6S-driven community dynamics. (a) Any cell can divide. Division results in an identical cell being placed in an adjacent site. If no adjacent site is available, cells are pushed out of the way to make room for the new cell (S1 Text). (b) T6S+ cells (red) can attack any cell. When a sensitive cell (blue) is attacked, it is "killed" (removed from the system). T6S+ strains are self-immune. (c-f) Time series of competitions between a T6S+ strain (red) and a sensitive strain (blue) during a range expansion in 2D. In all cases the T6S+ growth rate is $\alpha_t = 1$, and the sensitive strain growth rate is $\alpha_s = 4$. Initial sensitive strain fractions are 0.1 (c, d) and 0.5 (e, f). Attack rates are $\gamma = 5$ (c, e) and 15 (d, f). (g) Quantification of dynamics observed in panels (c-f). Thin colored lines are individual trajectories; dotted black lines are averages over 8 of the 10 cases shown (eliminating highest and lowest outliers). Parameters are as in the time series. Time is units of $1/\alpha_t$. Timestep multiplier $\lambda = 1$.

doi:10.1371/journal.pcbi.1004520.g002

there is one; otherwise do nothing. If the attack targets a sensitive cell or a cell of a different T6S+ strain, the target dies and its lattice site becomes unoccupied; T6S+ cells are immune to attack by cells of the same T6S+ strain, as observed experimentally [26]. The overall rate of events is controlled by the simulation timestep multiplier, λ (S1 Text).

Results

Competition between T6S+ and sensitive strains

To determine the effect of T6S on multi-species population dynamics, we simulated a competition between T6S+ and sensitive strains during a range expansion. The simulations begin with a well-mixed, fully occupied circular inoculum of approximately 500 individuals (S1 Text). For 2D simulations on a triangular lattice, the starting population is 469 individuals (i.e. inoculum radius $r_0 = 12$).

The T6S+ division rate is chosen as the unit of time, $\alpha_t = 1$. The three other parameters are the sensitive strain growth rate α_s, the initial sensitive strain fraction, and the attack rate γ. (In simulations in which there are no T6S+ cells, the unit of time is $\alpha_s = 1$.) The attack rate γ and the sensitive strain growth rate α_s are found to offset one another as discussed below. The parameter space was extensively explored. Fig 2 shows parameters chosen to emphasize the effect of varying the attack rate γ and the initial sensitive strain fraction. Specifically, we fixed the sensitive strain growth rate as $\alpha_s = 4$ and varied γ and the sensitive fraction.

When the attack rate is low ($\gamma = 5$), sensitive cells can ultimately dominate even when the sensitive strain fraction starts as only a 10% minority (Fig 2c, S2 Video). Initially, the sensitive population declines as isolated individuals are attacked and killed. Eventually, only a small number of surviving sensitive domains remain, concentrated along the periphery of the colony. However, because sensitive cells grow faster than T6S+ cells, these domains begin to outgrow the T6S+ strain, eventually leading to a majority sensitive population. By contrast, at high attack rate ($\gamma = 15$) and an initial 10% sensitive strain fraction all sensitive individuals are rapidly eliminated (Fig 2d). When the initial sensitive strain fraction is increased to 50%, a larger number of sensitive cells begin near to one another, accelerating the formation of sensitive domains; the early formation of these domains helps the sensitive strain to survive and eventually dominate the T6S+ strain, even under a high rate of attack (Fig 2e and 2f).

An analysis of multiple, independent simulations (Fig 2g) shows that sensitive populations decline and then recover when both the attack rate and initial sensitive strain fraction are low (upper left), or when both are high (lower right). During the period of decline, isolated sensitive cells are eliminated while clusters of sensitive cells enjoy a degree of protection from attack. The monotonic increase of the sensitive population fraction in the most favorable conditions—high initial sensitive strain fraction, low attack rate (lower left)—results from the early formation of sensitive domains, whereas adverse conditions—low initial sensitive strain fraction, high attack rate (upper right)—preclude sensitive domain formation and lead to elimination of the sensitive strain.

Smallest viable sensitive domain

Since T6S-mediated killing can take place only at the interface between T6S+ and sensitive strains, we hypothesized that the net growth rate of the sensitive strain depends on the difference between the area or volume of a sensitive domain and the extent of the interface between the strains. To identify the dependence of this relationship on attack rate and relative growth rates, we studied a simple sensitive domain model (Fig 3a and 3b). The 2D simulations begin with a fully-occupied, homogeneous circular sensitive inoculum. As in the competition model, all individuals are capable of cell division. As before, the model assumes that interior cells can

PLOS | COMPUTATIONAL BIOLOGY

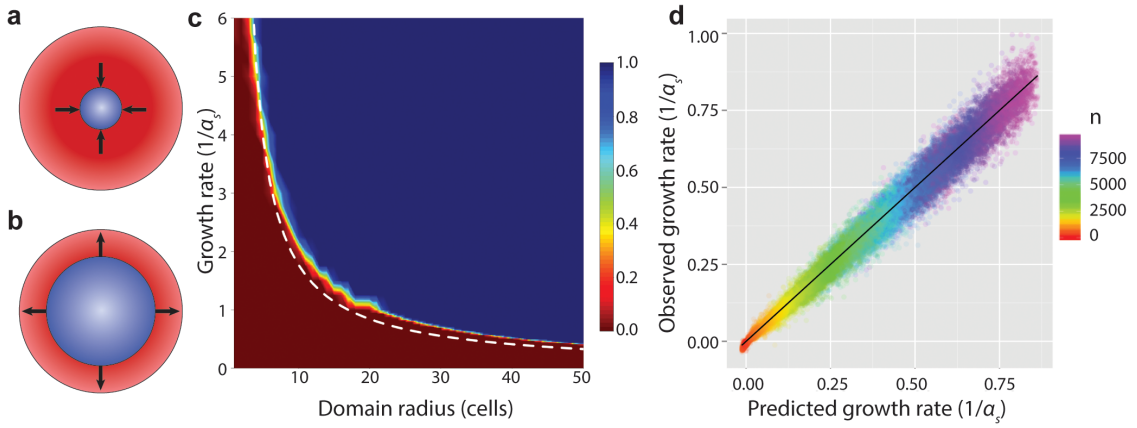

Fig 3. Sensitive T6S- individuals can dominate T6S+ competitors. (a-b) A ball of sensitive cells (blue) is surrounded by a thick layer of T6S+ cells (red). (a) Below a critical radius, the sensitive strain ball tends to shrink to extinction; (b) above it, the ball tends to expand. This behavior is demonstrated for 1D, 2D, and 3D. (c) Heat map of the probability that a 2D sensitive domain surrounded by T6S+ competitors achieves steady growth, as a function of sensitive strain growth rate and initial radius of the sensitive domain. Dashed curve indicates predicted critical parameter values based on Eq. S1. Attack rate $\tilde{\gamma} = 8$; interpolated from 80,250 simulations with timestep multiplier $\lambda = 500$. (Sensitive population either decreased or increased from near the outset of each simulation; consequently, simulations were run only until the sensitive population changed by a factor of three in either direction.) (d) Comparison of growth rate observed in single-domain sensitive 2D growth simulations (y-axis) to the values predicted for this regime in Eq 1 (x-axis). Points represent the average, by sensitive population, across all simulations with the same parameters (20 per condition; $\lambda = 2$). Color represents domain radius; black line is $y = x$.

doi:10.1371/journal.pcbi.1004520.g003

push other cells toward the surface of the colony to make room for their daughter cells (S1 Text). To simulate attack, individuals at the outer periphery are subject to being killed at a rate $\tilde{\gamma}$, essentially equivalent to embedding the sensitive domain in a larger T6S+ domain.

To explore the transition from sensitive strain collapse to sensitive strain growth observed in Fig 2, we varied the sensitive strain domain radius while holding constant the "attack" rate $\tilde{\gamma} = 8$, retaining the $\alpha_s = 4$ growth rate from the earlier competitions. Most sensitive strain domains with starting radius $r_0 \leq 5$ shrank toward zero, while larger domains survived (S3 Video). We then varied the sensitive strain growth rate, allowing it to fall below $\alpha_s = 1$. Strikingly, the minimum sensitive strain domain radius required for survival depends inversely on the relative sensitive strain growth rate, implying that a sufficiently large sensitive strain domain can resist displacement by even a faster-growing T6S+ attacker (Fig 3c).

We can readily estimate the critical population size n^* above which a sensitive strain domain is expected to enjoy a net positive growth rate. Above this value, a sensitive domain would not shrink as a result of T6S+ competition, although it could, depending on conditions, represent an increasingly small fraction of total population. Eq 1 represents a theoretical "worst-case" scenario for a domain of sensitive cells, in which they are completely surrounded by an infinite domain of T6S+ cells. The key observation is that the rate of killing is proportional to the length of the interface between strains, while the rate of sensitive strain population growth is proportional to the sensitive population. For a population size n in 2D, the size of the interface is simply the circumference of the circle. Hence,

$$\frac{dn}{dt} = \alpha_s n - 2\tilde{\gamma}(\pi n)^{\frac{1}{2}}. \quad (1)$$

Solving Eq 1 for n at $dn/dt = 0$, i.e. at the unstable fixed point between increasing and decreasing n, we find that

$$n^* = \frac{4\tilde{\gamma}^2\pi}{\alpha_s^2}, \tag{2}$$

which is shown as a dotted line on Fig 3c. The slight divergence at high radius between the predicted and simulated values is the result of accumulated simulation error (S1 Text). The finding suggests that, even at this theoretical limit of maximal contact with T6S+ competitors, a sensitive domain can persist for long times.

Fig 3d shows simulation results for dn/dt plotted against the prediction from Eq 1. The rate of change of sensitive strain population was measured periodically in simulations with initial domain radii from $r_0 = 3$ to $r_0 = 12$. Attack rates ranged from $\tilde{\gamma} = 0$ to $\tilde{\gamma} = 14$; sensitive strain growth rates ranged from $\alpha_s = 1$ to $\alpha_s = 4$. The simulations show excellent agreement with the predicted dynamics ($R^2 > .98$), despite deviations of the sensitive domain from a pure circle arising both from the lattice structure and from the stochasticity of the simulations. Similar results are obtained for a corresponding relationship in 1D and 3D (S2 Text).

Depletion of nutrients

The simulations described so far assume an unlimited supply of nutrients. To determine the effect of nutrient depletion on T6S population growth and competition, we developed a variant of the IBM that incorporates local depletion of nutrients. Even very limited nutrient concentrations still lead to exponential growth during range expansions, resulting in growth and competition dynamics that are nearly identical to those of the unlimited-nutrient case (S3 Text).

Live-culture competition assay

To validate our simulation results, we inoculated 2.5 μL each of of LacZ- T6S+ *V. cholerae* and LacZ+ T6S- *E. coli* onto X-Gal plates at various dilutions (see "Materials and Methods"). We compared the outcomes of these experiments with simulations for which the growth rates of sensitive and T6S+ cells were matched to those of *E. coli* and *V. cholerae*, respectively. In a preliminary estimate, *E. coli* was observed to grow slightly faster than *V. cholerae* (2.19 h^{-1} vs 2.05 h^{-1}), so this difference was also used in the simulations. The simulation attack rate was set to $\gamma = 5$, which yielded a rough parallel with the experimental images. These simulations were run until the colony had doubled in radius.

Fig 4a–4d compare the experimental and simulated competitions, with initial inoculum concentrations decreasing 9-fold with each successive panel. As the inoculum becomes more dilute, single-species domains become larger. Simultaneously, *E. coli* become more numerous (Fig 4f; S4 Video). In a micrograph of the experimental competition, large domains of *E. coli* are observed to grow, while smaller domains undergo proportionately higher cell death (Fig 4e). S5 Video suggests that these *E. coli* domains persist stably after 24h. In the simulations, the final sensitive population is seen to increase as initial inoculum density decreases. This is due to the formation of large sensitive domains prior to initial T6S+ encounter, leading to increased sensitive strain survival.

Interestingly, in the low-resolution images, a darkened region is observed along the interspecies interfaces, but not at same-species microcolony interfaces. We infer that the darkened zones represent an accumulation of *E. coli* lysates, due to the continual renewal of the interspecies front by cell division within the bulk.

PLOS | COMPUTATIONAL BIOLOGY

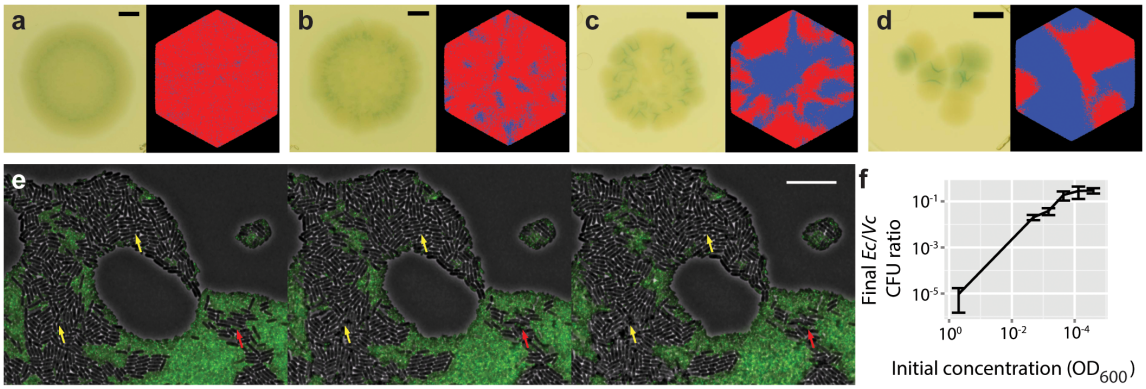

Fig 4. Domain size predicts T6S- survival. (a-d) Comparisons of experimental to simulation outcomes. (a) Left, overnight growth on X-Gal media from an inoculum consisting of *V. cholerae* str. 2740–80 (LacZ-) and *E. coli* MG1655 (LacZ+), starting from equal amounts of $OD_{600nm} = 2 \times 10^{-3}$ culture from each species. Right, simulated competition between 6,561 T6S+ individuals and an equal number of sensitive individuals, scattered randomly in an initial domain of $r_0 = 82$, and allowed to grow until the population radius has doubled ($\lambda = 500$). (b) 9-fold dilution (experiment and simulation); (c) 81-fold dilution; (d) 729-fold dilution. Scale bars 1mm. (e) Fluorescent micrograph of competition between *E. coli* and *V. cholerae*; shown as illustration of target cell killing. Scale bar 10 μm. Arrows indicate areas of *E. coli* net growth (yellow) and net decline (red). (f) Ratio of *E. coli* to *V. cholerae* CFUs, after overnight growth starting from equal initial amounts, as a function of initial inoculum concentration.

doi:10.1371/journal.pcbi.1004520.g004

T6S+ invasion dynamics

So far, we have considered competition between T6S+ and sensitive bacteria. We next investigated whether being T6S+ could help in the case of invasion by a T6S+ competitor. To answer this question, we simulated a competition between two T6S+ strains during a range expansion. Each strain can kill the other, but is immune to self-attack. Each strain has the same attack rate γ and cell division rate $\alpha_t = 1$. Fig 5 shows two T6S+ strains (yellow and red) that were allowed to compete during a range expansion from $n_0 = 469$ ($r_0 = 12$) to a final population of $n_f = 4690$. The relative success of the invasion was measured by comparing the initial yellow (minority) fraction to the final yellow fraction.

In the presence of attack, the minority population is quickly eliminated (Fig 5a). By contrast, in the absence of attack the minority fraction remains roughly constant throughout the course of the range expansion (Fig 5b, S6 Video). As the attack rate increases, the initial minority fraction needed for survival asymptotically approaches 50% (Fig 5c). Note that for equal initial numbers of red and yellow cells, attack leads to spontaneous segregation from a well-mixed inoculum, with higher attack rates leading to faster and more thorough sectoring (S6 Video). Equivalent competitions in 1D and 3D led to analogous results (S4 and S5 Figs). These results imply that T6S+ is useful for defending established populations against invasion.

Discussion

Gram-negative bacteria can employ T6S to kill competitors, yet the system is not found universally among these bacteria. To better understand the conditions favoring T6S, we modeled a competition between T6S+ and sensitive strains. In a range expansion from a well-mixed inoculum, we found that the sensitive cells can survive in the presence of T6S+ competitors by forming compact domains that protect interior cells from attack. To test these results, we competed T6S+ *V. cholerae* and T6S-, sensitive *E. coli* in an analogous range expansion. We observed that *E. coli* outcompeted *V. cholerae*, so long as the *E. coli* had the opportunity to

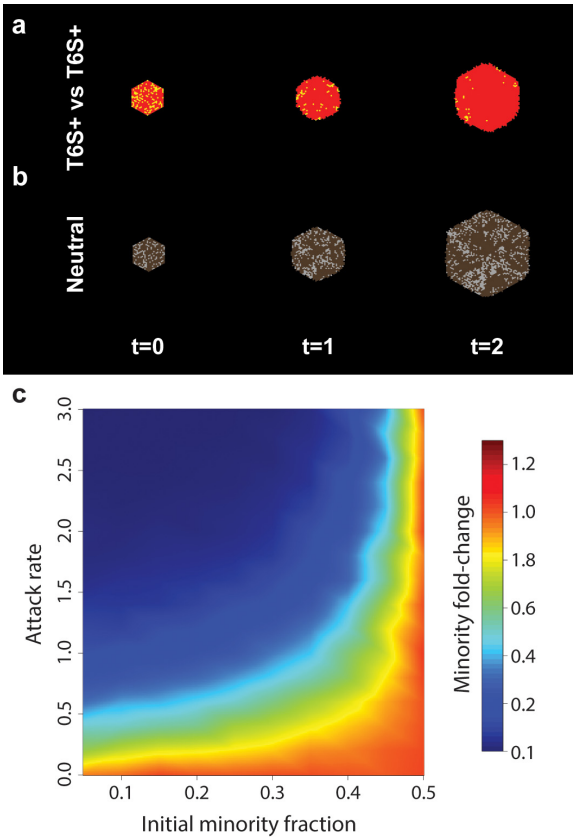

Fig 5. Competition between T6S+ strains. (a-b) Range expansion of two competing T6S+ strains. (a) Each strain kills only individuals of the other type. For each strain, the growth rate is $\alpha_t = 1$ and the attack rate is $\gamma = 2$. (b) No killing occurs; grey and brown cells grow neutrally ($\gamma = 0$) and at the same rate ($\alpha_t = 1$). Initial inoculum is well-mixed and has radius $r_0 = 12$; starting minority fraction is 25%. (c) Fold-change in minority fraction, starting at radius $r_0 = 12$ ($n_0 = 469$) and growing to exactly 10-fold larger. Orange (fold change = 1.0) indicates that the initial population ratio was retained. Values interpolated from 3,200 simulations. Simulation timestep multiplier $\lambda = 1$.

doi:10.1371/journal.pcbi.1004520.g005

form compact domains. Finally, we found that in a model competition between two equivalent T6S+ strains the more numerous strain always drove the minority to extinction.

It is informative to compare the current model to related model systems. For example, in a Lotka-Volterra model, a prey species grows in the absence of predation, and a predator grows faster in the presence of prey [48]; such systems have also been generalized to lattices [49]. By contrast, T6S+ does not grow faster as a result of killing, but potentially occupies more of the habitat. In this sense, the current model is more closely analogous to colicin dynamics in *E. coli* [50, 51]. Chao and Levin [52] observed that a colicin-producing strain of *E. coli* dominated a sensitive strain on soft agar by creating a zone of inhibition around itself, preventing the sensitive cells from exploiting the habitat. Colicin dynamics have also been studied using an IBM based on contact-mediated killing [53]. The colicin IBM differs from our T6S model in two respects: in [53], agents can only divide into adjacent vacancies, and sensitive cells have a strict

growth advantage. The colicin model predicts that either species can dominate, with dominance depending primarily on parameter choices. By contrast, in the current study, initial colony size determines the survivorship of sensitive cells at all parameter values. The difference comes from the fact that in our model for T6S-mediated competition, interior sensitive cells are protected from killing by the outermost layer of cells. Such a "refuge" effect has previously been studied in the context of predator-prey dynamics, where density-driven sheltering is observed to destabilize predator-prey ratios relative to a well mixed model [54].

Our model employs a number of simplifying assumptions. Most importantly, cells are represented as agents on a regular lattice, and cells divide stochastically. While cell shape can affect the details of colony morphology during range expansions, it does not seem to affect the qualitative population dynamics [55]; indeed, lattice population dynamics have been shown to be consistent with the dynamics of real microbial populations [56]. The similarity of our observations in 1D, 2D, and 3D further suggests that our results are not sensitive to cellular geometry. Similarly only overall growth rates, rather than the detailed timing of cell divisions, are important for long-term population dynamics [55].

It has been hypothesized that nutrient depletion may introduce a substantial advantage for T6S+ strains. In practice, cells at the interior of a natural community face nutrient and oxygen depletion [57]. Does this limitation result in a different competitive outcome? In a simple model of nutrient depletion, we found that a moderately nutrient-limited environment leads to dynamics extremely similar to those in the absence of limitation (S3 Text). This is because exponential growth ensures that only a very small fraction of the population occupies a fully depleted zone (S7 Fig). Thus, our preliminary results suggest that the effects of nutrient depletion on cell growth do not qualitatively alter the population dynamics arising from T6S-mediated competitions. Under special circumstances, such as burrowing invasions of a nutrient-depleted biofilm, T6S-mediated cell lysis could provide a significant nutrient benefit beyond the direct benefit of killing competitor cells. Typically, this effect would be limited, as the nutrient benefit would be divided among both T6S+ species and their prey. In an entirely nutrient-depleted environment, though, actively growing invaders would have an early growth advantage over previously quiescent resident cells.

In determining the ecological role of T6S, the costs of maintaining a T6SS must be taken into consideration. The T6SS requires the expression of 13 core genes, the assembly and disassembly of the baseplate structure and sheath, and the production of the secreted effectors [19, 27, 30]. Immunity to T6S requires the maintenance of a complementary immunity protein, and may require additional modifications to the attacker's peptidoglycan [26]. Selective use of T6S can mitigate these costs by reducing the frequency of wasteful attacks. To this end, bacteria have evolved a variety of T6SS regulatory schemes, including quorum-sensing and retaliation.

Quorum sensing can reduce wasteful attacks by repressing T6S until it is likely to provide a benefit [21, 58]. For example, QS regulates expression of T6SS in *V. cholerae* [59]. Interestingly, expression of T6SS and natural competence is induced by high cell density and growth on chitinous surfaces, which suggests a role of T6SS in horizontal gene transfer [60]. In addition, the *V. cholerae* QS signal integrates both species-specific and multigeneric signals [61], which means that the presence of competitors could also activate *V. cholerae*'s T6SS. However, reflecting the diversity of T6S roles, T6S is not always upregulated in response to high density. In *P. aeruginosa*, there are three T6SSs; species-specific QS signals LasR and MvfR activate two of these T6SSs, but repress the third [62].

Like quorum sensing, "retaliatory" T6S attack can prevent attack until a hostile cell is encountered. For example, *P. aeruginosa* is observed to engage in retaliatory T6S attack [27, 63, 64]. This 'tit-for-tat' strategy could limit wasteful T6S+ interactions within clonal populations, as well as facilitating coexistence within productive consortia. Notably, *P. aeruginosa* also

attacks its target repeatedly; by eliminating wasteful attacks, retaliators are also free to employ a more concerted (and damaging) series of attacks [27].

In considering the ecological role of T6S, it is instructive to consider an analogous system found in marine invertebrates. Members of the phylum *Cnidaria*, which includes corals, hydrae, and jellyfish, possess an explosive cell called a nematocyte containing a harpoon-like projectile [65]. Upon detonation, the effector is propelled with extreme force (up to 40,000g) into a target, leading to paralysis and death [66]. Among corals, nematocytes are used interspecifically to compete for habitat access. High attack rates are most commonly observed among slower-growing species, where nematocytes are used to defend against encroachment [67]. Our results suggest that, like nematocytes, T6S can also offset a growth rate disadvantage. The full breadth of its ecological role, however, is only beginning to come into focus.

Supporting Information

S1 Text. Simulation details.
(PDF)

S2 Text. Generalization of sensitive domain survival to 1D and 3D.
(PDF)

S3 Text. The impact of nutrient depletion on T6S-mediated population dynamics.
(PDF)

S1 Video. T6S-mediated interactions between bacteria. Competition between *V. cholerae* str. 2740–80 (sheath labeled with GFP) and *E. coli* MG1655 (unlabeled). 60 frames; frames are 30s apart.
(MP4)

S2 Video. A simple spatial model of T6S-driven community dynamics. Time series of simulated competitions between a T6S+ strain (red) and a sensitive strain (blue) during a range expansion in 2D. In all cases the T6S+ growth rate is $\alpha_t = 1$, and the sensitive strain growth rate is $\alpha_s = 4$. Initial sensitive strain fractions are 0.1 (upper) and 0.5 (lower). Attack rates are $\gamma = 5$ (left) and 15 (right). Timestep multiplier $\lambda = 1$.
(MP4)

S3 Video. Critical domain size for sensitive strain survival. Time series of a simulated range expansion of a sensitive strain subject to stochastic killing at the outer boundary of the colony. Initial colony radius varies from $r_0 = 4$ (left) to $r_0 = 7$ (right). The growth rate is $\alpha_s = 4$ and the killing rate at the outer boundary is $\tilde{\gamma} = 8$. Timestep multiplier $\lambda = 1$.
(MP4)

S4 Video. Community dynamics between T6S+ and T6S-sensitive populations. Fluorescent micrograph of competition between T6S+ *V. cholerae* and T6S-sensitive *E. coli* (see Fig 4e). two fields, 60 frames; frames are 20s apart. Shown as illustration of target cell killing.
(MP4)

S5 Video. Time series of T6S-mediated competition during range expansion. Overnight growth on X-Gal media from an inoculum consisting of *V. cholerae* str. 2740–80 (LacZ-) and *E. coli* MG1655 (LacZ+), starting from equal concentrations of $OD_{600} = 0.5$ culture from each species. Dilution shown at bottom of each panel. 1 frame = 10 minutes; scale bar = 1mm.
(MP4)

S6 Video. Competition between T6S+ strains. Time series of simulated range expansion of two competing T6S+ strains. Initial inoculum is well-mixed and has radius $r_0 = 12$. Starting

minority (yellow) inoculum fraction is 10% (bottom), 25% (middle), and 50% (top). Attack rates are $\gamma = 0$ (left), $\gamma = 1$ (middle), and $\gamma = 2$ (right). Timestep multiplier $\lambda = 1$.
(MP4)

S1 Fig. The effect of time step on simulation error at large population in 1D. (a) Plot of simulated growth rates (y-axis) vs. predicted growth rates from Eq. S1 (x-axis) for a sensitive domain with simulation timestep multiplier $\lambda = 0.25$. Each point represents the average, over identical conditions, from 5 simulations. (b) The same plot, averaging over 20 simulations with $\lambda = 2$.
(TIF)

S2 Fig. Sensitive domain growth dynamics in 1D. (a) Comparison of simulation results (y-axis) to predicted values from Eq. S1 (x-axis) for rate of growth of a 1D sensitive domain. Points represent the average, by sensitive population, across all simulations with the same parameters (40 per condition). Color represents domain radius; black line is $y = x$. Simulation timestep multiplier $\lambda = 0.01$. (b) Heat map of the probability that a 1D sensitive domain surrounded by T6S+ competitors achieves steady growth, as a function of sensitive strain growth rate and initial radius of the sensitive domain. Dashed line indicates predicted critical parameter values based on Eq. S1. Attack rate $\tilde{\gamma} = 20$; timestep multiplier $\lambda = 0.5$. Interpolated from 1.9 million simulations.
(TIF)

S3 Fig. Sensitive domain growth dynamics in 3D. (a) Comparison of simulation results (y-axis) to predicted values from Eq. S3 (x-axis) for rate of growth of a 3D sensitive domain. Points represent the average, by sensitive population, across all simulations with the same parameters (5 per condition; $\lambda = 2.0$). Color represents domain radius; black line is $y = x$. (b) Heat map of the probability that a 3D sensitive domain surrounded by T6S+ competitors achieves steady growth, as a function of sensitive strain growth rate and initial radius of the sensitive domain. Dashed curve indicates predicted critical parameter values based on Eq. S3. Attack rate $\tilde{\gamma} = 8$; interpolated from 6,090 simulations ($\lambda = 2000$).
(TIF)

S4 Fig. Range expansion of two competing T6S+ strains. Each strain kills only individuals of the other type; the two strains are otherwise identical. Initial inoculum is well-mixed; starting minority (yellow) fraction is 25%. For each strain, the growth rate is $\alpha_t = 1$ and the attack rate is $\gamma = 2$. (a) Kymograph of a 1D competition; time is shown on the x-axis. Initial innoculum $r_0 = 500$; timestep multiplier $\lambda = 1$. (b) Center slice through a 3D competition. Initial innoculum $r_0 = 6$; timestep multiplier $\lambda = 2$.
(TIF)

S5 Fig. Fold-change in minority fraction after 10-fold growth in population of two competing T6S+ strains. For each strain, the growth rate is $\alpha_t = 1$. (a) Competition in 1D. Initial innoculum $r_0 = 500$; timestep multiplier $\lambda = 1$. (b) Competition in 3D. Initial innoculum $r_0 = 6$; timestep multiplier $\lambda = 1$.
(TIF)

S6 Fig. Time series of nutrient-limited population expansion ($K = 2$). Time points shown are $t = 0$ (left), $t = 9$ (middle), and $t = 12$ (right). Lighter color corresponds to higher nutrient concentration. Simulation scaling factor $\lambda = 100$.
(TIF)

S7 Fig. Nutrient-limited population growth. (a) Population over time for nutrient-limited growth ($K = 2$, blue) and non-limited growth (green). Simulation results shown as solid lines

(n = 50 per condition, ribbon = 1 S.E.); numerical estimate for deterministic exponential growth (Eq. S11 for limited case, simple exponential growth for non-limited) shown as dashed lines. (b) Long-time inactive fraction as a function of division capacity K. Black points: final inactive fraction after range expansion from single cell to radius r = 164 (n = 10 per condition, bar = 1 S.E.). Green line: numerical estimate (from Eq. S11 and S21) for deterministic growth. Red line: analytical prediction (Eq. S25). For all simulations, scaling factor λ = 100.
(TIF)

S8 Fig. Nutrient limitation does not qualitatively alter dynamics of simulated T6S-mediated competition. Populations begin with an equal number of T6S+ and sensitive individuals at a specified per-species population, scattered over an r_0 = 84 domain, and grow until the radius has doubled. (a) Population over time for nutrient-limited growth (K = 2, left) and non-limited growth (right). Error ribbons smaller than data curve. (b) Mean sensitive fraction over time for nutrient-limited growth (K = 2, left) and non-limited growth (right). For both panels, n = 40 per condition; scaling factor λ = 100. Ribbons = 1 S.E.
(TIF)

S9 Fig. Effect of initial T6-sensitive cluster size on dynamics of simulated T6S-mediated competition. Initial populations are placed in compact groups of m = 1, 3, or 7 individuals, and with strict separation between these clusters. Shown is final sensitive fraction as a function of initial per-species count. Populations begin with a specified per-species population, scattered over an r_0 = 84 domain, and grow until the radius has doubled. n = 90 per condition; scaling factor λ = 100. Error bars = 1 S.E.
(TIF)

S1 Table. Simulation geometries for range expansions. For range expansion simulations, all cells within a specified Manhattan distance ("Innoculum radius") are included in the founding population. The resulting population ("Innoculum population") depends on the lattice geometry.
(PDF)

S2 Table. Simulation behavior definitions.
(PDF)

S3 Table. Parameter ranges for comparison of predicted to simulated rates of sensitive strain growth.
(PDF)

S4 Table. Active population growth rates for various division capacities.
(PDF)

Acknowledgments

The authors wish to thank Simon Levin, Annie Maslan and Stephen Pacala for valuable suggestions.

Author Contributions

Conceived and designed the experiments: DBB PR MB NSW. Performed the experiments: DBB PR MB. Analyzed the data: DBB PR MB NSW. Contributed reagents/materials/analysis tools: DBB PR MB. Wrote the paper: DBB PR NSW.

References

1. Novick R, Projan SJ, Kornblum J, Ross HF, Ji G, Kreiswirth B, et al. (1995) The agr p2 operon: An autocatalytic sensory transduction system in *Staphylococcus aureus*. Mol. Gen. Genet. 248:446–458. PMID: 7565609
2. Meibom KL, Li XB, Nielsen AT, Wu CY, Roseman S, Schoolnik GK (2004) The *Vibrio cholerae* chitin utilization program. Proc. Natl. Acad. Sci. U.S.A. 101:2524–2529. doi: 10.1073/pnas.0308707101 PMID: 14983042
3. Juhas M, Eberl L, Tümmler B (2005) Quorum sensing: the power of cooperation in the world of *Pseudomonas*. Environ. Microbiol. 7:459–471. doi: 10.1111/j.1462-2920.2005.00769.x PMID: 15816912
4. Mulcahy H, Charron-Mazenod L, Lewenza S (2008) Extracellular DNA chelates cations and induces antibiotic resistance in *Pseudomonas aeruginosa* biofilms. PLOS Pathog. 4:e1000213. doi: 10.1371/journal.ppat.1000213 PMID: 19023416
5. Gore J, Youk H, Van Oudenaarden A (2009) Snowdrift game dynamics and facultative cheating in yeast. Nature 459:253–256. doi: 10.1038/nature07921 PMID: 19349960
6. Flemming HC, Wingender J (2010) The biofilm matrix. Nat. Rev. Microbiol. 8:623–633. PMID: 20676145
7. Watnick P, Kolter R (2000) Biofilm, city of microbes. J. Bacteriol. 182:2675–2679. doi: 10.1128/JB.182.10.2675-2679.2000 PMID: 10781532
8. Parsek MR, Greenberg E (2005) Sociomicrobiology: the connections between quorum sensing and biofilms. Trends Microbiol. 13:27–33. doi: 10.1016/j.tim.2004.11.007 PMID: 15639629
9. West SA, Diggle SP, Buckling A, Gardner A, Griffin AS (2007) The social lives of microbes. Annu. Rev. Ecol. Evol. Syst. 53–77. doi: 10.1146/annurev.ecolsys.38.091206.095740
10. Nadell CD, Xavier JB, Foster KR (2009) The sociobiology of biofilms. FEMS. Microbiol. Rev. 33:206–224. doi: 10.1111/j.1574-6976.2008.00150.x PMID: 19067751
11. Zoued A, Brunet YR, Durand E, Aschtgen MS, Logger L, Douzi B, et al. (2014) Architecture and assembly of the Type VI secretion system. Biochim. Biophys. Acta 1843(8):1664–73. doi: 10.1016/j.bbamcr.2014.03.018 PMID: 24681160
12. Basler M. Type VI secretion system: secretion by a contractile nanomachine. Philos. Trans. R. Soc. Lond. B. Biol. Sci. 370:20150021. doi: 10.1098/rstb.2015.0021 PMID: 26370934
13. Pukatzki S, Ma AT, Revel AT, Sturtevant D, Mekalanos JJ (2007) Type VI secretion system translocates a phage tail spike-like protein into target cells where it cross-links actin. Proc. Natl. Acad. Sci. U.S.A. 104:15508–15513. doi: 10.1073/pnas.0706532104 PMID: 17873062
14. Leiman PG, Basler M, Ramagopal UA, Bonanno JB, Sauder JM, Burley SK, et al. (2009) Type VI secretion apparatus and phage tail-associated protein complexes share a common evolutionary origin. Proc. Natl. Acad. Sci. U.S.A. 106:4154–4159. doi: 10.1073/pnas.0813360106 PMID: 19251641
15. Kanamaru S (2009) Structural similarity of tailed phages and pathogenic bacterial secretion systems. Proc. Natl. Acad. Sci. U.S.A. 106:4067–4068. doi: 10.1073/pnas.0901205106 PMID: 19276114
16. Pell LG, Kanelis V, Donaldson LW, Howell PL, Davidson AR (2009) The phage λ major tail protein structure reveals a common evolution for long-tailed phages and the type VI bacterial secretion system. Proc. Natl. Acad. Sci. U.S.A. 106:4160–4165. doi: 10.1073/pnas.0900044106 PMID: 19251647
17. Kudryashev M, Wang RYR, Brackmann M, Scherer S, Maier T, Baker D, et al. (2015) Structure of the Type VI secretion system contractile sheath. Cell 160:952–962. doi: 10.1016/j.cell.2015.01.037 PMID: 25723169
18. Pukatzki S, Ma AT, Sturtevant D, Krastkins B, Sarracino D, Nelson WC, et al. (2006) Identification of a conserved bacterial protein secretion system in *Vibrio cholerae* using the *Dictyostelium* host model system. Proc. Natl. Acad. Sci. U.S.A. 103:1528–1533. doi: 10.1073/pnas.0510322103 PMID: 16432199
19. Basler M, Pilhofer M, Henderson G, Jensen G, Mekalanos J (2012) Type VI secretion requires a dynamic contractile phage tail-like structure. Nature 483:182–186. doi: 10.1038/nature10846 PMID: 22367545
20. Schneider MM, Buth SA, Ho BT, Basler M, Mekalanos JJ, Leiman PG (2013) PAAR-repeat proteins sharpen and diversify the type VI secretion system spike. Nature 500:350–353. doi: 10.1038/nature12453
21. Ho BT, Dong TG, Mekalanos JJ (2014) A view to a kill: the bacterial type VI secretion system. Cell Host Microbe 15:9–21. doi: 10.1016/j.chom.2013.11.008 PMID: 24332978
22. Durand E, Nguyen VS, Zoued A, Logger L, Péhau-Arnaudet G, Aschtgen MS, et al. (2015) Biogenesis and structure of a type VI secretion membrane core complex. Nature 523:555–560. doi: 10.1038/nature14667 PMID: 26200339

23. Ma AT, Mekalanos JJ (2010) In vivo actin cross-linking induced by *Vibrio cholerae* type VI secretion system is associated with intestinal inflammation. Proc. Natl. Acad. Sci. U.S.A. 107:4365–4370. doi: 10.1073/pnas.0915156107 PMID: 20150509
24. Russell AB, Hood RD, Bui NK, LeRoux M, Vollmer W, Mougous JD (2011) Type VI secretion delivers bacteriolytic effectors to target cells. Nature 475:343–347. doi: 10.1038/nature10244 PMID: 21776080
25. Zheng J, Ho B, Mekalanos JJ (2011) Genetic analysis of anti-amoebae and anti-bacterial activities of the type VI secretion system in *Vibrio cholerae*. PLOS ONE 6:e23876. doi: 10.1371/journal.pone.0023876 PMID: 21909372
26. Russell AB, Singh P, Brittnacher M, Bui NK, Hood RD, Agnello DM, et al. (2012) A widespread bacterial type VI secretion effector superfamily identified using a heuristic approach. Cell Host Microbe 11:538–549. doi: 10.1016/j.chom.2012.04.007 PMID: 22607806
27. Basler M, Ho BT, Mekalanos JJ (2013) Tit-for-tat: type VI secretion system counterattack during bacterial cell-cell interactions. Cell 152:884–894. doi: 10.1016/j.cell.2013.01.042 PMID: 23415234
28. Russell AB, Peterson SB, Mougos JD (2014) Type VI secretion system effectors: poisons with a purpose. Nat. Rev. Microbiol. 12:137–148. doi: 10.1038/nrmicro3185 PMID: 24384601
29. Schwarz S, West TE, Boyer F, Chiang WC, Carl MA, Hood RD, et al. (2010) *Burkholderia* type VI secretion systems have distinct roles in eukaryotic and bacterial cell interactions. PLOS Pathog. 6: e1001068. doi: 10.1371/journal.ppat.1001068 PMID: 20865170
30. Boyer F, Fichant G, Berthod J, Vandenbrouck Y, Attree I (2009) Dissecting the bacterial type VI secretion system by a genome wide in silico analysis: what can be learned from available microbial genomic resources? BMC genomics 10:104. doi: 10.1186/1471-2164-10-104 PMID: 19284603
31. Smith T, Huston M (1990) A theory of the spatial and temporal dynamics of plant communities. Progress in Theoretical Vegetation Science, eds Grabherr G, Mucina L, Dale MB, Ter Braak CJF (Kluwer, Dordrecht) 49–69.
32. Moreira J, Deutsch A (2002) Cellular automaton models of tumor development: a critical review. Adv. in Complex Syst. 5:247–267. doi: 10.1142/S0219525902000572
33. Grimm V (2005) Individual-based modeling and ecology. (Princeton University Press, Princeton).
34. White SH, del Rey AM, Sánchez GR (2007) Modeling epidemics using cellular automata. Appl. Math. Comput. 186:193–202. doi: 10.1016/j.amc.2006.06.126
35. Hellweger FL, Bucci V (2009) A bunch of tiny individuals–individual-based modeling for microbes. Ecol. Model. 220:8–22. doi: 10.1016/j.ecolmodel.2008.09.004
36. Lardon LA, Merkey BV, Martins S, Dötsch A, Picioreanu C, Kreft JU, et al. (2011) iDynoMiCS: next-generation individual-based modelling of biofilms. Environ. Microbiol. 13:2416–2434. doi: 10.1111/j.1462-2920.2011.02414.x PMID: 21410622
37. Jang SS, Oishi KT, Egbert RG, Klavins E (2012) Specification and simulation of synthetic multicelled behaviors. ACS Synth. Biol. 1:365–374. doi: 10.1021/sb300034m PMID: 23651290
38. Borenstein DB, Meir Y, Shaevitz JW, Wingreen NS (2013) Non-local interaction via diffusible resource prevents coexistence of cooperators and cheaters in a lattice model. PLOS ONE 8:e63304. doi: 10.1371/journal.pone.0063304 PMID: 23691017
39. Emonet T, Macal CM, North MJ, Wickersham CE, Cluzel P (2005) AgentCell: a digital single-cell assay for bacterial chemotaxis. Bioinformatics 21:2714–2721. doi: 10.1093/bioinformatics/bti391 PMID: 15774553
40. Axelrod R, Hamilton WD (1981) The evolution of cooperation. Science 211:1390–1396. doi: 10.1126/science.7466396 PMID: 7466396
41. Axelrod R (1984) The evolution of cooperation. (Basic Books, New York).
42. Nowak MA, May RM (1992) Evolutionary games and spatial chaos. Nature 359:826–829. doi: 10.1038/359826a0
43. Axelrod R (1997) The complexity of cooperation: agent-based models of competition and collaboration. (Princeton University Press, Princeton, N.J).
44. Hauert C, Doebeli M (2004) Spatial structure often inhibits the evolution of cooperation in the snowdrift game. Nature 428:643–646. doi: 10.1038/nature02360 PMID: 15074318
45. Goldsby HJ, Dornhaus A, Kerr B, Ofria C (2012) Task-switching costs promote the evolution of division of labor and shifts in individuality. Proc. Natl. Acad. Sci. U.S.A. 109:13686–13691. doi: 10.1073/pnas.1202233109 PMID: 22872867
46. Schindelin J, Arganda-Carreras I, Frise E, Verena K, Longair M, Pietzsch T, et al. (2012) Fiji: an open-source platform for biological-image analysis. Nature Methods 9(7): 676–682. doi: 10.1038/nmeth.2019 PMID: 22743772

47. Borenstein D (2015) Nanoverse: a constraints-based declarative framework for rapid agent-based modeling. Proceedings of the 2015 Winter Simulation Conference (in press).

48. Hofbauer J, Sigmund K (1998) Evolutionary Games and Population Dynamics. Cambridge University Press, New York.

49. Matsuda H, Ogita N, Sasaki A, Sato K (1992) Statistical Mechanics of Population: The Lattice Lotka-Volterra Model. Prog. Theor. Phys. 88(6):1035–1049. doi: 10.1143/ptp/88.6.1035

50. Frank SA (1994) Spatial polymorphism of bacteriocins and other allelopathic traits. Evol. Ecol. 8:369–386. doi: 10.1007/BF01238189

51. Cascales E, Buchanan SK, Duché D, Kleanthous C, Lloubès R, Postle K, et al. (2007) Colicin biology. Microbiol. Mol. Biol. R. 71(1):158–229. doi: 10.1128/MMBR.00036-06

52. Chao L, Levin BR (1981) Structured habitats and the evolution of anticompetitor toxins in bacteria. Proc. Natl. Acad. Sci. U.S.A. 78(10):6324–6328. doi: 10.1073/pnas.78.10.6324 PMID: 7031647

53. Iwasa Y, Nakamaru M, Levin SA (1998) Allelopathy of bacteria in a lattice population: Competition between colicin-sensitive and colicin-producing strains. Evol. Ecol. 12(7):785–802. doi: 10.1023/A:1006590431483

54. Sih A (1987) Prey refuges and predator-prey stability. Theor. Popul. Biol. 31(1):1–12. doi: 10.1016/0040-5809(87)90019-0

55. Hallatschek O, Hersen P, Ramanathan S, Nelson DR (2007) Genetic drift at expanding frontiers promotes gene segregation. Proc. Natl. Acad. Sci. U.S.A. 104:19926–19930. doi: 10.1073/pnas.0710150104 PMID: 18056799

56. Korolev K, Avlund M, Hallatschek O, Nelson DR (2010) Genetic demixing and evolution in linear stepping stone models. Rev. Mod. Phys. 82:1691. doi: 10.1103/RevModPhys.82.1691 PMID: 21072144

57. Stewart PS (2003) Diffusion in biofilms. J. Bacteriol. 185:1485–1491. doi: 10.1128/JB.185.5.1485-1491.2003 PMID: 12591863

58. Bernard CS, Brunet YR, Gueguen E, Cascales E (2010) Nooks and crannies in type VI secretion regulation. J. Bacteriol. 192:3850–3860. doi: 10.1128/JB.00370-10 PMID: 20511495

59. Zheng J, Shin OS, Cameron DE, Mekalanos JJ (2010) Quorum sensing and a global regulator TsrA control expression of type VI secretion and virulence in *Vibrio cholerae*. Proc. Natl. Acad. Sci. U.S.A. 107:21128–21133. doi: 10.1073/pnas.1014998107 PMID: 21084635

60. Borgeaud S, Metzger L, Scrignari T, Blokesch M (2015) The type VI secretion system of *Vibrio cholerae* fosters horizontal gene transfer. Science 347:63–67. doi: 10.1126/science.1260064 PMID: 25554784

61. Miller MB, Skorupski K, Lenz DH, Taylor RK, Bassler BL (2002) Parallel quorum sensing systems converge to regulate virulence in *Vibrio cholerae*. Cell 110:303–314. doi: 10.1016/S0092-8674(02)00829-2 PMID: 12176318

62. Lesic B, Starkey M, He J, Hazan R, Rahme LG (2009) Quorum sensing differentially regulates *Pseudomonas aeruginosa* type VI secretion locus I and homologous loci II and III, which are required for pathogenesis. Microbiology 155:2845–2855. doi: 10.1099/mic.0.029082-0 PMID: 19497948

63. LeRoux M, De Leon JA, Kuwada NJ, Russell AB, Pinto-Santini D, Hood RD, et al. (2012) Quantitative single-cell characterization of bacterial interactions reveals type VI secretion is a double-edged sword. Proc. Natl. Acad. Sci. U.S.A. 109:19804–19809. doi: 10.1073/pnas.1213963109 PMID: 23150540

64. LeRoux M, Kirkpatrick RL, Montauti EI, Tran BQ, Peterson SB, Harding BN, et al. (2015) Kin cell lysis is a danger signal that activates antibacterial pathways of *Pseudomonas aeruginosa*. eLife 10.7554.

65. Kass-Simon G, Scappaticci A Jr (2002) The behavioral and developmental physiology of nematocysts. Can. J. Zool. 80:1772–1794. doi: 10.1139/z02-135

66. Holstein T, Tardent P (1984) An ultrahigh-speed analysis of exocytosis: nematocyst discharge. Science 223:830–833. doi: 10.1126/science.6695186 PMID: 6695186

67. Lang J (1971) Interspecific aggression by scleractinian corals. 1. the rediscovery of *Scolymia cubensis* (Milne Edwards & Haime). Bull. Mar. Sci. 21:952–959.

Supplementary Data:

The supplementary data may be found in the appendix.

S1 Video. T6S-mediated interactions between bacteria.
Competition between *V. cholerae* str. 2740–80 (sheath labeled with GFP) and *E. coli* MG1655 (unlabeled). 60 frames; frames are 30s apart.
(available at: https://doi.org/10.1371/journal.pcbi.1004520.s004)

S2 Video. A simple spatial model of T6S-driven community dynamics.
Time series of simulated competitions between a T6S+ strain (red) and a sensitive strain (blue) during a range expansion in 2D. In all cases the T6S+ growth rate is $\alpha_t = 1$, and the sensitive strain growth rate is $\alpha_s = 4$. Initial sensitive strain fractions are 0.1 (upper) and 0.5 (lower). Attack rates are $\gamma = 5$ (left) and 15 (right). Timestep multiplier $\lambda = 1$.
(available at: https://doi.org/10.1371/journal.pcbi.1004520.s005)

S3 Video. Critical domain size for sensitive strain survival.
Time series of a simulated range expansion of a sensitive strain subject to stochastic killing at the outer boundary of the colony. Initial colony radius varies from $r_0 = 4$ (left) to $r_0 = 7$ (right). The growth rate is $\alpha_s = 4$ and the killing rate at the outer boundary is $\tilde{\gamma} = 8$. Timestep multiplier $\lambda = 1$.
(available at: https://doi.org/10.1371/journal.pcbi.1004520.s006)

S4 Video. Community dynamics between T6S+ and T6S-sensitive populations.
Fluorescent micrograph of competition between T6S+ *V. cholerae* and T6S-sensitive *E. coli* (see Fig 4e). two fields, 60 frames; frames are 20s apart. Shown as illustration of target cell killing.
(available at: https://doi.org/10.1371/journal.pcbi.1004520.s007)

S5 Video. Time series of T6S-mediated competition during range expansion.
Overnight growth on X-Gal media from an inoculum consisting of *V. cholerae* str. 2740-80 (LacZ-) and *E. coli* MG1655 (LacZ+), starting from equal concentrations of $OD_{600} = 0.5$ culture from each species. Dilution shown at bottom of each panel. 1 frame = 10 minutes; scale bar = 1mm.
(available at: https://doi.org/10.1371/journal.pcbi.1004520.s008)

S6 Video. Competition between T6S+ strains.
Time series of simulated range expansion of two competing T6S+ strains. Initial inoculum is well-mixed and has radius $r_0 = 12$. Starting minority (yellow) inoculum fraction is 10% (bottom), 25% (middle), and 50% (top). Attack rates are $\gamma = 0$ (left), $\gamma = 1$ (middle), and $\gamma = 2$ (right). Timestep multiplier $\lambda = 1$.
(available at: https://doi.org/10.1371/journal.pcbi.1004520.s009)

Chapter III

Discussion and Outlook

III.1 Discussion and outlook

The recently discovered T6SS has become an important player in the field of microbial interactions. Initially described to participate in the interaction with eukaryotic hosts it has become apparent that the T6SS also plays a crucial role in interbacterial interactions (Alteri and Mobley, 2016; Hachani et al., 2016). In fact, the interbacterial competition may contribute to the virulence towards a host (Fu et al., 2013; Ma et al., 2014; Sana et al., 2016) or protect a host from pathogens by their outcompetition (Hecht et al., 2016). The T6SS not only fosters inter-species, but also intra-species competition allowing for a discrimination between closely related species which may facilitate territorial behavior (Alteri et al., 2013; Hecht et al., 2016; Unterweger et al., 2014; Wenren et al., 2013). The diversity of processes to which the T6SS contributes is also reflected in the effector repertoire (Alcoforado Diniz et al., 2015; Hachani et al., 2016). However, the role of only few effectors was experimentally validated and even less effectors were biochemically characterized. Moreover, as described in the introduction, the canonical proteobacterial T6SS consists of 13 conserved core components, the role of which has been addressed in great detail (Alteri and Mobley, 2016; Boyer et al., 2009; Lin et al., 2013; Shalom et al., 2007; Weber et al., 2016; Zheng and Leung, 2007; Zheng et al., 2011). However, there are proteobacterial T6SSs which lack conserved core components, usually regarded to be essential (Boyer et al., 2009; Weber et al., 2013). Understanding how these T6SSs compensate for the loss of such a component may help elucidate the role of the conserved component.

III.1.1 Characterization of the T6SS in *A. baylyi* ADP1

At the beginning of this thesis the antibacterial T6SS of *A. baylyi* ADP1 had just been described, but the effector repertoire remained unknown (Basler et al., 2013; Shneider et al., 2013; Weber et al., 2013). Furthermore, *A. baylyi* ADP1 lacks the conserved outer membrane protein TssJ (Weber et al., 2013). Therefore, we set out to functionally characterize both the T6SS as well as the effector repertoire of *A. baylyi* ADP1.

Although shown to secrete Hcp constitutively, the dynamics of the T6SS in *A. baylyi* ADP1 had not yet been described (Basler et al., 2013; Shneider et al., 2013; Weber et al., 2013). Fluorescence microscopy of the T6SS in different organisms had revealed various modes of T6SS activity. The most direct observation was made by imaging fluorescently labeled VipA sheath dynamics (Basler et al., 2012). Also fluorescently labeled ClpV was used, which was later realized to be a proxy for sheath contractions (Basler and Mekalanos, 2012;

Mougous et al., 2006). This revealed the random deployment of the T6SS, exemplified by *V. cholerae*, and the intricate tit-for-tat retaliation strategy employed by *P. aeruginosa* (Basler et al., 2012, 2013). In *A. baylyi* ADP1 we observed a seemingly random deployment of the T6SS similar to what had been described for *V. cholerae* (see Fig. II.1.1) (Basler et al., 2012). However, unlike *V. cholerae* there were only one to three active sheaths which immediately contracted after polymerization (Basler et al., 2012). Interestingly, there were also sheaths which did not stop polymerizing when encountering the opposite side of the cell, but rather kept polymerizing and bending the structure.

As expected, the T6SS dynamics were abolished in both the TssM and the Hcp deficient strains (see Fig. II.1.2). However, the TssE deficient strain was still capable of forming small dynamic foci associated with the membrane, but neither Hcp secretion nor the reduction of prey recovery or its lysis were detected. Therefore, it is not possible to deduce that these foci constitute small but functional T6SS (see Fig. II.1.2). It should be noted, that the formation of functional T6SSs in absence of TssE has been observed in *V. cholerae* (Basler et al., 2012; Vettiger and Basler, 2016; Zheng et al., 2011). It is unclear how the T6SS forms in absence of TssE, which is thought to be a key component of the baseplate and to form the foundation for the contractile sheath (Basler et al., 2012; Brackmann et al., 2017a; Leiman et al., 2009; Lossi et al., 2011). It may be possible, that interactions with the peripheral baseplate components are sufficient for the formation of the contractile tail in *V. cholerae*.

As mentioned in the introduction, the T6SS of *A. baylyi* ADP1 is constitutively active under the conditions tested, despite the presence of TagF, which was found to act as a posttranslational repressor of the T6SS in *P. aeruginosa* (Basler et al., 2013; Shneider et al., 2013; Silverman et al., 2011; Weber et al., 2013, 2016). Furthermore, *A. baylyi* ADP1 does not encode an ortholog of Fha which is essential for the activation of the T6SS in *P. aeruginosa* upon TagF derepression (Silverman et al., 2011; Weber et al., 2013). The recently obtained RNA sequencing data revealed that *tagF* is actively transcribed (see section II.2.1). Nevertheless, we were unable to detect a phenotype of the TagF deficient strain in any of our assays (see Fig. II.1.2), although another study recently observed an increase in Hcp secretion (Weber et al., 2016). Thus, the role of TagF remains to be elucidated. Since TagF is thought to act as a posttranslational repressor it may be interesting to perform a pulldown or co-immuno precipitation assay to identify its interaction partners.

Although it cannot be ruled out that the protein is not functional in *A. baylyi* ADP1, these findings may have implications for other T6SSs bearing a TagF ortholog.

In agreement with previous results, TagN, which is thought to anchor the T6SS to the peptidoglycan (Aschtgen et al., 2010a), was found to be dispensable for T6SS activity (see Fig. II.1.2) (Weber et al., 2016). This result is supported by the recent observation that peptidoglycan is dispensable for T6SS activity in *V. cholerae* (Vettiger et al., 2017). However, it should be noted that *V. cholerae* is naturally devoid of any putative T6SS associated peptidoglycan anchoring protein (Aschtgen et al., 2010a). Moreover, even though TagN is dispensable, we observed a significant decrease in the number of active T6SSs in its absence (see Fig. II.1.2), whereas another study found an increase in Hcp secretion (Weber et al., 2016). Nonetheless, the sheath dynamics were not affected (see Fig. II.1.2). Although one would expect that such a powerful injection system should be anchored to the peptidoglycan, the membrane anchoring seems to be sufficient (Vettiger et al., 2017).

The recently discovered TagX, which is thought to locally degrade the peptidoglycan, enabling the envelope spanning complex to assemble, was described to be essential for Hcp secretion (Weber et al., 2016). Nevertheless, the fluorescence microscopy revealed that T6SS structures are occasionally forming and that those display wild type like sheath dynamics (see Fig. II.1.2). Additionally, the sensitive CPRG lysis assay confirmed that the assemblies are functional. This may indicate that large enough transient peptidoglycan pores form during ageing or remodelling of the peptidoglycan which allow the envelope spanning complex to assemble. To test this hypothesis, it may be interesting to inhibit peptidoglycan synthesis in absence of TagX which should result in more pores and thus in a higher number of active T6SSs.

The phenotype of the ACIAD2685 deficient strain mimicked that of the TagX deficient strain. Bioinformatic analysis only identified two putative N-terminal transmembrane helices and predicted that both the N- and C-termini reside in the cytoplasm. A previous study found ACIAD2685 to be essential for Hcp secretion confirming our result (Weber et al., 2016). The fluorescence microscopy revealed that the few T6SS structures formed had wild type like sheath dynamics suggesting that ACIAD2685 is likely involved in a step upstream of the sheath formation (see Fig. II.1.2). However, the role of ACIAD2685 remains elusive. Likely, the C-terminal part carries the functional domain, therefore it may

be interesting to determine its subcellular localization which may hint at whether ACIAD2685 contributes to a cytoplasmic process, such as the formation of the baseplate, or a periplasmic process.

Two *Acinetobacter* specific components, ACIAD2693 and ACIAD2698, were dispensable for T6SS activity (see Fig. II.1.2). A previous study reported that ACIAD2693 is essential for Hcp secretion, however, this is likely the result of a polar effect of the Tdk-Kan^R cassette, used for insertional mutagenesis, on the downstream VipA (Weber et al., 2016). The ACIAD2693 deficient strain displayed a reduced number of sheath assemblies the dynamics of which remained unaltered (see Fig. II.1.2). It is a predicted periplasmic protein and seemingly acts upstream of the sheath assembly, but its function remains unknown. The absence of the predicted membrane protein ACIAD2698 was reported to lead to a higher Hcp secretion (Weber et al., 2016). Nevertheless, in our assays the ACIAD2698 deficient strain was indistinguishable from the parental strain precluding a functional prediction.

It is noteworthy that both the fluorescence microscopy of the sheath dynamics and the CPRG assay are considerably more sensitive than the commonly employed Hcp secretion assay or the quantitative competition assay. Because the CPRG assay is highly sensitive, it also saturates at medium T6SS activity leaving the fluorescence microscopy as the method with the highest sensitivity and range (see Fig. II.1.2). It is therefore advisable to perform both the CPRG assay as well as the imaging of sheath dynamics to assign functions of T6SS components.

As part of observing the T6SS dynamics we also tried to visualize the actual T6SS injection and secretion events by labeling Hcp. Although we employed various strategies of both chemical as well as fluorescent protein labeling we were so far unsuccessful (see section II.2.2). However, the adaptation of different labeling protocols and plasmids may not only enable us to label Hcp, but might also yield a valuable tool to label other proteins in the less common model bacteria.

Although the T6SS activity in *A. baylyi* ADP1 is apparently random, other members of the group and myself have also observed some seemingly non-random activity, especially pronounced in less active mutants when imaged at lower cell density. In these strains the T6SS structures appeared to preferentially form at cell contact sites. However, since the neighboring cell also formed structures at this site it is unclear whether cell contact or cell

damage by another T6SS may act as a signal. Possibly, the random activity observed at high cell density is caused by triggering the signal all along the cell surface. However, unlike the retaliation in *P. aeruginosa* (Basler et al., 2013) also single *A. baylyi* ADP1 cells constitutively deploy their T6SS, suggesting that there is a random component to the activity. Currently there is no quantitation of the randomness of these events, but further investigation with a more automated image analysis may yield statistically significant numbers. Furthermore, we would like to understand the underlying molecular mechanism should there exist a trigger. Recently, the *in situ* structure of the T6SS in *Myxococcus xanthus* was solved by cryo-ET which also revealed bacteriophage tail fiber-like antennae (Chang et al., 2017). Although their role remains to be elucidated one might speculate that these tail fibers could be involved in such a contact dependent triggering of the T6SS. However, unlike the tail fibers in contractile bacteriophages these would not trigger the contraction of the sheath but rather induce the formation of a T6SS structure.

III.1.2 The T6SS effector repertoire of *A. baylyi* ADP1

We identified five antibacterial T6SS cargo effectors in *A. baylyi* ADP1 by virtue of their genetic linkage to spike components, one of which was disrupted by an IS1236 insertion element and could be restored (see Figs. II.1.3, II.1.5, S II.1.1 and S II.1.2). Additionally, the corresponding immunity proteins were identified and verified (see Fig. II.1.5). All of these are encoded in close proximity of their corresponding effector (see Fig. S II.1.1). The genes encoding the immunity proteins for Tse1 and Tse2 had undergone gene duplication events. Such duplications seem to be common and are thought to contribute to the resistance towards diverging effectors arising in the population (Kirchberger et al., 2017; Zhang et al., 2012). Indeed, we found up to five paralogous immunity proteins consecutively encoded downstream of a *tse2* ortholog in *Klebsiella pneumoniae* W14 (see Fig. S II.1.3). In some cases all of the paralogous immunity proteins contribute to the immunity (Jiang et al., 2014; Ma et al., 2017; Russell et al., 2013; Salomon et al., 2015). So far, we used strains lacking both paralogous immunity proteins, but it may be interesting to determine the contribution of the individual immunity proteins. None of the five effector immunity pairs cross react (see Fig. II.1.5).

An effector deficient strain was constructed which retained an unaltered T6SS activity but failed to permeabilize or inhibit *E. coli* as indicated by the quantitative competition assay, the CPRG assay and the competition microscopy (see Fig. II.1.3). Interestingly, the effector deficient strain was still capable of eliciting the retaliatory attack by *P. aeruginosa* PAO1

indicating that it is still able to inflict some damage in the target cell (see Fig. II.1.4) (Basler et al., 2013; Ho et al., 2013; Wilton et al., 2016). When comparing the transcriptomes of *E. coli* competed against a T6SS inactive TssM deficient *A. baylyi* ADP1 and against the effector deficient strain, we were unable to identify differentially regulated genes (see section II.2.1). This result still has to be confirmed by a biological replicate, nonetheless, taken together, these observations indicate that mere puncturing of the cell envelope by the T6SS is harmless to bacteria. This unexpected result is consistent with the observation that even multiple puncturing of diderm bacteria with an AFM tip did not affect their viability (Suo et al., 2009). The effector deficient strain may be useful to construct and test custom tailored chimeric effectors.

For three of the identified effectors the putative activity could be predicted by bioinformatic analysis (see Fig. S II.1.1). Tpe1 carries a neutral zinc metallopeptidase active site, Tae1 likely constitutes a peptidoglycan amidase and Tle1 is predicted to belong to the family 4 of T6SS associated phospholipases (Russell et al., 2013). Tpe1 did not affect *E. coli*, but was able to reduce the recovery of the non-immune *A. baylyi* ADP1 (see Figs. II.1.3 and II.1.5), suggesting that Tpe1 is secreted and functional, however, *E. coli* is resistant to its activity. Conducting a zymography with Tpe1 may help elucidate its target. The putative metallopeptidase active site indicates that Tpe1 may also be involved in the cleavage of peptidoglycan but seemingly not that of *E. coli*.

Consistent with its predicted peptidoglycan amidase activity, Tae1 induced the expected cell rounding and bursting usually observed for peptidoglycan targeting effectors (see Fig. II.1.3) (Dong et al., 2013). Further biochemical assays are needed to determine the cleavage site engaged by Tae1 which does not share homology with any of the four T6SS peptidoglycan amidase families currently identified (Russell et al., 2012).

In agreement with its predicted phospholipase activity, Tle1 also induces the lysis of prey bacteria (see Fig. II.1.3) (Russell et al., 2013). Interestingly, we observed that the targeted prey cell first shrinks and then abruptly reinflates coinciding with its lysis as indicated by SYTOX® Blue (see Fig. II.1.3). Recently it has been demonstrated that a T6SS phospholipase can liberate soluble lipolysis products, reducing the surface pressure of a phospholipid monolayer (Flaugnatti et al., 2016). The release of soluble lipolysis products may explain the shrinkage of the cells caused by the reduction of available phospholipids and thereby cell size. However, during the shrinkage the cells remain impermeable to

SYTOX® Blue, indicating that the solute concentration inside the cell increases, which in turn increases the turgor. It is unclear how the cell is capable of shrinking without lysing although the increasing turgor is no longer held by the peptidoglycan. So far, no member of the family 4 of T6SS phospholipases has been biochemically characterized, thus it may be interesting to determine the cleavage site of Tle1 (Russell et al., 2013).

No conserved domains or motifs could be predicted for the remaining effectors, Tse1 and Tse2, with the exception of a low quality match to short-chain dehydrogenases/reductases active sites for Tse1 (see Fig. S II.1.1). Interestingly, Tse1 harbors four predicted transmembrane helices as do its immunity proteins. Different lysis phenotypes were observed for Tse1, one resembling that of Tae1, the other was similar to that induced by Tle1, both of which took significantly longer than observed for Tae1 and Tle1 (see Fig. II.1.3). It is unclear which subcellular target Tse1 has, but according to an HHPred (Alva et al., 2016) analysis it shares weak homologies with ionophoric colicins spanning the region of three predicted transmembrane helices. However, the observed lysis phenotypes suggest that Tse1 is not just acting as a ionophore. The RNA sequencing data from the single effector competition did not yield an obvious candidate to follow up on (see section II.2.1). Thus, it may help to dissect the contributions of the N-terminal part and the transmembrane helices bearing C-terminal part with a special focus on an enzymatic activity of the N-terminal part. If acting as a colicin like ionophore, similar to VasX, the toxicity should require a translocation to the periplasm which may also be tested (Miyata et al., 2013).

Apart from a prior report, which identified a Tse2 homolog to constitute an antibacterial effector, the subcellular target of Tse2 remains elusive (Weber et al., 2016). The only hint is the putative periplasmic localization of the two immunity proteins, suggesting that its target is accessible from the periplasm. Although the Tse2 single effector strain reduced the recovery of *E. coli* significantly, the CPRG assay indicated that only very little lysis is occurring, which was confirmed by the competition microscopy (see Fig. II.1.3). The morphology of the slowly permeabilizing cells did not change significantly, however, a bright SYTOX® Blue stained spot formed in the cell which may indicate the compaction of the nucleoid (see Fig. II.1.3), regarded to be a general stress response of bacteria (Shechter et al., 2013). The RNA sequencing data revealed that the transcriptional response of the prey cells was similar to that elicited by the phospholipase Tle1 (see section II.2.1), however, the data did not reveal a discernable candidate to follow up on.

III.1.3 The contribution of the T6SS to horizontal gene transfer

As elaborated in the introduction, the T6SS of *V. cholerae* has been demonstrated to be involved in the acquisition of genetic material from prey cells and is even part of the competence regulon (Borgeaud et al., 2015). *A. baylyi* ADP1 is also naturally competent, but unlike *V. cholerae* retains this state throughout most of its growth (Juni and Janik, 1969; Palmen et al., 1992, 1993). Thus, we reasoned, that the T6SS in *A. baylyi* ADP1 may also contribute to horizontal gene transfer. Since we identified three lytic and one non-lytic T6SS effector in *A. baylyi* ADP1, we set out to determine the contribution of the T6SS and the lysis phenotype towards horizontal gene transfer. Indeed, we found that the lysis of sensitive strains by the T6SS facilitated horizontal gene transfer (see Fig. II.1.6). Moreover, the lysis of prey bacteria by Tle1 yielded a higher number of transformants than when the prey cells were inhibited by Tse2, even though Tse2 reduced the number of viable prey cells to a greater extent than Tle1 (see Fig. II.1.6). These results indicate, that lytic effectors are beneficial for horizontal gene transfer, likely because they liberate the genomic DNA making it accessible for the subsequent uptake.

Intra-species competition of *V. cholerae* is fostered by different T6SS effector sets which may be expanded or changed by exchanging effectors or acquiring new effector modules from competitors (Kirchberger et al., 2017; Thomas et al., 2017; Unterweger et al., 2014). This process is facilitated by the T6SS (Thomas et al., 2017). Some clinically relevant *A. baumannii* strains, which are close relatives of *A. baylyi* ADP1, are also known to be naturally competent and may carry a T6SS (Ramirez et al., 2010; Weber et al., 2017). Therefore, it is appealing to speculate that similar processes may contribute to the spread of antibiotic resistances among these strains (Lin and Lan, 2014). In fact, the intra-species competition may be especially suited for this purpose, because of the high sequence similarity shared between the strains, which facilitates the incorporation of the acquired genetic material by homologous recombination. Moreover, it may be beneficial to acquire genes from related species which have adapted to the niche. Some *A. baumannii* strains inject a DNAse effector which may preclude or reduce horizontal gene transfer (Weber et al., 2016). Thus, it could be interesting to investigate whether the presence of a DNAse effector reduces the horizontal gene transfer frequency.

Taken together, our data expands the applicability of the T6SS mediated horizontal gene transfer from *V. cholerae* to other naturally competent species carrying an antibacterial

T6SS. Furthermore, we could demonstrate, that the effector set significantly influences the horizontal gene transfer frequency with lytic effectors being beneficial.

III.1.4 Modelling of interbacterial competitions

Apart from trying to understand the mechanism of the T6SS we were also interested in how the T6SS mediated interbacterial competition contributes to population dynamics.

Quantitative competition assays with a T6SS sensitive prey strain are commonly used to determine the T6SS activity of the predator strain. These assays have been performed at various ratios and densities of the competitors (Basler et al., 2013; Hachani et al., 2013). While conducting such experiments it was noticed, that the sensitive prey strain could survive and form distinct colonies within the predator domain. When isolated and competed against the predator again, the prey strain did not exhibit increased resistance, indicating, that the cause for survival was not an inheritable resistance towards the predator (unpublished). This intriguing observation led us to investigate the reason for the survival of the prey strain.

To derive a more general description for this type of interaction, a mathematical modelling approach, based on individual-based models (IBMs), was chosen (see research article II). The models consisted of different entities occupying a position on a regular grid. These entities behave according to a specific rule set which defines growth, T6SS activity and resistance as well as the lysis behavior (for a complete description see section IV.1 Simulation details). In a model, where a sensitive prey strain and a T6SS active predator with random targeting activity were competed, the prey strain could survive depending on the initial degree of mixing. This observation may be explained as follows: The T6SS mediated killing of a target cell is contact dependent, therefore, prey cells residing behind other prey cells are protected from the attack. When a population starts out homogeneously mixed at a high space occupancy, most prey cells are in contact with a predator and may be killed. Is the initial space occupancy not as dense, the prey and predator strains first form microcolonies before encountering one another. The same is achieved when the population is not homogeneously mixed. During the competition the population segregates into domains consisting only of the predator or the prey thereby minimizing the contact surface at which the killing occurs. This behavior is comparable to the unmixing of oil and water where dispersed oil droplets will form continuous domains in order to minimize the contact surface. Since the killing can only occur at the surface, the prey can achieve net growth in

face of attack when the growth within the domain outweighs the killing on the surface. Indeed, the model was able to predict a critical domain radius beyond which the prey would survive the attack and possibly even outgrow the predator. This critical domain radius depends both on the growth rate ratio between the prey and the predator as well as the attack rate. Furthermore, the outcome of such a competition is only mildly affected by nutrient limitation.

By competing the prey *E. coli* MG1655 Gent^R against the predator *V. cholerae* 2740-80 at different ratios and different initial densities we were able to confirm these results obtained by modelling. These assays also demonstrated that it is imperative to conduct competition assays at high cell densities when aiming to determine the antibacterial T6SS activity of a predator.

Additionally, the modelling of the competition of two equivalent T6SS active populations, which could kill one another, showed that the more numerous strain would outcompete the minority suggesting that the T6SS is beneficial for defending an established population. This model also demonstrated that the competitors would segregate. Recently, such a competition has been observed by fluorescence microscopy. The T6SS active bacteria *A. hydrophila* SSU and *V. cholerae* V52, which are susceptible to each others attacks, were competed and were shown to be able to coexist in a T6SS dependent manner (Wong et al., 2016). To achieve this behavior in an IBM similar to our model, the authors proposed a model in which the dying cells are converted to “debris” which occupies the space for some time before being removed from the lattice. In the model this debris state acts as a shield and prevents the encounter with another competitor for some time (Wong et al., 2016). As predicted by our model, the competition mixture segregated and the interspersed bacteria were eliminated. However, in contrast to our model, the mutual killing formed a border which is maintained by the balanced antagonistic interactions (Wong et al., 2016). Furthermore, due to the continuous killing at the boundary, a large amount of cell debris accumulated, which, according to their model, the authors proposed, protects both competitors and thereby enables their coexistence (Wong et al., 2016). Interestingly, this model permitted the existence of “cheaters”, defined as bacteria which lost their T6SS activity but retained resistance to the attack of one of the competitors. Indeed, *V. cholerae* strains which do not possess an active T6SS were protected in a three strain competition mixture with wild type *A. hydrophila* by a *V. cholerae* strain harboring a constitutively active T6SS (Wong et al., 2016). A similar approach was recently used to demonstrate that

the segregation, driven by antagonistic processes, promotes the evolution of public goods. This is because in a segregated domain, a public good producer is mostly surrounded by its kin reducing the loss of the product to competitors (McNally et al., 2017). However, the model assumed a "cheater" to be sensitive to the antagonistic interaction, which results in the segregation of the producer and cheater. As mentioned above, the previous study could demonstrate that a cheater, which is resistant to the attack of one of the competitors, will even be protected by the respective competitor and reside in its domain thereby being able to exploit the public goods available in that domain (Wong et al., 2016). Interestingly, in *B. thailandensis* the formation of cheaters is suppressed by linking the production of T6SS immunity proteins to the production of public goods (Majerczyk et al., 2016). Unlike *V. cholerae*, which constitutively expresses the immunity protein encoding genes (Miyata et al., 2013), both the T6SS effectors and the immunity proteins are regulated by a quorum sensing system in *B. thailandensis* (Majerczyk et al., 2016). The same quorum sensing system regulates the expression of a large number of genes, the products of which may contribute to the production of public goods. A "cheater" strain, which is blind to the quorum sensing signal, and thereby does not contribute to the production of public goods, also does not express the T6SS immunity protein encoding genes. This sensitizes the cheater to T6SS killing by the parental strain and thus efficiently suppresses the formation of cheaters within the parental population (Majerczyk et al., 2016).

Taken together, the modelling approach may yield valuable insights and mechanistic explanations for an observed phenotype. Furthermore, the use of models also enables the generalization of the observation to comparable contact dependent inhibitory systems. Moreover, in a model a single parameter can be adjusted while keeping the remaining parameters constant which may be hard or even impossible to achieve in a biological system. The ability to predict the outcome of a competition with given parameters is an important trait of a model.

Apart from the quorum sensing regulated T6SS, all of the models described above assumed a random targeting activity of the T6SS. However, as elaborated in the introduction, the T6SS may also serve as a defensive weapon as exemplified by the retaliation strategy employed by *P. aeruginosa* (Basler et al., 2013), or it may be regulated to serve a specific purpose such as the repression of the T6SS by a resistance plasmid in *A. baumannii* (Weber et al., 2015). It may be instructive to study the benefits of such regulation strategies by modelling different types of competitions.

References

Abby, S.S., and Rocha, E.P.C. (2012). The Non-Flagellar Type III Secretion System Evolved from the Bacterial Flagellum and Diversified into Host-Cell Adapted Systems. PLOS Genet. *8*, e1002983.

Adams, S.R., Campbell, R.E., Gross, L.A., Martin, B.R., Walkup, G.K., Yao, Y., Llopis, J., and Tsien, R.Y. (2002). New Biarsenical Ligands and Tetracysteine Motifs for Protein Labeling in Vitro and in Vivo: Synthesis and Biological Applications. J. Am. Chem. Soc. *124*, 6063–6076.

Agard, N.J., Prescher, J.A., and Bertozzi, C.R. (2004). A Strain-Promoted [3 + 2] Azide−Alkyne Cycloaddition for Covalent Modification of Biomolecules in Living Systems. J. Am. Chem. Soc. *126*, 15046–15047.

Aigrain, L., Sustarsic, M., Crawford, R., Plochowietz, A., and Kapanidis, A.N. (2015). Internalization and Observation of Fluorescent Biomolecules in Living Microorganisms via Electroporation. JoVE J. Vis. Exp. e52208–e52208.

Akeda, Y., and Galán, J.E. (2005). Chaperone release and unfolding of substrates in type III secretion. Nature *437*, 911–915.

Akopyan, K., Edgren, T., Wang-Edgren, H., Rosqvist, R., Fahlgren, A., Wolf-Watz, H., and Fallman, M. (2011). Translocation of surface-localized effectors in type III secretion. Proc. Natl. Acad. Sci. *108*, 1639–1644.

Albert Griffin, B., Adams, S.R., Jones, J., and Tsien, R.Y. (2000). Fluorescent labeling of recombinant proteins in living cells with FlAsH. Methods Enzymol. *327*, 565–578.

Alcoforado Diniz, J., Liu, Y.-C., and Coulthurst, S.J. (2015). Molecular weaponry: diverse effectors delivered by the Type VI secretion system. Cell. Microbiol. *17*, 1742–1751.

Alteri, C.J., and Mobley, H.L.T. (2016). The Versatile Type VI Secretion System. Microbiol. Spectr. *4*.

Alteri, C.J., Himpsl, S.D., Pickens, S.R., Lindner, J.R., Zora, J.S., Miller, J.E., Arno, P.D., Straight, S.W., and Mobley, H.L.T. (2013). Multicellular Bacteria Deploy the Type VI Secretion System to Preemptively Strike Neighboring Cells. PLoS Pathog. *9*, e1003608.

Altindis, E., Dong, T., Catalano, C., and Mekalanos, J. (2015). Secretome Analysis of *Vibrio cholerae* Type VI Secretion System Reveals a New Effector-Immunity Pair. MBio *6*, e00075-15.

Alva, V., Nam, S.-Z., Söding, J., and Lupas, A.N. (2016). The MPI bioinformatics Toolkit as an integrative platform for advanced protein sequence and structure analysis. Nucleic Acids Res. *44*, W410-415.

Andrews, S. (2010). FastQC A Quality Control tool for High Throughput Sequence Data.

Armentrout, E.I., and Rietsch, A. (2016). The Type III Secretion Translocation Pore Senses Host Cell Contact. PLOS Pathog. *12*, e1005530.

Aschtgen, M.-S., Bernard, C.S., Bentzmann, S., Lloubès, R., and Cascales, E. (2008). SciN is an outer membrane lipoprotein required for type VI secretion in enteroaggregative *Escherichia coli*. J. Bacteriol. *190*, 7523–7531.

Aschtgen, M.-S., Thomas, M.S., and Cascales, E. (2010a). Anchoring the type VI secretion system to the peptidoglycan: TssL, TagL, TagP... what else? Virulence *1*, 535–540.

Aschtgen, M.-S., Gavioli, M., Dessen, A., Lloubès, R., and Cascales, E. (2010b). The SciZ protein anchors the enteroaggregative *Escherichia coli* Type VI secretion system to the cell wall. Mol. Microbiol. *75*, 886–899.

Aschtgen, M.-S., Zoued, A., Lloubès, R., Journet, L., and Cascales, E. (2012). The C-tail anchored TssL subunit, an essential protein of the enteroaggregative *Escherichia coli* Sci-1 Type VI secretion system, is inserted by YidC. MicrobiologyOpen *1*, 71–82.

Aubert, D.F., Xu, H., Yang, J., Shi, X., Gao, W., Li, L., Bisaro, F., Chen, S., Valvano, M.A., and Shao, F. (2016). A *Burkholderia* Type VI Effector Deamidates Rho GTPases to Activate the Pyrin Inflammasome and Trigger Inflammation. Cell Host Microbe *19*, 664–674.

Babić, A., Lindner, A.B., Vulić, M., Stewart, E.J., and Radman, M. (2008). Direct Visualization of Horizontal Gene Transfer. Science *319*, 1533–1536.

Backert, S., Tegtmeyer, N., and Fischer, W. (2015). Composition, structure and function of the *Helicobacter pylori cag* pathogenicity island encoded type IV secretion system. Future Microbiol. *10*, 955–965.

Ballister, E.R., Lai, A.H., Zuckermann, R.N., Cheng, Y., and Mougous, J.D. (2008). *In vitro* self-assembly of tailorable nanotubes from a simple protein building block. Proc. Natl. Acad. Sci. *105*, 3733–3738.

Barbe, V., Vallenet, D., Fonknechten, N., Kreimeyer, A., Oztas, S., Labarre, L., Cruveiller, S., Robert, C., Duprat, S., Wincker, P., et al. (2004). Unique features revealed by the genome sequence of *Acinetobacter* sp. ADP1, a versatile and naturally transformation competent bacterium. Nucleic Acids Res. *32*, 5766–5779.

Barker, J.R., Chong, A., Wehrly, T.D., Yu, J.-J., Rodriguez, S.A., Liu, J., Celli, J., Arulanandam, B.P., and Klose, K.E. (2009). The *Francisella tularensis* pathogenicity island encodes a secretion system that is required for phagosome escape and virulence. Mol. Microbiol. *74*, 1459–1470.

Barret, M., Egan, F., Fargier, E., Morrissey, J.P., and O'Gara, F. (2011). Genomic analysis of the type VI secretion systems in *Pseudomonas* spp.: novel clusters and putative effectors uncovered. Microbiology *157*, 1726–1739.

Barret, M., Egan, F., and O'Gara, F. (2013). Distribution and diversity of bacterial secretion systems across metagenomic datasets. Environ. Microbiol. Rep. *5*, 117–126.

Basler, M. (2015). Type VI secretion system: secretion by a contractile nanomachine. Phil Trans R Soc B *370*, 20150021.

Basler, M., and Mekalanos, J.J. (2012). Type 6 Secretion Dynamics Within and Between Bacterial Cells. Science *337*, 815.

Basler, M., Pilhofer, M., Henderson, G.P., Jensen, G.J., and Mekalanos, J.J. (2012). Type VI secretion requires a dynamic contractile phage tail-like structure. Nature *483*, 182–186.

Basler, M., Ho, B.T., and Mekalanos, J.J. (2013). Tit-for-tat: type VI secretion system counterattack during bacterial cell-cell interactions. Cell *152*, 884–894.

Berardinis, V. de, Vallenet, D., Castelli, V., Besnard, M., Pinet, A., Cruaud, C., Samair, S., Lechaplais, C., Gyapay, G., Richez, C., et al. (2008). A complete collection of single-gene deletion mutants of *Acinetobacter baylyi* ADP1. Mol. Syst. Biol. *4*, 174.

Bingle, L.E., Bailey, C.M., and Pallen, M.J. (2008). Type VI secretion: a beginner's guide. Curr. Opin. Microbiol. *11*, 3–8.

Blackman, M.L., Royzen, M., and Fox, J.M. (2008). Tetrazine Ligation: Fast Bioconjugation Based on Inverse-Electron-Demand Diels−Alder Reactivity. J. Am. Chem. Soc. *130*, 13518–13519.

Bladergroen, M.R., Badelt, K., and Spaink, H.P. (2003). Infection-Blocking Genes of a Symbiotic Rhizobium leguminosarum Strain That Are Involved in Temperature-Dependent Protein Secretion. Mol. Plant. Microbe Interact. *16*, 53–64.

Blocker, A., Gounon, P., Larquet, E., Niebuhr, K., Cabiaux, V., Parsot, C., and Sansonetti, P. (1999). The Tripartite Type III Secreton of *Shigella flexneri* Inserts IpaB and IpaC into Host Membranes. J. Cell Biol. *147*, 683–693.

Blomquist, A.T., and Liu, L.H. (1953). Many-membered Carbon Rings. VII. Cycloöctyne. J. Am. Chem. Soc. *75*, 2153–2154.

Blondel, C.J., Jiménez, J.C., Contreras, I., and Santiviago, C.A. (2009). Comparative genomic analysis uncovers 3 novel loci encoding type six secretion systems differentially distributed in *Salmonella* serotypes. BMC Genomics *10*, 354.

Blumofe, R.D., and Leiserson, C.E. (1999). Scheduling Multithreaded Computations by Work Stealing. J ACM *46*, 720–748.

Böck, D., Medeiros, J.M., Tsao, H.-F., Penz, T., Weiss, G.L., Aistleitner, K., Horn, M., and Pilhofer, M. (2017). In situ architecture, function, and evolution of a contractile injection system. Science *357*, 713–717.

Bondage, D.D., Lin, J.-S., Ma, L.-S., Kuo, C.-H., and Lai, E.-M. (2016). VgrG C terminus confers the type VI effector transport specificity and is required for binding with PAAR and adaptor–effector complex. Proc. Natl. Acad. Sci. *113*, E3931–E3940.

Bönemann, G., Pietrosiuk, A., Diemand, A., Zentgraf, H., and Mogk, A. (2009). Remodelling of VipA/VipB tubules by ClpV-mediated threading is crucial for type VI protein secretion. EMBO J. *28*, 315–325.

Borgeaud, S., Metzger, L.C., Scrignari, T., and Blokesch, M. (2015). The type VI secretion system of *Vibrio cholerae* fosters horizontal gene transfer. Science *347*, 63–67.

Boyer, F., Fichant, G., Berthod, J., Vandenbrouck, Y., and Attree, I. (2009). Dissecting the bacterial type VI secretion system by a genome wide *in silico* analysis: what can be learned from available microbial genomic resources? BMC Genomics *10*, 104.

Brackmann, M., Wang, J., and Basler, M. (2017a). VipA N-terminal linker and VipB-VipB interaction modulate the contraction of Type VI secretion system sheath. BioRxiv 152785.

Brackmann, M., Nazarov, S., Wang, J., and Basler, M. (2017b). Using Force to Punch Holes: Mechanics of Contractile Nanomachines. Trends Cell Biol. *27*, 623–632.

Brackmann, M., Wang, J., Castano-Diez, D., Kudryashev, M., Goldie, G., Maier, T., Stahlberg, H., and Basler, M. Structure and mechanism of contraction of the extended Type VI secretion system sheath. Be Publ.

Brennan, C.A., and Garrett, W.S. (2016). Gut Microbiota, Inflammation, and Colorectal Cancer. Annu. Rev. Microbiol. *70*, 395–411.

Brodmann, M., Dreier, R.F., Broz, P., and Basler, M. (2017). *Francisella* requires dynamic type VI secretion system and ClpB to deliver effectors for phagosomal escape. Nat. Commun. *8*, 15853.

Brooks, T.M., Unterweger, D., Bachmann, V., Kostiuk, B., and Pukatzki, S. (2013). Lytic Activity of the *Vibrio cholerae* Type VI Secretion Toxin VgrG-3 Is Inhibited by the Antitoxin TsaB. J. Biol. Chem. *288*, 7618–7625.

de Bruin, O.M., Ludu, J.S., and Nano, F.E. (2007). The *Francisella* pathogenicity island protein IglA localizes to the bacterial cytoplasm and is needed for intracellular growth. BMC Microbiol. *7*, 1.

Brunet, Y.R., Hénin, J., Celia, H., and Cascales, E. (2014). Type VI secretion and bacteriophage tail tubes share a common assembly pathway. EMBO Rep. *15*, 315–321.

Brunet, Y.R., Zoued, A., Boyer, F., Douzi, B., and Cascales, E. (2015). The Type VI Secretion TssEFGK-VgrG Phage-Like Baseplate Is Recruited to the TssJLM Membrane Complex via Multiple Contacts and Serves As Assembly Platform for Tail Tube/Sheath Polymerization. PLoS Genet. *11*, e1005545.

Brzuszkiewicz, E., Brüggemann, H., Liesegang, H., Emmerth, M., Ölschläger, T., Nagy, G., Albermann, K., Wagner, C., Buchrieser, C., Emődy, L., et al. (2006). How to become a uropathogen: Comparative genomic analysis of extraintestinal pathogenic *Escherichia coli* strains. Proc. Natl. Acad. Sci. *103*, 12879–12884.

Busby, J.N., Panjikar, S., Landsberg, M.J., Hurst, M.R.H., and Lott, J.S. (2013). The BC component of ABC toxins is an RHS-repeat-containing protein encapsulation device. Nature *501*, 547–550.

Busse, B., and Miura (2016). MultiStackRegistration.

Büttner, D. (2012). Protein Export According to Schedule: Architecture, Assembly, and Regulation of Type III Secretion Systems from Plant- and Animal-Pathogenic Bacteria. Microbiol. Mol. Biol. Rev. *76*, 262–310.

Büttner, D. (2016). Behind the lines–actions of bacterial type III effector proteins in plant cells. FEMS Microbiol. Rev. *40*, 894–937.

Carboni, R.A., and Lindsey, R.V. (1959). Reactions of Tetrazines with Unsaturated Compounds. A New Synthesis of Pyridazines. J. Am. Chem. Soc. *81*, 4342–4346.

Cardarelli, L., Saak, C., and Gibbs, K.A. (2015). Two Proteins Form a Heteromeric Bacterial Self-Recognition Complex in Which Variable Subdomains Determine Allele-Restricted Binding. MBio *6*, e00251-15.

Carlson, J.C.T., Meimetis, L.G., Hilderbrand, S.A., and Weissleder, R. (2013). BODIPY–Tetrazine Derivatives as Superbright Bioorthogonal Turn-on Probes. Angew. Chem. Int. Ed. *52*, 6917–6920.

Casabona, M.G., Silverman, J.M., Sall, K.M., Boyer, F., Couté, Y., Poirel, J., Grunwald, D., Mougous, J.D., Elsen, S., and Attree, I. (2013). An ABC transporter and an outer membrane lipoprotein participate in posttranslational activation of type VI secretion in *Pseudomonas aeruginosa*. Environ. Microbiol. *15*, 471–486.

Chang, Y.-W., Rettberg, L.A., Ortega, D.R., and Jensen, G.J. (2017). *In vivo* structures of an intact type VI secretion system revealed by electron cryotomography. EMBO Rep. *18*, 1090–1099.

Chatzidaki-Livanis, M., Geva-Zatorsky, N., and Comstock, L.E. (2016). *Bacteroides fragilis* type VI secretion systems use novel effector and immunity proteins to antagonize human gut Bacteroidales species. Proc. Natl. Acad. Sci. *113*, 3627–3632.

Chen, X., and Wu, Y.-W. (2016). Selective chemical labeling of proteins. Org. Biomol. Chem. *14*, 5417–5439.

Chen, H., Yang, D., Han, F., Tan, J., Zhang, L., Xiao, J., Zhang, Y., and Liu, Q. (2017). The Bacterial T6SS Effector EvpP Prevents NLRP3 Inflammasome Activation by Inhibiting the Ca^{2+}-Dependent MAPK-Jnk Pathway. Cell Host Microbe *21*, 47–58.

Chen, W., Wang, D., Dai, C., Hamelberg, D., and Wang, B. (2012). Clicking 1,2,4,5-tetrazine and cyclooctynes with tunable reaction rates. Chem. Commun. *48*, 1736–1738.

Cherradi, Y., Schiavolin, L., Moussa, S., Meghraoui, A., Meksem, A., Biskri, L., Azarkan, M., Allaoui, A., and Botteaux, A. (2013). Interplay between predicted inner-rod and gatekeeper in controlling substrate specificity of the type III secretion system. Mol. Microbiol. *87*, 1183–1199.

Chou, S., Bui, N.K., Russell, A.B., Lexa, K.W., Gardiner, T.E., LeRoux, M., Vollmer, W., and Mougous, J.D. (2012). Structure of a Peptidoglycan Amidase Effector Targeted to Gram-Negative Bacteria by the Type VI Secretion System. Cell Rep. *1*, 656–664.

Christie, P.J., Whitaker, N., and González-Rivera, C. (2014). Mechanism and structure of the bacterial type IV secretion systems. Biochim. Biophys. Acta BBA - Mol. Cell Res. *1843*, 1578–1591.

Cianfanelli, F.R., Alcoforado Diniz, J., Guo, M., Cesare, V., Trost, M., and Coulthurst, S.J. (2016). VgrG and PAAR Proteins Define Distinct Versions of a Functional Type VI Secretion System. PLoS Pathog. *12*, e1005735.

Clemens, D.L., Ge, P., Lee, B.-Y., Horwitz, M.A., and Zhou, Z.H. (2015). Atomic Structure of T6SS Reveals Interlaced Array Essential to Function. Cell *160*, 940–951.

Crawford, R., Torella, J.P., Aigrain, L., Plochowietz, A., Gryte, K., Uphoff, S., and Kapanidis, A.N. (2013). Long-Lived Intracellular Single-Molecule Fluorescence Using Electroporated Molecules. Biophys. J. *105*, 2439–2450.

Cserép, G.B., Herner, A., and Kele, P. (2015). Bioorthogonal fluorescent labels: a review on combined forces. Methods Appl. Fluoresc. *3*, 042001.

Das, S., and Chaudhuri, K. (2003). Identification of a unique IAHP (IcmF associated homologous proteins) cluster in Vibrio cholerae and other proteobacteria through in silico analysis. In Silico Biol. *3*, 287–300.

Das, S., Chakrabortty, A., Banerjee, R., Roychoudhury, S., and Chaudhuri, K. (2000). Comparison of global transcription responses allows identification of *Vibrio cholerae* genes differentially expressed following infection. FEMS Microbiol. Lett. *190*, 87–91.

Debets, M.F., Berkel, S.S. van, Schoffelen, S., Rutjes, F.P.J.T., Hest, J.C.M. van, and Delft, F.L. van (2010). Aza-dibenzocyclooctynes for fast and efficient enzyme PEGylation *via* copper-free (3+2) cycloaddition. Chem. Commun. *46*, 97–99.

Deng, W., Marshall, N.C., Rowland, J.L., McCoy, J.M., Worrall, L.J., Santos, A.S., Strynadka, N.C.J., and Finlay, B.B. (2017). Assembly, structure, function and regulation of type III secretion systems. Nat. Rev. Microbiol. *15*, 323–337.

Desvaux, M., Hébraud, M., Talon, R., and Henderson, I.R. (2009). Secretion and subcellular localizations of bacterial proteins: a semantic awareness issue. Trends Microbiol. *17*, 139–145.

Devaraj, N.K., Upadhyay, R., Haun, J.B., Hilderbrand, S.A., and Weissleder, R. (2009). Fast and Sensitive Pretargeted Labeling of Cancer Cells through a Tetrazine/*trans*-Cyclooctene Cycloaddition. Angew. Chem. Int. Ed. *48*, 7013–7016.

Devaraj, N.K., Hilderbrand, S., Upadhyay, R., Mazitschek, R., and Weissleder, R. (2010). Bioorthogonal Turn-On Probes for Imaging Small Molecules inside Living Cells. Angew. Chem. Int. Ed. *49*, 2869–2872.

Dienes, L. (1946). Reproductive processes in Proteus cultures. Proc. Soc. Exp. Biol. Med. Soc. Exp. Biol. Med. N. Y. N *63*, 265–270.

Dieterich, D.C., Link, A.J., Graumann, J., Tirrell, D.A., and Schuman, E.M. (2006). Selective identification of newly synthesized proteins in mammalian cells using bioorthogonal noncanonical amino acid tagging (BONCAT). Proc. Natl. Acad. Sci. *103*, 9482–9487.

Dieterich, D.C., Hodas, J.J.L., Gouzer, G., Shadrin, I.Y., Ngo, J.T., Triller, A., Tirrell, D.A., and Schuman, E.M. (2010). *In situ* visualization and dynamics of newly synthesized proteins in rat hippocampal neurons. Nat. Neurosci. *13*, 897–905.

Diniz, J.A., and Coulthurst, S.J. (2015). Intraspecies Competition in *Serratia marcescens* Is Mediated by Type VI-Secreted Rhs Effectors and a Conserved Effector-Associated Accessory Protein. J. Bacteriol. *197*, 2350–2360.

Dohlich, K., Zumsteg, A.B., Goosmann, C., and Kolbe, M. (2014). A Substrate-Fusion Protein Is Trapped inside the Type III Secretion System Channel in *Shigella flexneri*. PLOS Pathog. *10*, e1003881.

Dommerholt, J., Schmidt, S., Temming, R., Hendriks, L.J.A., Rutjes, F.P.J.T., van Hest, J.C.M., Lefeber, D.J., Friedl, P., and van Delft, F.L. (2010). Readily Accessible Bicyclononynes for Bioorthogonal Labeling and Three-Dimensional Imaging of Living Cells. Angew. Chem. Int. Ed. *49*, 9422–9425.

Dommerholt, J., Rutjes, F.P.J.T., and Delft, F.L. van (2016). Strain-Promoted 1,3-Dipolar Cycloaddition of Cycloalkynes and Organic Azides. Top. Curr. Chem. *374*, 16.

Dong, T.G., Ho, B.T., Yoder-Himes, D.R., and Mekalanos, J.J. (2013). Identification of T6SS-dependent effector and immunity proteins by Tn-seq in *Vibrio cholerae*. Proc. Natl. Acad. Sci. *110*, 2623–2628.

Dong, T.G., Dong, S., Catalano, C., Moore, R., Liang, X., and Mekalanos, J.J. (2015). Generation of reactive oxygen species by lethal attacks from competing microbes. Proc. Natl. Acad. Sci. *112*, 2181–2186.

Douzi, B., Spinelli, S., Blangy, S., Roussel, A., Durand, E., Brunet, Y.R., Cascales, E., and Cambillau, C. (2014). Crystal Structure and Self-Interaction of the Type VI Secretion Tail-Tube Protein from Enteroaggregative *Escherichia coli*. PLOS ONE *9*, e86918.

Douzi, B., Brunet, Y.R., Spinelli, S., Lensi, V., Legrand, P., Blangy, S., Kumar, A., Journet, L., Cascales, E., and Cambillau, C. (2016). Structure and specificity of the Type VI secretion system ClpV-TssC interaction in enteroaggregative *Escherichia coli*. Sci. Rep. *6*, srep34405.

Dudley, E.G., Thomson, N.R., Parkhill, J., Morin, N.P., and Nataro, J.P. (2006). Proteomic and microarray characterization of the AggR regulon identifies a pheU pathogenicity island in enteroaggregative *Escherichia coli*. Mol. Microbiol. *61*, 1267–1282.

Dumas, A., Lercher, L., D. Spicer, C., and G. Davis, B. (2015). Designing logical codon reassignment – Expanding the chemistry in biology. Chem. Sci. *6*, 50–69.

Durand, E., Zoued, A., Spinelli, S., Watson, P.J.H., Aschtgen, M.-S., Journet, L., Cambillau, C., and Cascales, E. (2012). Structural Characterization and Oligomerization of the TssL Protein, a Component Shared by Bacterial Type VI and Type IVb Secretion Systems. J. Biol. Chem. *287*, 14157–14168.

Durand, E., van Nguyen, S., Zoued, A., Logger, L., Péhau-Arnaudet, G., Aschtgen, M.-S., Spinelli, S., Desmyter, A., Bardiaux, B., Dujeancourt, A., et al. (2015). Biogenesis and structure of a type VI secretion membrane core complex. Nature *523*, 555–560.

Edgren, T., Forsberg, Å., Rosqvist, R., and Wolf-Watz, H. (2012). Type III Secretion in *Yersinia*: Injectisome or Not? PLoS Pathog. *8*, e1002669.

English, G., Trunk, K., Rao, V.A., Srikannathasan, V., Hunter, W.N., and Coulthurst, S.J. (2012). New secreted toxins and immunity proteins encoded within the Type VI secretion system gene cluster of *Serratia marcescens*. Mol. Microbiol. *86*, 921–936.

English, G., Byron, O., Cianfanelli, F.R., Prescott, A.R., and Coulthurst, S.J. (2014). Biochemical analysis of TssK, a core component of the bacterial Type VI secretion system, reveals distinct oligomeric states of TssK and identifies a TssK-TssFG subcomplex. Biochem. J. *461*, 291–304.

Enninga, J., Mounier, J., Sansonetti, P., and Nhieu, G.T.V. (2005). Secretion of type III effectors into host cells in real time. Nat. Methods *2*, 959–965.

Enos-Berlage, J.L., Guvener, Z.T., Keenan, C.E., and McCarter, L.L. (2005). Genetic determinants of biofilm development of opaque and translucent *Vibrio parahaemolyticus*. Mol. Microbiol. *55*, 1160–1182.

Erhardt, M., Mertens, M.E., Fabiani, F.D., and Hughes, K.T. (2014). ATPase-Independent Type-III Protein Secretion in *Salmonella enterica*. PLOS Genet. *10*, e1004800.

Espesset, D., Corda, Y., Cunningham, K., Bénédetti, H., Lloubès, R., Lazdunski, C., and Géli, V. (1994). The colicin A pore-forming domain fused to mitochondrial intermembrane space sorting signals can be functionally inserted into the *Escherichia coli* plasma membrane by a mechanism that bypasses the Tol proteins. Mol. Microbiol. *13*, 1121–1131.

Fauvart, M., and Michiels, J. (2008). Rhizobial secreted proteins as determinants of host specificity in the rhizobium–legume symbiosis. FEMS Microbiol. Lett. *285*, 1–9.

Felisberto-Rodrigues, C., Durand, E., Aschtgen, M.-S., Blangy, S., Ortiz-Lombardia, M., Douzi, B., Cambillau, C., and Cascales, E. (2011). Towards a Structural Comprehension of Bacterial Type VI Secretion Systems: Characterization of the TssJ-TssM Complex of an *Escherichia coli* Pathovar. PLOS Pathog. *7*, e1002386.

Filippova, E.V., Halavaty, A., Minasov, G., Shuvalova, L., Dubrovska, I., Winsor, J., Papazisi, L., Anderson, W.F., and Diseases (CSGID), C. for S.G. of I. Crystal structure of a type VI secretion system effector from Yersinia pestis. Be Publ.

Flaugnatti, N., Le, T.T.H., Canaan, S., Aschtgen, M.-S., Nguyen, V.S., Blangy, S., Kellenberger, C., Roussel, A., Cambillau, C., Cascales, E., et al. (2016). A phospholipase A_1 antibacterial Type VI secretion effector interacts directly with the C-terminal domain of the VgrG spike protein for delivery. Mol. Microbiol. *99*, 1099–1118.

Folkesson, A., Löfdahl, S., and Normark, S. (2002). The *Salmonella enterica* subspecies I specific centisome 7 genomic island encodes novel protein families present in bacteria living in close contact with eukaryotic cells. Res. Microbiol. *153*, 537–545.

Förster, A., Planamente, S., Manoli, E., Lossi, N.S., Freemont, P.S., and Filloux, A. (2014). Coevolution of the ATPase ClpV, the sheath proteins TssB and TssC, and the accessory protein TagJ/HsiE1 distinguishes type VI secretion classes. J. Biol. Chem. *289*, 33032–33043.

Fritsch, M.J., Trunk, K., Diniz, J.A., Guo, M., Trost, M., and Coulthurst, S.J. (2013). Proteomic Identification of Novel Secreted Antibacterial Toxins of the *Serratia marcescens* Type VI Secretion System. Mol. Cell. Proteomics *12*, 2735–2749.

Fu, Y., Waldor, M.K., and Mekalanos, J.J. (2013). Tn-Seq Analysis of *Vibrio cholerae* Intestinal Colonization Reveals a Role for T6SS-Mediated Antibacterial Activity in the Host. Cell Host Microbe *14*, 652–663.

Fujii, T., Cheung, M., Blanco, A., Kato, T., Blocker, A.J., and Namba, K. (2012). Structure of a type III secretion needle at 7-Å resolution provides insights into its assembly and signaling mechanisms. Proc. Natl. Acad. Sci. *109*, 4461–4466.

Ge, P., Scholl, D., Leiman, P.G., Yu, X., Miller, J.F., and Zhou, Z.H. (2015). Atomic structures of a bactericidal contractile nanotube in its pre- and postcontraction states. Nat. Struct. Mol. Biol. *22*, 377–382.

Gerc, A.J., Diepold, A., Trunk, K., Porter, M., Rickman, C., Armitage, J.P., Stanley-Wall, N.R., and Coulthurst, S.J. (2015). Visualization of the *Serratia* Type VI Secretion System Reveals Unprovoked Attacks and Dynamic Assembly. Cell Rep. *12*, 2131–2142.

Ghosal, D., Chang, Y.-W., Jeong, K.C., Vogel, J.P., and Jensen, G.J. (2017). *In situ* structure of the *Legionella* Dot/Icm type IV secretion system by electron cryotomography. EMBO Rep. *18*, 726–732.

Golovliov, I., Ericsson, M., Sandström, G., Tärnvik, A., and Sjöstedt, A. (1997). Identification of Proteins of *Francisella tularensis* Induced during Growth in Macrophages and Cloning of the Gene Encoding a Prominently Induced 23-Kilodalton Protein. Infect. Immun. *65*, 2183–2189.

Gonzalez-Rivera, C., Bhatty, M., and Christie, P.J. (2016). Mechanism and Function of Type IV Secretion During Infection of the Human Host. Microbiol. Spectr. *4*.

Griffin, B.A., Adams, S.R., and Tsien, R.Y. (1998). Specific Covalent Labeling of Recombinant Protein Molecules Inside Live Cells. Science *281*, 269–272.

Guignot, J., and Tran Van Nhieu, G. (2016). Bacterial Control of Pores Induced by the Type III Secretion System: Mind the Gap. Front. Immunol. *7*.

Gupta, R.S. (1998). What are archaebacteria: life's third domain or monoderm prokaryotes related to Gram-positive bacteria? A new proposal for the classification of prokaryotic organisms. Mol. Microbiol. *29*, 695–707.

Hachani, A., Lossi, N.S., Hamilton, A., Jones, C., Bleves, S., Albesa-Jové, D., and Filloux, A. (2011). Type VI Secretion System in *Pseudomonas aeruginosa*: SECRETION AND MULTIMERIZATION OF VgrG PROTEINS. J. Biol. Chem. *286*, 12317–12327.

Hachani, A., Lossi, N.S., and Filloux, A. (2013). A Visual Assay to Monitor T6SS-mediated Bacterial Competition. JoVE J. Vis. Exp. e50103–e50103.

Hachani, A., Allsopp, L.P., Oduko, Y., and Filloux, A. (2014). The VgrG Proteins Are "à la Carte" Delivery Systems for Bacterial Type VI Effectors. J. Biol. Chem. *289*, 17872–17884.

Hachani, A., Wood, T.E., and Filloux, A. (2016). Type VI secretion and anti-host effectors. Curr. Opin. Microbiol. *29*, 81–93.

Hamilton, H.L., Domínguez, N.M., Schwartz, K.J., Hackett, K.T., and Dillard, J.P. (2005). *Neisseria gonorrhoeae* secretes chromosomal DNA via a novel type IV secretion system. Mol. Microbiol. *55*, 1704–1721.

Hatzenpichler, R., Scheller, S., Tavormina, P.L., Babin, B.M., Tirrell, D.A., and Orphan, V.J. (2014). *In situ* visualization of newly synthesized proteins in environmental microbes using amino acid tagging and click chemistry. Environ. Microbiol. *16*, 2568–2590.

Hecht, A.L., Casterline, B.W., Earley, Z.M., Goo, Y.A., Goodlett, D.R., and Wardenburg, J.B. (2016). Strain competition restricts colonization of an enteric pathogen and prevents colitis. EMBO Rep. *17*, 1281–1291.

van der Heijden, J., and Finlay, B.B. (2012). Type III effector-mediated processes in *Salmonella* infection. Future Microbiol. *7*, 685–703.

Ho, B.T., Basler, M., and Mekalanos, J.J. (2013). Type 6 Secretion System-Mediated Immunity to Type 4 Secretion System-Mediated Gene Transfer. Science *342*, 250–253.

Ho, B.T., Dong, T.G., and Mekalanos, J.J. (2014). A View to a Kill: The Bacterial Type VI Secretion System. Cell Host Microbe *15*, 9–21.

Ho, B.T., Fu, Y., Dong, T.G., and Mekalanos, J.J. (2017). *Vibrio cholerae* type 6 secretion system effector trafficking in target bacterial cells. Proc. Natl. Acad. Sci. *114*, 9427–9432.

Hofreuter, D., Odenbreit, S., and Haas, R. (2001). Natural transformation competence in *Helicobacter pylori* is mediated by the basic components of a type IV secretion system. Mol. Microbiol. *41*, 379–391.

Hood, R.D., Singh, P., Hsu, F., Güvener, T., Carl, M.A., Trinidad, R.R.S., Silverman, J.M., Ohlson, B.B., Hicks, K.G., Plemel, R.L., et al. (2010). A Type VI Secretion System of *Pseudomonas aeruginosa* Targets a Toxin to Bacteria. Cell Host Microbe *7*, 25–37.

Hsu, F., Schwarz, S., and Mougous, J.D. (2009). TagR promotes PpkA-catalysed type VI secretion activation in *Pseudomonas aeruginosa*. Mol. Microbiol. *72*, 1111–1125.

Hu, B., Morado, D.R., Margolin, W., Rohde, J.R., Arizmendi, O., Picking, W.L., Picking, W.D., and Liu, J. (2015). Visualization of the type III secretion sorting platform of *Shigella flexneri*. Proc. Natl. Acad. Sci. *112*, 1047–1052.

Hu, B., Lara-Tejero, M., Kong, Q., Galán, J.E., and Liu, J. (2017). In Situ Molecular Architecture of the *Salmonella* Type III Secretion Machine. Cell *168*, 1065-1074.e10.

Hu, H., Zhang, H., Gao, Z., Wang, D., Liu, G., Xu, J., Lan, K., and Dong, Y. (2014). Structure of the type VI secretion phospholipase effector Tle1 provides insight into its hydrolysis and membrane targeting. Acta Crystallogr. D Biol. Crystallogr. *70*, 2175–2185.

Ilangovan, A., Connery, S., and Waksman, G. (2015). Structural biology of the Gram-negative bacterial conjugation systems. Trends Microbiol. *23*, 301–310.

Jamet, A., and Nassif, X. (2015). New Players in the Toxin Field: Polymorphic Toxin Systems in Bacteria. MBio *6*, e00285-15.

Ji, X., Ji, K., Chittavong, V., Aghoghovbia, R.E., Zhu, M., and Wang, B. (2017). Click and Fluoresce: A Bioorthogonally Activated Smart Probe for Wash-Free Fluorescent Labeling of Biomolecules. J. Org. Chem. *82*, 1471–1476.

Jiang, F., Waterfield, N.R., Yang, J., Yang, G., and Jin, Q. (2014). A *Pseudomonas aeruginosa* Type VI Secretion Phospholipase D Effector Targets Both Prokaryotic and Eukaryotic Cells. Cell Host Microbe *15*, 600–610.

Jobichen, C., Chakraborty, S., Li, M., Zheng, J., Joseph, L., Mok, Y.-K., Leung, K.Y., and Sivaraman, J. (2010). Structural Basis for the Secretion of EvpC: A Key Type VI Secretion System Protein from *Edwardsiella tarda*. PLOS ONE *5*, e12910.

Johnson, B.K., Scholz, M.B., Teal, T.K., and Abramovitch, R.B. (2016). SPARTA: Simple Program for Automated reference-based bacterial RNA-seq Transcriptome Analysis. BMC Bioinformatics *17*, 66.

Juhas, M. (2015). Horizontal gene transfer in human pathogens. Crit. Rev. Microbiol. *41*, 101–108.

Juni, E., and Janik, A. (1969). Transformation of *Acinetobacter calco-aceticus* (*Bacterium anitratum*). J. Bacteriol. *98*, 281–288.

Kapitein, N., Bönemann, G., Pietrosiuk, A., Seyffer, F., Hausser, I., Locker, J.K., and Mogk, A. (2013). ClpV recycles VipA/VipB tubules and prevents non-productive tubule formation to ensure efficient type VI protein secretion. Mol. Microbiol. *87*, 1013–1028.

Kaur, J., and Jain, S.K. (2012). Role of antigens and virulence factors of *Salmonella enterica* serovar Typhi in its pathogenesis. Microbiol. Res. *167*, 199–210.

Kiick, K.L., Saxon, E., Tirrell, D.A., and Bertozzi, C.R. (2002). Incorporation of azides into recombinant proteins for chemoselective modification by the Staudinger ligation. Proc. Natl. Acad. Sci. *99*, 19–24.

Kipper, K., Lundius, E.G., Ćurić, V., Nikić, I., Wiessler, M., Lemke, E.A., and Elf, J. (2017). Application of Noncanonical Amino Acids for Protein Labeling in a Genomically Recoded *Escherichia coli*. ACS Synth. Biol. *6*, 233–255.

Kirchberger, P.C., Unterweger, D., Provenzano, D., Pukatzki, S., and Boucher, Y. (2017). Sequential displacement of Type VI Secretion System effector genes leads to evolution of diverse immunity gene arrays in *Vibrio cholerae*. Sci. Rep. *7*, 45133.

Knorr, G., Kozma, E., Herner, A., Lemke, E.A., and Kele, P. (2016). New Red-Emitting Tetrazine-Phenoxazine Fluorogenic Labels for Live-Cell Intracellular Bioorthogonal Labeling Schemes. Chem. – Eur. J. *22*, 8972–8979.

Koskiniemi, S., Lamoureux, J.G., Nikolakakis, K.C., t'Kint de Roodenbeke, C., Kaplan, M.D., Low, D.A., and Hayes, C.S. (2013). Rhs proteins from diverse bacteria mediate intercellular competition. Proc. Natl. Acad. Sci. U. S. A. *110*, 7032–7037.

Krishnan, B., and Gierasch, L.M. (2008). Cross-Strand Split Tetra-Cys Motifs as Structure Sensors in a β-Sheet Protein. Chem. Biol. *15*, 1104–1115.

Kube, S., Kapitein, N., Zimniak, T., Herzog, F., Mogk, A., and Wendler, P. (2014). Structure of the VipA/B Type VI Secretion Complex Suggests a Contraction-State-Specific Recycling Mechanism. Cell Rep. *8*, 20–30.

Kubori, T., Matsushima, Y., Nakamura, D., Uralil, J., Lara-Tejero, M., Sukhan, A., Galán, J.E., and Aizawa, S.-I. (1998). Supramolecular Structure of the *Salmonella typhimurium* Type III Protein Secretion System. Science *280*, 602–605.

Kudryashev, M., Wang, R.Y.-R., Brackmann, M., Scherer, S., Maier, T., Baker, D., DiMaio, F., Stahlberg, H., Egelman, E.H., and Basler, M. (2015). Structure of the Type VI Secretion System Contractile Sheath. Cell *160*, 952–962.

Lang, K., and Chin, J.W. (2014). Bioorthogonal Reactions for Labeling Proteins. ACS Chem. Biol. *9*, 16–20.

Lang, K., Davis, L., Wallace, S., Mahesh, M., Cox, D.J., Blackman, M.L., Fox, J.M., and Chin, J.W. (2012). Genetic Encoding of Bicyclononynes and *trans*-Cyclooctenes for Site-Specific Protein Labeling in Vitro and in Live Mammalian Cells via Rapid Fluorogenic Diels–Alder Reactions. J. Am. Chem. Soc. *134*, 10317–10320.

Lara-Tejero, M., Kato, J., Wagner, S., Liu, X., and Galan, J.E. (2011). A Sorting Platform Determines the Order of Protein Secretion in Bacterial Type III Systems. Science *331*, 1188–1191.

Lasica, A.M., Ksiazek, M., Madej, M., and Potempa, J. (2017). The Type IX Secretion System (T9SS): Highlights and Recent Insights into Its Structure and Function. Front. Cell. Infect. Microbiol. *7*.

Lederberg, J., and Tatum, E.L. (1953). Sex in Bacteria: Genetic Studies, 1945-1952. Science *118*, 169–175.

Lee, P.-C., and Rietsch, A. (2015). Fueling type III secretion. Trends Microbiol. *23*, 296–300.

Lee, C.-R., Lee, J.H., Park, M., Park, K.S., Bae, I.K., Kim, Y.B., Cha, C.-J., Jeong, B.C., and Lee, S.H. (2017). Biology of *Acinetobacter baumannii*: Pathogenesis, Antibiotic Resistance Mechanisms, and Prospective Treatment Options. Front. Cell. Infect. Microbiol. *7*.

Leiman, P.G., and Shneider, M.M. (2012). Contractile Tail Machines of Bacteriophages. In Viral Molecular Machines, (Springer, Boston, MA), pp. 93–114.

Leiman, P.G., Basler, M., Ramagopal, U.A., Bonanno, J.B., Sauder, J.M., Pukatzki, S., Burley, S.K., Almo, S.C., and Mekalanos, J.J. (2009). Type VI secretion apparatus and phage tail-associated protein complexes share a common evolutionary origin. Proc. Natl. Acad. Sci. U. S. A. *106*, 4154–4159.

Li, M., Trong, I.L., Carl, M.A., Larson, E.T., Chou, S., Leon, J.A.D., Dove, S.L., Stenkamp, R.E., and Mougous, J.D. (2012). Structural Basis for Type VI Secretion Effector Recognition by a Cognate Immunity Protein. PLOS Pathog. *8*, e1002613.

Liang, X., Moore, R., Wilton, M., Wong, M.J.Q., Lam, L., and Dong, T.G. (2015). Identification of divergent type VI secretion effectors using a conserved chaperone domain. Proc. Natl. Acad. Sci. U. S. A. *112*, 9106–9111.

Liebling, M. (2010). PoorMan3DReg.

Lim, Y.T., Jobichen, C., Wong, J., Limmathurotsakul, D., Li, S., Chen, Y., Raida, M., Srinivasan, N., MacAry, P.A., Sivaraman, J., et al. (2015). Extended Loop Region of Hcp1 is Critical for the Assembly and Function of Type VI Secretion System in *Burkholderia pseudomallei*. Sci. Rep. *5*, 8235.

Lin, M.-F., and Lan, C.-Y. (2014). Antimicrobial resistance in *Acinetobacter baumannii*: From bench to bedside. World J. Clin. Cases WJCC *2*, 787–814.

Lin, J., Zhang, W., Cheng, J., Yang, X., Zhu, K., Wang, Y., Wei, G., Qian, P.-Y., Luo, Z.-Q., and Shen, X. (2017). A *Pseudomonas* T6SS effector recruits PQS-containing outer membrane vesicles for iron acquisition. Nat. Commun. *8*, 14888.

Lin, J.-S., Ma, L.-S., and Lai, E.-M. (2013). Systematic Dissection of the *Agrobacterium* Type VI Secretion System Reveals Machinery and Secreted Components for Subcomplex Formation. PLOS ONE *8*, e67647.

Lin, J.-S., Wu, H.-H., Hsu, P.-H., Ma, L.-S., Pang, Y.-Y., Tsai, M.-D., and Lai, E.-M. (2014). Fha Interaction with Phosphothreonine of TssL Activates Type VI Secretion in *Agrobacterium tumefaciens*. PLOS Pathog. *10*, e1003991.

Locht, C., Coutte, L., and Mielcarek, N. (2011). The ins and outs of pertussis toxin. FEBS J. *278*, 4668–4682.

Logger, L., Aschtgen, M.-S., Guérin, M., Cascales, E., and Durand, E. (2016). Molecular Dissection of the Interface between the Type VI Secretion TssM Cytoplasmic Domain and the TssG Baseplate Component. J. Mol. Biol. *428*, 4424–4437.

L. Oliveira, B., Guo, Z., and L. Bernardes, G.J. (2017). Inverse electron demand Diels–Alder reactions in chemical biology. Chem. Soc. Rev. *46*, 4895–4950.

Loquet, A., Sgourakis, N.G., Gupta, R., Giller, K., Riedel, D., Goosmann, C., Griesinger, C., Kolbe, M., Baker, D., Becker, S., et al. (2012). Atomic model of the type III secretion system needle. Nature *486*, nature11079.

Lossi, N.S., Dajani, R., Freemont, P., and Filloux, A. (2011). Structure-function analysis of HsiF, a gp25-like component of the type VI secretion system, in *Pseudomonas aeruginosa*. Microbiol. Read. Engl. *157*, 3292–3305.

Lossi, N.S., Manoli, E., Simpson, P., Jones, C., Hui, K., Dajani, R., Coulthurst, S.J., Freemont, P., and Filloux, A. (2012). The archetype *Pseudomonas aeruginosa* proteins TssB and TagJ form a novel subcomplex in the bacterial type VI secretion system. Mol. Microbiol. *86*, 437–456.

Lossi, N.S., Manoli, E., Förster, A., Dajani, R., Pape, T., Freemont, P., and Filloux, A. (2013). The HsiB1C1 (TssB-TssC) Complex of the *Pseudomonas aeruginosa* Type VI Secretion System Forms a Bacteriophage Tail Sheathlike Structure. J. Biol. Chem. *288*, 7536–7548.

Lotze, J., Reinhardt, U., Seitz, O., and G. Beck-Sickinger, A. (2016). Peptide-tags for site-specific protein labelling *in vitro* and *in vivo*. Mol. Biosyst. *12*, 1731–1745.

Low, H.H., Gubellini, F., Rivera-Calzada, A., Braun, N., Connery, S., Dujeancourt, A., Lu, F., Redzej, A., Fronzes, R., Orlova, E.V., et al. (2014). Structure of a type IV secretion system. Nature *508*, 550–553.

Ma, A.T., and Mekalanos, J.J. (2010). In vivo actin cross-linking induced by *Vibrio cholerae* type VI secretion system is associated with intestinal inflammation. Proc. Natl. Acad. Sci. *107*, 4365–4370.

Ma, A.T., McAuley, S., Pukatzki, S., and Mekalanos, J.J. (2009a). Translocation of a *Vibrio cholerae* Type VI Secretion Effector Requires Bacterial Endocytosis by Host Cells. Cell Host Microbe *5*, 234–243.

Ma, J., Pan, Z., Huang, J., Sun, M., Lu, C., and Yao, H. (2017). The Hcp proteins fused with diverse extended-toxin domains represent a novel pattern of antibacterial effectors in type VI secretion systems. Virulence *8*, 1189–1202.

Ma, L.-S., Lin, J.-S., and Lai, E.-M. (2009b). An IcmF Family Protein, $ImpL_M$, Is an Integral Inner Membrane Protein Interacting with $ImpK_L$, and Its Walker A Motif Is Required for Type VI Secretion System-Mediated Hcp Secretion in *Agrobacterium tumefaciens*. J. Bacteriol. *191*, 4316–4329.

Ma, L.-S., Narberhaus, F., and Lai, E.-M. (2012). IcmF Family Protein TssM Exhibits ATPase Activity and Energizes Type VI Secretion. J. Biol. Chem. *287*, 15610–15621.

Ma, L.-S., Hachani, A., Lin, J.-S., Filloux, A., and Lai, E.-M. (2014). *Agrobacterium tumefaciens* Deploys a Superfamily of Type VI Secretion DNase Effectors as Weapons for Interbacterial Competition In Planta. Cell Host Microbe *16*, 94–104.

MacIntyre, D.L., Miyata, S.T., Kitaoka, M., and Pukatzki, S. (2010). The *Vibrio cholerae* type VI secretion system displays antimicrobial properties. Proc. Natl. Acad. Sci. *107*, 19520–19524.

Madani, F., Lind, J., Damberg, P., Adams, S.R., Tsien, R.Y., and Gräslund, A.O. (2009). Hairpin Structure of a Biarsenical−Tetracysteine Motif Determined by NMR Spectroscopy. J. Am. Chem. Soc. *131*, 4613–4615.

Majerczyk, C., Schneider, E., and Greenberg, E.P. (2016). Quorum sensing control of Type VI secretion factors restricts the proliferation of quorum-sensing mutants. ELife *5*, e14712.

Makino, F., Shen, D., Kajimura, N., Kawamoto, A., Pissaridou, P., Oswin, H., Pain, M., Murillo, I., Namba, K., and Blocker, A.J. (2016). The Architecture of the Cytoplasmic Region of Type III Secretion Systems. Sci. Rep. *6*, srep33341.

Martin, B.R., Giepmans, B.N.G., Adams, S.R., and Tsien, R.Y. (2005). Mammalian cell–based optimization of the biarsenical-binding tetracysteine motif for improved fluorescence and affinity. Nat. Biotechnol. *23*, 1308–1314.

Maximo, A. (2016). Efficient finite impulse response filters in massively-parallel recursive systems. J. Real-Time Image Process. *12*, 603–611.

Mayer, S., and Lang, K. (2017). Tetrazines in Inverse-Electron-Demand Diels–Alder Cycloadditions and Their Use in Biology. Synthesis *49*, 830–848.

McNally, L., Bernardy, E., Thomas, J., Kalziqi, A., Pentz, J., Brown, S.P., Hammer, B.K., Yunker, P.J., and Ratcliff, W.C. (2017). Killing by Type VI secretion drives genetic phase separation and correlates with increased cooperation. Nat. Commun. *8*, 14371.

Meimetis, L.G., Carlson, J.C.T., Giedt, R.J., Kohler, R.H., and Weissleder, R. (2014). Ultrafluorogenic Coumarin–Tetrazine Probes for Real-Time Biological Imaging. Angew. Chem. Int. Ed. *53*, 7531–7534.

Metzgar, D., Bacher, J.M., Pezo, V., Reader, J., Döring, V., Schimmel, P., Marlière, P., and de Crécy-Lagard, V. (2004). *Acinetobacter* sp. ADP1: an ideal model organism for genetic analysis and genome engineering. Nucleic Acids Res. *32*, 5780–5790.

Michiels, T., Wattiau, P., Brasseur, R., Ruysschaert, J.M., and Cornelis, G. (1990). Secretion of Yop proteins by Yersiniae. Infect. Immun. *58*, 2840–2849.

Mills, E., Baruch, K., Charpentier, X., Kobi, S., and Rosenshine, I. (2008). Real-Time Analysis of Effector Translocation by the Type III Secretion System of Enteropathogenic *Escherichia coli*. Cell Host Microbe *3*, 104–113.

Miyata, S.T., Kitaoka, M., Brooks, T.M., McAuley, S.B., and Pukatzki, S. (2011). *Vibrio cholerae* Requires the Type VI Secretion System Virulence Factor VasX To Kill *Dictyostelium discoideum*. Infect. Immun. *79*, 2941–2949.

Miyata, S.T., Unterweger, D., Rudko, S.P., and Pukatzki, S. (2013). Dual Expression Profile of Type VI Secretion System Immunity Genes Protects Pandemic *Vibrio cholerae*. PLOS Pathog. *9*, e1003752.

Moody, M.F. (1967). Structure of the sheath of bacteriophage T4: II. Rearrangement of the sheath subunits during contraction. J. Mol. Biol. *25*, 201–208.

Moody, M.F. (1973). Sheath of bacteriophage T4: III. Contraction mechanism deduced from partially contracted sheaths. J. Mol. Biol. *80*, 613–635.

Moore, M.M., Fernandez, D.L., and Thune, R.L. (2002). Cloning and characterization of *Edwardsiella ictaluri* proteins expressed and recognized by the channel catfish *Ictalurus punctatus* immune response during infection. Dis. Aquat. Organ. *52*, 93–107.

Mougous, J.D., Cuff, M.E., Raunser, S., Shen, A., Zhou, M., Gifford, C.A., Goodman, A.L., Joachimiak, G., Ordoñez, C.L., Lory, S., et al. (2006). A Virulence Locus of *Pseudomonas aeruginosa* Encodes a Protein Secretion Apparatus. Science *312*, 1526–1530.

Mougous, J.D., Gifford, C.A., Ramsdell, T.L., and Mekalanos, J.J. (2007). Threonine phosphorylation post-translationally regulates protein secretion in *Pseudomonas aeruginosa*. Nat. Cell Biol. *9*, 797–803.

Mukherjee, A., Weyant, K.B., Agrawal, U., Walker, J., Cann, I.K.O., and Schroeder, C.M. (2015). Engineering and Characterization of New LOV-Based Fluorescent Proteins from *Chlamydomonas reinhardtii* and *Vaucheria frigida*. ACS Synth. Biol. *4*, 371–377.

Murillo, I., Martinez-Argudo, I., and Blocker, A.J. (2016). Genetic Dissection of the Signaling Cascade that Controls Activation of the *Shigella* Type III Secretion System from the Needle Tip. Sci. Rep. *6*, srep27649.

Murrey, H.E., Judkins, J.C., am Ende, C.W., Ballard, T.E., Fang, Y., Riccardi, K., Di, L., Guilmette, E.R., Schwartz, J.W., Fox, J.M., et al. (2015). Systematic Evaluation of Bioorthogonal Reactions in Live Cells with Clickable HaloTag Ligands: Implications for Intracellular Imaging. J. Am. Chem. Soc. *137*, 11461–11475.

Nano, F.E., Zhang, N., Cowley, S.C., Klose, K.E., Cheung, K.K.M., Roberts, M.J., Ludu, J.S., Letendre, G.W., Meierovics, A.I., Stephens, G., et al. (2004). A *Francisella tularensis* Pathogenicity Island Required for Intramacrophage Growth. J. Bacteriol. *186*, 6430–6436.

Nans, A., Kudryashev, M., Saibil, H.R., and Hayward, R.D. (2015). Structure of a bacterial type III secretion system in contact with a host membrane *in situ*. Nat. Commun. *6*, ncomms10114.

Nazarov, S., Schneider, J.P., Brackmann, M., Goldie, K.N., Stahlberg, H., and Basler, M. (2018). Cryo-EM reconstruction of Type VI secretion system baseplate and sheath distal end. EMBO J. *37*, e97103.

Nehab, D., Maximo, A., Lima, R.S., and Hoppe, H. (2011). GPU-efficient Recursive Filtering and Summed-area Tables. In Proceedings of the 2011 SIGGRAPH Asia Conference, (New York, NY, USA: ACM), pp. 176:1–176:12.

Neidhardt, F.C., Bloch, P.L., and Smith, D.F. (1974). Culture Medium for Enterobacteria. J. Bacteriol. *119*, 736–747.

Nguyen, V.S., Logger, L., Spinelli, S., Legrand, P., Pham, T.T.H., Trinh, T.T.N., Cherrak, Y., Zoued, A., Desmyter, A., Durand, E., et al. (2017). Type VI secretion TssK baseplate protein exhibits structural similarity with phage receptor-binding proteins and evolved to bind the membrane complex. Nat. Microbiol. *2*, nmicrobiol2017103.

Nikić, I., and Lemke, E.A. (2015). Genetic code expansion enabled site-specific dual-color protein labeling: superresolution microscopy and beyond. Curr. Opin. Chem. Biol. *28*, 164–173.

Nikić, I., Plass, T., Schraidt, O., Szymański, J., Briggs, J.A.G., Schultz, C., and Lemke, E.A. (2014). Minimal Tags for Rapid Dual-Color Live-Cell Labeling and Super-Resolution Microscopy. Angew. Chem. Int. Ed. *53*, 2245–2249.

Ning, X., Guo, J., Wolfert, M.A., and Boons, G.-J. (2008). Visualizing Metabolically Labeled Glycoconjugates of Living Cells by Copper-Free and Fast Huisgen Cycloadditions. Angew. Chem. Int. Ed. *47*, 2253–2255.

Osipiuk, J., Xu, X., Cui, H., Savchenko, A., Edwards, A., and Joachimiak, A. (2011). Crystal structure of secretory protein Hcp3 from *Pseudomonas aeruginosa*. J. Struct. Funct. Genomics *12*, 21.

Palmen, R., Vosman, B., Kok, R., Zee, J.R., and Hellingwerf, K.J. (1992). Characterization of transformation-deficient mutants of *Acinetobacter calcoaceticus*. Mol. Microbiol. *6*, 1747–1754.

Palmen, R., Vosman, B., Buijsman, P., Breek, C.K.D., and Hellingwerf, K.J. (1993). Physiological characterization of natural transformation in *Acinetobacter calcoaceticus*. J. Gen. Microbiol. *139*, 295–305.

Pantoja, M., Chen, L., Chen, Y., and Nester, E.W. (2002). *Agrobacterium* type IV secretion is a two-step process in which export substrates associate with the virulence protein VirJ in the periplasm. Mol. Microbiol. *45*, 1325–1335.

Paolo, D.D., Afanzar, O., Armitage, J.P., and Berry, R.M. (2016). Single-molecule imaging of electroporated dye-labelled CheY in live *Escherichia coli*. Phil Trans R Soc B *371*, 20150492.

Parsons, D.A., and Heffron, F. (2005). *sciS*, an *icmF* Homolog in *Salmonella enterica* Serovar Typhimurium, Limits Intracellular Replication and Decreases Virulence. Infect. Immun. *73*, 4338–4345.

Pell, L.G., Kanelis, V., Donaldson, L.W., Howell, P.L., and Davidson, A.R. (2009). The phage λ major tail protein structure reveals a common evolution for long-tailed phages and the type VI bacterial secretion system. Proc. Natl. Acad. Sci. *106*, 4160–4165.

Persson, O.P., Pinhassi, J., Riemann, L., Marklund, B.-I., Rhen, M., Normark, S., González, J.M., and Hagström, Å. (2009). High abundance of virulence gene homologues in marine bacteria. Environ. Microbiol. *11*, 1348–1357.

Pettersen, E.F., Goddard, T.D., Huang, C.C., Couch, G.S., Greenblatt, D.M., Meng, E.C., and Ferrin, T.E. (2004). UCSF Chimera—A visualization system for exploratory research and analysis. J. Comput. Chem. *25*, 1605–1612.

Pietrosiuk, A., Lenherr, E.D., Falk, S., Bönemann, G., Kopp, J., Zentgraf, H., Sinning, I., and Mogk, A. (2011). Molecular Basis for the Unique Role of the AAA^+ Chaperone ClpV in Type VI Protein Secretion. J. Biol. Chem. *286*, 30010–30021.

Pitzschke, A., and Hirt, H. (2010). New insights into an old story: *Agrobacterium*-induced tumour formation in plants by plant transformation. EMBO J. *29*, 1021–1032.

Plamont, M.-A., Billon-Denis, E., Maurin, S., Gauron, C., Pimenta, F.M., Specht, C.G., Shi, J., Quérard, J., Pan, B., Rossignol, J., et al. (2016). Small fluorescence-activating and absorption-shifting tag for tunable protein imaging in vivo. Proc. Natl. Acad. Sci. *113*, 497–502.

Planamente, S., Salih, O., Manoli, E., Albesa-Jové, D., Freemont, P.S., and Filloux, A. (2016). TssA forms a gp6-like ring attached to the type VI secretion sheath. EMBO J. *35*, 1613–1627.

Plano, G.V., and Schesser, K. (2013). The *Yersinia pestis* type III secretion system: expression, assembly and role in the evasion of host defenses. Immunol. Res. *57*, 237–245.

Plass, T., Milles, S., Koehler, C., Szymański, J., Mueller, R., Wießler, M., Schultz, C., and Lemke, E.A. (2012). Amino Acids for Diels–Alder Reactions in Living Cells. Angew. Chem. Int. Ed. *51*, 4166–4170.

Portaliou, A.G., Tsolis, K.C., Loos, M.S., Zorzini, V., and Economou, A. (2016). Type III Secretion: Building and Operating a Remarkable Nanomachine. Trends Biochem. Sci. *41*, 175–189.

Potvin, E., Lehoux, D.E., Kukavica-Ibrulj, I., Richard, K.L., Sanschagrin, F., Lau, G.W., and Levesque, R.C. (2003). *In vivo* functional genomics of *Pseudomonas aeruginosa* for high-throughput screening of new virulence factors and antibacterial targets. Environ. Microbiol. *5*, 1294–1308.

Pukatzki, S., Ma, A.T., Sturtevant, D., Krastins, B., Sarracino, D., Nelson, W.C., Heidelberg, J.F., and Mekalanos, J.J. (2006). Identification of a conserved bacterial protein secretion system in *Vibrio cholerae* using the *Dictyostelium* host model system. Proc. Natl. Acad. Sci. *103*, 1528–1533.

Pukatzki, S., Ma, A.T., Revel, A.T., Sturtevant, D., and Mekalanos, J.J. (2007). Type VI secretion system translocates a phage tail spike-like protein into target cells where it cross-links actin. Proc. Natl. Acad. Sci. U. S. A. *104*, 15508–15513.

Radics, J., Königsmaier, L., and Marlovits, T.C. (2013). Structure of a pathogenic type 3 secretion system in action. Nat. Struct. Mol. Biol. *21*, 82–87.

Ramirez, M.S., Don, M., Merkier, A.K., Bistué, A.J.S., Zorreguieta, A., Centrón, D., and Tolmasky, M.E. (2010). Naturally Competent *Acinetobacter baumannii* Clinical Isolate as a Convenient Model for Genetic Studies. J. Clin. Microbiol. *48*, 1488–1490.

Raymond, B., Young, J.C., Pallett, M., Endres, R.G., Clements, A., and Frankel, G. (2013). Subversion of trafficking, apoptosis, and innate immunity by type III secretion system effectors. Trends Microbiol. *21*, 430–441.

Redzej, A., Ukleja, M., Connery, S., Trokter, M., Felisberto-Rodrigues, C., Cryar, A., Thalassinos, K., Hayward, R.D., Orlova, E.V., and Waksman, G. (2017). Structure of a VirD4 coupling protein bound to a VirB type IV secretion machinery. EMBO J. *36*, 3080–3095.

Repizo, G.D., Gagne, S., Foucault-Grunenwald, M.-L., Borges, V., Charpentier, X., Limansky, A.S., Gomes, J.P., Viale, A.M., and Salcedo, S.P. (2015). Differential Role of the T6SS in *Acinetobacter baumannii* Virulence. PloS One *10*, e0138265.

Rigard, M., Bröms, J.E., Mosnier, A., Hologne, M., Martin, A., Lindgren, L., Punginelli, C., Lays, C., Walker, O., Charbit, A., et al. (2016). *Francisella tularensis* IglG Belongs to a Novel Family of PAAR-Like T6SS Proteins and Harbors a Unique N-terminal Extension Required for Virulence. PLOS Pathog. *12*, e1005821.

Robb, C.S., Robb, M., Nano, F.E., and Boraston, A.B. (2016). The Structure of the Toxin and Type Six Secretion System Substrate Tse2 in Complex with Its Immunity Protein. Structure *24*, 277–284.

Robinson, M.D., McCarthy, D.J., and Smyth, G.K. (2010). edgeR: a Bioconductor package for differential expression analysis of digital gene expression data. Bioinformatics *26*, 139–140.

Roest, H.P., Mulders, I.H.M., Spaink, H.P., Wijffelman, C.A., and Lugtenberg, B.J.J. (1997). A *Rhizobium leguminosarum* Biovar *trifolii* Locus Not Localized on the Sym Plasmid Hinders Effective Nodulation on Plants of the Pea Cross-Inoculation Group. Mol. Plant. Microbe Interact. *10*, 938–941.

Rostovtsev, V.V., Green, L.G., Fokin, V.V., and Sharpless, K.B. (2002). A Stepwise Huisgen Cycloaddition Process: Copper(I)-Catalyzed Regioselective "Ligation" of Azides and Terminal Alkynes. Angew. Chem. Int. Ed. *41*, 2596–2599.

Rotman, B., and Papermaster, B.W. (1966). Membrane properties of living mammalian cells as studied by enzymatic hydrolysis of fluorogenic esters. Proc. Natl. Acad. Sci. *55*, 134–141.

Ruijters, D., and Thévenaz, P. (2012). GPU Prefilter for Accurate Cubic B-spline Interpolation. Comput. J. *55*, 15–20.

Ruiz, F.M., Santillana, E., Spínola-Amilibia, M., Torreira, E., Culebras, E., and Romero, A. (2015). Crystal Structure of Hcp from *Acinetobacter baumannii*: A Component of the Type VI Secretion System. PLOS ONE *10*, e0129691.

Russell, A.B., Hood, R.D., Bui, N.K., LeRoux, M., Vollmer, W., and Mougous, J.D. (2011). Type VI secretion delivers bacteriolytic effectors to target cells. Nature *475*, 343–347.

Russell, A.B., Singh, P., Brittnacher, M., Bui, N.K., Hood, R.D., Carl, M.A., Agnello, D.M., Schwarz, S., Goodlett, D.R., Vollmer, W., et al. (2012). A Widespread Bacterial Type VI Secretion Effector Superfamily Identified Using a Heuristic Approach. Cell Host Microbe *11*, 538–549.

Russell, A.B., LeRoux, M., Hathazi, K., Agnello, D.M., Ishikawa, T., Wiggins, P.A., Wai, S.N., and Mougous, J.D. (2013). Diverse type VI secretion phospholipases are functionally plastic antibacterial effectors. Nature *496*, 508–512.

Russell, A.B., Wexler, A.G., Harding, B.N., Whitney, J.C., Bohn, A.J., Goo, Y.A., Tran, B.Q., Barry, N.A., Zheng, H., Peterson, S.B., et al. (2014). A Type VI Secretion-Related Pathway in Bacteroidetes Mediates Interbacterial Antagonism. Cell Host Microbe *16*, 227–236.

Russo, B.C., Stamm, L.M., Raaben, M., Kim, C.M., Kahoud, E., Robinson, L.R., Bose, S., Queiroz, A.L., Herrera, B.B., Baxt, L.A., et al. (2016). Intermediate filaments enable pathogen docking to trigger type 3 effector translocation. Nat. Microbiol. *1*, nmicrobiol201625.

Sahdev, R., Sage, D., Prodanov, D., and Konopczyński, T. (2017). TimeLapseReg.

Salomon, D. (2016). MIX and match: mobile T6SS MIX-effectors enhance bacterial fitness. Mob. Genet. Elem. *6*, e1123796.

Salomon, D., Kinch, L.N., Trudgian, D.C., Guo, X., Klimko, J.A., Grishin, N.V., Mirzaei, H., and Orth, K. (2014). Marker for type VI secretion system effectors. Proc. Natl. Acad. Sci. U. S. A. *111*, 9271–9276.

Salomon, D., Klimko, J.A., Trudgian, D.C., Kinch, L.N., Grishin, N.V., Mirzaei, H., and Orth, K. (2015). Type VI Secretion System Toxins Horizontally Shared between Marine Bacteria. PLoS Pathog. *11*, e1005128.

Sana, T.G., Hachani, A., Bucior, I., Soscia, C., Garvis, S., Termine, E., Engel, J., Filloux, A., and Bleves, S. (2012). The Second Type VI Secretion System of *Pseudomonas aeruginosa* Strain PAO1 Is Regulated by Quorum Sensing and Fur and Modulates Internalization in Epithelial Cells. J. Biol. Chem. *287*, 27095–27105.

Sana, T.G., Baumann, C., Merdes, A., Soscia, C., Rattei, T., Hachani, A., Jones, C., Bennett, K.L., Filloux, A., Superti-Furga, G., et al. (2015). Internalization of *Pseudomonas aeruginosa* Strain PAO1 into Epithelial Cells Is Promoted by Interaction of a T6SS Effector with the Microtubule Network. MBio *6*, e00712-15.

Sana, T.G., Flaugnatti, N., Lugo, K.A., Lam, L.H., Jacobson, A., Baylot, V., Durand, E., Journet, L., Cascales, E., and Monack, D.M. (2016). *Salmonella* Typhimurium utilizes a T6SS-mediated antibacterial weapon to establish in the host gut. Proc. Natl. Acad. Sci. *113*, E5044–E5051.

Santin, Y.G., and Cascales, E. (2017). Domestication of a housekeeping transglycosylase for assembly of a Type VI secretion system. EMBO Rep. *18*, 138–149.

Schell, M.A., Ulrich, R.L., Ribot, W.J., Brueggemann, E.E., Hines, H.B., Chen, D., Lipscomb, L., Kim, H.S., Mrázek, J., Nierman, W.C., et al. (2007). Type VI secretion is a major virulence determinant in *Burkholderia mallei*. Mol. Microbiol. *64*, 1466–1485.

Schneider, J.P., and Basler, M. (2016). Shedding light on biology of bacterial cells. Phil Trans R Soc B *371*, 20150499.

Schneider, C.A., Rasband, W.S., and Eliceiri, K.W. (2012). NIH Image to ImageJ: 25 years of image analysis. Nat. Methods *9*, 671–675.

Schwarz, S., West, T.E., Boyer, F., Chiang, W.-C., Carl, M.A., Hood, R.D., Rohmer, L., Tolker-Nielsen, T., Skerrett, S.J., and Mougous, J.D. (2010). Burkholderia Type VI Secretion Systems Have Distinct Roles in Eukaryotic and Bacterial Cell Interactions. PLOS Pathog. *6*, e1001068.

Schwarz, S., Singh, P., Robertson, J.D., LeRoux, M., Skerrett, S.J., Goodlett, D.R., West, T.E., and Mougous, J.D. (2014). VgrG-5 Is a *Burkholderia* Type VI Secretion System-Exported Protein Required for Multinucleated Giant Cell Formation and Virulence. Infect. Immun. *82*, 1445–1452.

Scouras, A.D., and Daggett, V. (2011). The dynameomics rotamer library: Amino acid side chain conformations and dynamics from comprehensive molecular dynamics simulations in water. Protein Sci. *20*, 341–352.

Seshadri, R., Joseph, S.W., Chopra, A.K., Sha, J., Shaw, J., Graf, J., Haft, D., Wu, M., Ren, Q., Rosovitz, M.J., et al. (2006). Genome Sequence of *Aeromonas hydrophila* ATCC 7966^{T}: Jack of All Trades. J. Bacteriol. *188*, 8272–8282.

Shalom, G., Shaw, J.G., and Thomas, M.S. (2007). *In vivo* expression technology identifies a type VI secretion system locus in *Burkholderia pseudomallei* that is induced upon invasion of macrophages. Microbiology *153*, 2689–2699.

Shang, X., Song, X., Faller, C., Lai, R., Li, H., Cerny, R., Niu, W., and Guo, J. (2017). Fluorogenic protein labeling using a genetically encoded unstrained alkene. Chem. Sci. *8*, 1141–1145.

Sharma, V.P. (2015). HyperStackReg.

Shechter, N., Zaltzman, L., Weiner, A., Brumfeld, V., Shimoni, E., Fridmann-Sirkis, Y., and Minsky, A. (2013). Stress-induced Condensation of Bacterial Genomes Results in Re-pairing of Sister Chromosomes IMPLICATIONS FOR DOUBLE STRAND DNA BREAK REPAIR. J. Biol. Chem. *288*, 25659–25667.

Shneider, M.M., Buth, S.A., Ho, B.T., Basler, M., Mekalanos, J.J., and Leiman, P.G. (2013). PAAR-repeat proteins sharpen and diversify the type VI secretion system spike. Nature *500*, 350–353.

Shrivastava, S., and Mande, S.S. (2008). Identification and Functional Characterization of Gene Components of Type VI Secretion System in Bacterial Genomes. PLOS ONE *3*, e2955.

Shu, A.-C., Wu, C.-C., Chen, Y.-Y., Peng, H.-L., Chang, H.-Y., and Yew, T.-R. (2008). Evidence of DNA Transfer through F-pilus Channels during *Escherichia coli* Conjugation. Langmuir *24*, 6796–6802.

Si, M., Zhao, C., Burkinshaw, B., Zhang, B., Wei, D., Wang, Y., Dong, T.G., and Shen, X. (2017). Manganese scavenging and oxidative stress response mediated by type VI secretion system in *Burkholderia thailandensis*. Proc. Natl. Acad. Sci. *114*, E2233–E2242.

Silverman, J.M., Austin, L.S., Hsu, F., Hicks, K.G., Hood, R.D., and Mougous, J.D. (2011). Separate inputs modulate phosphorylation-dependent and -independent type VI secretion activation. Mol. Microbiol. *82*, 1277–1290.

Silverman, J.M., Agnello, D.M., Zheng, H., Andrews, B.T., Li, M., Catalano, C.E., Gonen, T., and Mougous, J.D. (2013). Haemolysin Coregulated Protein Is an Exported Receptor and Chaperone of Type VI Secretion Substrates. Mol. Cell *51*, 584–593.

So, E.C., Mattheis, C., Tate, E.W., Frankel, G., and Schroeder, G.N. (2015). Creating a customized intracellular niche: subversion of host cell signaling by *Legionella* type IV secretion system effectors. Can. J. Microbiol. *61*, 617–635.

Souza, D.P., Oka, G.U., Alvarez-Martinez, C.E., Bisson-Filho, A.W., Dunger, G., Hobeika, L., Cavalcante, N.S., Alegria, M.C., Barbosa, L.R.S., Salinas, R.K., et al. (2015). Bacterial killing via a type IV secretion system. Nat. Commun. *6*, ncomms7453.

Spínola-Amilibia, M., Davó-Siguero, I., Ruiz, F.M., Santillana, E., Medrano, F.J., and Romero, A. (2016). The structure of VgrG1 from *Pseudomonas aeruginosa*, the needle tip of the bacterial type VI secretion system. Acta Crystallogr. Sect. Struct. Biol. *72*, 22–33.

Srikannathasan, V., English, G., Bui, N.K., Trunk, K., O'Rourke, P.E.F., Rao, V.A., Vollmer, W., Coulthurst, S.J., and Hunter, W.N. (2013). Structural basis for type VI secreted peptidoglycan DL-endopeptidase function, specificity and neutralization in *Serratia marcescens*. Acta Crystallogr. D Biol. Crystallogr. *69*, 2468–2482.

Srinivasa Rao, P.S., Yamada, Y., Tan, Y.P., and Leung, K.Y. (2004). Use of proteomics to identify novel virulence determinants that are required for *Edwardsiella tarda* pathogenesis. Mol. Microbiol. *53*, 573–586.

Stone, J.E., Gohara, D., and Shi, G. (2010). OpenCL: A Parallel Programming Standard for Heterogeneous Computing Systems. Comput. Sci. Eng. *12*, 66–73.

Suarez, G., Sierra, J.C., Sha, J., Wang, S., Erova, T.E., Fadl, A.A., Foltz, S.M., Horneman, A.J., and Chopra, A.K. (2008). Molecular characterization of a functional type VI secretion system from a clinical isolate of *Aeromonas hydrophila*. Microb. Pathog. *44*, 344–361.

Suarez, G., Sierra, J.C., Kirtley, M.L., and Chopra, A.K. (2010a). Role of Hcp, a type 6 secretion system effector, of *Aeromonas hydrophila* in modulating activation of host immune cells. Microbiology *156*, 3678–3688.

Suarez, G., Sierra, J.C., Erova, T.E., Sha, J., Horneman, A.J., and Chopra, A.K. (2010b). A Type VI Secretion System Effector Protein, VgrG1, from *Aeromonas hydrophila* That Induces Host Cell Toxicity by ADP Ribosylation of Actin. J. Bacteriol. *192*, 155–168.

Suarez, G., Romero-Gallo, J., Piazuelo, M.B., Wang, G., Maier, R.J., Forsberg, L.S., Azadi, P., Gomez, M.A., Correa, P., and Peek, R.M. (2015). Modification of *Helicobacter pylori* Peptidoglycan Enhances NOD1 Activation and Promotes Cancer of the Stomach. Cancer Res. *75*, 1749–1759.

Suo, Z., Avci, R., Deliorman, M., Yang, X., and Pascual, D.W. (2009). Bacteria Survive Multiple Puncturings of Their Cell Walls. Langmuir *25*, 4588–4594.

Sustarsic, M., Plochowietz, A., Aigrain, L., Yuzenkova, Y., Zenkin, N., and Kapanidis, A. (2014). Optimized delivery of fluorescently labeled proteins in live bacteria using electroporation. Histochem. Cell Biol. *142*, 113–124.

Sycheva, L.V., Shneider, M.M., Basler, M., Ho, B.T., Mekalanos, J.J., and Leiman, P.G. The conserved architecture of the T6SS central spike complex. Be Publ.

Taylor, M.T., Blackman, M.L., Dmitrenko, O., and Fox, J.M. (2011). Design and Synthesis of Highly Reactive Dienophiles for the Tetrazine–*trans*-Cyclooctene Ligation. J. Am. Chem. Soc. *133*, 9646–9649.

Taylor, N.M.I., Prokhorov, N.S., Guerrero-Ferreira, R.C., Shneider, M.M., Browning, C., Goldie, K.N., Stahlberg, H., and Leiman, P.G. (2016). Structure of the T4 baseplate and its function in triggering sheath contraction. Nature *533*, 346–352.

Thalhammer, F., Wallfahrer, U., and Sauer, J. (1990). Reaktivität einfacher offenkettiger und cyclischer dienophile bei Diels-Alder-reaktionen mit inversem elektronenbedarf. Tetrahedron Lett. *31*, 6851–6854.

Thévenaz, P., Ruttimann, U.E., and Unser, M. (1998). A pyramid approach to subpixel registration based on intensity. IEEE Trans. Image Process. Publ. IEEE Signal Process. Soc. *7*, 27–41.

Thomas, J., Watve, S.S., Ratcliff, W.C., and Hammer, B.K. (2017). Horizontal Gene Transfer of Functional Type VI Killing Genes by Natural Transformation. MBio *8*, e00654-17.

Tornøe, C.W., Christensen, C., and Meldal, M. (2002). Peptidotriazoles on Solid Phase: [1,2,3]-Triazoles by Regiospecific Copper(I)-Catalyzed 1,3-Dipolar Cycloadditions of Terminal Alkynes to Azides. J. Org. Chem. *67*, 3057–3064.

Trokter, M., Felisberto-Rodrigues, C., Christie, P.J., and Waksman, G. (2014). Recent advances in the structural and molecular biology of type IV secretion systems. Curr. Opin. Struct. Biol. *27*, 16–23.

Uchida, K., Leiman, P.G., Arisaka, F., and Kanamaru, S. (2014). Structure and properties of the C-terminal β-helical domain of VgrG protein from *Escherichia coli* O157. J. Biochem. (Tokyo) *155*, 173–182.

Unser, M., Aldroubi, A., and Eden, M. (1991). Fast B-spline transforms for continuous image representation and interpolation. IEEE Trans. Pattern Anal. Mach. Intell. *13*, 277–285.

Unser, M., Aldroubi, A., and Eden, M. (1993a). The L_2-polynomial spline pyramid. IEEE Trans. Pattern Anal. Mach. Intell. *15*, 364–379.

Unser, M., Aldroubi, A., and Eden, M. (1993b). B-spline signal processing. I. Theory. IEEE Trans. Signal Process. *41*, 821–833.

Unser, M., Aldroubi, A., and Eden, M. (1993c). B-spline signal processing. II. Efficiency design and applications. IEEE Trans. Signal Process. *41*, 834–848.

Unterweger, D., Miyata, S.T., Bachmann, V., Brooks, T.M., Mullins, T., Kostiuk, B., Provenzano, D., and Pukatzki, S. (2014). The *Vibrio cholerae* type VI secretion system employs diverse effector modules for intraspecific competition. Nat. Commun. *5*, 3549.

Unterweger, D., Kostiuk, B., Ötjengerdes, R., Wilton, A., Diaz-Satizabal, L., and Pukatzki, S. (2015). Chimeric adaptor proteins translocate diverse type VI secretion system effectors in *Vibrio cholerae*. EMBO J. *34*, 2198–2210.

VanEngelenburg, S.B., and Palmer, A.E. (2008). Quantification of Real-Time *Salmonella* Effector Type III Secretion Kinetics Reveals Differential Secretion Rates for SopE2 and SptP. Chem. Biol. *15*, 619–628.

Vázquez, A., Dzijak, R., Dračínský, M., Rampmaier, R., Siegl, S.J., and Vrabel, M. (2017). Mechanism-Based Fluorogenic *trans*-Cyclooctene–Tetrazine Cycloaddition. Angew. Chem. Int. Ed. *56*, 1334–1337.

Veenendaal, A.K.J., Hodgkinson, J.L., Schwarzer, L., Stabat, D., Zenk, S.F., and Blocker, A.J. (2007). The type III secretion system needle tip complex mediates host cell sensing and translocon insertion. Mol. Microbiol. *63*, 1719–1730.

Vettiger, A., and Basler, M. (2016). Type VI Secretion System Substrates Are Transferred and Reused among Sister Cells. Cell *167*, 99-110.e12.

Vettiger, A., Winter, J., Lin, L., and Basler, M. (2017). The type VI secretion system sheath assembles at the end distal from the membrane anchor. Nat. Commun. *8*, ncomms16088.

Viala, J., Chaput, C., Boneca, I.G., Cardona, A., Girardin, S.E., Moran, A.P., Athman, R., Mémet, S., Huerre, M.R., Coyle, A.J., et al. (2004). Nod1 responds to peptidoglycan delivered by the *Helicobacter pylori cag* pathogenicity island. Nat. Immunol. *5*, ni1131.

Viprey, V., Del Greco, A., Golinowski, W., Broughton, W.J., and Perret, X. (1998). Symbiotic implications of type III protein secretion machinery in *Rhizobium*. Mol. Microbiol. *28*, 1381–1389.

Walker, A.S., Rablen, P.R., and Schepartz, A. (2016). Rotamer-Restricted Fluorogenicity of the Bis-Arsenical ReAsH. J. Am. Chem. Soc. *138*, 7143–7150.

Wan, B., Zhang, Q., Ni, J., Li, S., Wen, D., Li, J., Xiao, H., He, P., Ou, H., Tao, J., et al. (2017). Type VI secretion system contributes to Enterohemorrhagic *Escherichia coli* virulence by secreting catalase against host reactive oxygen species (ROS). PLOS Pathog. *13*, e1006246.

Wang, J., Li, C., Yang, H., Mushegian, A., and Jin, S. (1998). A Novel Serine/Threonine Protein Kinase Homologue of *Pseudomonas aeruginosa* Is Specifically Inducible within the Host Infection Site and Is Required for Full Virulence in Neutropenic Mice. J. Bacteriol. *180*, 6764–6768.

Wang, J., Brackmann, M., Castaño-Díez, D., Kudryashev, M., Goldie, K.N., Maier, T., Stahlberg, H., and Basler, M. (2017). Cryo-EM structure of the extended type VI secretion system sheath–tube complex. Nat. Microbiol. *2*, 1507–1512.

Wang, L., Nie, J., Sicotte, H., Li, Y., Eckel-Passow, J.E., Dasari, S., Vedell, P.T., Barman, P., Wang, L., Weinshiboum, R., et al. (2016). Measure transcript integrity using RNA-seq data. BMC Bioinformatics *17*, 58.

Wang, T., Si, M., Song, Y., Zhu, W., Gao, F., Wang, Y., Zhang, L., Zhang, W., Wei, G., Luo, Z.-Q., et al. (2015). Type VI Secretion System Transports Zn^{2+} to Combat Multiple Stresses and Host Immunity. PLOS Pathog. *11*, e1005020.

Weber, B.S., Miyata, S.T., Iwashkiw, J.A., Mortensen, B.L., Skaar, E.P., Pukatzki, S., and Feldman, M.F. (2013). Genomic and Functional Analysis of the Type VI Secretion System in *Acinetobacter*. PLOS ONE *8*, e55142.

Weber, B.S., Ly, P.M., Irwin, J.N., Pukatzki, S., and Feldman, M.F. (2015). A multidrug resistance plasmid contains the molecular switch for type VI secretion in *Acinetobacter baumannii*. Proc. Natl. Acad. Sci. *112*, 9442–9447.

Weber, B.S., Hennon, S.W., Wright, M.S., Scott, N.E., Berardinis, V. de, Foster, L.J., Ayala, J.A., Adams, M.D., and Feldman, M.F. (2016). Genetic Dissection of the Type VI Secretion System in *Acinetobacter* and Identification of a Novel Peptidoglycan Hydrolase, TagX, Required for Its Biogenesis. MBio *7*, e01253-16.

Weber, B.S., Kinsella, R.L., Harding, C.M., and Feldman, M.F. (2017). The Secrets of *Acinetobacter* Secretion. Trends Microbiol. *25*, 532–545.

Wenren, L.M., Sullivan, N.L., Cardarelli, L., Septer, A.N., and Gibbs, K.A. (2013). Two Independent Pathways for Self-Recognition in *Proteus mirabilis* Are Linked by Type VI-Dependent Export. MBio *4*, e00374-13.

Wexler, A.G., Bao, Y., Whitney, J.C., Bobay, L.-M., Xavier, J.B., Schofield, W.B., Barry, N.A., Russell, A.B., Tran, B.Q., Goo, Y.A., et al. (2016). Human symbionts inject and neutralize antibacterial toxins to persist in the gut. Proc. Natl. Acad. Sci. *113*, 3639–3644.

Whitney, J.C., Chou, S., Russell, A.B., Biboy, J., Gardiner, T.E., Ferrin, M.A., Brittnacher, M., Vollmer, W., and Mougous, J.D. (2013). Identification, Structure, and Function of a Novel Type VI Secretion Peptidoglycan Glycoside Hydrolase Effector-Immunity Pair. J. Biol. Chem. *288*, 26616–26624.

Whitney, J.C., Beck, C.M., Goo, Y.A., Russell, A.B., Harding, B.N., De Leon, J.A., Cunningham, D.A., Tran, B.Q., Low, D.A., Goodlett, D.R., et al. (2014). Genetically distinct pathways guide effector export through the type VI secretion system. Mol. Microbiol. *92*, 529–542.

Whitney, J.C., Quentin, D., Sawai, S., LeRoux, M., Harding, B.N., Ledvina, H.E., Tran, B.Q., Robinson, H., Goo, Y.A., Goodlett, D.R., et al. (2015). An Interbacterial NAD(P)$^+$ Glycohydrolase Toxin Requires Elongation Factor Tu for Delivery to Target Cells. Cell *163*, 607–619.

Wieczorek, A., Buckup, T., and Wombacher, R. (2014). Rigid tetrazine fluorophore conjugates with fluorogenic properties in the inverse electron demand Diels–Alder reaction. Org. Biomol. Chem. *12*, 4177–4185.

Wieczorek, A., Werther, P., Euchner, J., and Wombacher, R. (2017). Green- to far-red-emitting fluorogenic tetrazine probes – synthetic access and no-wash protein imaging inside living cells. Chem. Sci. *8*, 1506–1510.

Wilharm, G., Lehmann, V., Krauss, K., Lehnert, B., Richter, S., Ruckdeschel, K., Heesemann, J., and Trülzsch, K. (2004). *Yersinia enterocolitica* Type III Secretion Depends on the Proton Motive Force but Not on the Flagellar Motor Components MotA and MotB. Infect. Immun. *72*, 4004–4009.

Williams, S.G., Varcoe, L.T., Attridge, S.R., and Manning, P.A. (1996). *Vibrio cholerae* Hcp, a Secreted Protein Coregulated with HlyA. Infect. Immun. *64*, 283–289.

Wilton, M., Wong, M.J.Q., Tang, L., Liang, X., Moore, R., Parkins, M.D., Lewenza, S., and Dong, T.G. (2016). Chelation of Membrane-Bound Cations by Extracellular DNA Activates the Type VI Secretion System in *Pseudomonas aeruginosa*. Infect. Immun. *84*, 2355–2361.

Wong, M.J.Q., Liang, X., Smart, M., Tang, L., Moore, R., Ingalls, B., and Dong, T.G. (2016). Microbial Herd Protection Mediated by Antagonistic Interaction in Polymicrobial Communities. Appl. Environ. Microbiol. *82*, 6881–6888.

Wu, H., Cisneros, B.T., Cole, C.M., and Devaraj, N.K. (2014a). Bioorthogonal Tetrazine-Mediated Transfer Reactions Facilitate Reaction Turnover in Nucleic Acid-Templated Detection of MicroRNA. J. Am. Chem. Soc. *136*, 17942–17945.

Wu, H., Yang, J., Šečkutė, J., and Devaraj, N.K. (2014b). In Situ Synthesis of Alkenyl Tetrazines for Highly Fluorogenic Bioorthogonal Live-Cell Imaging Probes. Angew. Chem. Int. Ed. *53*, 5805–5809.

Yang, X., Xu, M., Wang, Y., Xia, P., Wang, S., Ye, B., Tong, L., Jiang, T., and Fan, Z. (2014). Molecular mechanism for self-protection against the type VI secretion system in *Vibrio cholerae*. Acta Crystallogr. D Biol. Crystallogr. *70*, 1094–1103.

Zhang, D., de Souza, R.F., Anantharaman, V., Iyer, L.M., and Aravind, L. (2012). Polymorphic toxin systems: Comprehensive characterization of trafficking modes, processing, mechanisms of action, immunity and ecology using comparative genomics. Biol. Direct *7*, 18.

Zheng, J., and Leung, K.Y. (2007). Dissection of a type VI secretion system in *Edwardsiella tarda*. Mol. Microbiol. *66*, 1192–1206.

Zheng, J., Ho, B., and Mekalanos, J.J. (2011). Genetic Analysis of Anti-Amoebae and Anti-Bacterial Activities of the Type VI Secretion System in *Vibrio cholerae*. PLOS ONE *6*, e23876.

Zhou, Y., Tao, J., Yu, H., Ni, J., Zeng, L., Teng, Q., Kim, K.S., Zhao, G.-P., Guo, X., and Yao, Y. (2012). Hcp Family Proteins Secreted via the Type VI Secretion System Coordinately Regulate *Escherichia coli* K1 Interaction with Human Brain Microvascular Endothelial Cells. Infect. Immun. *80*, 1243–1251.

Zoued, A., Durand, E., Bebeacua, C., Brunet, Y.R., Douzi, B., Cambillau, C., Cascales, E., and Journet, L. (2013). TssK Is a Trimeric Cytoplasmic Protein Interacting with Components of Both Phage-like and Membrane Anchoring Complexes of the Type VI Secretion System. J. Biol. Chem. *288*, 27031–27041.

Zoued, A., Durand, E., Brunet, Y.R., Spinelli, S., Douzi, B., Guzzo, M., Flaugnatti, N., Legrand, P., Journet, L., Fronzes, R., et al. (2016). Priming and polymerization of a bacterial contractile tail structure. Nature *531*, 59–63.

Zoued, A., Durand, E., Santin, Y.G., Journet, L., Roussel, A., Cambillau, C., and Cascales, E. (2017). TssA: The cap protein of the Type VI secretion system tail. BioEssays *39*, 1600262.

(2016). Correction for Plamont et al., Small fluorescence-activating and absorption-shifting tag for tunable protein imaging in vivo. Proc. Natl. Acad. Sci. *113*, E1412–E1412.

Abbreviations

AAA	ATPases associated with diverse cellular activities
ADP	adenosine diphosphate
ATP	adenosine triphosphate
BONCAT	bioorthogonal noncanonical amino acid tagging
CFU	colony forming units
CPRG	chlorophenol red-β-D-galactopyranoside
CPU	central processing unit
cryo-EM	cryo-electron microscopy
cryo-ET	cryo-electron tomography
DMSO	dimethyl sulfoxide
DNA	deoxyribonucleic acid
EAEC	enteroaggregative *Escherichia coli*
EM	electron microscopy
FRAP	fluorescence recovery after photobleaching
FUNCAT	fluorescent noncanonical amino acid tagging
FIR	finite impulse response
GPU	graphics processing unit
IAHP	IcmF associated homologous proteins
IBM	individual based model
ICE	integrative and conjugative element
IIR	infinite impulse response
IPTG	isopropyl-β-D-thiogalactopyranoside
MGE	mobile genetic element
MNGC	multinucleated giant cells
NAD	nicotinamide adenine dinucleotide
OD	optical density
PAGE	polyacrylamide gel electrophoresis
PBS	phosphate-buffered saline
PCR	polymerase chain reaction
PG	peptidoglycan
RHS	rearrangement hotspot
RNA	ribonucleic acid
ROS	reactive oxygen species
rpm	revolutions per minute
SIMT	single instruction multiple thread
SPAAC	strain-promoted azide-alkyne cycloaddition
SPI	*Salmonella* pathogenicity island
SPIEDAC	strain promoted inverse electron demand Diels-Alder cycloaddition
T3SS	type III secretion system
T4SS	type IV secretion system
T6SS	type VI secretion system
TCA	trichloroacetic acid

List of Figures

Acknowledgements

At this point I would like to take the opportunity to thank the people who have supported me throughout the endeavor towards my PhD. First, I would like to thank my thesis supervisor Prof. Basler for having allowed me to start my PhD in his group while it was still setting up in Basel. I would also like to thank him for his continuous support of my projects, the frequent inspiring discussions and his encouragement as well as support to attend conferences, courses and seminars whenever possible and also the scientific freedom to explore unrelated topics and ideas. Moreover, his patience was very much appreciated, not only when experiments sometimes simply had a mind of their own, but also when e-mail communications and discussions were continuing until the early morning hours.

Furthermore, I would also like to thank my PhD advisory committee members Prof. Jenal and Prof. Maier for their input to my projects as well as their career advice given during the yearly PAC meetings. Especially, I would like to thank Prof. Maier for taking over the chair of my PhD exam despite additional difficulties. Moreover, I would like to thank Prof. Dehio for providing a rotation project when I started my PhD.

Additionally, I would like to thank the current and former members of our group for the great atmosphere and the scientific as well as the not so scientific discussions, especially Dr. Brackmann, Dr. Ionescu and Dr. Kudryashev for their contributions to setting up the group. Furthermore, I would like to thank Dr. Lin for bearing me in the laboratory when it got late again.

Moreover, I very much appreciated the continuous supply with media and glassware by the 4th floor media kitchen staff as well as the outstanding organization in all matters by Michaela Hanisch and Marina Rüfenacht.

I am deeply grateful for the funding I have received from the “Fellowships for Excellence” program and the Werner Siemens-Foundation for financing the amazing study trips.

Last but not least, I would like to thank my parents and my brother Michael for their continuing support beyond any expectations, without whom this venture would not have been possible.

Chapter IV

Appendix

IV.1 Supplemental Data for Research Article I

The Role of Type VI Secretion System Effectors in Target Cell Lysis and Subsequent Horizontal Gene Transfer

Peter David Ringel,[1] Di Hu,[1,2] and Marek Basler[1,3,*]

[1] Focal Area Infection Biology, Biozentrum, University of Basel, Klingelbergstrasse 50/70, CH - 4056 Basel, Switzerland

[2] Present address: GE Healthcare Shanghai, No. 1 Huatuo Road, Pudong New District, Shanghai, China

[3] Lead Contact

* Correspondence: marek.basler@unibas.ch

Cell Reports, Volume 21, Issue 13, December 26th, 2017, Pages 3927-3940

```
LOCUS       Exported               1668 bp ds-DNA     linear   SYN 29-NOV-2017
DEFINITION  Counterselectable cassette for Acinetobacter baylyi ADP1
ACCESSION   .
VERSION     .
KEYWORDS    Counterselectable cassette
SOURCE      synthetic DNA construct
  ORGANISM  synthetic DNA construct
REFERENCE   1  (bases 1 to 1668)
  AUTHORS   Peter D. Ringel, Di Hu, Marek Basler
  TITLE     The role of Type VI secretion system effectors in target
                  cell lysis and subsequent horizontal gene transfer.
  JOURNAL   Cell Reports
FEATURES             Location/Qualifiers
     source          1..1668
                     /organism="synthetic DNA construct"
                     /mol_type="other DNA"
     misc_feature    1..20
                     /note="Upstream random linker"
     misc_feature    21..143
                     /note="Native rpsL upstream region containing the native
                           promoter"
     CDS             144..518
                     /codon_start=1
                     /note="rpsL'"
                     /translation="MATTNQLIRKGRTTLVEKSKVPALKACPQRRGVCTRVYTTTPKKP
                     NSAMRKVCRVRLTSGFEVSSYIGGEGHNLQEHSVVLIRGGRVKDLPGVRYHTVRGSLDC
                     AGVKDRNQSRSKYGTKRPKK"
     misc_feature    519..561
                     /note="Native rpsL downstream region"
     misc_feature    562..1648
                     /note="From pRSFDuet-1 (Novagen(R) Cat. No. 71341-3)"
     promoter        657..748
                     /gene="bla"
                     /note="P_bla"
     CDS             749..1564
                     /codon_start=1
                     /gene="aph(3')-Ia"
                     /product="aminoglycoside phosphotransferase"
                     /note="confers resistance to kanamycin in bacteria or G418
                     (Geneticin(R)) in eukaryotes"
                     /translation="MSHIQRETSCSRPRLNSNMDADLYGYKWARDNVGQSGATIYRLYG
                     KPDAPELFLKHGKGSVANDVTDEMVRLNWLTEFMPLPTIKHFIRTPDDAWLLTTAIPGK
                     TAFQVLEEYPDSGENIVDALAVFLRRLHSIPVCNCPFNSDRVFRLAQAQSRMNNGLVDA
                     SDFDDERNGWPVEQVWKEMHKLLPFSPDSVVTHGDFSLDNLIFDEGKLIGCIDVGRVGI
                     ADRYQDLAILWNCLGEFSPSLQKRLFQKYGIDNPDMNKLQFHLMLDEFF"
     misc_feature    1649..1668
                     /note="Downstream random linker"
ORIGIN
        1 ctcatagcgc ctttggctac gggctggtca acatttgcta atgatgccga tgttgaccat
       61 tcttgtatct tggcttacaa ttgcatgccc tcaaaaagag gtgttttctt tttgaggttt
      121 ttaattaacg ggagaattgc catatggcta ccaccaacca attaattcgc aaaggccgta
      181 ccacattagt ggagaagagt aaggtgccag cattaaaagc atgccctcag cgccgcggcg
      241 tgtgcacccg cgtgtacaca acaaccccaa agaagccaaa tagtgcaatg cgcaaagtgt
      301 gtcgcgtgcg tttaacaagt ggcttcgagg ttagtagtta tattggcggc gagggccaca
      361 atttacagga acattcagtg gtgttaattc gcggtggtcg cgtgaaggat ttgcctggcg
      421 ttcgctatca cacagtgcgc ggcagtttgg attgcgcagg cgtgaaggac cgcaatcaaa
      481 gtcgcagtaa gtacggcaca aagcgcccaa aaaagtgatt cttagttgtt gaatgccgca
      541 atcctttagc gtttcgcttg ttaccgcttt tgagtgagct gacaccgctc gccgcagtcg
      601 aacgaccgag cgtagcgagt cagtgagcga ggaagcggaa gagcgctgca tgcctatttg
      661 tttatttttc taaatacatt caaatatgta tccgctcatg agacaataac cctgataaat
      721 gcttcaataa tattgaaaaa ggaagagtat gagccatatt caacgggaaa cgtcttgctc
      781 taggccgcga ttaaattcca acatggatgc tgatttatat gggtataaat gggctcgcga
      841 taatgtcggg caatcaggtg cgacaatcta tcgattgtat gggaagcccg atgcgccaga
      901 gttgtttctg aaacatggca aaggtagcgt tgccaatgat gttacagatg agatggtcag
      961 actaaactgg ctgacggaat ttatgcctct tccgaccatc aagcatttta tccgtactcc
     1021 tgatgatgca tggttactca ccactgcgat ccccgggaaa acagcattcc aggtattaga
     1081 agaatatcct gattcaggtg aaaatattgt tgatgcgctg gcagtgttcc tgcgccggtt
     1141 gcattcgatt cctgtttgta attgtccttt taacagcgac cgcgtatttc gtctcgctca
     1201 ggcgcaatca cgaatgaata acggtttggt tgatgcgagt gattttgatg acgagcgtaa
     1261 tggctggcct gttgaacaag tctggaaaga aatgcataaa cttttgccat tctcaccgga
     1321 ttcagtcgtc actcatggtg atttctcact tgataacctt atttttgacg aggggaaatt
     1381 aataggttgt attgatgttg gacgagtcgg aatcgcagac cgataccagg atcttgccat
     1441 cctatggaac tgcctcggtg agttttctcc ttcattacag aaacggcttt ttcaaaaata
     1501 tggtattgat aatcctgata tgaataaatt gcagtttcat ttgatgctcg atgagttttt
     1561 ctaagaatta attcatgagc ggatacatat ttgaatgtat ttagaaaaat aaacaaatag
     1621 gggttccgcg cacatttccc cgaaaagtcc caattctagc gcgtagag
//
```

IV.2 Supplementary Data for Research Article II

Established Microbial Colonies Can Survive Type VI Secretion Assault

David Bruce Borenstein[1], Peter Ringel[2], Marek Basler[2], Ned S. Wingreen[1,3*]

[1] Princeton University, Lewis-Sigler Institute for Integrative Genomics, Princeton, New Jersey, United States of America

[2] Universität Basel, Biozentrum, Basel, Switzerland

[3] Princeton University, Department of Molecular Biology, Princeton, New Jersey, United States of America

* correspondence to: wingreen@princeton.edu

PLoS Computational Biology, Volume 11, Issue 10, October 20th, 2015, e1004520

Simulation details

Lattice geometries

Simulations were run in a 1D linear, 2D triangular, or 3D cubic lattice. Founding populations were well-mixed and occupied all positions within a specified Manhattan radius of the center point. Unless otherwise specified, the founding population size was chosen to be close to $n_0 = 500$ (Table S1). Each lattice was much larger than required for the maximum final population, such that the population never reached the boundary.

Cell displacement

Our model makes the simplifying assumption that all cells can divide (Fig. 2a). If a cell has one or more adjacent vacancies, it will randomly select one of these to divide into. If all neighbor sites are occupied, then one of the occupied neighbors is chosen at random. Next, the nearest vacancy to the original location is located as is the nearest vacancy to the chosen neighbor, as measured by Manhattan distance. If the original cell is closer to a vacancy, the cells along a randomly-selected shortest path from the original cell to the vacancy are pushed leaving the vacancy occupied; otherwise, cells are pushed in a similar way from the chosen neighbor to the nearest vacancy. If both the original cell and the chosen neighbor are equidistant to a vacancy, the tie is broken at random. The benefit of this approach is that it respects the "inertia" of existing cells, while introducing some nondeterminism in order to reduce artifacts from the regular lattice.

Events

Every cell in the system has a number of "behaviors" or events (Table S2). Behaviors may be probabilistic, meaning that sometimes nothing may happen when the event is triggered. During each simulation step, each cell is instructed to trigger its "attack" behavior. The attack events are resolved one at a time in a random order. The remaining cells are then instructed to trigger their "divide" behaviors. Finally, the state is compared to the halt condition(s) for the simulation (specified population reached, specified cell type constitutes a defined fraction of the population etc.). Images and data points are taken before attack events take place.

Integration error

The base unit of time in the simulations is the generation time for a T6S+ strain, defined as $\tau = 1/\alpha_t$. (In simulations with only sensitive individuals, the unit of time $\tau = 1/\alpha_s$.) The definition of the T6S+ generation time implies that, in each time unit, on average every T6S+ individual will divide once. As with many agent-based simulation schemes, special consideration is needed to resolve simultaneous events in a manner that minimizes error. To this end, we employ a null-event scheme [1] in which, each time the simulation updates its state, time is advanced only a fraction of a step. In each of these simulation updates, the system time advances by only a fraction of τ.

To implement this scheme, we first scale the probability of events from probability per τ to probability per simulation update. We define the interval between simulation updates as $\Delta t = \tau\lambda/N$, where N is the total number of lattice positions and λ is a

scaling factor used to control simulation speed and divergence from an "ideal" simulation with perfect separation of events (i.e., no integration error). If $\lambda = 1$ for example, then a lattice that is entirely full of T6S+ cells would have an average of one cell division per simulation update cycle. The parameter λ represents a tradeoff between the speed at which simulations can be run on a computer and the error due to overlapping events. That is, integration error increases with the value of λ (Fig. S1).

Depending on the system configuration, integration error can create an advantage either for a T6S+ or a sensitive strain. As discussed above, every cell is triggered to consider attacking; once these events are resolved, the cells are triggered to consider dividing. In situations with extensive surface area between strains, therefore, $\lambda \gg 1$ would result in extensive killing prior to cell division, creating an advantage for T6S+ strains. However, when large sensitive domains exist, high λ leads to many individuals dividing before they are at risk of being killed; the result is an advantage to sensitive strains.

Using $\lambda > 1$ allowed us to run large-scale simulations at high replicate. Whenever $\lambda > 1$ was used, we first tested the dynamics at smaller scale with $\lambda = 1$ to verify that the observed results were consistent. In all cases, dynamics were qualitatively equivalent to both smaller scale tests and to analytical predictions.

References

1. Chaterjee A, Vlachos D G (2007) An overview of spatial microscopic and accelerated kinetic Monte Carlo methods. *J Computer-Aided Mater. Des.* 14:253-308

Generalization of sensitive domain survival to 1D and 3D

Critical sensitive domain in 1D

Given a linear sensitive domain embedded in an arbitrarily large, 1D T6S+ population, the minimum surviving sensitive domain population n^* is found in a manner analogous to that of a circular sensitive domain in 2D. The birth rate of the sensitive strain scales like the length of the line, and the death rate (due to killing at the interface) is $2\tilde{\gamma}$. Hence the total growth rate is

$$\frac{dn}{dt} = \alpha_s n - 2\tilde{\gamma}. \tag{S1}$$

The observed value of dn/dt is plotted against the predicted value in Fig. S2a; the parameter range is given in Table S3. Solving Eq. S1 for n^*, we find that

$$n^* = \frac{2\tilde{\gamma}}{\alpha_s}, \tag{S2}$$

which is shown as a dashed curve on Fig. S2b.

Critical sensitive domain in 3D

Given a spherical sensitive domain embedded in an arbitrarily large 3D T6S+ population, the minimum surviving sensitive domain population n^* is found in a manner analogous to that of a circular sensitive domain in 2D. We assume that the sensitive domain is spherical. The birth rate of the sensitive strain scales like the total volume of this sphere (i.e., n), and the death rate (due to killing at the interface) scales like its surface area. Hence the total growth rate is

$$\frac{dn}{dt} = \alpha_s n - \tilde{\gamma}\pi^{1/3}(6n)^{2/3}. \tag{S3}$$

The observed value of dn/dt is plotted against the predicted value in Fig. S3a; the parameter range is given in Table S3.

We can predict the transition from sensitive strain extinction to survival. Solving Eq. S3 for n at $dn/dt = 0$, we find that

$$n^* = \frac{36\pi\tilde{\gamma}^3}{\alpha_s^2}, \tag{S4}$$

which is shown as a dashed curve on Fig. S3b.

Mean-field model

The simulations and experiments described in the paper suggest that sensitive domains tend to survive encounters with T6S+ attackers provided those domains have reached a sufficient size. At a population level, this phenomenon is a simple consequence of geometry: population scales with the volume of the sensitive domain, while killing scales only with the surface area. At the scale of individuals, however, the probability of sensitive strain survival is determined by the fraction of neighbors that are capable of

T6S attack. It is therefore useful to consider the conditions required for sensitive strain dominance in the absence of spatial structure. To this end, we consider a mean-field model for a well-mixed system.

Assume that each cell has some fixed number of neighbors z, but that these neighbors are drawn at random from a total population with fraction φ_t of T6S+ individuals and fraction φ_s of sensitive individuals, such that $\varphi_t + \varphi_s = 1$.

The net growth rate for a sensitive individual, i.e. the bare growth rate minus the rate of being attacked and killed depends on the number of T6S+ neighbors. Since each T6S+ individual can attack any of its z neighbors, for a sensitive cell the expected rate of being attacked and killed per T6S+ neighbor is γ/z. The expected growth rates for each type as a function of its randomly sampled neighborhood is

$$g_t = \alpha_t, \tag{S5}$$

$$g_s = \alpha_s - \gamma\varphi_t. \tag{S6}$$

The difference in growth rate between the two strains is

$$\Delta g = \alpha_s - \alpha_t - \gamma\varphi_t. \tag{S7}$$

Sensitive strains are expected to grow more quickly than T6S+ individuals when $\Delta g > 0$, i.e. when

$$\frac{\alpha_s - \alpha_t}{\gamma} > \varphi_t. \tag{S8}$$

If one assumes T6S to incur a non-zero cost, such that $\alpha_s - \alpha_t > 0$, the mean-field model implies that sensitive strains grow faster than T6S+ strains so long as the T6S+ fraction φ_t is not too large. This result holds for a system of any dimensionality. The spatial structure of populations exaggerates this effect by decreasing the probability of sensitive individuals having T6S+ neighbors. Space also allows an arbitrarily small global fraction of the sensitive strain to survive, so long as they have a sufficiently large local population somewhere in the community. For this reason, the spatial model allows sensitive domains to survive attack even if they grow more slowly than T6S+ competitors, whereas this is not possible in the mean-field model.

The impact of nutrient depletion on T6S-mediated population dynamics

Nutrient depletion model

Microbial communities deplete nutrients from their environment as they grow. To explore the impact of nutrient depletion, we studied a simple resource-limited variant of our competition model. The variant is identical to the original model except that we now assume each lattice site starts with a finite nutrient supply, and thus a finite "division capacity" K. Every time a cell divides at a particular location, the nutrient supply k at that site is decreased by one unit: $k \to k-1$. Once the local nutrient supply reaches zero, no further cell divisions can take place at that location (Fig. S6). Thus every lattice site can support exactly K cell-division events.

Analysis of growth dynamics

To understand the effect of resource depletion on T6S-mediated competition, it is first helpful to understand its effect on growth in the absence of killing. In this case, each cell division leads to exactly one cell being placed in a previously unoccupied lattice site. By assumption, this newly occupied lattice site has K cell divisions remaining. All other previously occupied lattice sites remain occupied; individual cells may change lattice sites, but overall there is the same number of sites with k cell divisions remaining, except for the new site with K divisions remaining, and the site of the cell-division event, for which $k \to k-1$.

We ignore the case of $K = 1$ (i.e., fixed active population), which implies linear population growth. For all $K > 1$, we can classify all occupied lattice sites by the number of cell divisions remaining. We can then stratify the cell population by the remaining capacity of the site each cell occupies. Let p_k represent the number of cells that occupy lattice sites with k cell divisions remaining, and let us consider the average behavior of p_k.

Let α be the growth rate for cells, i.e. cells on sites with $k > 0$ divide at a rate α. The population of cells on new, capacity K sites increases due to all cell divisions, but decreases due to division of cells on capacity K sites. Hence, on average,

$$\frac{dp_K}{dt} = \alpha \sum_{k=1}^{K-1} p_k. \tag{S9}$$

The populations of all other cell classes p_k likewise decrease due to their own divisions and increase due to divisions of the next higher class p_{k+1}:

$$\frac{dp_k}{dt} = \alpha \left(p_{k+1} - p_k\right), \qquad 0 < k < K. \tag{S10}$$

Setting aside depleted sites (p_0) for the moment, this relation can be expressed by the matrix equation

$$\frac{d\mathbf{p}}{dt} = L\mathbf{p}, \tag{S11}$$

where $\mathbf{p} = (p_1, p_2, \ldots, p_K)$ and

$$L = \begin{pmatrix} -\alpha & \alpha & \ldots & 0 & 0 & 0 \\ \vdots & \vdots & \ddots & \vdots & \vdots & \vdots \\ 0 & 0 & \ldots & -\alpha & \alpha & 0 \\ \alpha & \alpha & \ldots & \alpha & \alpha & 0 \end{pmatrix}. \tag{S12}$$

We observe numerically that the matrix L always has exactly one eigenvalue with positive real part (Table S4). The growth of the population is therefore driven by this dominant eigenvalue. To understand the dynamics of the system, therefore, we seek a positive eigenvalue λ of L such that

$$\frac{d\mathbf{p}}{dt} = \lambda\mathbf{p}. \tag{S13}$$

We further simplify the system by factoring out the growth rate α, defining $\hat{L} = L/\alpha$ and $\mu = \lambda/\alpha$, such that

$$\hat{L}\mathbf{p} = \mu\mathbf{p}. \tag{S14}$$

We make the ansatz that at long times the population structure approaches a geometric series

$$\mathbf{p} = \left(1,\ \beta,\ \ldots, \beta^{k-2}, \beta^{k-1}\right). \tag{S15}$$

Substituting this ansatz into Eq. S14, we obtain the relation

$$\begin{pmatrix} -1 & 1 & \ldots & 0 & 0 & 0 \\ \vdots & \vdots & \ddots & \vdots & \vdots & \vdots \\ 0 & 0 & \ldots & -1 & 1 & 0 \\ 1 & 1 & \ldots & 1 & 1 & 0 \end{pmatrix} \begin{pmatrix} 1 \\ \beta \\ \vdots \\ \beta^{k-2} \\ \beta^{k-1} \end{pmatrix} = \mu \begin{pmatrix} 1 \\ \beta \\ \vdots \\ \beta^{k-2} \\ \beta^{k-1} \end{pmatrix}. \tag{S16}$$

For the last line (corresponding to p_K), we have

$$1 + \sum_{k=1}^{K-2} \beta^k = \mu\beta^{K-1}, \tag{S17}$$

and for all other lines we obtain

$$\beta = \mu + 1. \tag{S18}$$

Substituting Eq. S18 into Eq. S17, we obtain the polynomial expression for the eigenvalues of $\hat{L}$

$$1 + \sum_{k=1}^{K-2} (\mu + 1)^k = \mu (\mu + 1)^{K-1}. \tag{S19}$$

The largest root of Eq. S19 (by real value) is shown in Table S4. The table also shows the dominant eigenvalues of the matrix $\hat{L}$, demonstrating agreement between the two, and confirming the ansatz (Eq. S15) for the asymptotic population structure.

We observe from Table S4 that μ approaches 1 with with increasing K. We therefore write $\mu = 1 - \epsilon$ and expand Eq. S19 to obtain the estimate

$$\mu(K) \approx 1 - 2^{-K}. \tag{S20}$$

Turning our attention to the inactive population p_0, we note that p_0 grows as a result of cell division by subpopulation p_1. Since p_1 divides at a rate α, we have

$$\frac{dp_0}{dt} = \alpha p_1. \tag{S21}$$

At long times, p_1 grows at a rate set by the dominant eigenvalue. At long times, therefore,

$$\frac{dp_1}{dt} \longrightarrow \lambda p_1. \tag{S22}$$

By inspection of these two equations, we observe that for long times

$$\frac{dp_0}{dt} \longrightarrow \frac{\alpha}{\lambda}\frac{dp_1}{dt}, \tag{S23}$$

which implies

$$p_0 \longrightarrow \frac{\alpha}{\lambda} p_1 = \frac{1}{\mu} p_1. \tag{S24}$$

Substituting Eq. S20 and the ansatz from Eq. S15 into Eq. S24 and simplifying, we obtain the estimate

$$p_0 = \frac{1}{2^K}. \tag{S25}$$

Fig. S7a shows predicted and observed population growth over time, both without and with nutrient depletion ($K = 2$). As predicted, nutrient-limited populations grow exponentially, albeit at a slower rate than non-limited populations. The inactive population fraction asymptotically approaches zero as K increases, as predicted by Eq. S25 (Fig. S7b).

Effects of nutrient depletion on T6S competition dynamics

Fig. S8 presents the results of competition between T6S+ and sensitive individuals during a range expansion. The initial conditions and parameters are identical to those used for Figs. 4a-d. In the absence of nutrient limitation, the overall population grows more quickly than when nutrients are limited (Fig. S8a). Nevertheless, even in a

strongly nutrient-limited case ($K = 2$), the qualitative dynamics of the competition are essentially identical whether nutrients are limited or not (Fig. S8b).

Since nutrients are depleted from the inside of a colony outward, might varying the initial microcolony size reveal differences between nutrient-limited and non-limited conditions? Fig. S9 explores competitive dynamics in range expansions for which the cells are initially dispersed into clusters of a specific size. Larger clusters provide an advantage to sensitive cells by giving them more time to form large domains before T6S assault. However, no qualitative difference was observed between nutrient-limited and non-limited conditions. Intuitively, because of exponential growth, only a small fraction of the population is ever in the p_0 state for which division is not possible, so the effects of nutrient depletion are small.

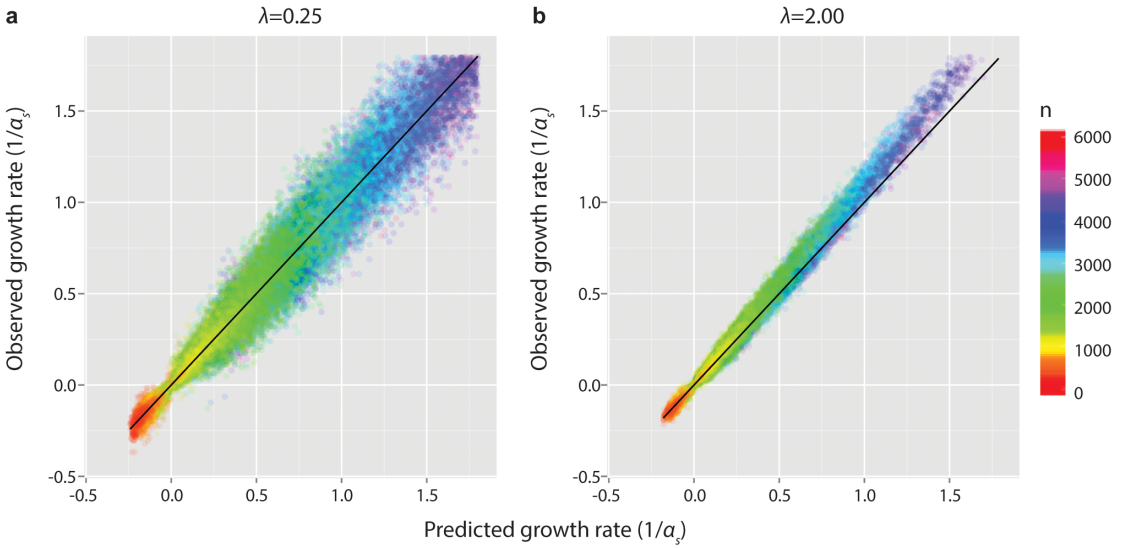

S1 Fig. The effect of time step on simulation error at large population in 1D.
(a) Plot of simulated growth rates (y-axis) vs. predicted growth rates from Eq. S1 (x-axis) for a sensitive domain with simulation timestep multiplier $\lambda = 0.25$. Each point represents the average, over identical conditions, from 5 simulations. (b) The same plot, averaging over 20 simulations with $\lambda = 2$.

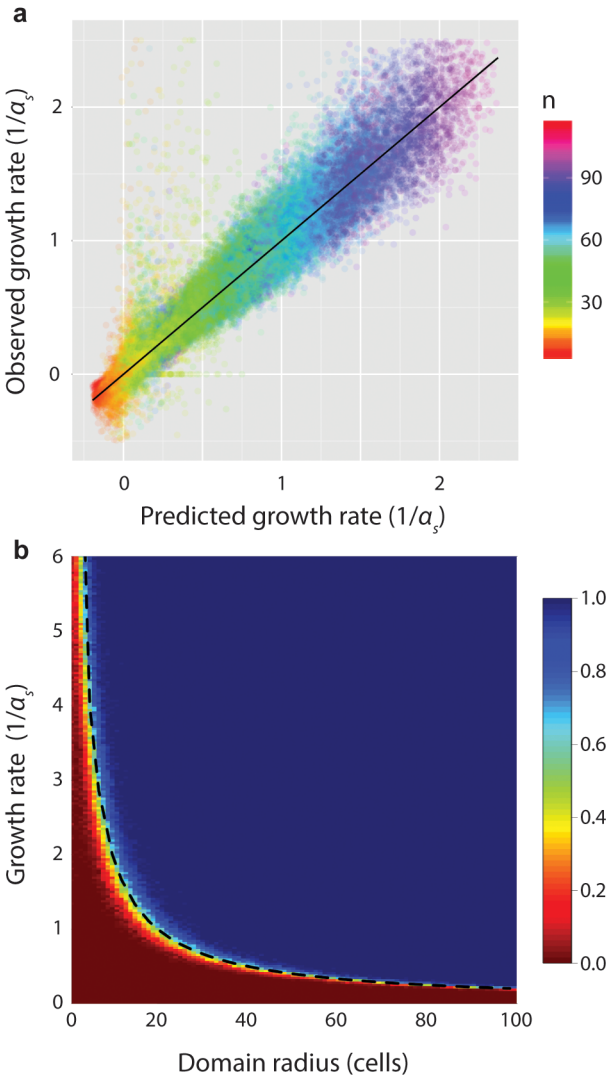

S2 Fig. Sensitive domain growth dynamics in 1D.
(a) Comparison of simulation results (y-axis) to predicted values from Eq. S1 (x-axis) for rate of growth of a 1D sensitive domain. Points represent the average, by sensitive population, across all simulations with the same parameters (40 per condition). Color represents domain radius; black line is $y = x$. Simulation timestep multiplier $\lambda = 0.01$. (b) Heat map of the probability that a 1D sensitive domain surrounded by T6S+ competitors achieves steady growth, as a function of sensitive strain growth rate and initial radius of the sensitive domain. Dashed line indicates predicted critical parameter values based on Eq. S1. Attack rate $\tilde{\gamma} = 20$; timestep multiplier $\lambda = 0.5$. Interpolated from 1.9 million simulations.

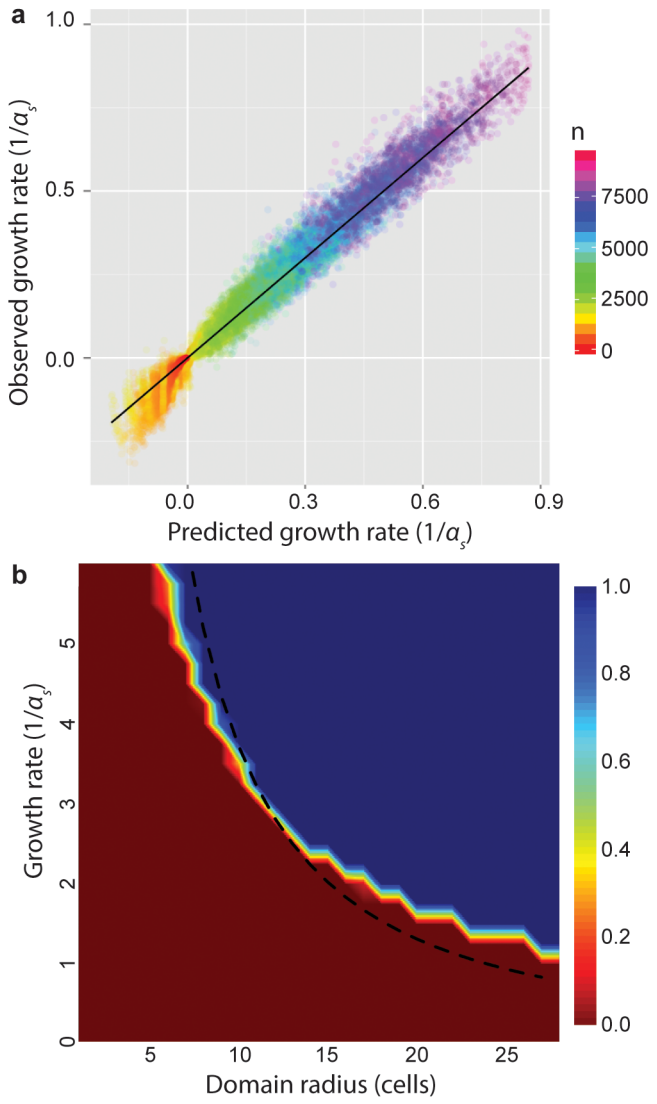

S3 Fig. Sensitive domain growth dynamics in 3D.
(a) Comparison of simulation results (y-axis) to predicted values from Eq. S3 (x-axis) for rate of growth of a 3D sensitive domain. Points represent the average, by sensitive population, across all simulations with the same parameters (5 per condition; $\lambda = 2.0$). Color represents domain radius; black line is $y = x$. (b) Heat map of the probability that a 3D sensitive domain surrounded by T6S+ competitors achieves steady growth, as a function of sensitive strain growth rate and initial radius of the sensitive domain. Dashed curve indicates predicted critical parameter values based on Eq. S3. Attack rate $\tilde{\gamma} = 8$; interpolated from 6,090 simulations ($\lambda = 2000$).

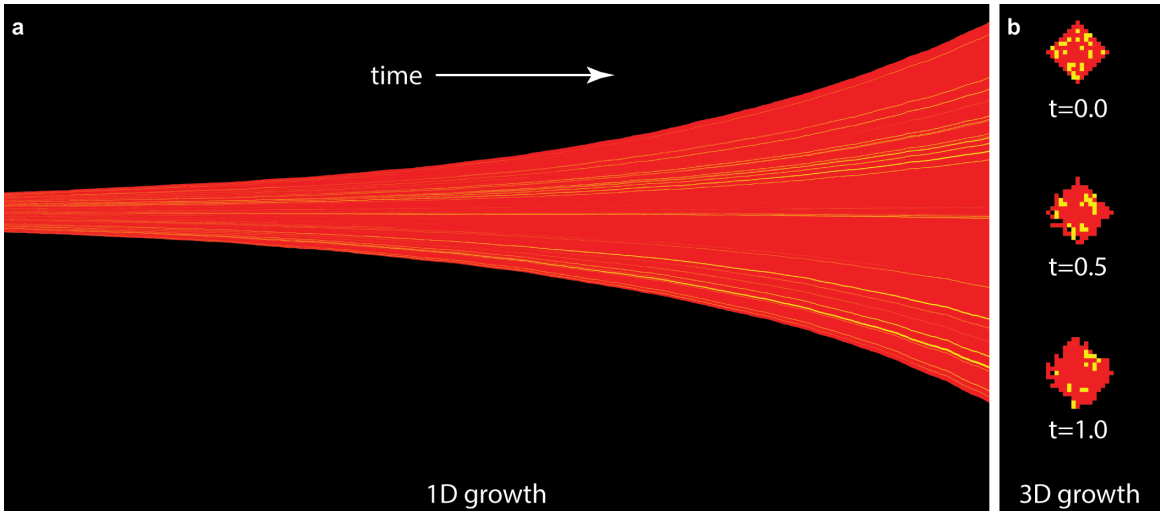

S4 Fig. Range expansion of two competing T6S+ strains.
Each strain kills only individuals of the other type; the two strains are otherwise identical. Initial inoculum is well-mixed; starting minority (yellow) fraction is 25%. For each strain, the growth rate is $\alpha_t = 1$ and the attack rate is $\gamma = 2$. (a) Kymograph of a 1D competition; time is shown on the x-axis. Initial innoculum $r_0 = 500$; timestep multiplier $\lambda = 1$. (b) Center slice through a 3D competition. Initial innoculum $r_0 = 6$; timestep multiplier $\lambda = 2$.

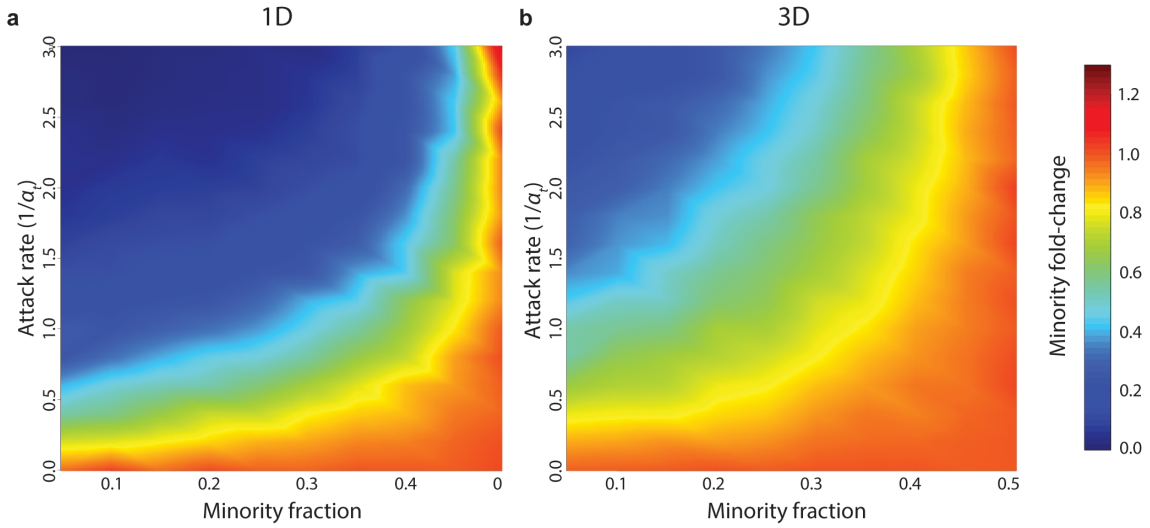

S5 Fig. Fold-change in minority fraction after 10-fold growth in population of two competing T6S+ strains.
For each strain, the growth rate is $\alpha_t = 1$. (a) Competition in 1D. Initial innoculum $r_0 = 500$; timestep multiplier $\lambda = 1$. (b) Competition in 3D. Initial innoculum $r_0 = 6$; timestep multiplier $\lambda = 1$.

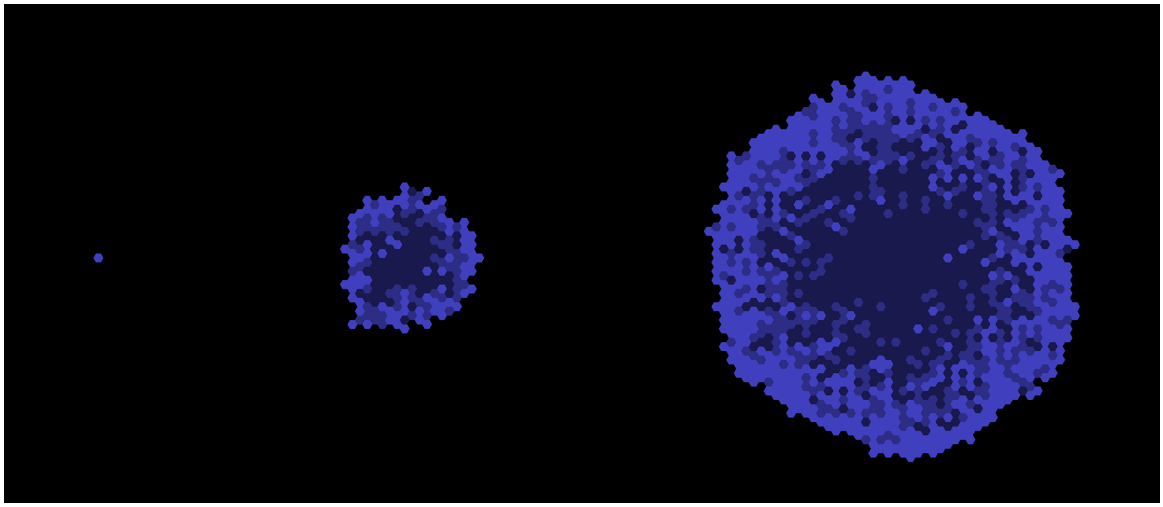

S6 Fig. Time series of nutrient-limited population expansion (*K* = *2*).
Time points shown are $t = 0$ (left), $t = 9$ (middle), and $t = 12$ (right). Lighter color corresponds to higher nutrient concentration. Simulation scaling factor $\lambda = 100$.

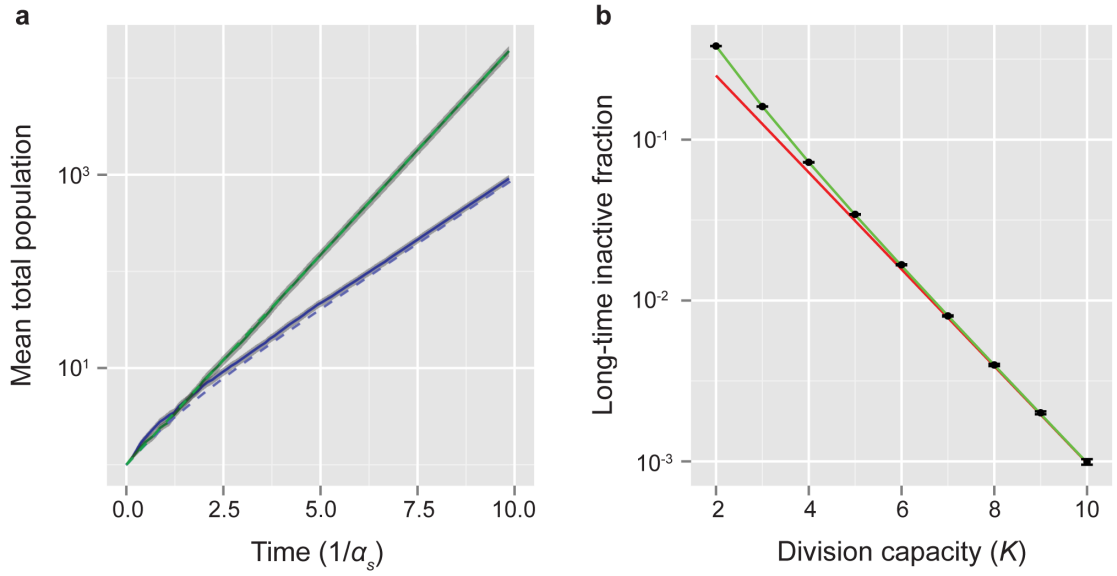

S7 Fig. Nutrient-limited population growth.
(a) Population over time for nutrient-limited growth ($K = 2$, blue) and non-limited growth (green). Simulation results shown as solid lines ($n = 50$ per condition, ribbon = 1 S.E.); numerical estimate for deterministic exponential growth (Eq. S11 for limited case, simple exponential growth for non-limited) shown as dashed lines. (b) Long-time inactive fraction as a function of division capacity K. Black points: final inactive fraction after range expansion from single cell to radius $r = 164$ ($n = 10$ per condition, bar = 1 S.E.). Green line: numerical estimate (from Eq. S11 and S21) for deterministic growth. Red line: analytical prediction (Eq. S25). For all simulations, scaling factor $\lambda = 100$.

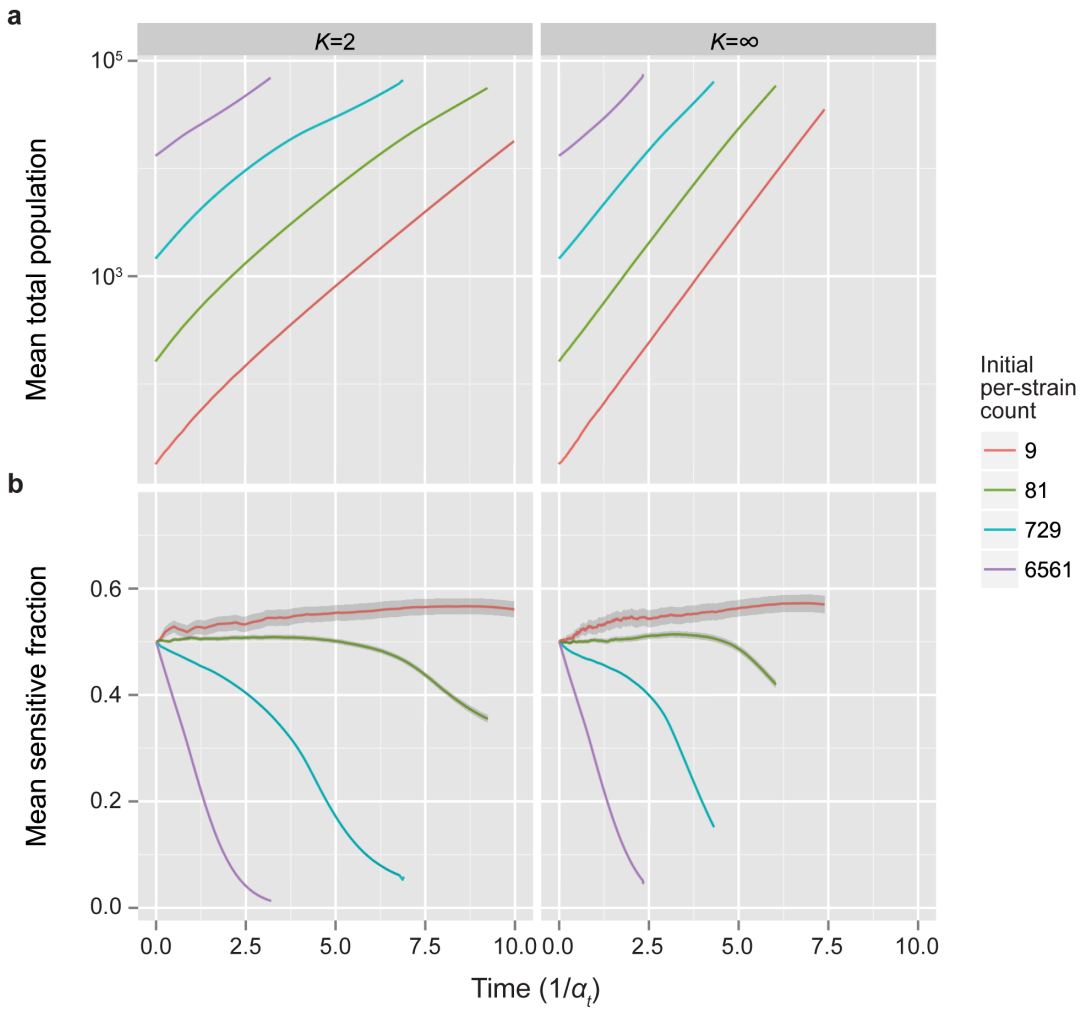

S8 Fig. Nutrient limitation does not qualitatively alter dynamics of simulated T6S-mediated competition.
Populations begin with an equal number of T6S+ and sensitive individuals at a specified per-species population, scattered over an $r_0 = 84$ domain, and grow until the radius has doubled. (a) Population over time for nutrient-limited growth ($K = 2$, left) and non-limited growth (right). Error ribbons smaller than data curve. (b) Mean sensitive fraction over time for nutrient-limited growth ($K = 2$, left) and non-limited growth (right). For both panels, $n = 40$ per condition; scaling factor $\lambda = 100$. Ribbons = 1 S.E.

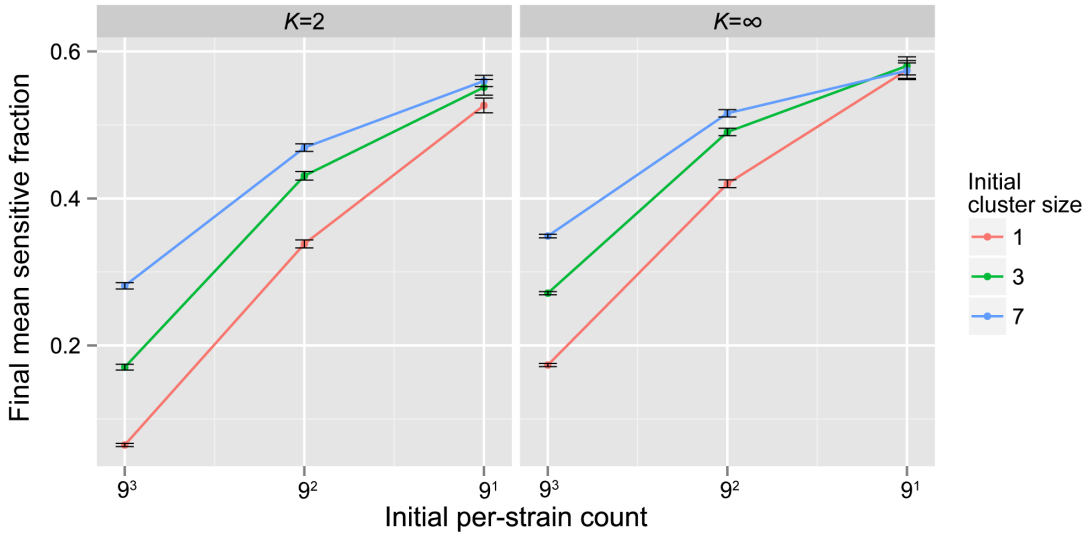

S9 Fig. Effect of initial T6-sensitive cluster size on dynamics of simulated T6S-mediated competition. Initial populations are placed in compact groups of m = 1, 3, or 7 individuals, and with strict separation between these clusters. Shown is final sensitive fraction as a function of initial per-species count. Populations begin with a specified per-species population, scattered over an r_0 = 84 domain, and grow until the radius has doubled. n = 90 per condition; scaling factor λ = 100. Error bars = 1 S.E.

Table S1. Simulation geometries for range expansions.

Lattice	Inoculum population	Inoculum radius
1D (linear)	500	250
2D (triangular)	469	12
3D (cubic)	377	6

Table S2. Simulation behavior definitions.

Name	T6S- (sensitive)	T6S+ (self-immune)
`attack`	Do nothing.	With probability γ, trigger the `be-attacked` behavior in one occupied neighbor (if one exists); otherwise, do nothing.
`be-attacked`	Die.	Do nothing.
`reproduce`	With probability α_s, divide into an adjacent space; otherwise do nothing.	With probability α_t, divide into an adjacent space; otherwise do nothing.

Table S3. Parameter ranges for comparison of predicted to simulated rates of sensitive strain growth.

	Attack rate ($\tilde{\gamma}$)			Sensitive strain growth rate (α_s)			Inoculum radius (r_0)		
	min	max	step	min	max	step	min	max	step
1D	1	20	1	1	4	1	1	20	1
2D	0	14	2	1	4	1	3	11	2
3D	0	14	2	1	4	1	3	11	2

Table S4. Active population growth rates for various division capacities.

Division capacity (K)	Highest root of μ	Dominant eigenvalue of $\hat{L}$
2	0.618	0.618
3	0.839	0.839
4	0.928	0.928
5	0.966	0.966